

**I: Seismotectonics of the San Jacinto Fault Zone and the
Anza Seismic Gap**

**II: Imaging the Shallow Crust in Volcanic Areas with
Earthquake Shear Waves**

Thesis by
Christopher O'Neill Sanders

In Partial Fulfillment of the Requirements
for the Degree of
Doctor of Philosophy

California Institute of Technology
Pasadena, California

1987

(submitted September 10, 1986)

Acknowledgements

I particularly wish to acknowledge two people who have influenced me most in my scientific career; my undergraduate advisor, David B. Slemmons, and my graduate thesis advisor, Hiroo Kanamori. Burt encouraged me to stay in the geological sciences, and his enthusiasm and competence were valuable guides for a young student. Hiroo has, by example, opened my eyes to the value of careful but imaginative science, and his insights and interest were invaluable to this thesis.

I lovingly acknowledge the love and support of my parents, O'Neill and Catharine Sanders, and my brothers, Scott and Eric. Life in this family is a happy experience, and we each have learned to follow our dreams and to have confidence that others are interested in our lives and care for us. My grandparents Robert and Alice Downer, Eunice and Curly Ingram, and David and Clara Sanders are appreciated as well for their loving interest and support.

My years in Pasadena have been made more comfortable by the friendliness of many people. Charles and Midge Downer, Suzanne, Christopher, Dan, and Jay were pleasant company on many afternoons. My many good friends in the Seismo Lab and in the Division are all thanked for the comfortable environment they have created. Gene Humphries and John Louie were helpful in many ways, and Bob Svendsen kindly helped program plotting routines. Harold Magistrale and Phyllis Ho-Liu were enjoyable collaborators on two projects. Marianne Walck was a helpful editor. Jiajun, Allison, Cindy, and Phyllis were unselfish number pasters. Kerry and Laurie Sieh were friendly to a new graduate student, and I enjoyed discussions on neotectonics with Kerry. Karen McNally encouraged work in the Anza area. I enjoyed work with Alan and Flori Ryall during my leave-of-absence. The years of undergraduate classwork were made bearable by the company of Cherie Valcarce.

I thank my thesis committee, Clarence Allen, Rob Clayton, Tom Heaton, Hiroo Kanamori, and Kerry Sieh, for their comments and suggestions. I thank Don Anderson for allowing me to begin research on the Anza seismic gap as a project for his class Physics of the Earth's Interior. I thank Brad Hager for suggestions on Chapter 3. Lucy Jones showed me how to retrieve earthquake data on the U.S.G.S. computer.

Joyfully, I acknowledge the love and affection of Susan Boundy. Without her care and companionship my last few years in Pasadena would have been difficult indeed.

Abstract

Chapters 1, 2, and 3 consider the characteristics of the earthquake stress release along the San Jacinto fault zone and in the San Jacinto-southern San Andreas fault region. In Chapter 1 we locate the historic $M \geq 6$ earthquakes in the San Jacinto fault zone. Intensity data are used to locate earthquakes in 1899, 1918, and 1923. Limited seismic data are also used for the 1923 location. Southern California stations and empirical station corrections obtained from recent small events are used to locate earthquakes in 1937, 1942, and 1954 and their aftershocks and preshocks. The locations and rupture zones of these earthquakes, including the 1968 Borrego Mountain earthquake, help define patterns of large earthquake occurrence in the fault zone and sections of fault which have not ruptured historically. One historic seismic-slip gap is located in the central San Jacinto fault zone near the town of Anza.

We present in Chapter 2 details of the small earthquake stress release in the San Jacinto fault zone near Anza. Small earthquake epicenters near the Anza seismic gap define a 18-km quiescent segment of fault which is bounded to the northwest and southeast by areas of relatively high seismicity. Recent moderate earthquakes on and near the San Jacinto fault in the gap and their relatively depressed aftershock activity indicate that the fault is seismogenic and highly stressed but generally locked by some mechanism. The locked nature of the fault may be due to relatively high stress normal to the fault resulting from the convergent geometries of the local, active, discontinuous faults and the oblique orientation of the regional maximum compressive stress. Strain is not being relieved by aseismic fault creep. A swarm of small earthquakes in the crustal block 13 km southwest of the Anza gap beneath the Cahuilla Valley recently released stress in an area which was previously highly active before the 1918 (M 6.8) and 1937 (M_L 5.9) earthquakes. The occurrence of these periods of increased seismicity near Cahuilla in the years immediately before the nearby large earthquakes and the recent swarm suggest that the ground beneath Cahuilla may be acting as a stress meter signaling the presence of high stresses before large local earthquakes. The length of the quiescent fault segment suggests potential for an earthquake of about M 6.5 if the entire segment ruptures at once.

In Chapter 3 we investigate variations in the depths of earthquakes in the San Jacinto fault zone and in the San Jacinto-southern San Andreas fault region. We observe that the maximum depths of earthquakes in the San Jacinto fault zone vary from 20 to 10 km along strike. The earthquake hypocenters are progressively shallower nearer to the Imperial Valley region of high heat flow. This observation illustrates the effect heat flow has on the maximum thickness of the seismogenic zone. In addition, earthquakes occur predominantly in a band along the bottom of the seismogenic zone;

few earthquakes occur in the shallower portions of the fault zone. This implies that shear stresses must be greater in the deeper parts of the brittle fault zone than in the shallower fault zone. This implies that loading of the brittle crust occurs by aseismic displacement along deeper extensions of the brittle fault zones. Furthermore, we observe that deeper earthquakes in the region of the San Jacinto and southern San Andreas faults occur principally in the major fault zones and that shallow earthquakes occur principally in the adjacent crust. Interpretation of these observations is less clear, but they, in combination with other observations about deep and shallow earthquakes near Anza on the San Jacinto fault, seem to suggest that stresses in the deep brittle fault zone and in the adjacent crust are similar and that stresses in the shallow fault zone are low.

In Chapter 4 shear-wave seismograms are used to image anomalous attenuation regions in the shallow crust beneath the Coso volcanic/geothermal region of eastern California. Vertical-component seismograms archived by CUSP (Caltech-USGS Seismic Processor) for earthquakes which occurred in the Indian Wells Valley-Coso-southern Sierra Nevada region from October 1983 to February 1984 were analyzed to determine whether attenuated S_v -wave signals were present along some raypaths. Signals of this type have previously been documented in the Long Valley magmatic area and elsewhere. We have analyzed sixteen small earthquakes with S_v signals that change considerably with azimuth and take-off angle. Forward modeling and a tomographic inversion illuminate several small regions within a 20 by 30 km area of the shallow crust (some shallower than 5 km) which severely attenuate S waves passing through them. This area is beneath the Indian Wells Valley south of the Coso Range and is coincident with the epicentral location of earthquake swarms which occurred in 1982-1983. This swarm sequence began in a centralized cluster which, with time, became two clusters that migrated several kilometers north and south. No attenuating effects were seen for rays passing beneath the Coso geothermal area above about 5 km depth.

Table of Contents

Acknowledgements	ii
Abstract	iii
 Part I: Seismotectonics of the San Jacinto Fault Zone and the Anza Seismic Gap	
 Introduction	 2
 Chapter 1: Historic Large Earthquakes in the San Jacinto Fault Zone	
1.1 Introduction	5
1.2 Earthquakes Northwest of Anza	6
1.3 1923 Earthquake	8
1.4 1899 and 1918 Earthquakes	9
1.5 Earthquakes Southeast of Anza	11
1.6 Relocating the 1937, 1942, and 1954 Earthquakes: Introduction	11
1.7 Relocating the 1937, 1942, and 1954 Earthquakes: Technique	13
1.8 1937 Buck Ridge Earthquake	20
1.9 Observations on the Use of Older CIT Catalog Locations and Archived Data	25
1.10 1954 Arroyo Salada Earthquake	33
1.11 1942 Earthquake	35
1.12 1968 Borrego Mountain and 1969 Coyote Mountain Earthquakes	40
1.13 Relative Sizes of the 1937, 1942, 1954, and 1968 Earthquakes	45
1.14 Older Large Earthquakes	48
1.15 Discussion	49
1.16 Conclusions	51
 Chapter 2: Small Earthquakes in the San Jacinto Fault Zone and the Anza Seismic Gap	
2.1 Introduction	54
2.2 Seismicity in the San Jacinto Fault Zone	56
2.3 Subsurface Fault Geometry in the Central San Jacinto Fault Zone	58
2.4 Recent Moderate Earthquakes Near the Anza Gap	72
2.5 Cahuilla Swarm	78
2.6 Local Geologic Structure	86
2.7 Regional and Local Strain	90

2.8	Implications of Focal Mechanisms	92
2.9	Fault Creep Near Anza	94
2.10	Conclusions	95
2.11	Appendix	97

Chapter 3: Depths of Earthquakes in the San Jacinto-Southern San Andreas Region

3.1	Introduction	108
3.2	Data	108
3.3	Shear Strength of the Crust and the Depths of Earthquakes	110
3.4	Depths of Earthquakes in the San Jacinto Fault Zone	119
3.5	Deep and Shallow Seismicity in the San Jacinto-Southern San Andreas Region	124
3.6	Conclusions	127
3.7	References for Part I	138

Part II: Imaging the Shallow Crust in Volcanic Areas with Earthquake Shear Waves

Chapter 4: Anomalous S-Wave Attenuation in the Coso Region, California

4.1	Introduction	145
4.2	Long Valley Caldera, California	147
4.3	Coso Seismogram Analysis	152
4.4	Earthquake Locations	157
4.5	Results	160
4.6	Tomographic Inversion	168
4.7	Earthquake Swarms	175
4.8	Conclusions	175
4.9	References	179

**Part I: Seismotectonics of the San Jacinto Fault Zone
and the Anza Seismic Gap**

Introduction

The San Jacinto fault zone is a major member of the group of faults which accommodate relative dextral motion of the Pacific and North American lithospheric plates in southernmost California. Over half of the displacement along this section of the plate boundary (Figure 0.1), which is calculated to accumulate at about $5\frac{1}{2}$ cm/yr (Minster and Jordan, 1978), is taken up along the San Andreas ($2\frac{1}{2}$ cm/yr; Weldon and Sieh, 1985) and San Jacinto faults (1 cm/yr; Sharp, 1967, 1981). The southern San Andreas fault zone appears to have accommodated about 240 km of right-slip displacement in the past 30 my, while the San Jacinto fault zone has accommodated about 29 km of displacement (Sharp, 1967; Hill, 1984). Major studies of the San Jacinto fault zone include that by Sharp (1967) whose extensive mapping of the central section of the fault zone identified geologic relations with which to estimate the total offset and recent slip rate along the fault zone. The Coyote Creek fault of the southern San Jacinto fault zone was extensively studied following the 1968 Borrego Mountain earthquake (*U. S. Geol. Surv. Prof. Paper 787*, 1972). Thatcher et al. (1975) summarized the major historic earthquakes in the San Jacinto fault zone and identified seismic-slip gaps, including one near the town of Anza. The high rate of small earthquake occurrence on the San Jacinto fault zone near Anza attracted the attention of seismologists who conducted seismic field studies of the area (Arabasz et al., 1970), analyzed moderate earthquakes on the fault (Hartzell and Brune, 1979), and used the seismicity patterns to define a seismic gap in southern California (Kanamori, 1980a). An M_L 5.5 earthquake in February 1980 on the San Jacinto fault near Anza spurred further interest in this section of the fault (Sanders et al., 1981; Sanders and Kanamori, 1982, 1984; Given, 1983). Chapters 1 and 2 of this thesis began as a result of interest in the Anza section of the San Jacinto fault zone inspired by questions from and discussions with Professor Hiroo Kanamori. Most of the contents of these chapters are published in Sanders and Kanamori (1984) and Sanders, Magistrale, and Kanamori (1986). Parts

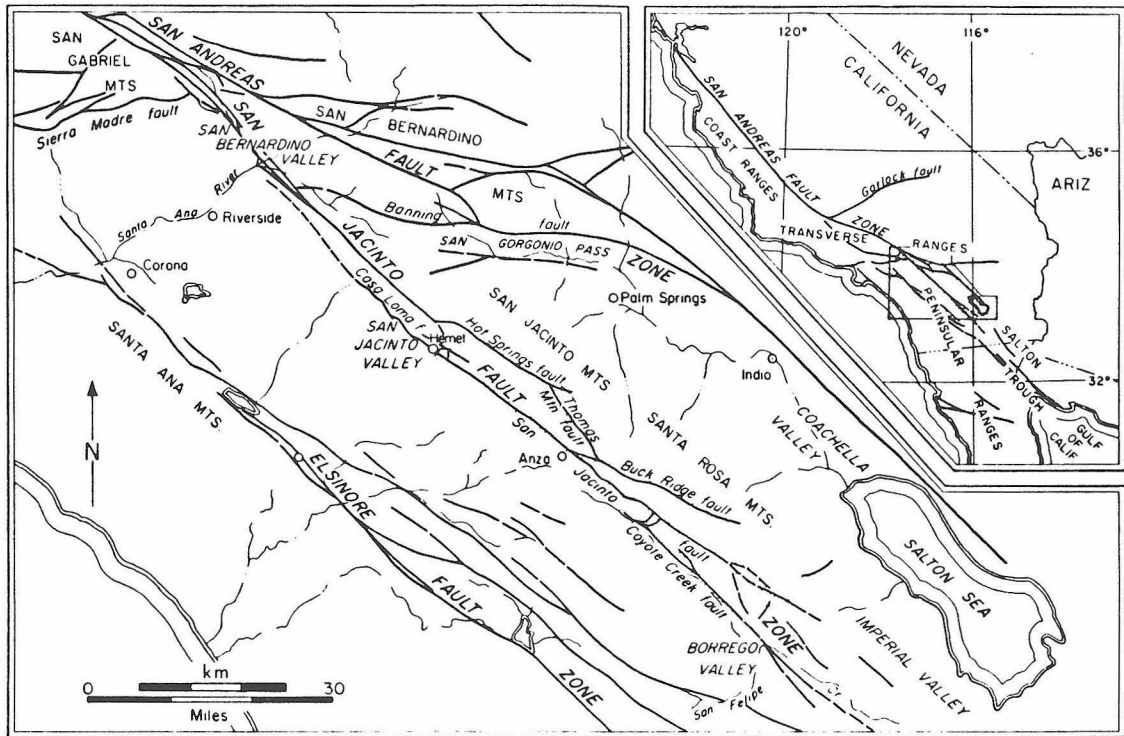


Figure 0.1. San Andreas and San Jacinto fault zones in southern California (from Sharp, 1967).

of Chapter 1 were also done in collaboration with H. Magistrale.

Chapter 1 of this thesis deals with the problem of the locations of the large historic earthquakes in and near the San Jacinto fault zone. Most of these locations were previously only approximate, and important information on the particular fault strand that ruptured and the length and direction of rupture were unknown. We have tried in this chapter to determine epicenters of these earthquakes as precisely as possible given the available data. These locations are useful for evaluation of the recent seismic history of the fault zone and for evaluation of the seismic hazard along different segments of the fault zone.

In Chapter 2 we study small earthquakes in the San Jacinto fault zone, particularly near Anza, using data obtained by the CalTech-USGS southern California seismic array since about 1976. In this chapter we attempt to define and explain small earthquake occurrence on and near the Anza seismic gap. In this analysis we seek to understand relationships between the small earthquake stress release, historic large earthquakes, local structural geology, and regional and local strain. Since this stretch of the San Jacinto fault zone has been recognized as a historic seismic-slip gap (Thatcher et al., 1975) and a recent seismicity gap (Kanamori, 1980*a*), knowledge of the patterns of small earthquake stress release in the area is important for understanding phenomena precursory to a large earthquake ($M 6\frac{1}{2}$) in the gap.

Chapter 3 of this thesis deals with the depths of recent, well-located earthquakes in the San Jacinto fault zone and in the San Jacinto-southern San Andreas fault region. This study originated from observations of cross-sectional plots of earthquake hypocenters in the San Jacinto fault zone and depth-slice maps of hypocenters in the San Jacinto-southern San Andreas fault region. Major lateral changes in the maximum depth of earthquake occurrence, both in the San Jacinto fault zone and in the region, required further investigation and explanation. Some of the observations discussed in this chapter have implications about the manner of strain accumulation on the San Jacinto and southern San Andreas faults.

Chapter 1

Historical Large Earthquakes in the San Jacinto Fault Zone

1.1 Introduction

The history of large earthquakes associated with the San Jacinto fault zone is important for identifying the areas of greatest and least historic stress release and for indicating the maximum size of earthquakes associated with the faults in this zone. All large earthquakes which have occurred in or near this fault zone since 1890 are known, though some locations are uncertain. No earlier large events are reported (Topozada et al., 1981), but the early historical record is undoubtedly incomplete.

In this chapter we attempt to determine precise epicenters for and approximate rupture zones of the historic $M \geq 6$ earthquakes in the San Jacinto fault zone. The events which occurred prior to 1923 are located solely from published reports of shaking intensity. In some cases, these reports, usually from towns very near the source, can be used to determine the earthquake source with some confidence, although determination of the exact fault strand which ruptured is difficult. Since about 1923 arrival time data from at least one recording seismograph in Pasadena are available, and since 1932 the number of stations has increased to seven or more in the southern California region. We use this travel time information to determine precise epicentral locations for the post-1932 earthquakes.

In evaluating the seismic potential of the San Jacinto fault zone, which is composed of many en echelon, branching, and overlapping fault strands, and where earthquake size seems to be controlled by fault segmentation, knowledge of which segments have broken historically is very important. Observation and theory of seismic gaps suggest that segments of the fault zone which have ruptured more recently have less likelihood of rupturing again soon.

Since this seismological study of the San Jacinto fault zone grew naturally from

an initial study of the Anza seismic gap (Chapter 2), which is located in the central part of the 180 km long fault zone, the discussion of the large historical earthquakes will be separated into two parts, those large events which occurred northwest of the Anza gap and those which occurred southeast. This simple geographic division also turns out to be a temporal division with the three events between 1899 and 1923 occurring northwest of the Anza gap and the four events from 1937 to 1968 occurring to the southeast. The epicenters of these significant historic earthquakes and their aftershock zones are shown in Figure 1.1. Also shown on Figure 1.1 are other significant large earthquakes in the region including the 1915 (M_L 6.3, M_L 6.3), 1940 (M_L 6.7), and 1979 (M_L 6.6) earthquakes which were caused by rupture of parts of the Imperial fault (e.g. Doser and Kanamori, 1986a), and the 1948 (M_L 6½) Desert Hot Springs earthquake (Richter et al., 1958).

1.2 Earthquakes Northwest of Anza

At least two and perhaps four large earthquakes have occurred in the San Jacinto fault zone northwest of Anza since 1890 (Figure 1.1). The two earthquakes definitely associated with this zone occurred on December 25, 1899 (M 7; this magnitude is inferred by comparison of the intensities of this and the 1918 earthquake), and April 21, 1918 (M 6.8; Richter, 1958). An event on July 22, 1923 (M 6¼; Richter, 1958), is quite possibly associated with the San Jacinto fault. Another earthquake on July 22, 1899 (M_I 6.5; M_I signifies magnitude determined from intensity data; Toppozada et al., 1981), was strongly felt in the Cajon Pass region, near the intersection of the San Jacinto and San Andreas faults, but could be associated with either of these faults or others in the area. The magnitudes of the 1918 and 1923 earthquakes are approximate Richter magnitudes obtained from a comparison of the earthquake seismograms recorded at a few regional seismograph stations with the seismograms of modern earthquakes recorded on the same instruments at those stations but also on Wood-Anderson instruments (C. Richter, personal communication, December 1982).

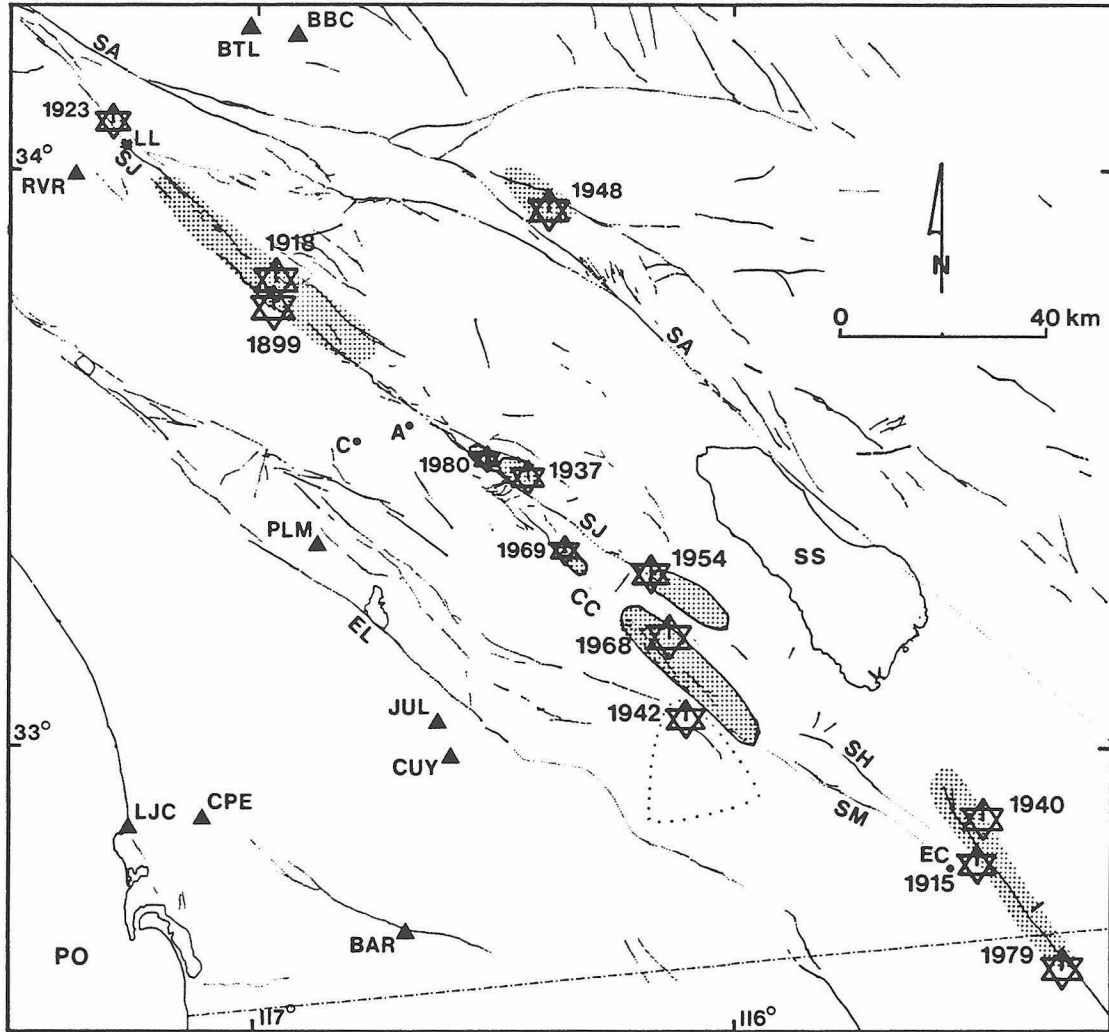


Figure 1.1. Map of historic large earthquake rupture zones on the San Jacinto, southern San Andreas, and Imperial faults in southern California. The main shock epicenters are indicated by stars and the aftershock zones of the 1937 (M_L 5.9), 1940 (M_L 6.7), 1948 (M_L 6½), 1954 (M_L 6.2), 1968 (M_L 6.8), 1969 (M_L 5.8), 1979 (M_L 6.6) and 1980 (M_L 5.5) events are shaded. The principal 1942 (M_L 6.3) earthquake aftershocks lie within the dotted outline. The 1923 earthquake was M_L 6¼ and both 1915 mainshocks were M_L 6.3. The combined rupture zone of the 1899 (M 7) and 1918 (M_L 6.8) San Jacinto-Hemet earthquakes is approximated from empirical data. A, Anza; C, Cahuilla; CC, Coyote Creek fault; EC, El Centro; EL, Elsinore fault; I, Imperial fault; LL, Loma Linda; PO, Pacific Ocean, SA, San Andreas fault; SH, Superstition Hills fault; SJ, San Jacinto fault; SM, Superstition Mountain fault; SS, Salton Sea. Triangles mark seismograph stations used in this study.

1.3 1923 Earthquake

The July 22, 1923 earthquake is located only approximately, based on damage reports and one seismograph reading, but is very likely associated with the San Jacinto fault in the San Bernardino Valley (Figures 0.1 and 1.1). The P- and S-wave arrivals of this and sixteen probable aftershocks between then and August 3, 1923 were recorded at the seismological station in Pasadena. The S-P time of the main shock is reported as 9 s (Townley and Allen, 1939), which indicates a hypocentral distance of about 83 km from Pasadena. The S-P times of the sixteen aftershocks were obtained from phase cards stored at the Seismological Laboratory of the California Institute of Technology and have a range of values from 8 to 10 s (hypocentral distances of 74-92 km) with an average of 8.9 s (82 km). These S-P times do not precisely constrain the locations of the large earthquake and aftershocks; however, given that the event probably occurred near the area of greatest damage in the eastern San Bernardino Valley, the 83-km epicentral distance from Pasadena implies rupture on a fault within or very near San Bernardino Valley, most likely the San Jacinto fault near Loma Linda or the San Andreas fault northeast of San Bernardino Valley. Minor faults in the San Bernardino Valley between the San Jacinto and San Andreas faults are secondary features, and major seismic displacements probably do not occur on them. If the aftershocks are assumed to be aligned along a single, northwest trending fault trace, then the S-P times suggest a fault rupture of about 20 km.

The 1923 earthquake effects were investigated by Laughlin et al. (1923). In particular, they compiled locations of broken chimneys and found that the maximum number occurred in areas of the eastern San Bernardino Valley, 2-15 km southwest of the trace of the San Andreas fault. Other fallen chimneys were found south of there and in the city of Loma Linda, which lies just east of the trace of the San Jacinto fault (Figure 1.1). On a farm west of Loma Linda a chimney was destroyed, and a concrete municipal water pipe was broken. Laughlin et al. also inspected the San Andreas fault directly northeast of the area of heaviest damage in San Bernardino

Valley and commented on the easy traceability of the fault in this region due to the unusual topographic features. They remark, however, that "although there are not many houses along the fault, those examined showed that the destruction had been much less there than at points in the valley. No chimneys were destroyed and relatively few articles overturned." They also apparently saw no surface rupture along the fault trace here. This seems to be evidence that the earthquake was not produced by rupture of this segment of the San Andreas fault.

Assignment of an epicenter for the 1923 earthquake can not be made with confidence. The S-P times at Pasadena and the intensity data seem to constrain the epicenter to the San Bernardino Valley area which includes the San Andreas and San Jacinto faults. The relatively mild intensities reported along the trace of the San Andreas fault bordering the San Bernardino Valley suggest that the earthquake was not located on this fault. The relatively severe intensities reported in the San Bernardino Valley may suggest rupture of a small fault beneath the valley, however this is by no means required since the young sedimentary deposits beneath San Bernardino Valley could have served to intensify the shaking in the valley from a nearby large earthquake. The large size of the earthquake suggests rupture of a major fault structure. No major faults are mapped in the Quaternary alluvium of San Bernardino Valley (Rogers, 1967). The nearest major active fault trace other than the San Andreas is the San Jacinto fault near Loma Linda. At present this fault appears to be the most probable causative structure for the 1923 earthquake.

Historic reports document an increase in local seismicity at the M 3-4 level in the 3 months preceding the 1923 earthquake (see Townley and Allen, 1939, for earthquake listings).

1.4 1899 and 1918 Earthquakes

Both the December 1899 and 1918 earthquakes occurred along the segment of the San Jacinto fault zone near the towns of San Jacinto and Hemet (Figures 0.1, 1.1,

and 2.1). This location is well determined by intensity reports which document the heaviest damage and largest concentrations of ground failure near these two towns. The greater intensities near San Jacinto of MM VIII-IX suggest that neither earthquake ruptured into the Anza gap where intensities were only MM VI-VII (Claypole, 1900; Danes, 1907; Rolfe and Strong, 1918; Townley, 1918; Topozada et al., 1981). The distribution of secondary ground breakage was similar for both earthquakes and was generally reported as sunken ground, probably due to liquefaction and landsliding. Rolfe and Strong (1918) determined from their geologic investigation several weeks after the 1918 earthquake that the secondary ground movement in certain areas during this shock was less severe than that during the 1899 earthquake. Local residents reported similar intensities for both earthquakes. Far-field intensity reports, however, suggest that the 1899 earthquake was slightly larger in magnitude (see isoseismal maps by Townley, 1918, and Topozada et al., 1981). Subsurface fault rupture probably extended southeast to the area of the zone of present high seismicity just northwest of the Anza gap. The epicentral region of these two earthquakes is now characterized by low seismicity (Chapter 2).

It is not known exactly which faults broke during the 1899 and 1918 earthquakes. No definite surficial fault rupture was reported for either earthquake, and reports of damage and secondary ground disruption do not provide conclusive evidence. Intensity reports, though, strongly imply that both earthquakes were caused by subsurface slippage on faults very near to San Jacinto and Hemet. These towns are located on young sedimentary rocks deposited in a subsiding basin between the right-stepping traces of the San Jacinto fault here (Figure 1.1). These faults, the Claremont fault and the Casa Loma fault, bound the depression on the northeast and southwest, respectively, and show geologic evidence of both right-lateral and normal movement (Sharp, 1975; Rasmussen, 1981). One possible interpretation, which can explain the apparently coincident locations of the two large earthquakes, is that each earthquake ruptured on one of the bounding faults. Rupture of the 1899 earthquake

on the Casa Loma fault would have produced a stress change in the graben block, which 18 years later helped precipitate the 1918 earthquake on the opposing Claremont fault less than 6 km away. The lack of reported surface rupture, though, is puzzling, and hypocentral locations east of San Jacinto on the Hot Springs fault or somewhat south of Hemet on the San Jacinto fault can not be ruled out. Hill (1984) reports no features along the Hot Springs fault suggestive of Holocene fault rupture, however the fault does seem to have small earthquake activity at depth near its southeast end (Chapter 2).

1.5 Earthquakes Southeast of Anza

Southeast of Anza four large earthquakes have occurred since 1890 (Figure 1.1). Those associated with the fault zone occurred on March 25, 1937 (M_L 5.9), March 19, 1954 (M_L 6.2), and April 19, 1968 (M_L 6.8). A large earthquake on October 21, 1942 (M_L 6.3) does not seem to be directly related to the major faults of the fault zone but is located southwest of the southeast end of the Coyote Creek fault. The aftershock zones of the 1968 Borrego Mountain (M_L 6.8) and 1969 Coyote Mountain (M_L 5.8) earthquakes are well determined by readings from five regional stations ($\Delta = 50$ -75 km) and tens of temporary stations installed immediately after the main shocks (Allen and Nordquist, 1972; Hamilton, 1972; Thatcher and Hamilton, 1973). We relocated the 1937, 1942, and 1954 earthquakes to obtain a better understanding of their rupture zones. These relocations are described in the next section.

1.6 Relocating the 1937, 1942, and 1954 Earthquakes: Introduction

To improve our understanding of the seismic history of this fault zone we relocated the large 1937 (M_L 5.9), 1942 (M_L 6.3), and 1954 (M_L 6.2) earthquakes and aftershocks which were caused by rupture of segments of the San Jacinto and Coyote Creek faults and a fault southwest of the Coyote Creek fault. Together with the 1968 (M_L 6.8) Borrego Mountain earthquake, these events represent the greatest stress

release along the southern half of the San Jacinto fault zone since at least the late 1890's, and their rupture zones help define those segments of the fault zone which have ruptured historically and those segments which have not.

Originally the large earthquakes were located by graphical techniques using S-P times from distant ($\Delta = 100-500$ km) unclipped stations, and the numerous aftershocks were given the same epicenters as the associated main shocks (Hileman et al., 1973). Other researchers have attempted relocations of some of the mainshocks. The 1937 earthquake was originally located by Wood (1937; he called it the Terwilliger Valley earthquake after a local place name near his epicenter) and relocated by Gutenberg (1943), Richter (1958), Hileman et al. (1973), Hanks et al. (1975) and Sanders and Kanamori (1984). The 1942 and 1954 earthquakes were originally located by Richter (1958) and also relocated by Hanks et al. (1975). Wood, Gutenberg, and Richter used mainshock S-P times recorded at some of the seven or more southern California seismograph stations in operation at the time and then graphically located the events using empirical S-P versus Δ curves. Hanks et al. also graphically located the mainshocks but used the average aftershock S-P times to approximate the mainshock times. This increased the number of S-P readings, since some of the mainshock S-wave arrival times are unreadable. Hileman et al. located the 1937 mainshock using available P- and S-wave arrival times, a least-squares computer routine, and a single layer crustal velocity model. Sanders and Kanamori located the 1937 mainshock using a modern computer location program, a multi-layer crustal velocity model, P-wave arrival times at six southern California stations ($\Delta = 100-400$ km), and P- and S-wave arrivals at one station ($\Delta = 100$ km). No station corrections were used for this later location, however.

Since very few seismograms are available for locating these large earthquakes, and since these are from large distances and limited azimuths, all of the previous locations suffer from large uncertainties ($\pm 10-15$ km). In order to minimize the effects of the sparse, heterogeneous data set, we include data on the lateral variations in the

regional velocity structure. This data is introduced into the earthquake location procedure in the form of empirical station corrections as explained in the next section. The resulting epicentral locations hopefully suffer less from the sparse travel-time data set. We feel that these more precise epicentral locations for the mainshocks, plus the first locations of the aftershocks, will help clarify the recent seismic history of the San Jacinto fault zone.

1.7 Relocating the 1937, 1942, and 1954 Earthquakes: Technique

We precisely relocated the 1937, 1942, and 1954 mainshocks and aftershocks and the 1937 and 1954 preshocks using a simple technique. P- and S-wave arrival times from some or all of the California Institute of Technology seismograph stations located at Riverside (RVR), La Jolla (LJC), Palomar (PLM), Barrett Dam (BAR), Big Bear (BBC), and Cuyamaca Reservoir (CUY) are used to find the epicentral locations (Figure 1.1). Usually only two stations separated by about 75° azimuth are available for use in our relocations (since we try to use only P_g and S_g arrivals), so very accurate delay values are needed to account for the deviation between the observed travel time through the real earth and the travel time calculated through the idealized crustal velocity model used in the earthquake location program (unpublished program; Johnson, 1979). The delay values vary from station to station and also somewhat from source area to source area. Thus, we determined accurate delay values to each station for many different subareas in the general region of the southern San Jacinto fault zone (Figure 1.2, Tables 1.1 and 1.2). These values were obtained by averaging the residuals (observed travel time minus calculated travel time) at the above named stations from many recent (1977-1985) small earthquakes. These small earthquakes were all carefully relocated using the dense USGS-CIT southern California seismograph network and stations within 60 to 80 km of the epicenter (to minimize the effect of uncertainties in the velocity model; Pechmann, 1983). We used a crustal P-wave velocity model characteristic of the Peninsular Ranges of southern California

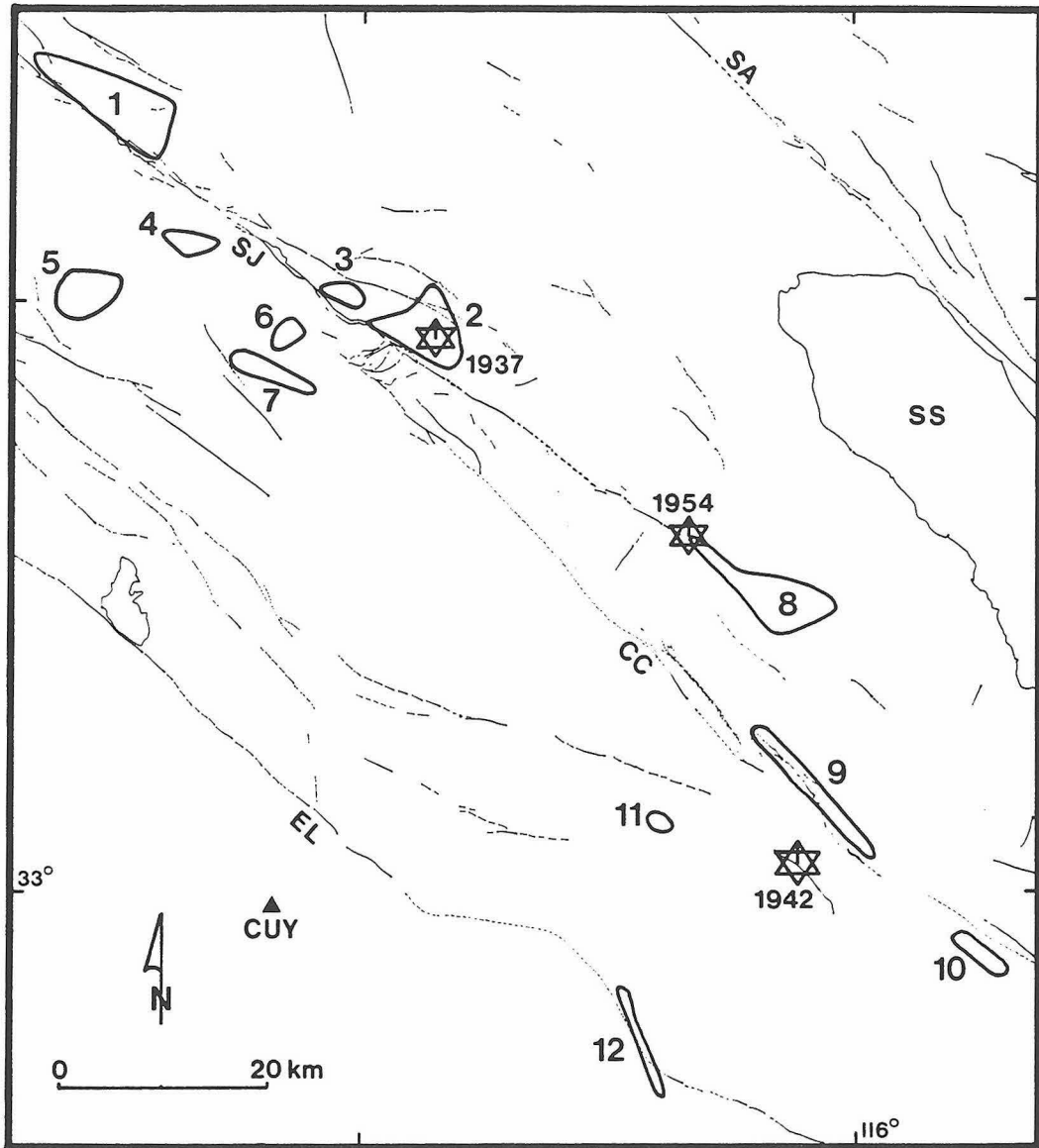


Figure 1.2. Map of areas along the southern San Jacinto fault zone for which travel time delays have been determined. The numbers are referred to in the text and in Tables 1.1 and 1.2.

TABLE 1.1. Recent Earthquake Residuals Near the 1937 and 1954 Earthquakes

#	Yr	Mo	Da	HrMn	Latitude	Longitude	Depth	M_L	RVR		LJC (CPE)		BAR		PLM	
									P	S	P	S	P	S	P	S
1	77	07	02	0122	33° 37.10'	116° 42.97'	14.1	3.0	-0.18	-1.12	-0.07					0.56
	79	08	03	0430	33° 40.44'	116° 41.19'	15.2	3.5			-0.55		-0.25			0.14
	79	08	22	0201	33° 42.39'	116° 50.07'	15.5	4.0	-0.15		-0.33		-0.02			0.32
									-0.17	-1.12	-0.32		-0.14			+0.34
2	76	07	14	2019	33° 29.40'	116° 26.86'	9.6	2.7		-1.31	-0.40	-1.26			0.15	0.22
	76	07	17	1121	33° 29.45'	116° 26.54'	8.6	2.8		-1.56		-1.32			0.13	
	77	02	08	1239	33° 28.77'	116° 27.35'	13.3	2.5			-0.27	-1.44			0.10	
	77	10	22	0933	33° 27.89'	116° 24.27'	9.3	2.3			-0.42	-1.53			0.05	
	77	10	25	1531	33° 28.92'	116° 26.03'	12.9	2.7			-0.47	-1.86			0.05	
	77	11	28	1857	33° 26.86'	116° 24.34'	11.6	3.1		-1.14		-0.54			0.16	
	78	03	01	1141	33° 27.82'	116° 24.05'	9.8	2.1			-0.14					
	78	05	12	1549	33° 29.55'	116° 26.19'	12.8	2.8			-0.26	-1.62	-0.19	-1.47	0.12	0.27
	78	10	08	0652	33° 30.53'	116° 25.62'	9.6	2.3			-0.33	-1.34			0.18	
	78	12	01	0229	33° 28.93'	116° 26.91'	14.0	3.0			-0.31	-1.62	-0.19	-1.29	0.14	
	79	02	12	0448	33° 27.60'	116° 25.71'	5.5	4.2	-0.24		-0.38		-0.22		0.20	
	79	02	12	0455	33° 27.49'	116° 25.67'	4.6	3.2			-0.37		-0.14		0.19	0.18
	79	02	12	0515	33° 27.51'	116° 25.97'	5.0	3.0			-0.38		-0.22		0.20	
	79	08	12	1958	33° 29.99'	116° 25.58'	10.0	2.6			-0.33	-1.27		-1.13	0.14	0.21
79	09	16	0855	33° 28.96'	116° 29.58'	7.5	3.0	-0.16		-0.24	-1.24	-0.26	-1.51	0.25		
								-0.20	-1.34	-0.33	-1.45	-0.20	-1.35	+0.15	+0.22	
3	79	07	02	1151	33° 29.98'	116° 29.96'	13.7	3.7	-0.25		-0.33		-0.20		0.11	
	79	07	02	1242	33° 30.55'	116° 30.44'	12.6	3.6	-0.28	-1.41	-0.33	-1.64	-0.21	-1.42	0.18	
	80	02	25	1053	33° 30.44'	116° 30.97'	12.8	5.5	-0.29		-0.47		-0.32		0.15	
	80	02	25	1141	33° 30.64'	116° 31.42'	10.5	2.7	-0.31	-1.37	-0.59		-0.45	-1.82	0.13	0.24
	80	02	25	1147	33° 30.53'	116° 31.37'	11.5	2.4		-1.31	-0.26	-1.82	-0.21	-1.61	0.21	0.25
	80	02	25	1149	33° 30.49'	116° 32.20'	11.5	2.5			-0.37	-1.74	-0.32	-1.66	0.21	0.31
	80	02	25	1203	33° 30.58'	116° 31.11'	10.8	2.7			-0.46	-1.87	-0.33	-1.66	0.15	
	80	02	25	1207	33° 30.42'	116° 31.29'	10.0	2.1			-0.43	-1.80			0.11	
	80	02	25	1300	33° 30.33'	116° 31.24'	11.2	2.1			-0.24	-1.78	-0.26	-1.65	0.22	0.32
	80	02	25	1451	33° 30.49'	116° 31.75'	11.2	3.3	-0.12	-1.10	-0.38	-1.70	-0.32	-1.71	0.28	
	80	02	25	1907	33° 30.26'	116° 31.51'	10.4	2.4			-0.44	-1.78	-0.33	-1.59	0.16	
	81	04	30	2009	33° 30.70'	116° 30.37'	13.8	3.2	-0.03	-1.24			-0.20	-1.38	0.15	
								-0.21	-1.28	-0.38	-1.75	-0.29	-1.61	+0.17	+0.28	
4	80	09	07	0326	33° 32.28'	116° 40.54'	8.4	2.7	-0.23				-0.22		0.30	0.46
	81	07	18	1248	33° 33.35'	116° 40.73'	11.9	2.9	-0.24				-0.25		0.24	
	82	06	15	2349	33° 33.16'	116° 40.51'	11.4	4.5	-0.27				-0.36		0.22	
								-0.25				-0.28		+0.25	+0.46	

TABLE 1.1. (continued)

#	Yr	Mo	Da	HrMn	Latitude	Longitude	Depth	M_L	RVR		LJC (CPE)		BAR		PLM	
									P	S	P	S	P	S	P	S
	78	04	26	1440	33° 31.64'	116° 44.43'	5.6	2.3	-0.04		-0.51	-1.47	-0.29		0.04	
	78	06	14	1944	33° 29.83'	116° 46.24'	13.9	3.0	-0.18	-1.05	-0.39	-1.06	-0.22	-1.21		
	79	09	15	1101	33° 31.50'	116° 47.34'	5.0	2.1			-0.49		-0.30		0.12	
	81	02	01	1927	33° 30.20'	116° 46.12'	4.4	3.4	-0.03				-0.20		0.09	
	81	03	09	0336	33° 30.48'	116° 46.20'	6.0	2.7	-0.08							
	81	03	12	1501	33° 29.77'	116° 46.78'	5.8	2.6	-0.00	-0.53			-0.21	-1.07	0.05	
	81	04	02	0343	33° 30.22'	116° 46.06'	4.6	2.3	-0.01						0.08	
	81	06	20	1949	33° 30.73'	116° 46.76'	2.4	2.8	-0.14				-0.34		0.19	
	81	07	01	0625	33° 30.49'	116° 46.03'	2.4	2.5	-0.11						0.16	
5	81	07	25	0624	33° 29.13'	116° 46.81'	1.5	3.1	-0.07				-0.23			
	81	08	06	0218	33° 29.49'	116° 46.53'	2.2	2.7	-0.07				-0.28			
	81	08	13	0509	33° 28.96'	116° 48.12'	4.9	2.5	-0.19						0.16	
	81	10	15	1441	33° 32.15'	116° 47.60'	4.5	2.2	-0.03				-0.31		0.04	0.27
	81	10	21	0537	33° 30.28'	116° 46.06'	4.6	3.1	-0.10	-0.80			-0.32		0.10	
	81	10	31	1951	33° 29.54'	116° 46.15'	5.0	2.7	-0.03	-0.60			-0.26			
	82	10	22	1053	33° 29.96'	116° 45.67'	7.0	2.4	-0.30	-0.97			-0.45	-1.36	0.12	
	84	03	25	0147	33° 29.68'	116° 48.01'	4.3	2.4	-0.10		-0.56		-0.40		0.18	
	84	08	18	0712	33° 30.00'	116° 47.55'	4.9	3.0			-0.59					
									-0.09	-0.79	-0.51	-1.27	-0.29	-1.21	+0.11	+0.27
	78	07	03	0834	33° 27.63'	116° 35.86'	8.6	2.9			-0.35		-0.33	-1.53	0.19	
	78	10	26	1014	33° 28.19'	116° 34.22'	11.0	2.5				-1.68	-0.33	-1.45	0.16	0.23
6	79	08	02	1304	33° 29.21'	116° 34.16'	5.3	2.7	-0.17		-0.44	-1.51	-0.37	-1.52	0.15	0.12
	80	03	10	2332	33° 28.27'	116° 34.43'	10.0	3.0	-0.24	-1.43	-0.49	-1.72	-0.39		0.14	0.21
	81	12	30	0138	33° 28.11'	116° 33.79'	11.0	2.6	-0.31						0.11	
									-0.24	-1.43	-0.43	-1.64	-0.36	-1.50	+0.15	+0.19
	79	04	22	1652	33° 25.63'	116° 32.92'	12.0	3.3		-1.54	-0.35	-1.52	-0.34	-1.46	0.19	
	79	08	01	0831	33° 26.57'	116° 37.97'	11.4	2.8	0.23		-0.09		-0.06		0.39	0.40
7	79	08	16	0220	33° 26.67'	116° 37.94'	8.2	3.0	0.27		-0.14	-1.20	-0.13		0.47	
	79	08	19	2255	33° 27.03'	116° 37.75'	8.2	2.8	0.17	-1.44	-0.25	-1.44	-0.23		0.36	
	79	08	25	1340	33° 27.30'	116° 37.28'	7.4	2.3			-0.49		-0.39		0.19	0.50
									+0.22	-1.49	-0.26	-1.39	-0.23	-1.46	+0.32	+0.45
	78	11	09	2300	33° 13.98'	116° 04.46'	6.0	3.1			-0.19	-1.28	-0.23	-1.29	0.22	
	80	02	13	0631	33° 18.09'	116° 09.90'	8.7	3.2			-0.27		-0.36		0.21	
	81	06	23	0136	33° 14.27'	116° 05.32'	10.5	2.1					-0.17	-1.09	0.54	-0.14
	81	09	13	1553	33° 13.00'	116° 04.94'	10.1	2.7					-0.06	-0.99	0.20	
	81	09	21	1521	33° 14.15'	116° 05.35'	10.0	2.6					-0.13	-1.38	0.23	-0.14
	81	09	22	1011	33° 14.13'	116° 04.94'	8.9	2.1					-0.06		0.24	
	81	10	17	1947	33° 14.41'	116° 04.16'	4.9	3.8	-1.21	-1.31			-0.30		0.29	
8	81	10	17	1953	33° 14.29'	116° 03.56'	8.7	2.4					-0.07	-1.33	0.38	
	81	10	17	1954	33° 14.47'	116° 03.81'	7.0	3.2					-0.19	-1.38	0.35	
	81	12	05	1556	33° 13.98'	116° 05.20'	9.7	2.2							0.31	
	82	01	25	2347	33° 14.27'	116° 05.32'	10.5	3.1		-1.28			-0.21		0.30	-0.08
	82	09	07	0400	33° 14.16'	116° 05.66'	9.3	2.2					-0.13	-1.29	0.28	-0.03
	82	09	15	1803	33° 14.51'	116° 01.17'	10.9	2.8					-0.06	-1.19	0.57	
	82	12	12	1409	33° 15.92'	116° 06.79'	10.4	2.5					-0.10	-1.49	0.62	0.12
	84	10	07	1544	33° 16.14'	116° 04.04'	6.3	3.0					-0.11			
									-1.21	-1.30	-0.23	-1.28	-0.16	-1.27	+0.34	-0.05

For this and all following tables the origin times are GMT, the residuals and travel times are in units of seconds, and depths are in kilometers.

TABLE 1.2. Recent Earthquake Residuals Near the 1942 Earthquake

#	Yr	Mo	Da	HrMn	Latitude	Longitude	Depth	M_L	CUY (JUL)		PLM		LJC (CPE)		RVR	
									P	S	P	S	P	S	P	S
9	84	02	29	0207	33° 08.11'	116° 05.49'	6.5	4.3	0.21		0.41		-0.06		-1.17	-1.12
	85	06	03	0653	33° 02.05'	115° 59.30'	4.0	3.3	0.11		0.30		-0.33	-1.21		
	85	06	14	2242	33° 05.91'	116° 03.50'	1.6	2.5	0.02	-0.42	0.15		-0.18	-1.28		
									<u>+0.11</u>	<u>-0.42</u>	<u>+0.29</u>		<u>-0.19</u>	<u>-1.25</u>	<u>-1.17</u>	<u>-1.12</u>
10	82	09	05	0521	32° 55.88'	116° 51.07'	4.2	4.4	0.16	-0.33	-0.25					
	83	11	11	1636	32° 57.23'	115° 53.05'	5.0	3.3			-0.27	0.07				-1.36
	83	11	11	1715	32° 57.43'	115° 53.35'	4.8	3.8	0.11	-0.15	-0.24	0.18	-0.17			-1.41
									<u>+0.14</u>	<u>-0.24</u>	<u>-0.25</u>	<u>+0.13</u>	<u>-0.17</u>			<u>-1.39</u>
11	83	09	20	0008	33° 03.28'	116° 11.93'	4.4	3.5	0.08	-0.35	0.34	-0.21				
	83	12	06	0120	33° 03.85'	116° 11.54'	5.6	2.9	0.02			-0.19	-0.23	-1.40		
	83	12	06	0910	33° 03.16'	116° 11.77'	4.0	3.2	0.06		0.29	-0.31	-0.28	-1.52		
	83	12	06	2322	33° 03.45'	116° 11.76'	4.2	3.1	0.03		0.30	-0.18	-0.30	-1.30		
	83	12	07	1519	33° 03.11'	116° 11.77'	3.4	3.1	0.01		0.24	-0.41	-0.16	-1.48		
									<u>+0.04</u>	<u>-0.35</u>	<u>+0.29</u>	<u>-0.26</u>	<u>-0.24</u>	<u>-1.43</u>		
12	84	02	02	2330	32° 50.14'	116° 11.46'	4.6	2.8	0.09		0.43		-0.25	-1.38		
	84	02	26	1904	32° 55.02'	116° 14.05'	5.2	2.7	0.15	-0.18	0.54	0.44	-0.05			
									<u>+0.12</u>	<u>-0.18</u>	<u>+0.49</u>	<u>+0.44</u>	<u>-0.15</u>	<u>-1.38</u>		

(Table 1.3) (Kanamori and Hadley, 1975; Hadley and Kanamori, 1977), and the S-wave velocities were calculated with $V_P/V_S=1.78$. The residuals at a particular station from well located earthquakes in a given small area are consistent, and we are able to obtain average residual values for many areas along the San Jacinto fault. These average residual values become the delay values we use in relocating the older events.

Since the seismograph stations LJC, CUY, and BBC are no longer in operation we use the nearby modern stations CPE, JUL, and BTL for determining station delays for the old stations. The relative locations are shown in Figure 1.1; CPE is 14 km east of LJC, JUL is 8 km north of CUY, and BTL is 8 km west of BBC. We assume that the delays we have determined from the modern stations are also applicable to the old stations. The elevations and site geology are nearly identical in each case.

As a test, some of the recent earthquakes in the area of the 1937 earthquake southeast of Anza were relocated using only P- and S-wave arrival times at stations RVR and CPE, the delays determined for that area, and with depths fixed at 12 km. These events all relocated to within 3 km of their epicenters determined by the more dense local USGS-CIT array. The same test was performed on recent events in the area of the 1954 earthquake using P- and S-wave readings from BAR and PLM only, the delays determined for that area, and with depths fixed at 8 km. The events relocated to within 2 km of their catalog epicenters. Also the 1968 Borrego Mountain mainshock was relocated to within 3 km of its epicenter (Allen and Nordquist, 1972) using only P- and S-wave arrival times at station RVR, a P-wave arrival time at station PLM, the station delays for that area, and fixing the depth at 10 km. Thus we feel that our locations for the 1937 and 1954 events for which good P- and S-wave readings are available are accurate to within about 5 km. This is a significant improvement over the old location errors of 10 km or more.

TABLE 1.3. Crustal Velocity Model

V_p , km/s	Depth to Top of Layer, km
5.5	0.0
6.3	5.5
6.7	16.0
7.8	32.0

1.8 1937 Buck Ridge Earthquake

We relocated the March 25, 1937 earthquake (M_L 5.9) and aftershocks ($M_L \geq 3.0$) using arrival-time data from stations RVR and LJC, both about 100 km distant and 75° apart in azimuth. We repicked the P- and S-wave arrival times from the short period vertical seismograms and from the Wood-Anderson horizontal seismograms and relocated the events using the delay values appropriate for that area of the fault and those stations (area 2, Figure 1.2, Table 1.1). The epicenters of the main shock and most of the aftershocks lie between the surface traces of the San Jacinto and Buck Ridge faults (Figure 1.3) beneath the physiographic feature called Buck Ridge. We cannot constrain the depths of these events, but the recent seismicity in the area occurs at an average depth of about 12 km. The aftershocks located during the first 2 hours lie northwest of the main shock, as do most of the other aftershocks, indicating predominantly unilateral rupture of about 6 km to the northwest (Figure 1.4). Early aftershocks southeast of the main shock suggest perhaps 1 km of rupture in that direction as well, for a total rupture of about 7 km. A rupture length less than 10 km was also suggested by Wood (1937), Thatcher et al. (1975), and Sanders and Kanamori (1984) based on the differences in aftershock S-P times. The arrival times and new locations for these earthquakes are listed in Table 1.4. The P-wave first motions are consistent with right-slip faulting on a northwest trending fault (Figure 1.5).

Previous locations for the 1937 mainshock are shown in Figure 1.3. They span a 30 by 10 km area and give no consistent indication of the fault which produced this earthquake. The current CIT catalog location (Hileman et al., 1973) marked 'c' in Figure 1.3 seems to be in error by about 16 km.

The 1980 (M_L 5.5) Whitewash earthquake, which is very well located by the dense southern California array, occurred at the northwest end of the 1937 aftershock zone, and its rupture extended another couple of kilometers further northwest (Figure 1.3).

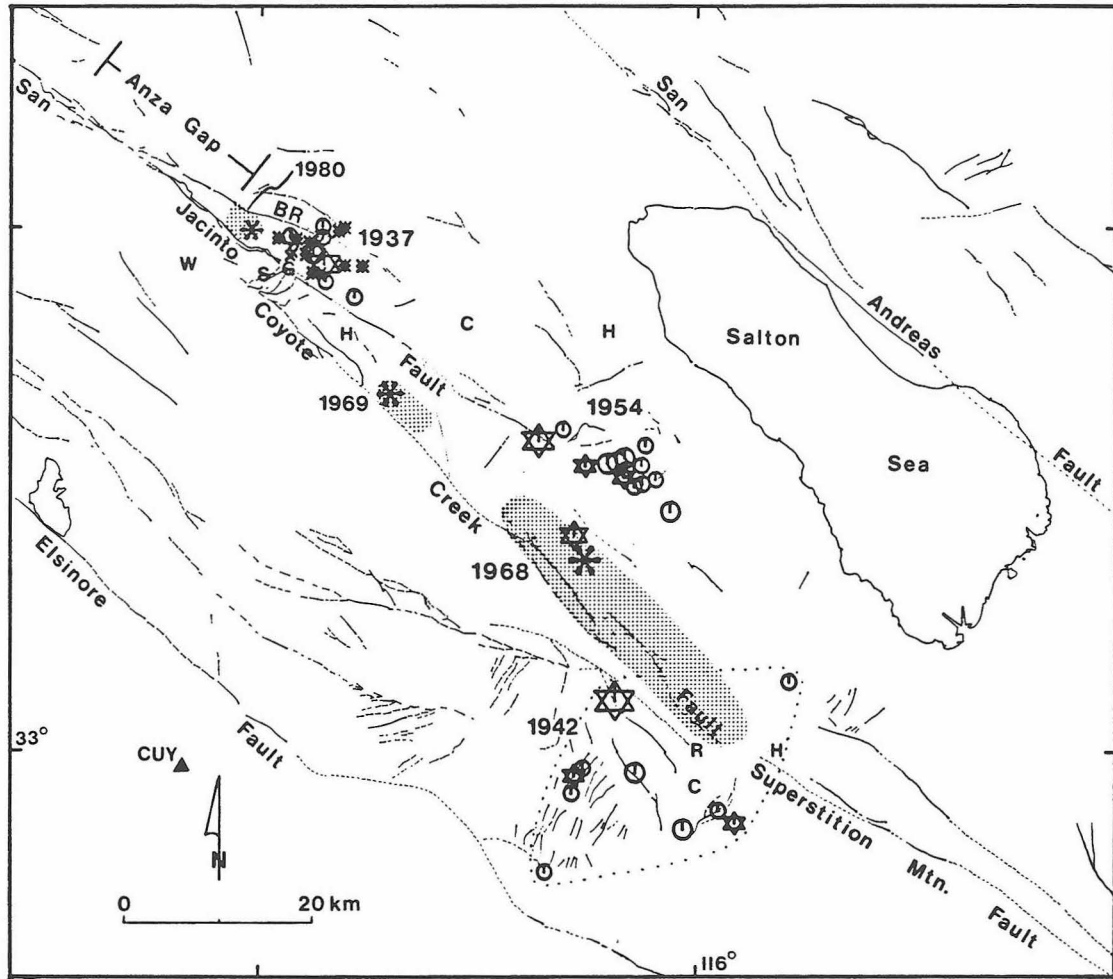


Figure 1.3. Map of relocated epicenters of the 1937 (M_L 5.9), 1942 (M_L 6.3), 1954 (M_L 6.2) earthquakes and large aftershocks. The aftershock zones of the 1968, 1969, and 1980 earthquakes are shaded and the respective main shock epicenters marked by flower symbols. Previous mainshock locations are indicated by single letters, C = CIT catalog, G, Gutenberg (1943); H, Hanks et al. (1975); R, Richter (1958); S, Sanders and Kanamori (1984); W, Wood (1937). The 1937 Catalog location is also the Hileman et al. (1973) location and is about 16 km southeast of our 1937 epicenter. The 1937 Richter location is coincident with the 1980 mainshock epicenter. The 1954 Catalog and Richter locations are within 1 km of our 1954 epicenter and are not plotted. The 1954 location by Hanks et al. is about 14 km northeast of our 1954 epicenter. BR = Buck Ridge fault. The magnitude symbol key for this and subsequent figures in this chapter is: x = M_L 3.0, * = M_L 3.5, o = M_L 4.0, O = M_L 4.5, small star = M_L 5.0, medium star = M_L 5.5, large stars = main shocks.

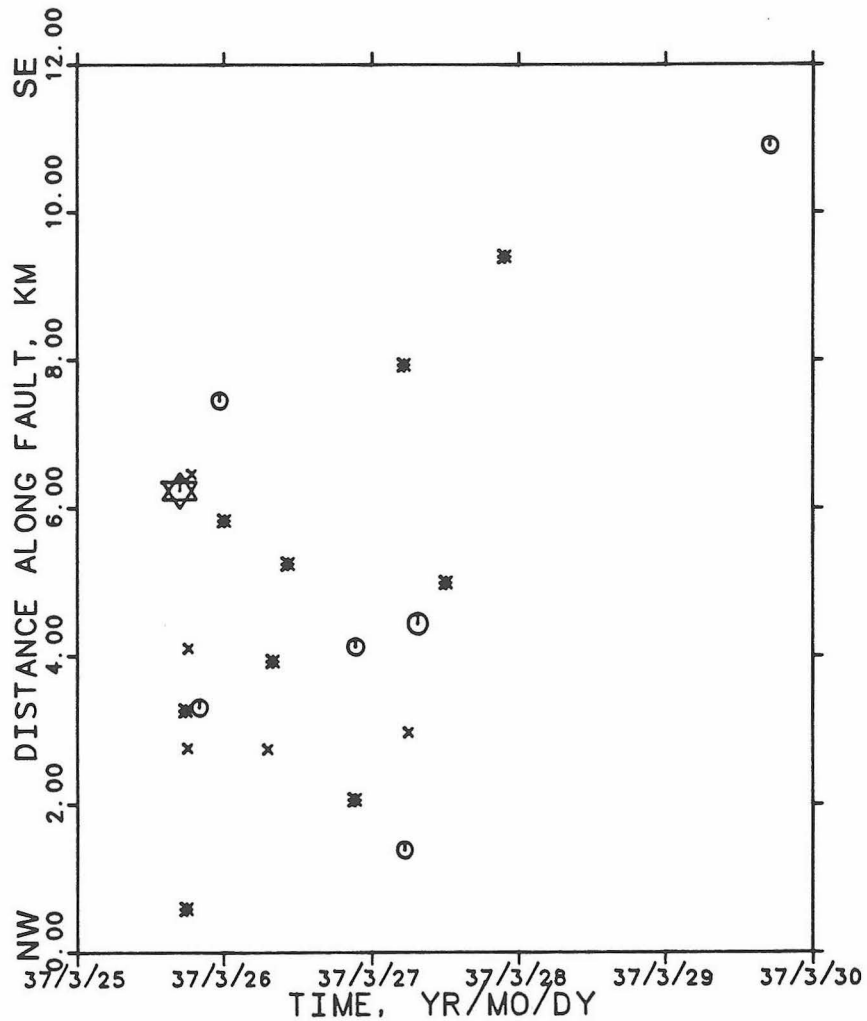


Figure 1.4. Time-distance plot of the 1937 earthquake and aftershocks. The distance axis is parallel to the San Jacinto fault. The early aftershocks and most of those in the following 2 days lie northwest of the mainshock suggesting a unilateral rupture length of about 7 km.

TABLE 1.4. Relocated 1937 Main Shock and $M_L \geq 3.0$ Aftershocks

Yr Mo Da	HrMn	M_L	RVR			LJC			Latitude	Longitude	Depth	
			P	S	S-P	P	S	S-P				
37 03 25	1649	6.0	21.26	33.68	12.42	20.70			33° 27.90'	116° 24.89'	12	
	1747	3.5	25.73	37.91	12.18	25.71	37.41	11.70	33° 29.09'	116° 26.19'	12	
	1754	3.5	51.59	63.53	11.94	51.82	63.18	11.36	33° 29.32'	116° 28.26'	12	
	1804	3.0	46.10	57.99	11.89	45.64	57.30	11.66	33° 28.47'	116° 27.29'	12	
	1812	3.0	31.58	43.85	12.27	31.51	43.31	11.80	33° 29.05'	116° 25.51'	12	
	1842	3.0	26.74	39.15	12.41	25.98	37.67	11.67	33° 27.36'	116° 25.27'	12	
	2004	4.0	24.73	36.85	12.12	24.85	36.91	12.06	33° 29.98'	116° 25.22'	12	
	2320	4.0	43.58	56.14	12.56	42.69	54.30	11.61	33° 26.81'	116° 25.00'	12	
	37 03 26	0010	3.5	03.30	15.69	12.39	02.61	14.14	11.53	33° 27.29'	116° 25.89'	12
		0717	3.0	43.01	55.04	12.03	42.68	54.14	11.46	33° 28.29'	116° 27.49'	12
0806		3.5	36.96	49.31	12.35	36.85	48.31	11.46	33° 28.38'	116° 26.37'	12	
1033		3.5	19.77	32.12	12.35	19.80	32.08	12.28	33° 29.89'	116° 23.65'	12	
2117		3.5	48.40	60.42	12.02	48.45	60.07	11.62	33° 29.27'	116° 27.04'	12	
2124		4.0	11.93	24.04	12.11	11.73	23.79	12.06	33° 29.34'	116° 25.19'	12	
37 03 27	0524	3.5	36.91	49.62	12.71	36.37	48.24	11.87	33° 27.71'	116° 23.63'	12	
	0528	4.0	59.9	71.8	11.9	59.96	71.58	11.62	33° 29.41'	116° 27.48'	12	
	0607	3.0	30.76	43.03	12.27	30.99	42.62	11.63	33° 29.38'	116° 26.14'	12	
	0742	4.5	36.90	49.10	12.20	36.52	48.27	11.75	33° 28.43'	116° 25.88'	12	
	1227	3.5	41.85	54.33	12.48	42.05	54.07	12.02	33° 29.69'	116° 24.08'	12	
	2150	3.5	20.54	33.16	12.62	19.61	31.93	12.32	33° 27.67'	116° 22.41'	12	
37 03 29	1703	4.0	33.31	46.35	13.04	32.20	43.90	11.70	33° 25.91'	116° 22.97'	12	

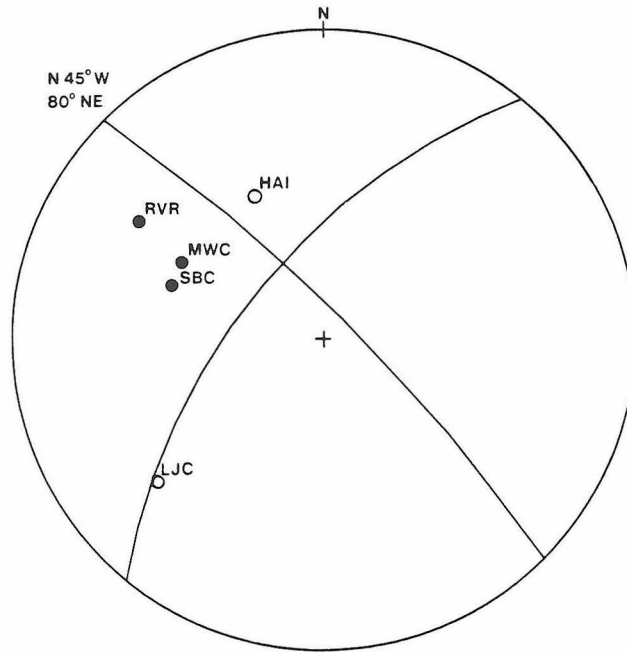


Figure 1.5. P-wave first motion source mechanism for the 1937 Buck Ridge earthquake. Solid circles, compression; open circles, dilatation. Lower hemisphere, equal angle projection. The southern California seismograph stations are Haiwee (HAI), La Jolla (LJC), Mount Wilson (MWC), Riverside (RVR), and Santa Barbara (SBC). Station LJC is nodal.

We also relocated most of the $M_L \geq 3.0$ seismicity from January 1932 through March 24, 1937, which have a CIT catalog location inside the box shown in Figure 1.6. The earthquakes were relocated using arrival times from the original phase cards and station delays from the appropriate areas; their new locations are listed in Table 1.5 and shown in Figure 1.6a. Four main areas of earthquake concentration are seen: in the epicentral region of the 1937 main shock; beneath the Cahuilla Valley area; on the San Jacinto fault north of Anza; and in the general area of the future 1954 and 1968 events. The time-distance plot (Figure 1.7) illustrates the relationships in the pre-1937 seismicity. Some preshock activity is concentrated in the rupture zone of the 1937 event with very little activity for about 20 km or more on either side. These earthquakes stopped about one year before the main shock. The cluster of activity at Cahuilla began abruptly about $1\frac{1}{2}$ years before the 1937 earthquake and continued until about 4 months before the M_L 5.9 mainshock. This cluster of activity is outlined in Figure 1.6a. The concentration of activity near Cahuilla is interesting because many of the events were clustered in time with five (M_L 3.0-4.5) occurring on November 4, 1935 and five more (M_L 3.0) during the following week. This increase in activity at Cahuilla in the year and a half before the 1937 earthquake is also interesting, since a similar increase has occurred recently and also may have preceded the nearby 1918 (M 7) San Jacinto-Hemet earthquake (Chapter 2).

1.9 Observations on the Use of Older CIT Catalog Locations and Archived Data

Location of $M_L \geq 2\frac{1}{2}$ - 3 earthquakes in southern California began on a routine basis in 1932 with the installation of seven continuously recording seismograph stations. Since that time the number of seismograph stations has increased, but the quality of epicentral location did not increase dramatically until the mid-1970's following the initial installation of stations of the current dense southern California array. Prior to the mid-1970's most routine earthquake epicenters seem to have

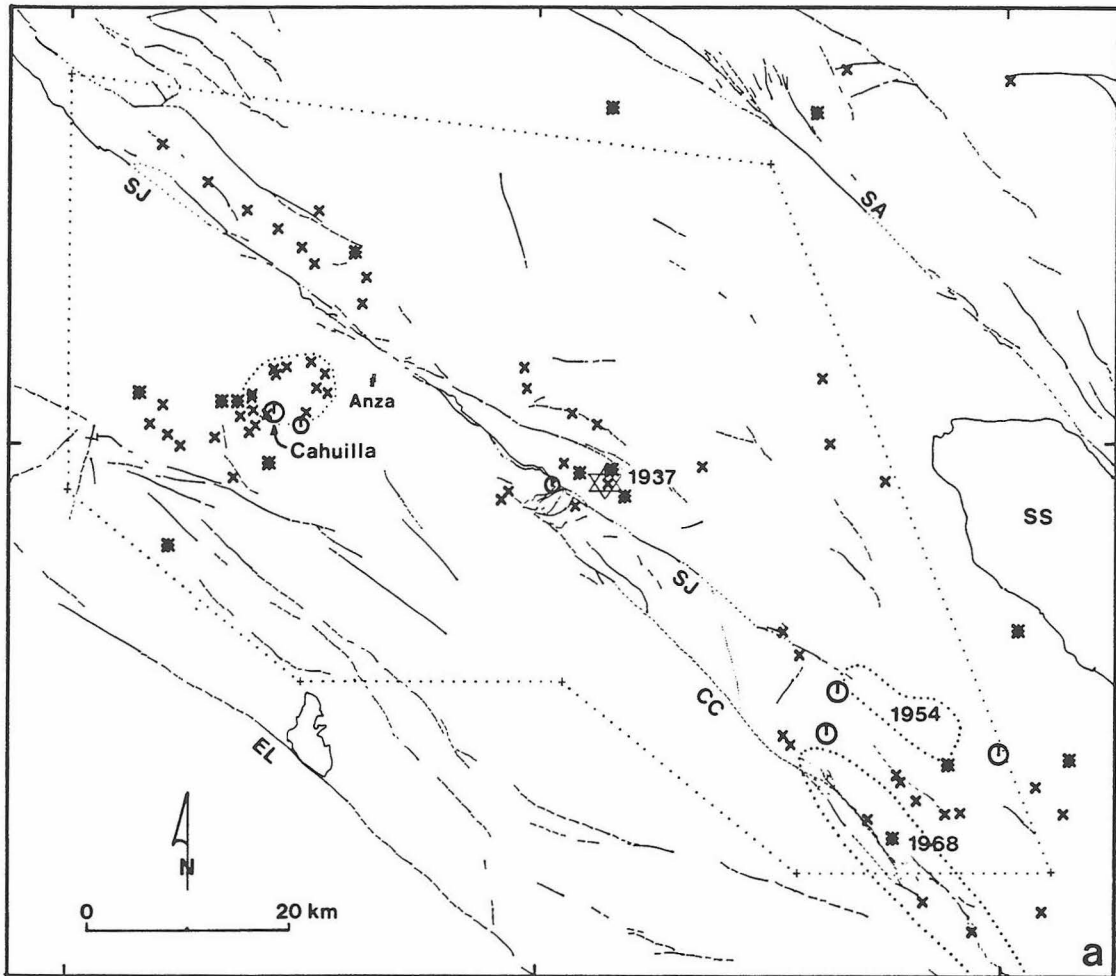


Figure 1.6. (a) Relocated epicenters of $M_L \geq 3.0$ earthquakes near the southern San Jacinto fault in the time period January 1932 to March 1937. The earthquakes originally all had catalog locations within the box described by the dotted line segments. The Cahuilla swarm is outlined. The 1937 main shock and the 1954 and 1968 rupture zones are indicated. (b) Catalog locations of these same events.

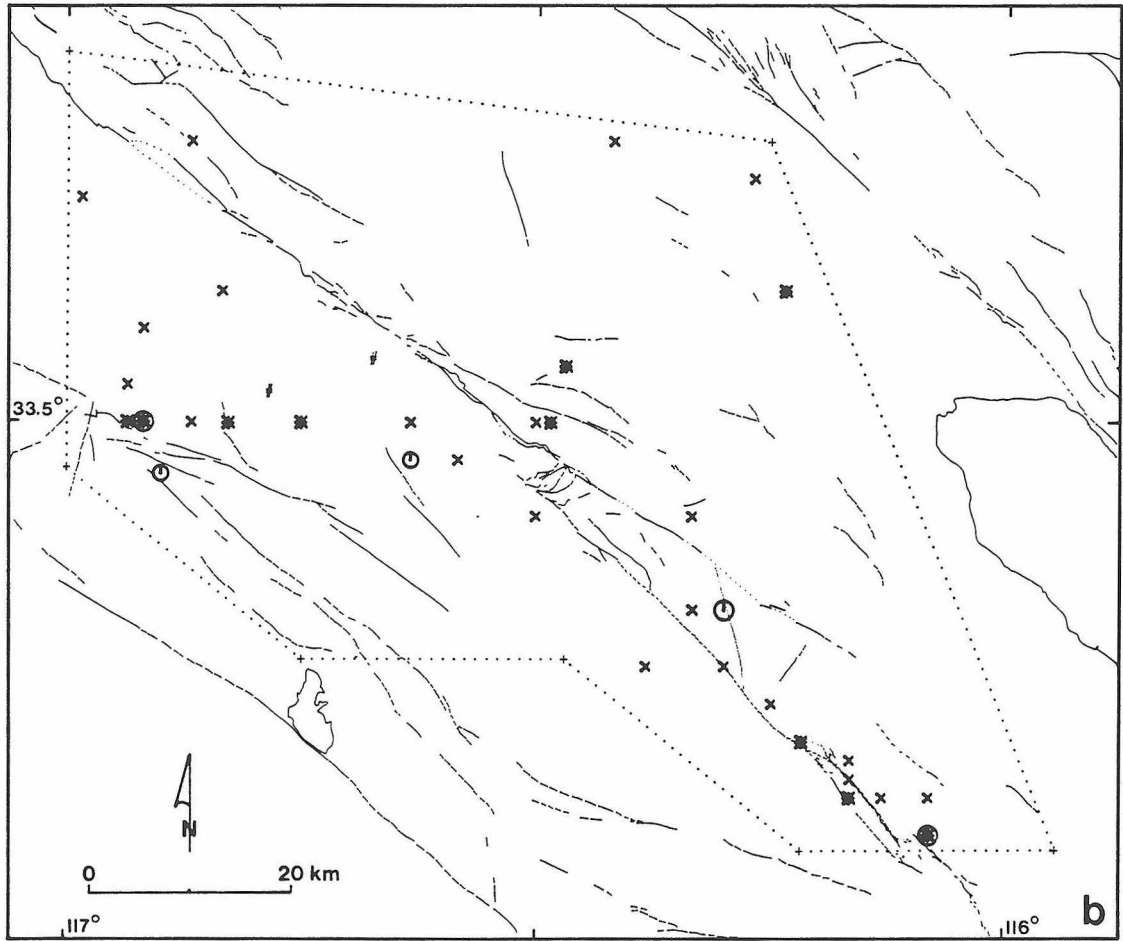


TABLE 1.5. Relocated 1932-1937,3,24 Activity

Yr	Mo	Da	HrMn	M _L	RVR			LJC			Latitude	Longitude	Depth
					P	S	S-P	P	S	S-P			
32	01	10	1539	3.0			8.0				33° 41.5'	116° 46.5'	-
32	07	10	0833	3.0			13.5			14.0	33° 33.5'	116° 11.5'	-
32	09	05	0832	3.0	57.7	69.1	11.4	59.5	70.8	11.3	33° 33.0'	116° 30.5'	12
32	10	02	0448	3.0			16.8			13.5	33° 12'	116° 06.5'	+
32	10	02	1623	3.0			16.1			12.1	33° 14'	116° 13.5'	+
32	10	10	2312	3.0			15.2			13.5	33° 28'	116° 07.5'	-
32	11	16	0947	3.0			7.3				33° 42.5'	116° 48.5'	-
32	12	09	1304	3.5	45.4	53.7	8.3	48.3	57.8	9.5	33° 32.7'	116° 55.3'	4
32	12	29	1931	3.5			17.5			15	33° 20'	115° 59'	-
33	01	18	1921	3.0			16.8			13	33° 10'	116° 08.6'	-
33	01	31	2031	3.5			10.8			15	33° 48'	116° 25'	-
33	03	08	1058	3.5			11.8			11.5	33° 28.5'	116° 27'	+
33	08	05	2331	4.4	38.4	54.7	16.3	34.9	47.4	12.5	33° 16.8'	116° 10.5'	10
33	08	06	0332	4.7	53.6	69.8	16.2	49.1			33° 14.6'	116° 11.2'	10
33	10	05	2020	3.0	36.3	45.7	9.4	36.1	45.7	9.6	33° 28.2'	116° 49.3'	4
33	10	05	2220	2.9	51.0	69.1	18.1	44.3	57.4	13.1	33° 05.6'	116° 05.1'	10
33	10	21	0406	3.3			9.3			8.8	33° 24.6'	116° 53.4'	-
33	12	22	0818	3.0	54.5	65.6	11.1	53.2	64.6	11.2	33° 27.1'	116° 32.1'	10
34	01	13	2226	3.5	16.0	24.7	8.7	21.0	32.7	11.7	33° 40.2'	116° 41.5'	16
34	02	07	0927	3.2	48.9	60.0	11.1	50.9	62.5	11.6	33° 34.1'	116° 30.7'	12
34	02	20	1035	4.0	21.2	32.8	11.6	20.3	31.7	11.4	33° 27.9'	116° 28.8'	12
34	03	02	1940	3.0			13.2			12.2	33° 28.8'	116° 19.2'	-
34	04	07	1343	3.0	36.2	54.8	18.6	29.3	44.2	14.9	33° 05.0'	115° 57.5'	10
34	04	08	1014	3.0	44.8	52.9	8.1	48.1	60.5	12.4	33° 38.9'	116° 40.8'	16
34	06	02	2115	3.0	65.7	84.1	18.4	60.9	75.5	14.6	33° 11.7'	115° 57.9'	10
34	07	22	0718	3.0	41.9	50.2	8.3	46.8	58.2	11.4	33° 39.6'	116° 44.2'	16
34	08	14	1129	3.5			17.8				33° 09'	116° 07'	-
34	09	02	1016	3.0			14.3			13.3	33° 30'	116° 11'	-
34	10	30	0451	3.0	57.2	65.8	8.6	59.1	68.4	9.3	33° 31.1'	116° 54.6'	4
34	11	15	0717	3.5	47.2	64.9	17.7	42.7	56.2	13.5	33° 12.9'	116° 03.5'	10
34	12	07	0334	3.0	35.7	48.0	12.3	35.0	46.7	11.7	33° 27.9'	116° 25.3'	12
34	12	21	1224	3.0			6.3				33° 46'	116° 54'	-
35	01	29	2104	3.0	55.1	70.5	15.4	51.7	64.3	12.6	33° 18.8'	116° 12.9'	10
35	03	12	1351	3.0	06.7	14.6	7.9	12.5	24.6	12.1	33° 42.5'	116° 43.9'	16
35	04	07	0932	3.5	19.2	31.5	12.3	18.8	30.6	11.8	33° 28.7'	116° 25.0'	12
35	04	15	0421	3.0	56.9	76.3	19.4	52.7	66.9	14.2	33° 10.2'	115° 56.1'	10
35	05	27	0843	3.0	10.0	21.7	11.7	10.9	22.6	11.7	33° 31.7'	116° 27.8'	12
35	07	15	1002	3.0	38.9	47.9	9.0	40.0	50.6	10.6	33° 31.6'	116° 47.1'	4
35	08	22	1624	3.0			12.5			17.1	33° 50'	116° 10'	+
35	09	02	0344	3.0			9.2				33° 31.8'	116° 48'	-
35	10	18	1350	3.0	52.9	70.8	17.9	47.6	61.0	13.4	33° 10.3'	116° 03.7'	10
35	11	02	1734	3.5	24.5	37.3	12.8	23.9	35.4	11.5	33° 27.3'	116° 24.2'	12
35	11	04	0355	4.5	63.6	72.6	9.1	64.8	75.4	10.6	33° 31.7'	116° 46.7'	4
35	11	04	0547	3.0	64.6	73.5	8.9	66.9	78.0	11.1	33° 34.1'	116° 45.9'	4
35	11	04	0657	3.0	76.0	85.4	9.4	78.1	89.3	11.2	33° 33.8'	116° 43.4'	4
35	11	04	0714	3.0	53.4	63.1	9.7	55.2	66.1	10.9	33° 32.7'	116° 43.2'	4
35	11	04	0911	3.0	47.6	56.6	9.0	49.5	59.9	10.4	33° 32.5'	116° 48.1'	4
35	11	08	1002	3.0	18.7	27.7	9.0	20.9	32.3	11.4	33° 34.4'	116° 44.4'	4
35	11	10	0021	3.0	19.8	28.7	8.9	21.7			33° 32.7'	116° 48.1'	4
35	11	11	1544	3.0	51.3	61.6	9.3	52.4	62.4	10.0	33° 30.6'	116° 48.3'	4
35	11	12	1145	3.0	33.1	42.5	9.4	34.2	45.0	10.8	33° 31.7'	116° 44.7'	4
35	11	12	1346	3.0	48.2	57.0	8.8	50.5	61.5	11.0	33° 34.0'	116° 46.7'	4
35	11	19	2205	3.0			8.9				33° 33.7'	116° 46.6'	-
35	11	20	1616	3.0			7.0				33° 44'	116° 51'	-
35	11	24	2352	3.0			8.2				33° 40.5'	116° 45'	-
35	11	26	1200	3.0			9.7				33° 33'	116° 44'	-
36	01	24	1749	3.0			16				33° 14.5'	116° 14'	-
36	01	26	1413	3.0	33.6	44.6	11.0	32.3	44.0	11.7	33° 27.5'	116° 31.7'	10
36	01	30	1714	3.0	31.9			28.6			33° 20'	116° 14'	-
36	01	31	0909	3.0			11.5			11.2	33° 29'	116° 28'	+

TABLE 1.5. (continued)

Yr Mo Da	HrMn	M_L	RVR			LJC			Latitude	Longitude	Depth
			P	S	S-P	P	S	S-P			
36 02 01	0501	3.0			9.0			11.3	33° 37.5'	116° 41'	+
36 02 05	2109	3.0	55.8	64.6	8.8	56.7	66.2	9.5	33° 29.9'	116° 52.7'	4
36 02 06	0813	3.0	57.0	69.4	12.4	58.1	69.6	11.5	33° 31.1'	116° 25.9'	12
36 02 06	1856	3.5	32.1	51.0	18.9	28.2	42.9	14.7	33° 13.1'	115° 55.7'	10
36 02 10	0946	3.0	40.0	49.8	9.8	41.9	51.5	9.6	33° 31.0'	116° 47.9'	4
36 03 17	1227	3.0			8.7			9.6	33° 30.5'	116° 53.5'	+
36 03 19	1639	3.5			9.5			9.8	33° 29'	116° 47'	+
36 04 05	1958	3.0	31.3	43.5	12.2	30.3			33° 26.7'	116° 27.3'	12
36 05 07	0346	3.5	68.6	89.2	20.6	59.4	75.9	16.5	32° 52.0'	115° 49.8'	10
36 05 07	1147	4.5	51.5	69.5	18.0	47.1	61.3	14.2	33° 13.5'	116° 00.3'	10
36 05 07	1446	3.0	12.5	29.2	16.7	7.0	20.5	13.5	33° 12.4'	116° 06.8'	10
36 05 12	1206	3.0	13.7	23.0	9.3	15.5	25.4	9.9	33° 31.5'	116° 48.8'	4
36 06 14	2305	3.0			17.0			13.5	33° 11'	116° 05.5'	+
36 06 21	1419	3.5			9.0			10.3	33° 32.3'	116° 49'	+
36 07 29	1422	4.0			9.5				33° 31'	116° 45'	-
36 08 10	0759	3.0	43.3	58.3	15.0	47.3	65.4	18.1	33° 49.4'	115° 59.5'	16
36 08 19	1318	3.0	46.0	55.2	9.2	47.0	56.8	9.8	33° 30.4'	116° 50.4'	4
36 09 05	1024	3.5			8.8			10.0	33° 32.3'	116° 50'	+
36 09 11	0932	3.0			19			12.8	33° 04'	116° 02'	-
36 10 14	0630	3.5	27.2	40.1	12.9	31.9	48.4	16.5	33° 47.7'	116° 11.8'	16
36 12 02	0433	3.0	40.1	48.5	8.4	42.3	52.0	9.7	33° 32.1'	116° 53.8'	4
36 12 07	2344	3.0	29.0	46.6	17.6	23.2	37.2	14.0	33° 10.4'	116° 02.7'	10

In the depth column the numbers indicate the assumed depth based on local seismicity and used in the location calculations. + means good relative location based on two S-P values; - means poor relative location.

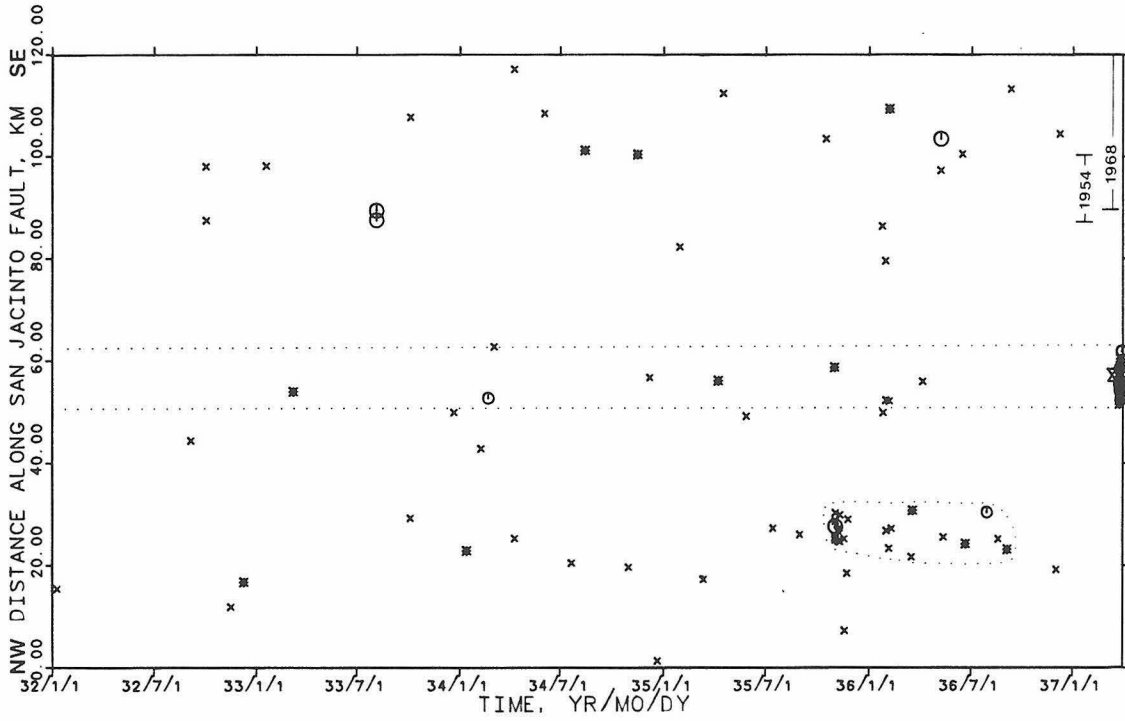


Figure 1.7. Time-distance plot of earthquakes shown on Figure 1.6a. The distance axis parallels the San Jacinto fault. All earthquakes on Figure 1.6a are plotted except for the eight northeasternmost and the one southwesternmost. The 1937 aftershock zone is marked. The Cahuilla cluster is outlined. The future rupture zones of the 1954 and 1968 earthquakes are indicated.

errors of about 10 to 15 km, and some are in error by as much as 20 km. We would like to illustrate the problem of using the older epicenter and phase data by looking at the example of the 1937 earthquake mainshock, aftershocks, and preshock seismicity.

Figure 1.6 shows two maps with the locations of $M_L \geq 2.5$ earthquakes in the area of and prior to the 1937 earthquake. On one map (Figure 1.6*b*) the epicenters are taken from the CIT catalog of southern California earthquakes. These events are located in general to the nearest tenth of a degree, and swarm events are given the same location as the largest event in the swarm. The alignment of epicenters along the southeastern Coyote Creek fault may be an indication of some subjectivity in the epicenter assignment. On the other map (Figure 1.6*a*) the same earthquakes are plotted after relocation as described in the preceding sections. Many features become more apparent after relocation, including the concentrated activity near Cahuilla, some activity near the epicenter of the 1937 mainshock, activity on the San Jacinto fault northwest of Anza, and the concentration of epicenters along the southeastern Coyote Creek fault disappears. The differences between the catalog locations and the relocations seem great enough that researchers who wish to study the historic seismicity should relocate the earthquakes with a technique such as we have used before attempting detailed analysis.

Another illustrative example of how the catalog data should be used with caution is given by the 1937 earthquake mainshock and aftershocks. Figure 1.8 shows the same data set processed in three different ways. Within the close-spaced dotted enclosure lie the epicenters of the 1937 mainshock and twenty aftershocks (Table 1.4) determined after the P- and S-wave arrival times at stations RVR and LJC were carefully picked from the original seismograms and each earthquake located with appropriate station delays. Within the wide-spaced dotted enclosure lie the same earthquakes but relocated using the original phase data. The relocations using the original phase data show a larger spread in epicenters by about 6 to 8 km. This is

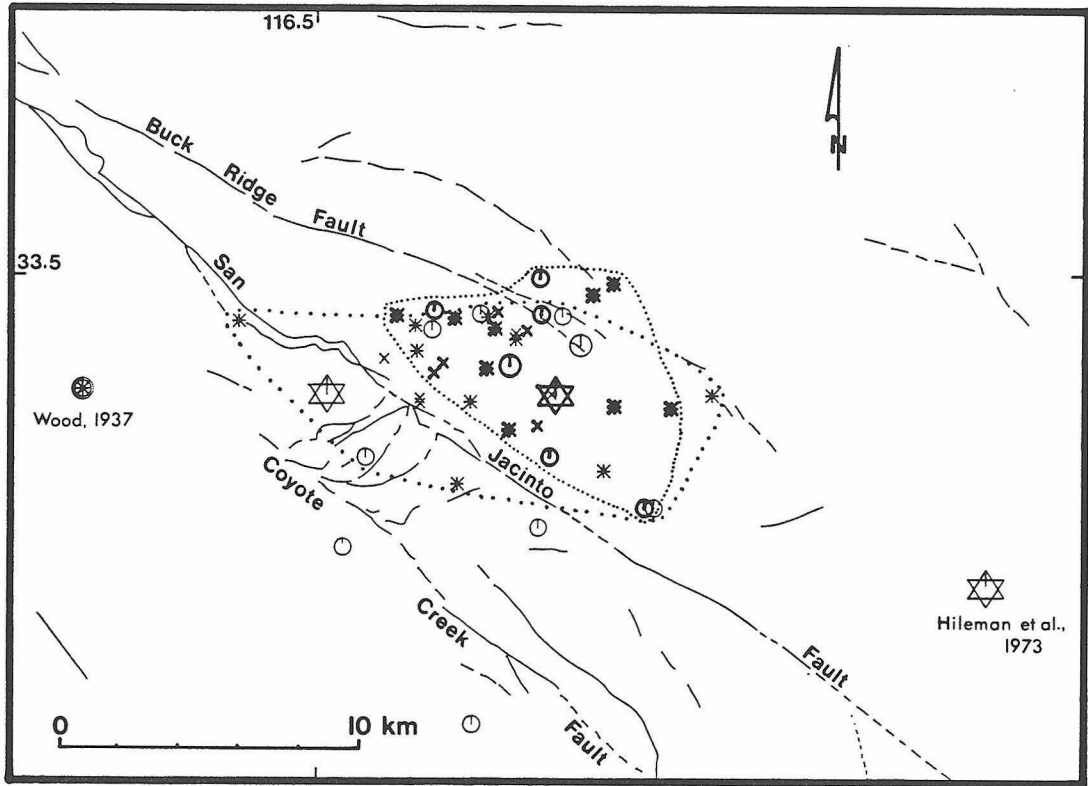


Figure 1.8. Epicenters of the 1937 mainshock and twenty aftershocks. The bold symbols within the close-spaced dotted outline are the epicenters determined from relocation of the events using arrival times at stations RVR and LJC repicked from the original seismograms and station delays determined for area 2 (Figure 1.2, Table 1.1). The lighter symbols within the wide-spaced dotted outline are the epicenters determined from relocation of the events using the original phase data from stations RVR and LJC and the station delays for area 2. The symbols outside the dotted enclosures are the CIT catalog locations for these earthquakes. The mainshock locations by Wood and Hileman et al. are indicated. Note how the seismicity pattern becomes much clearer when the data is reanalyzed with modern techniques.

partly due to the absence of an S-wave arrival time for some of the events. Often these S-wave arrival times can be obtained from close examination of the seismograms. The CIT catalog locations for these earthquakes are all outside of the dot enclosed areas. The catalog epicenters for most of the aftershocks are the same as that assigned to the mainshock by Wood (1937). The catalog location for the mainshock was changed by Hileman et al. (1973) and is 32 km east of the catalog aftershock epicenters and 16 km southeast of our relocation.

In these two examples relocations using the original phase data give dramatically improved pictures of seismicity patterns compared to the routine pre-mid-1970's catalog locations. This level of refinement probably is sufficient for most seismicity studies. Repicking arrival times from the original seismograms (which is time consuming) and adding missing phase data when possible seems to further improve the epicentral locations for more detailed seismicity pictures.

1.10 1954 Arroyo Salada Earthquake

We relocated the March 19, 1954 earthquake (M_L 6.2) using P-wave arrival times at stations PLM, BAR, RVR, and BBC, ranging in distance from 60 to 140 km and spanning 110° in azimuth. The $M_L \geq 3.9$ aftershocks were relocated using P- and S-wave arrival times recorded at stations PLM and BAR, both about 75 km distant and 60° apart in azimuth. Except for the main shock all of the arrival times were obtained from the original phase cards. The delays used are those determined for the area numbered 8 in Figure 1.2 and Table 1.1. The new epicenters are shown in Figure 1.3 and listed in Table 1.6. The main shock is located at the southeastern mapped termination of the San Jacinto (Clark) fault, and the aftershocks extend about 15 km further southeast beneath Arroyo Salada indicating unilateral rupture to the southeast. Most of the aftershocks cluster at the southeast end of the apparent rupture zone. One of the largest aftershocks (M_L 5.5) occurred near or on the Coyote Creek fault near the future epicenter of the 1968 Borrego Mountain earthquake. The

TABLE 1.6. Relocated 1954 Main Shock, $M_L \geq 3.9$ Aftershocks, and a Preshock Cluster

Yr Mo Da	HrMn	M_L	PLM		BAR		RVR	BBC	Latitude	Longitude	Depth	
			P	S	P	S	P	P				
54 01 04	1513	3.1	40.90	48.90	42.60	52.70			33° 17.71'	116° 08.35'	8	
	1850	3.9	68.40		69.90	79.60			33° 16.00'	116° 06.00'	8	
	1949	3.0	20.50	29.00	21.80	31.60			33° 15.97'	116° 06.82'	8	
	2106	3.0	22.70	30.90	24.60	34.50			33° 17.59'	116° 08.28'	8	
	2331	4.2	63.90		65.90	75.80			33° 17.63'	116° 06.77'	8	
54 01 07	2122	3.2	22.30	30.90	24.50	34.40			33° 18.09'	116° 07.23'	8	
54 03 19	0954	6.2	40.30		42.60		51.20	49.70	33° 17.73'	116° 10.58'	8	
	1015	4.5	32.80	42.30	34.90	44.50			33° 16.75'	116° 04.64'	8	
	1020	4.5	8.00	16.80	9.30	19.40			33° 16.52'	116° 05.16'	8	
	1021	5.5	28.60	37.20	29.30				33° 12.49'	116° 08.17'	8	
	1026	4.0		30.70	23.00	33.30			33° 17.48'	116° 03.24'	8	
	1201	3.9	28.50		29.90	39.80			33° 16.10'	116° 04.53'	8	
	1308	4.3	15.30	25.30	16.10	25.80			33° 13.70'	116° 01.49'	8	
	1401	4.1	8.80		9.90	19.80			33° 15.28'	116° 03.43'	8	
	1438	4.0	1.30		2.40	12.20			33° 15.12'	116° 03.99'	8	
	1604	3.9	31.90	41.40	33.50	43.40			33° 16.34'	116° 03.50'	8	
	54 03 20	0419	4.9	30.80		32.10	41.90			33° 15.66'	116° 04.71'	8
		0604	4.3	4.70		6.30	16.10			33° 16.44'	116° 05.81'	8
54 03 23	0414	5.1	1.60		3.30	12.90			33° 16.31'	116° 07.30'	8	
	0423	3.9	41.50		43.90	53.70			33° 18.38'	116° 08.84'	8	
54 04 04	0429	4.1	31.40	41.10	32.70	42.60			33° 15.53'	116° 02.52'	8	

A station delay of -0.16 s for the BBC P wave was determined from three recent earthquakes in the 1954 area recorded at station BTL (Figure 1.1). A station delay of -0.20 s was used for the P_g arrival at RVR from the 1954 main shock. The P-wave station delay for area 8 listed in Table 1.1 is for the P_n arrival which is the first arrival for most of the aftershocks.

original mainshock location by Richter (1958) is essentially identical to ours, but the relocation by Hanks et al. (1975) lies about 14 km northeast (Figure 1.3). The P-wave first motions constrain a source mechanism that indicates right-slip on a N 56° W trending fault (Figure 1.9).

The aftershock (rupture) zone of the 1954 earthquake occurred in an area where no surface expression of strike-slip faulting is mapped. Instead, folded late Tertiary and Quaternary sediments are seen (Sharp, 1975, 1981; Bartholomew, 1970).

Relocated $M_L \geq 2.5$ seismicity in the region of the 1954 earthquake for the six years preceding the main shock is shown in Figure 1.10*a*. Although some seismicity occurred in the area of the eventual aftershock zone, small earthquakes are noticeably absent from the main shock epicentral area. Ten weeks before the main shock a burst of five earthquakes (M_L 3.0-4.2) occurred during an eight-hour period. These earthquakes occurred in the center of the future rupture zone between the main shock and the cluster of aftershocks (Figure 1.10*b*).

1.11 1942 Earthquake

The October 21, 1942 earthquake (M_L 6.3) was determined by Richter (1958) to have an epicenter a few kilometers west of the junction of the Coyote Creek and Superstition Mountain faults. Taking into account the error possible in that epicentral determination, previous researchers (e.g. Thatcher et al., 1975; Sanders and Kanamori, 1984) assumed that the 1942 earthquake was very likely situated on the northwest end of the Superstition Mountain fault abutting the southeast end of the 1968 Borrego Mountain earthquake rupture. Such a location would fit nicely into a picture of large earthquake rupture on adjoining segments of the San Jacinto fault zone. Our analysis of the P- and S-wave arrival-time data from stations PLM, LJC, CUY, and RVR, however, indicates that the 1942 event is probably not located on the Superstition Mountain fault but rather is located near the Fish Creek Mountains southwest of the 1968 Borrego Mountain fault rupture.

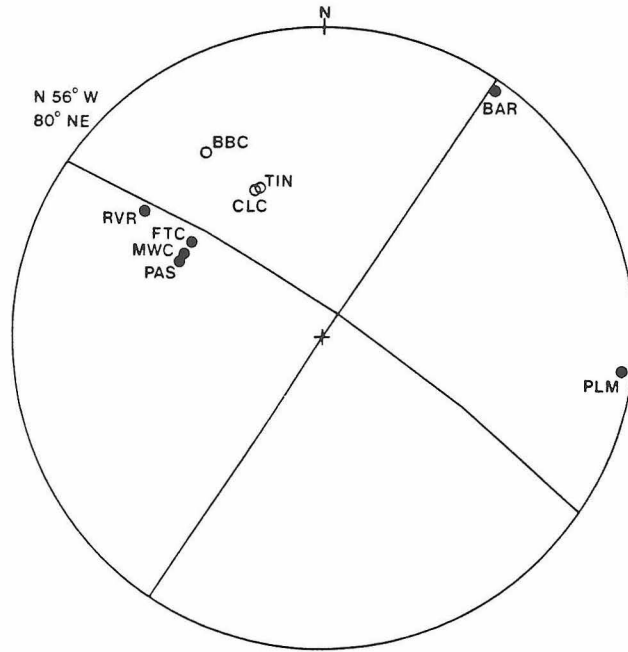


Figure 1.9. P-wave first motion source mechanism for the 1954 Salada Wash earthquake. Solid circles, compression; open circles, dilatation. Lower hemisphere, equal angle projection. The southern California seismograph stations are Barrett Dam (BAR), Big Bear (BBC), China Lake (CLC), Fort Tejon (FTC), Mount Wilson (MWC), Pasadena (PAS), Palomar (PLM), Riverside (RVR), and Tinemaha (TIN). Stations BAR and RVR are nodal.

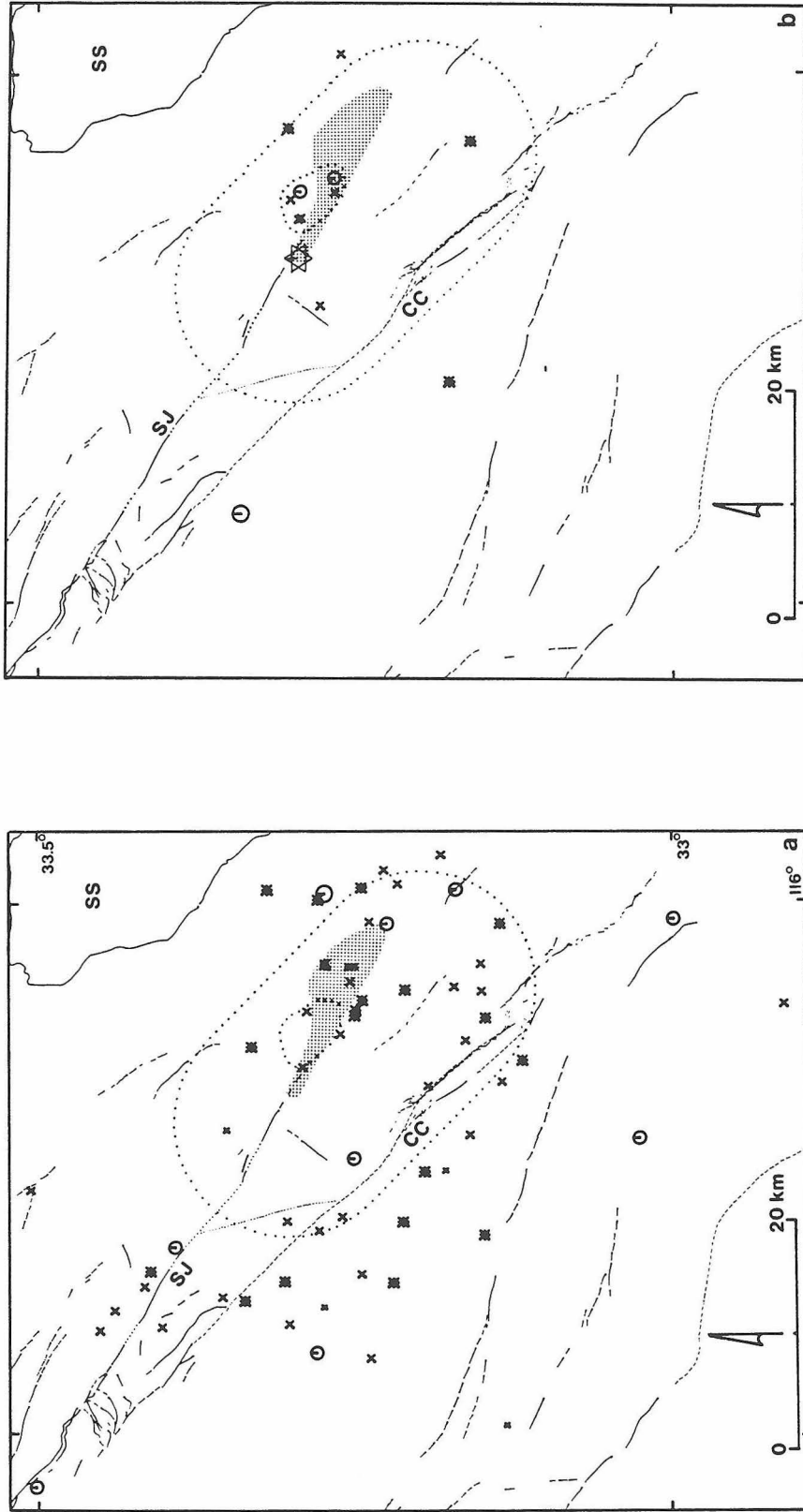


Figure 1.10. (a) Relocated earthquakes $M_L \geq 2.5$ in the area of the 1954 earthquake which occurred between January 1, 1948 and January 3, 1954. The earthquakes have catalog locations within the large area outlined by dots. The magnitude key is the same as in Figure 1.3 with the addition that small x = $M_L < 2.5$. The 1954 mainshock and aftershock zone is indicated by shading. (b) Relocated earthquakes which occurred between January 4, 1954 and March 19, 1954. The burst of earthquakes which occurred January 4, 1954 ten weeks before the March 19, 1954 main shock are contained within the small dotted outline. The 1954 main shock epicenter is plotted and the aftershock zone is indicated by shading. This small burst of seismicity occurred in an area that was relatively non-seismic at the $M_L \geq 2.5$ level for the preceding six years.

For the 1942 main shock the only arrival times available from nearby stations (80-160 km) are P-wave times at stations PLM, LJC, and RVR. At these stations no main shock S-wave times can be read since the seismograms are clipped after the first arrivals. Since the use of these three arrival times would result in a poorly constrained location we have attempted to determine the range of possible S-P times at PLM, LJC, and RVR from the seismograms of the early aftershocks. At station LJC the S-P times of five larger ($M_L \geq 3.5$) early aftershocks from 10 to 105 minutes after the main shock range from 12.8 to 13.6 seconds. At station RVR four aftershocks from $2\frac{1}{2}$ to 8 minutes after the main shock have S-P times ranging from 19.3 to 21.8 seconds. The similar record from station PLM is missing from the Caltech seismogram library, so we cannot determine the S-P times of the early aftershocks recorded at this station. We calculated main shock epicenters using the delay values from area 9 (Figure 1.2, Table 1.2), the extreme LJC S-P times, and the smaller RVR S-P time, and find that they fall within an area about 5 km in radius centered on the epicenter shown in Figure 1.3 and listed in Table 1.7. The larger RVR S-P time gives large location errors and so is not used. A location determined using only the three P-wave times lies 15 km west of our preferred location. We feel that the epicentral location error for the 1942 mainshock is about 10-15 km.

Even with the location uncertainty it appears that the 1942 earthquake was not caused by rupture of the Superstition Mountain fault. Rupture of the southeastern part of the Coyote Creek fault, though, may be considered a possibility. The surface displacement along this section of the Coyote Creek fault during the 1968 Borrego Mountain earthquake was only about 25 per cent of the maximum measured further northwest near the 1968 main shock epicenter, suggesting that this section of the fault may have slipped during an earlier event. However, eight of the best located 1942 aftershocks (M_L 4.0-4.5, location error about 5 km) are located within a 15 by 18 km area not associated with any one fault strand, and all have epicenters southwest of the Coyote Creek fault (Figure 1.3) in an area of intensely faulted Pliocene

TABLE 1.7. Relocated 1942 Main Shock and Some $M_L \geq 4.0$ Aftershocks

Yr	Mo	Da	HrMn	M_L	CUY		PLM		LJC		RVR		Latitude	Longitude	Depth
					P	S	P	S	P	S	P	S			
42	10	21	1622	6.5			30.0		34.43		40.96		33° 02.93'	116° 05.28'	7
			1625	5.0							46.06	67.85			
			1626	5.0					16.62		23.72	43.06	32° 58.64'	116° 08.07'	10
			1634	4.5					00.51	14.08		28.55	32° 55.53'	116° 00.64'	10
			1910	4.5					48.83	61.34	58.70	80.26	32° 44.04'	116° 07.90'	10
			2149	4.5			45.6		49.2	62.2			32° 58.81'	116° 03.94'	10
			2250	4.0			49.0		52.3	64.5			32° 57.62'	116° 08.22'	10
42	10	22	1139	4.0	02.7	09.5			12.1	26.2	18.7	40.2	32° 56.60'	115° 58.24'	9
			1255	4.0	05.2	13.1			15.0	30.1	19.8	41.2	33° 04.03'	115° 53.40'	6
			1813	5.0					46.8	60.8	53.2	74.9	32° 55.89'	115° 57.16'	10
42	10	25	1859	4.0			53.8		57.5	70.0	64.8		32° 59.07'	116° 07.45'	7
42	10	26	0434	4.0			21.8		24.2	36.0		53.2	32° 53.16'	116° 10.12'	10

sediments. This suggests that a main shock location on the Coyote Creek fault is unlikely since large aftershocks would be expected to lie along the fault trace, as was observed for aftershocks of the 1968 Borrego Mountain earthquake. In addition, the dissimilarity of strong motion seismograms recorded at El Centro for the 1942 and 1968 earthquakes supports the conclusion that the two events were not produced by the same fault. The P-wave first motions provide some constraint on one of the source nodal planes; however a unique solution cannot be obtained (Figure 1.11).

1.12 1968 Borrego Mountain and 1969 Coyote Mountain Earthquakes

The Borrego Mountain earthquake (M_L 6.8) of April 28, 1968 occurred on the southern extension of the Coyote Creek fault (Figures 1.1 and 1.3). Seismicity of the 8 years prior to the main shock has been relocated by Corbett and McNally (1978; E. Corbett, personal communication, 1982), who found two clusters of small earthquakes that preceded the main shock by several years. These clusters occurred in the crustal blocks northeast and southwest of the Coyote Creek fault. Both were 10-15 km from the fault in a direction nearly perpendicular to the fault at the eventual main shock epicenter (Figure 1.12). The southwest cluster was active during late summer 1961 and winter 1962-1963, and the northeast cluster was active during late summer 1965, nearly three years before the main shock. A foreshock (M_L 3.7) occurred about 1 minute before and in nearly the same location as the main shock.

The aftershocks associated with this earthquake have been analyzed by Hamilton (1972) and Allen and Nordquist (1972). Most of the aftershocks are located parallel to the northwest trending surface rupture and slightly to the northeast, suggesting a steeply northeast dipping fault plane (Figure 1.12). The aftershock zone extended northwest and southeast from the main shock, but aftershocks were much more numerous to the southeast. There is a 6-km gap in the aftershock pattern where the main shock is located. This is consistent with complete stress release on a 8-km-diameter source area due to the breaking of an asperity (Ebel and Helmberger, 1982).

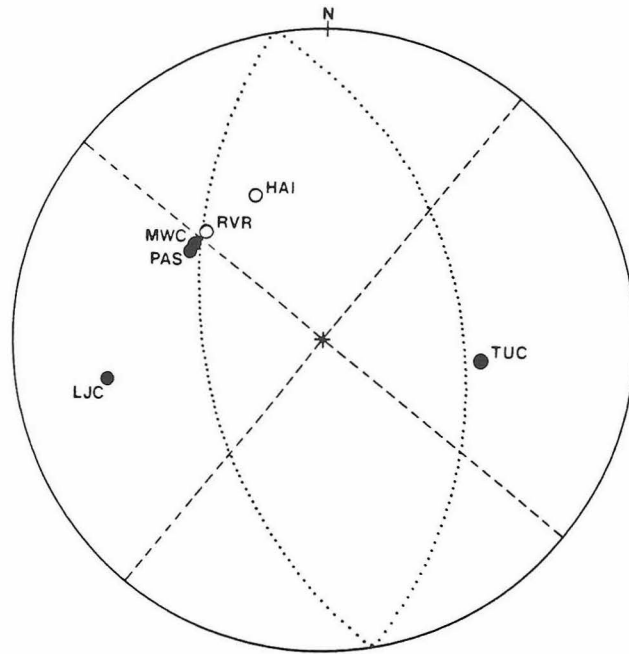


Figure 1.11. P-wave first motions for the 1942 main shock. The dashed and dotted lines indicate two of the different mechanisms permissible by the data. Closed circles, compression; open circles, dilatation. Lower hemisphere, equal angle projection. The seismograph stations are Haiwee (HAI), La Jolla (LJC), Mount Wilson (MWC), Pasadena (PAS), Riverside (RVR), and Tucson (TUC).

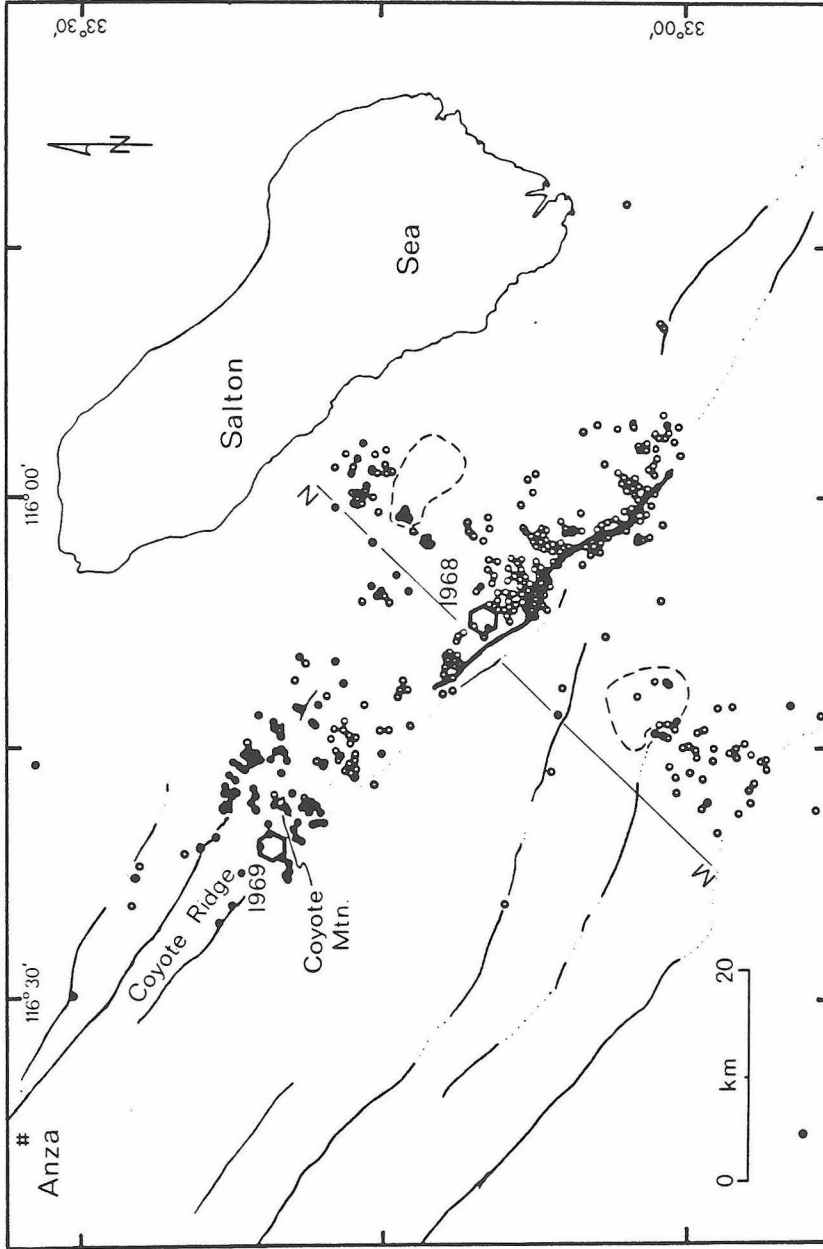


Figure 1.12. Main shock epicenters (hexagons) and combined aftershocks of the 1968 Borrego Mountain (open circles) and the 1969 Coyote Mountain (solid circles) earthquakes. The heavy fault line is the 1968 surface rupture. The dashed outlined areas indicate the locations of "preshock" clusters preceding the 1968 earthquake (Corbett and McNally, 1978) (after Thatcher and Hamilton, 1973).

The aftershock distribution is similar to the distribution of surface rupture which extended about 7 km northwest and 25 km southeast from the main shock epicenter. Aftercreep was reported southeast of the main shock for at least 1000 days following the earthquake, more than doubling the initial slip on portions of the central break (Burford, 1972). Creep has continued on the southeastern Coyote Creek fault since at least 1971 at an average rate of 5.8 mm/yr (Louie et al., 1985).

Figure 1.13a is a cross section parallel to the Coyote Creek fault showing the combined aftershocks of the Borrego Mountain and Coyote Mountain earthquakes. One of the apparent features of the distribution of hypocenters is the abrupt termination of the northwest group of Borrego Mountain aftershocks, perhaps suggesting that rupture was stopped by a barrier. This abrupt end coincides with the southeast extent of the Coyote Ridge uplift block (Figures 1.12 and 2.19). The few Borrego Mountain aftershocks which do occur farther northwest are in the eventual rupture area of the Coyote Mountain event.

The aftershocks of the 1969 Coyote Mountain earthquake (M_L 5.8) were analyzed by Thatcher and Hamilton (1973). They found relatively few aftershocks compared to other events of similar magnitude (5 $M_L \geq 2.5$ in 1 month). The aftershocks were distributed about equally on the Coyote Creek and adjacent San Jacinto faults (Figure 1.12). The main shock ruptured at a depth of about 12 km on the Coyote Creek fault. The aftershocks which occurred on the Coyote Creek fault were some of the largest and extended southeast from the main shock at depths between 10 and 14 km suggesting a rupture zone 8 km long by 4 km thick. A high percentage of these aftershocks were deep (Sibson, 1982) suggesting that rupture was not allowed to propagate to shallower depths. Teleseismic short-period P-wave spectra indicate that the main shock was a high stress drop event on a small source area (Thatcher and Hamilton, 1973). The P-wave first motions in Thatcher and Hamilton (1973; the fault plane solution they give does not have perpendicular nodal planes) constrain a source mechanism which indicates right-oblique slip on a near vertical, N 50° W trending

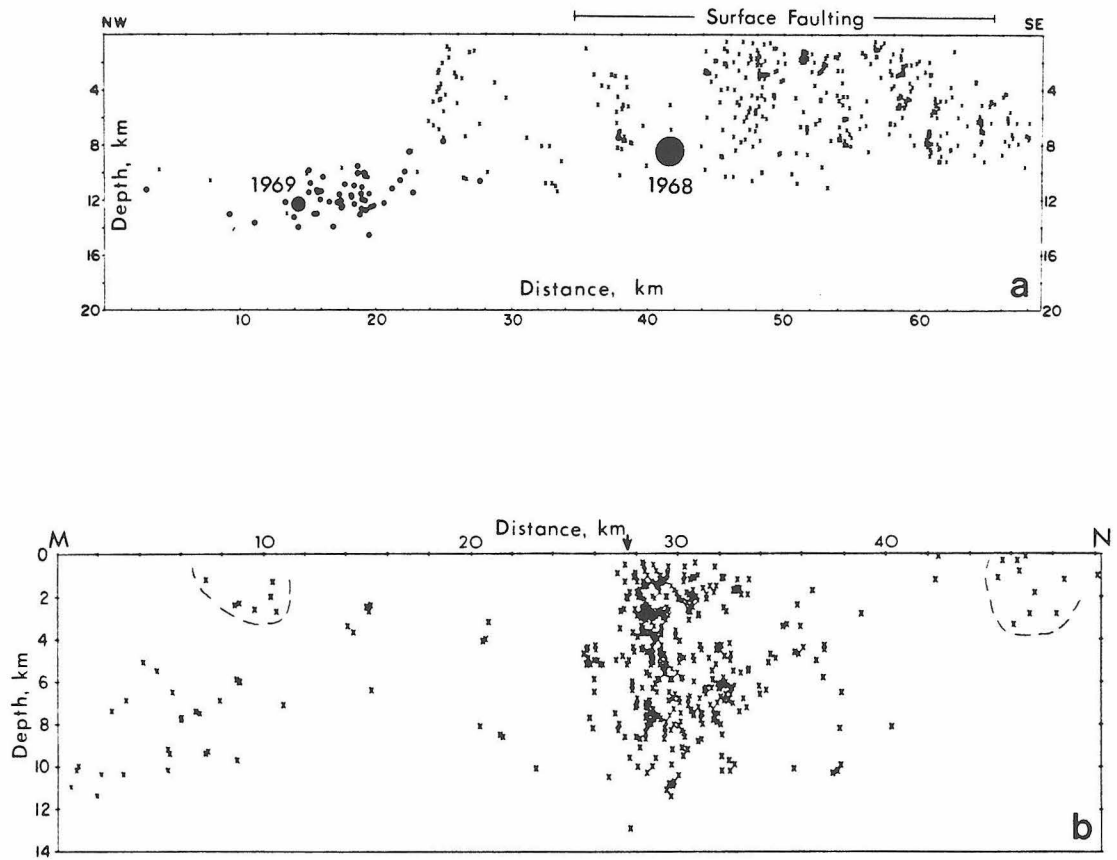


Figure 1.13. (a) Vertical section parallel to the aftershock zones of the Borrego Mountain (crosses) and Coyote Mountain (dots) earthquakes. The 1968 and 1969 main shock locations are shown. The extent of the 1968 surface rupture is indicated (after Thatcher and Hamilton, 1973). (b) Vertical section M-N (Figure 1.12) perpendicular to the 1968 rupture zone. The dashed outlines enclose the shallow aftershocks discussed in the text. The arrow indicates the position of the surface fault trace (after Hamilton, 1972).

fault plane. The oblique component indicates relative uplift of Coyote Mountain. No preshock or foreshock activity is apparent before this earthquake, since these events cannot be distinguished from the Borrego Mountain aftershocks.

1.13 Relative Sizes of the 1937, 1942, 1954, and 1968 Earthquakes

The local magnitudes determined by Richter for the 1937, 1942, 1954, and 1968 earthquakes are 6.0, $6\frac{1}{2}$, 6.2, and 6.4. Depending on the availability of on-scale Wood-Anderson recordings, each of the M_L values was determined by Richter in a slightly different manner.

Richter found the 1937 and 1954 local magnitudes by averaging the magnitudes at three of the southern California seismograph stations which recorded the maximum S wave on scale. For the 1954 earthquake there are on-scale recordings at HAI, PAS, and TIN, and for the 1937 earthquake there are recordings at these same stations plus SBC (Table 1.8). To obtain the 1937 magnitude Richter threw out the lowest value at PAS before averaging to obtain M_L 6.0. PAS is also the low value in the 1954 readings but was included in the calculations for the average M_L 6.2. It seems that for consistency the PAS amplitude data for each earthquake should be given the same consideration. Whether the PAS data is used or not the 1954 earthquake is, by comparison of individual stations, 0.3-0.5 M_L units larger than the 1937 earthquake. The median local magnitudes of the 1937 and 1954 earthquakes are 5.9 and 6.2, respectively.

The amplitude data for the 1942 mainshock are shown in Table 1.8. Richter's approximate M_L $6\frac{1}{2}$ for the 1942 event seems to have resulted from his uncertainty in the readings at the nearly clipped southern California stations and the high M_L values at the stations in the central California area (Berkeley, BRK; Fresno, FRE; Mount Hamilton, MHC; Palo Alto, PAC; San Francisco, SFB). Of course the central California stations are well beyond the distance range originally intended by Richter for use in M_L determinations, and he must have extrapolated his attenuation curve somehow

TABLE 1.8. 1937, 1942, 1954, and 1968 Main Shock Magnitudes

Station	1937				1942				1954				1968			
	Δ	N-S	E-W	M_L	Δ	N-S	E-W	M_L	Δ	N-S	E-W	M_L	Δ	N-S	E-W	M_L
CWC-WA			54	5.9	380	99	102	6.4	354	94	87	6.2	402	58		6.4
HAI-WA	326															
MWC-WA	221	130+	139+	5.9+												
PAS-WA	178	64	52	5.4	225	90+	119	6.0	206	152	154	5.9				
RVR-WA	156	136+	150+	5.8+												
SBC-WA	322	114	73	5.9	366	135	133	6.3								
TIN-WA	430	51	62	6.1					456	93	85	6.4				
WDY-WA													374		49.6	6.0
				<u>5.9</u>				<u>6.3</u>				<u>6.2</u>				<u>6.2</u>
CWC-LG													402	4.6	5.0	6.6
PAS-LG													217	25.0	31.1	6.7
RVR-LG													146	59	42	6.7
SBC-LG													359	25.3	17.0	6.9
																<u>6.7</u>
ECC-SM								6.4								7.0
BRK					771	9.7	8.3	6.5								
FRE					531	65		6.5								
MHC					691	11	9.5	6.3								
PAC					745	18	24	6.2								
SFB						7.8	4.7	6.6								

Units of Δ are kilometers. The values beneath N-S and E-W are the maximum 0-peak amplitude in millimeters on the respective north-south or east-west component Wood-Anderson seismogram.

in order to obtain the magnitudes. If we use only the southern California amplitude data we determine a median M_L 6.3 for the 1942 main shock. Station by station comparison with the 1937 earthquake shows that the 1942 event was 0.4-0.6 M_L units larger. Stations HAI and PAS suggest that the 1942 earthquake may have a slightly greater M_L than the 1954 earthquake.

The 1968 mainshock was clipped on most of the southern California Wood-Anderson seismograms, so Richter used an M_L 5.2 aftershock to calibrate several low-magnification torsion instruments which recorded both the aftershock and mainshock on scale (Allen and Nordquist, 1972). From this calibration he found an M_L 6.4 for the main shock. Four pairs of these 100x torsion seismometers were also used by Kanamori and Jennings (1978) to obtain an M_L 6.7 for the Borrego Mountain mainshock. The 0.3 M_L unit discrepancy between the Richter and the Kanamori and Jennings values may not be significant due to measurement errors of the small amplitudes of the M_L 5.2 aftershock on the low-gain instruments and also due to the uncertainty in the response of the 100x torsion instruments (they are supposed to be essentially the same as the regular Wood-Anderson instruments) and the true gain of the regular Wood-Anderson instruments. The preferred M_L is 6.8 (the average of the 100x torsion and strong motion local magnitudes; Kanamori and Jennings, 1978) since it is based on the largest number of data and, hopefully, errors are averaged out.

The strong-motion records at El Centro (ECC) can also be used to compare the relative sizes of the 1942 and 1968 earthquakes. Kanamori and Jennings (1978) used these strong-motion records to synthesize the equivalent Wood-Anderson response and found local magnitudes of 6.4 and 7.0 for the 1942 and 1968 events at El Centro, indicating an M_L difference of 0.6 units.

In conclusion, it appears that local magnitudes of 6.8, 6.3, 6.2, and 5.9 reflect the short-period sizes of the 1968, 1942, 1954, and 1937 earthquakes, respectively.

1.14 Older Large Earthquakes

Earthquakes in February 1890 (M_I 6.3) and May 1892 (M_I 6.3) are poorly located, but a comparison of the reported intensities (Topozada et al., 1981) with those of the 1937 and 1954 events indicates similar general locations somewhere along the central section of the San Jacinto fault zone. In particular, the 1890 earthquake was reported to be "felt with equal severity in each town on the Southern Pacific line between Pomona and Yuma" (Topozada et al., 1981). Since this railroad line runs near the trace of the San Jacinto and San Andreas faults north and east of Riverside, along the Banning fault through San Gorgonio Pass, and near the San Andreas fault east of the Salton Sea, the fact that the earthquake was felt with equal severity all along the train route suggests that the earthquake did not occur on any of the fault segments near the railroad (such as the December 14, 1948, earthquake which produced widely differing intensities along the train route; Topozada and Parke, 1982). In this case the most likely causative structure is near the central San Jacinto fault zone southeast of Anza. The relatively moderate description of the shaking in San Jacinto seems to rule out a location very near San Jacinto or at Anza. This earthquake may not have been generated by the southeasternmost Elsinore or San Jacinto faults, since a similar sized event near the southeastern San Jacinto fault in October 1942 (Figure 1.1) produced lower intensities in the Los Angeles County region (intensity map by Topozada and Parke, 1982).

The 1890 earthquake had a local magnitude larger than 6.0 based on a comparison of the areas of MM V and greater shaking for this and the 1937 earthquake (M_L 6.0).

The May 1892 earthquake had an intensity distribution similar to the February 1890 event. The area of MM V and greater shaking appears to be the same size for both events suggesting similar magnitudes. The 1892 earthquake, however, had lower intensities in the Los Angeles area, implying a location farther southeast than the 1890 epicenter.

Prior to 1890, the largest reported earthquake possibly associated with the central or northern San Jacinto fault zone occurred on December 16, 1858, and was felt with MM VII-IX intensities near San Bernardino (Topozada et al., 1981). This can perhaps be regarded as an aftershock of the great 1857 earthquake which resulted from slip on the San Andreas fault northwest of San Bernardino (Sieh, 1978; Agnew and Sieh, 1978).

Since 1899 the time between $M \geq 6$ earthquakes in the San Jacinto fault zone, excluding the 1942 earthquake, has been 18, 5, 14, 17, and 14 years; the latest occurring in 1968.

1.15 Discussion

The locations of most of the historical large earthquakes in the San Jacinto fault zone are now known with varying degrees of confidence. These locations and their approximate rupture zones based on aftershock locations delineate those sections of the fault that have ruptured historically and those that have not. The San Jacinto fault zone is a member of the group of strike-slip faults which accommodate the right-lateral shear displacement in southern California due to the relative movement of the Pacific and North American lithospheric plates. The slip rate on the San Jacinto fault near Anza (where the offset appears to occur principally on one strand) has been about 1 cm/yr for the last 700,000 years (Sharp, 1967). It is assumed that this slip rate applies along the entire fault zone, though individual overlapping fault strands may have smaller slip rates. If shear strain is accumulating at about this rate on the faults in the San Jacinto fault zone, and if we know the time since a section of fault last ruptured (assuming nearly complete strain release), we can approximately predict the current accumulated strain along many sections of the fault zone. Sections which have not ruptured recently or have not ruptured completely and have significant strain accumulation relative to other ruptured sections of the fault are called seismic slip gaps (e.g. Thatcher et al., 1975) and are assumed to have a higher

potential for generating large earthquakes than the already ruptured sections.

In Figure 1.1 the rupture zones of larger earthquakes in the San Jacinto fault zone are shown. The combined rupture zones of the 1899 and 1918 earthquakes are approximated based on magnitude versus fault length relations (Slemmons, 1977). From this map alone, and assuming that complete strain release accompanied each earthquake, we can identify the sections of the fault zone where strain accumulation is relatively high, and thus fault rupture more probable. These are the northwest section of the fault zone near San Bernardino, the section of the San Jacinto fault near Anza, the San Jacinto fault between the 1937 and 1954 breaks, the northwestern Coyote Creek fault, and the Superstition Mountain and Superstition Hills faults. Except for the northwest section of the fault zone, portions of which may have ruptured to cause earthquakes in 1899 and 1923, these sections of the San Jacinto fault zone have not released significant strain since at least 1892. In addition, the section of the fault zone which ruptured in 1899-1918 has by now accumulated significant potential slip.

Thatcher and others (1975) used seismic moments determined for these large earthquakes to show that two major seismic-slip gaps exist along the San Jacinto fault zone. These are the northwestern section of the fault zone between the end of the 1899-1918 rupture and the intersection of the San Jacinto and San Andreas faults (Cajon Pass to Riverside) and the central section of the fault zone between the northwest end of the 1968 rupture and the southeast end of the 1899-1918 ruptures (Anza to Coyote Mountain). Even though the seismic moments they determined may be in error by a factor of two or more (since data is often from only one station), the great difference in the moments of the largest events (1899, 1918, 1954, 1968) compared to the smaller events (1923, 1937) leaves no doubt about the existence and location of the seismic-slip gaps in the fault zone. Since the 1942 earthquake is no longer thought to be located on the Superstition Mountain fault, this section of the fault zone may also be considered a seismic slip gap. The seismic moments determined for

the large San Jacinto earthquakes are listed in Table 1.9.

1.16 Conclusions

The purpose of this work is to locate as precisely as possible the large earthquakes in the San Jacinto fault zone. This is done so that we can understand better the spatial relationships between the large earthquakes in this fault zone and also the patterns of preshock and aftershock activity. Our locations reveal many new facts about the historical earthquakes in the San Jacinto fault zone. They are:

1. The 1899 and 1918 San Jacinto-Hemet earthquakes severely damaged the small towns of San Jacinto and Hemet and very likely were caused by ruptures on separate en echelon strands of the San Jacinto fault zone near these towns.

2. The 1923 earthquake location is ambiguous, however, seismic and intensity data suggest a location on the San Jacinto fault near the town of Loma Linda.

3. The 1937 Buck Ridge earthquake has an epicenter between the surface traces of the San Jacinto and Buck Ridge faults. Aftershocks suggest a rupture length of about 7 km, mostly to the northwest.

4. The 1980 Whitewash earthquake occurred on the San Jacinto fault at the northwest end of the 1937 aftershock zone and broke another couple of kilometers further northwest into the edge of the Anza seismic gap.

5. A significant earthquake cluster occurred near the Cahuilla Valley $1\frac{1}{2}$ years before the 1937 event.

6. The 1954 Arroyo Salada earthquake epicenter is located at the southeast end of the Clark strand of the San Jacinto fault, and aftershocks suggest unilateral rupture to the southeast of about 15 km. No evidence of major faulting is apparent in the surface rocks of this area; instead folded young sediments are seen. The P-wave first motions indicate right-slip faulting on a subsurface extension of the San Jacinto fault.

7. A significant cluster of seismicity occurred in the center of the 1954 rupture

TABLE 1.9. Seismic Moments of Some Larger Earthquakes, San Jacinto Fault Zone

Year	M	M_o ($\times 10^{25}$)	Method (# of readings or name of station used), (reference)
1890	M_I 6.3		
1892	M_I 6.3		
1899	M 7	15	A_{VI} , comparison with 1918, (Hanks et al., 1975)
1918	M_L 6.8	15	AR (Berkeley), A_{VI} , (Hanks et al., 1975)
1923	M_L 6 $\frac{1}{4}$	1.0	surface wave (1), AR (Berkeley), A_{VI} , (Hanks et al., 1975)
1937	M_L 5.9	0.3	surface wave (1), AR (Berkeley), A_{VI} , (Hanks et al., 1975)
1942	M_L 6.3	9.4	S-spectra (Pasadena), (Thatcher and Hanks, 1973)
1954	M_L 6.2	4.4	S-spectra (Pasadena), (Thatcher and Hanks, 1973)
1968	M_L 6.8	8.3	teleseismic P-spectra (8) and S-spectra (4), (Hanks and Wyss, 1972)
		11.2	teleseismic long period body waves (28), (Burdick and Mellman, 1976)
		7	strong motion (El Centro), (Heaton and Helmberger, 1977)
		6.3	teleseismic short period body waves (11), (Ebel and Helmberger, 1982)
		8.2	teleseismic long period body waves (11), (Ebel and Helmberger, 1982)
1969	M_L 5.8	0.5	teleseismic long and short period body waves (9), surface wave (1), (Thatcher and Hamilton, 1973)
1975	M_L 4.7	0.03	surface waves (several), (Kanamori, 1976; Hartzell and Brune, 1979)
		0.019	Love waves (4), (Frankel, 1984)
1980	M_L 5.5	0.025	strong motion (4), (Frankel, 1984)
		0.056	Love waves (4), (Frankel, 1984)
1982	M_L 4.8	0.011	strong motion (4), (Frankel, 1984)
		0.023	Love waves (5), (Frankel, 1984)

M_o units are dyne/cm

AR = surface wave envelope

A_{VI} = area MM VI intensity

zone ten weeks before the main shock.

8. We locate the 1942 earthquake mainshock near the Fish Creek Mountains area southwest of and parallel to the southern end of the Coyote Creek fault. This earthquake is probably not located on the Superstition Mountain nor Superstition Hills faults. Eight $M_L \geq 4.0$ aftershocks are spread over a 15 by 18 km area and do not cluster on any one fault. Differences in the strong motion seismograms at El Centro between the 1968 and 1942 earthquakes support the relative locations of the two events.

9. The relation of the 1942 earthquake to slip in the San Jacinto fault zone is unknown.

10. Segments of the San Jacinto fault zone that have not slipped in large earthquakes since at least 1892 include the northwest end of the San Jacinto fault near San Bernardino, the 20-km-long Anza seismic gap, the 25 km segment of the San Jacinto fault between the 1937 and 1954 events, the northwest end of the Coyote Creek fault, the 45-km-long Superstition Mountain fault, and the 40-km-long Superstition Hills fault. Some of these fault sections may have accumulated a meter or more of potential seismic slip.

11. Large earthquakes may be expected to occur on structures not presently considered as major parts of the San Jacinto fault zone. The 1942 and 1954 earthquakes are examples of this.

Chapter 2

Small Earthquakes in the San Jacinto Fault Zone and the Anza Seismic Gap

2.1 Introduction

Historically the San Jacinto fault zone has been the most seismically active fault system in southern California. Since 1890 at least seven and perhaps as many as ten earthquakes greater than $M 6$ have been associated with faults in or very near this zone (Chapter 1). The relatively short recurrence time for $M \geq 6$ earthquakes makes this fault zone desirable for studying earthquake sequences. In addition, the record of $M \geq 3$ earthquakes in this area is relatively complete since 1932, though the locations of most of the events prior to the mid-1970's are known only to a precision of about 10-20 km. In Chapter 1 we attempted to obtain precise locations for the seven large earthquakes in and near the fault zone since 1899. In this chapter we analyze the seismicity in the fault zone since about 1976 and in particular focus on a section of the fault zone near the town of Anza. The goal of this analysis is to understand relationships between the small earthquake stress release, historic large earthquakes, local structural geology, and regional strain.

The spatial distribution and sizes of the large earthquakes in the San Jacinto fault zone indicate that three sections of the fault zone are relatively deficient in seismic slip and can be considered seismic-slip gaps (Chapter 1). One of these, the "Anza to Coyote Mountain seismic slip gap" is defined as the 40-km stretch of the fault zone between the 1918 San Jacinto and 1968 Borrego Mountain earthquake ruptures (Figures 1.1 and 2.1) (Thatcher et al., 1975). The "Anza seismic gap" as presented in this discussion is defined as the 18 km long currently aseismic section of the San Jacinto fault centered near the town of Anza and is coincident with the northern half of the larger seismic slip gap (Figure 2.1) (Kanamori, 1980*a*; Sanders et al., 1981). The length

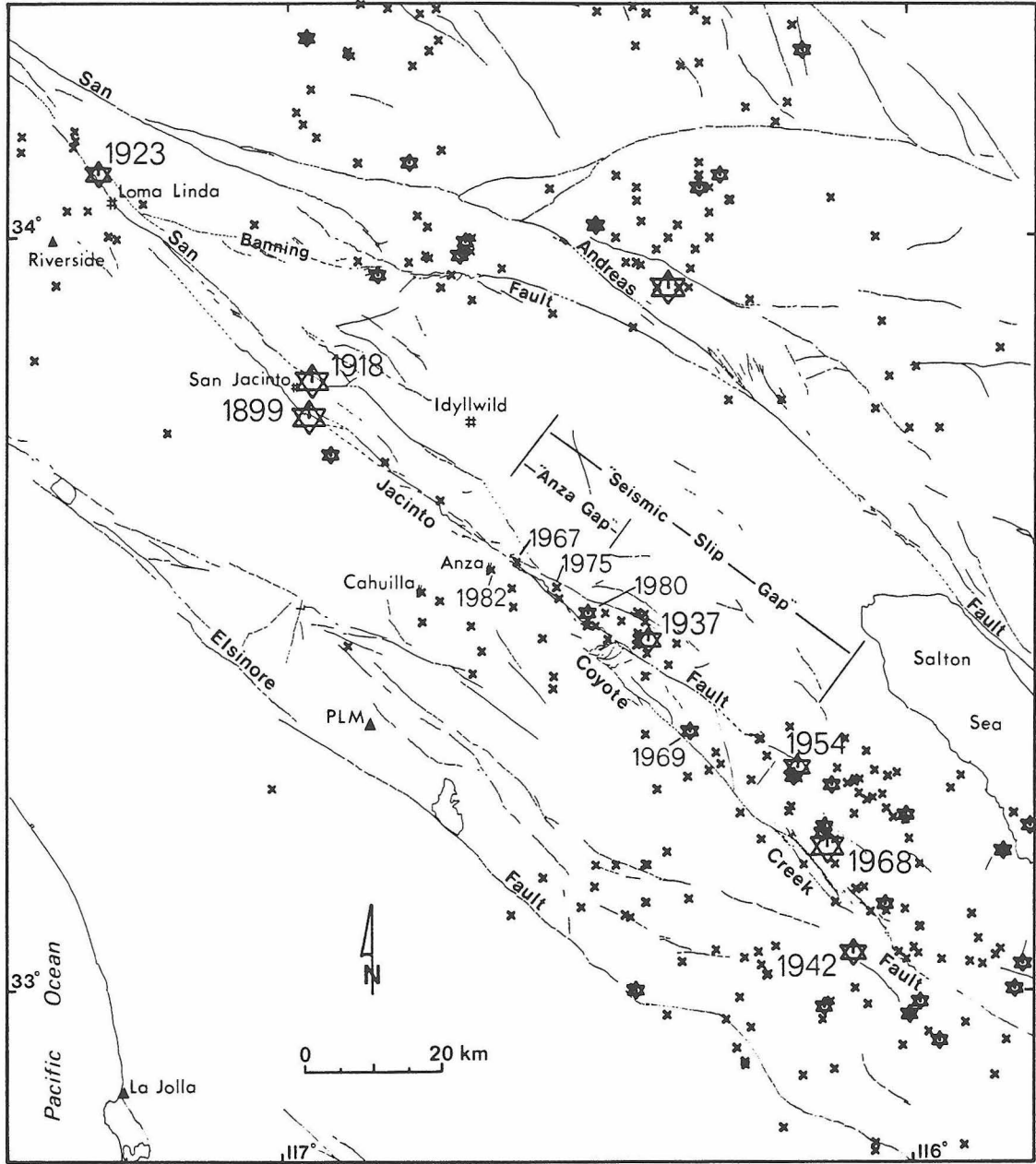


Figure 2.1. Map of all $M \geq 4$ earthquakes located during the time period January 1932 to June 1985. Locations of large earlier events are also plotted. Specific earthquakes are mentioned in the text. x, $M 4+$; small star, $M 5+$; medium star, $M 6+$; large star, $M 6.5+$.

of the Anza seismic gap implies potential for a magnitude 6.5 event, similar to historic large earthquakes in other parts of the fault zone.

The details of the current seismicity along the San Jacinto fault zone and near Anza are studied using the earthquake locations provided by the California Institute of Technology-U.S. Geological Survey southern California seismic network (SCARLET). The epicentral location uncertainty for most earthquakes in this area since about 1978 is less than a couple kilometers, and the catalog since about 1976 is reasonably complete for earthquakes with magnitudes greater than 2. The study of the earthquakes in the Anza area was undertaken in order to understand better the relation between the geology and seismicity in the area of the seismic gap and to determine the nature of seismic stress release near the gap. The data for the analysis includes the historical seismicity, present day seismicity and source mechanisms, local three-dimensional fault geometries, tectonic and geologic setting, and local and regional strain measurements.

2.2 Seismicity in the San Jacinto Fault Zone

The small earthquakes which occurred in the region of the San Jacinto fault zone during the years 1980 through June 1985 are shown in Figure 2.2. The San Jacinto fault zone is one of the three most active fault zones in the region along with the Brawley-Imperial and Banning fault areas. In general seismicity is not distributed evenly along the San Jacinto fault zone but clusters in certain areas. Three clusters predominate: one where the Banning fault intersects the San Jacinto fault; one on the San Jacinto and Hot Springs faults north of the town of Anza; and one southeast of Anza on the San Jacinto and Buck Ridge faults. These clusters are defined not only by the number of small events but also by the sizes of the events, with many $M \geq 4$ earthquakes occurring in these clusters. In addition numerous small earthquakes occur along the northwest section of the San Jacinto fault zone near San Bernardino, off the southeast end of the San Jacinto fault, along the northern half of the Coyote Creek fault, and at the northern end of the Superstition Mountain fault. Sections of the fault

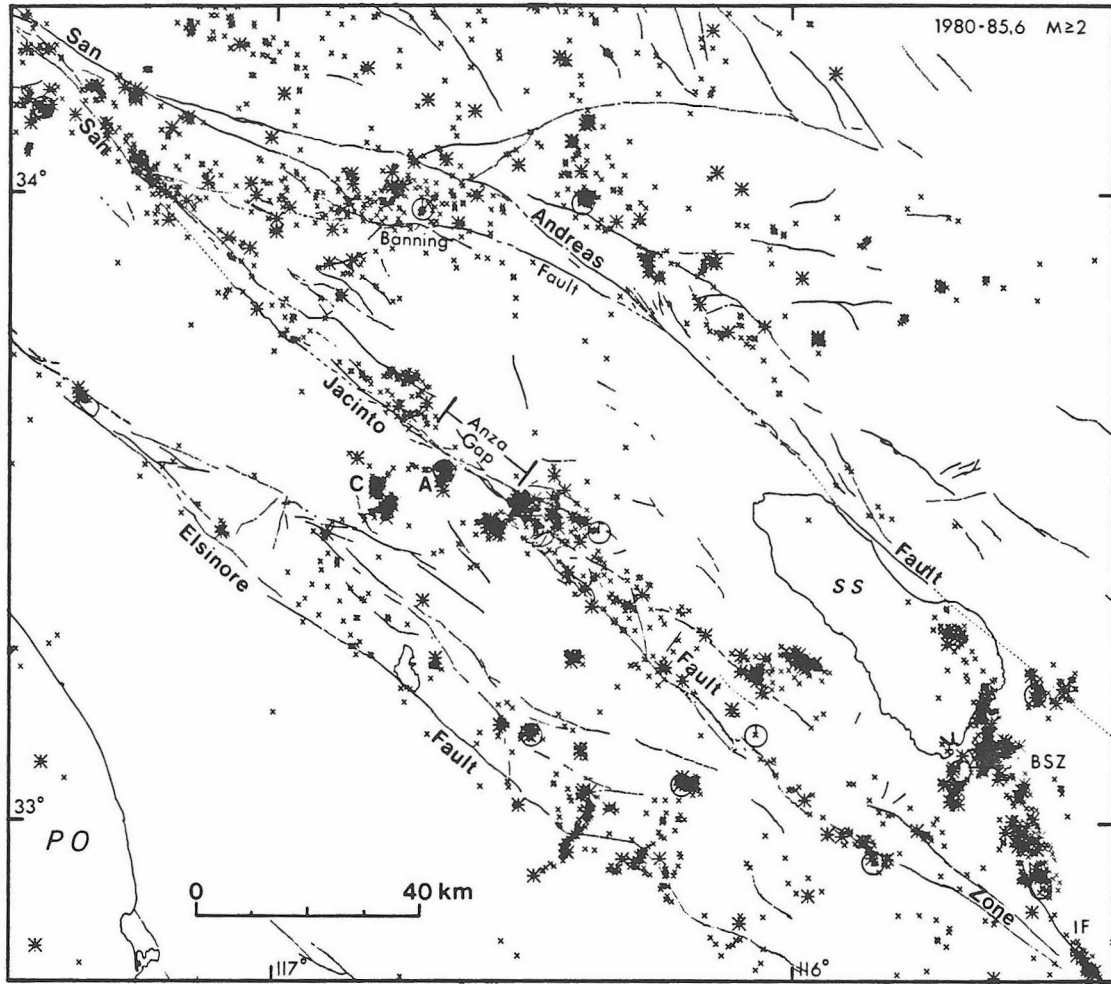


Figure 2.2. Map of $M \geq 2$ earthquakes located in the region of the San Jacinto fault zone during the time period January 1980 to June 1985. Note the clustering of seismicity in the San Jacinto fault zone. A, Anza; C, Cahuilla; BSZ, Brawley Seismic Zone; IF, Imperial Fault; SS, Salton Sea; PO, Pacific Ocean. x, M 2+; *, M 3+; o, M 4+; star, M 5+.

zone which have relatively fewer earthquakes include the section of fault northwest of the town of San Jacinto, the section of fault near Anza, the southeast end of the San Jacinto fault, the southern half of the Coyote Creek fault, and most of the Superstition Mountain and Superstition Hills faults. These relations are also seen in Figures 2.3 and 2.4.

The distribution of recent seismicity seems to correlate with the locations of the large historic earthquakes in the fault zone. The rupture zones of these large events are shown in Figures 2.3, 2.4, and 2.5. It appears that the sections of fault which broke with earthquakes having large seismic moments (1899, 1918, 1954, 1968; Table 1.9) are now characterized by moderate to low seismicity. The ends of these ruptures, however, are sites of concentrated seismicity. In contrast, the sections of fault zone which have ruptured in earthquakes having smaller seismic moment (1923?, 1937, 1969) are currently sites of continued seismicity.

2.3 Subsurface Fault Geometry in the Central San Jacinto Fault Zone

The gross geometry of the major faults at depth can be determined using the earthquake locations for the years 1978 through 1985 (Figure 2.6). The subsurface expression of the San Jacinto fault near Anza is shown in the fault-parallel cross section Figure 2.7. The relatively aseismic Anza gap is readily apparent, as are the concentrations of activity northwest and southeast of the gap. Earthquakes occur deeper northwest of the Anza gap, possibly in part due to a lower geothermal gradient (Chapter 3). Figures 2.8 through 2.12 are transverse vertical sections across segments of the fault zone near Anza. The hypocentral locations of small earthquakes suggest that the San Jacinto fault dips roughly the same throughout this area at about 80°-85° to the northeast. Earthquake focal mechanisms support this direction of dip (Figure 2.13, mechanisms a,c,d,h,i,k). The Hot Springs fault appears to be near vertical (Figure 2.8). The Buck Ridge fault appears to be vertical to steeply southwest dipping (Figures 2.10, 2.11, and 2.13, mechanism j) which is consistent with the linear

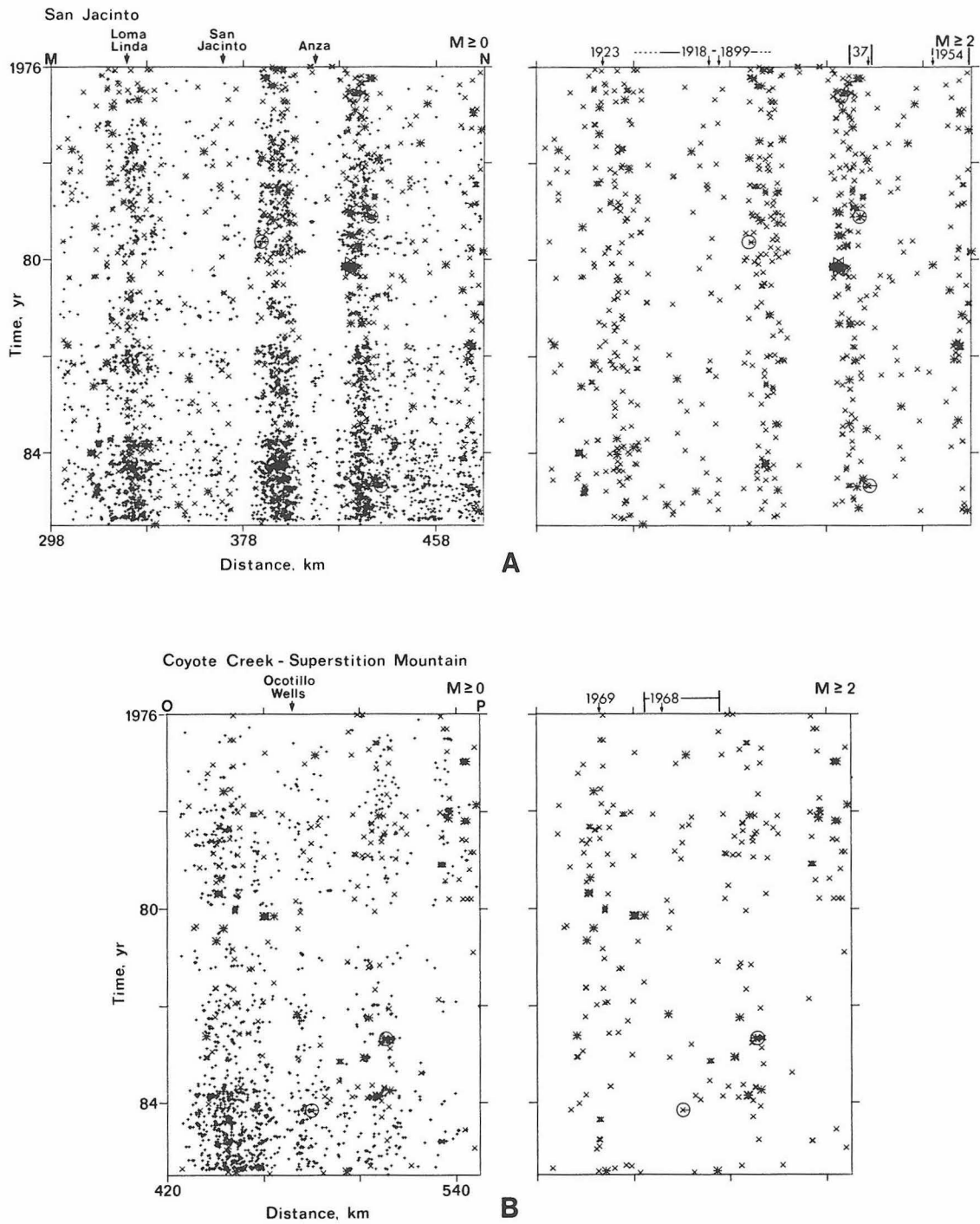


Figure 2.4. Time-distance plots of earthquakes along the San Jacinto (a) and Coyote Creek-Superstition Mountain (b) faults. Plots with all $M \geq 0$ and all $M \geq 2$ events are shown. Historic rupture zones are indicated. Note the relatively aseismic nature of the stretch of fault near Anza. +, $M 0+$; x, $M 2+$; *, $M 3+$; o, $M 4+$; star, $M 5+$.

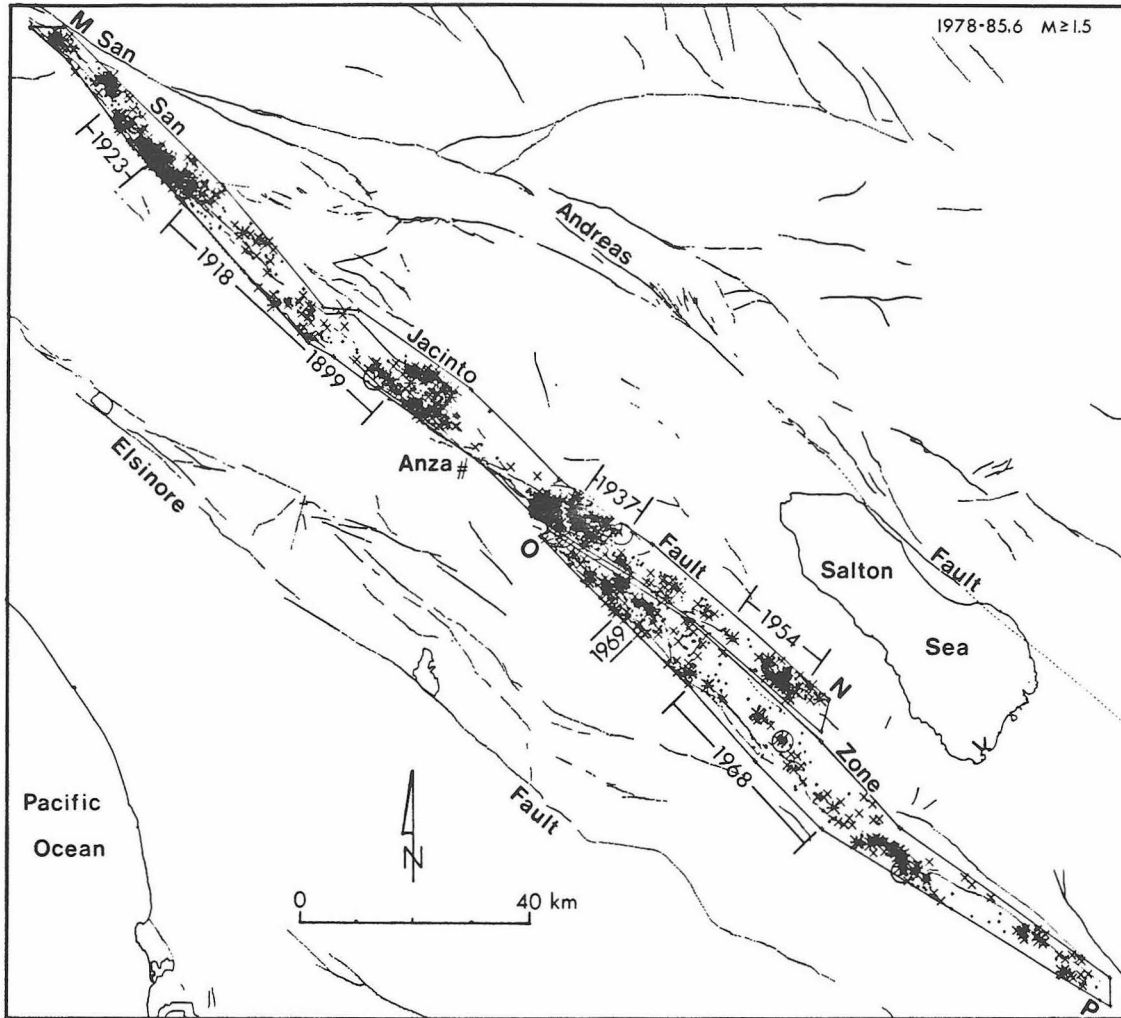


Figure 2.3. Map showing the boxes from which earthquakes are taken for specific analysis of the San Jacinto fault and the Coyote Mountain-Superstition Mountain faults. The coordinates of the boxes were chosen so that only earthquakes on the major faults are observed. The rupture zones of historic large earthquakes are indicated. The earthquakes plotted are those $M \geq 1.5$ which had epicenters within the boxes during the time period January 1978 to June 1985. The end points of the plots in Figures 2.4 and 2.5 are lettered.

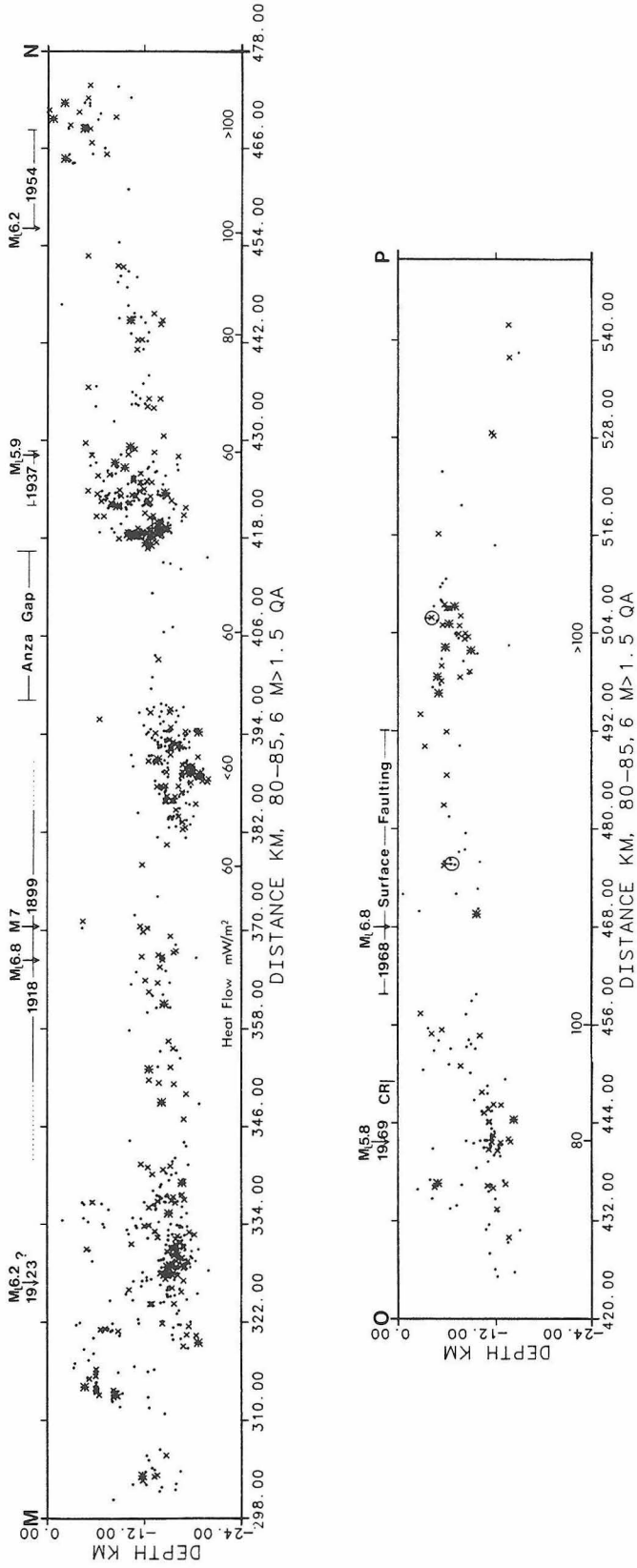


Figure 2.5. Vertical cross sections M-N and O-P along the San Jacinto and Coyote Creek-Superstition Mountain faults. The earthquakes plotted are all $M \geq 1.5$ with quality A locations located in the boxes shown in Figure 2.3 during the time period January 1980 to June 1985. The rupture zones of historic large earthquakes are shown. CR, southeast end of Coyote Ridge. dot, M 1.5+; x, M 2+; *, M 3+; o, M 4+; star, M 5+.

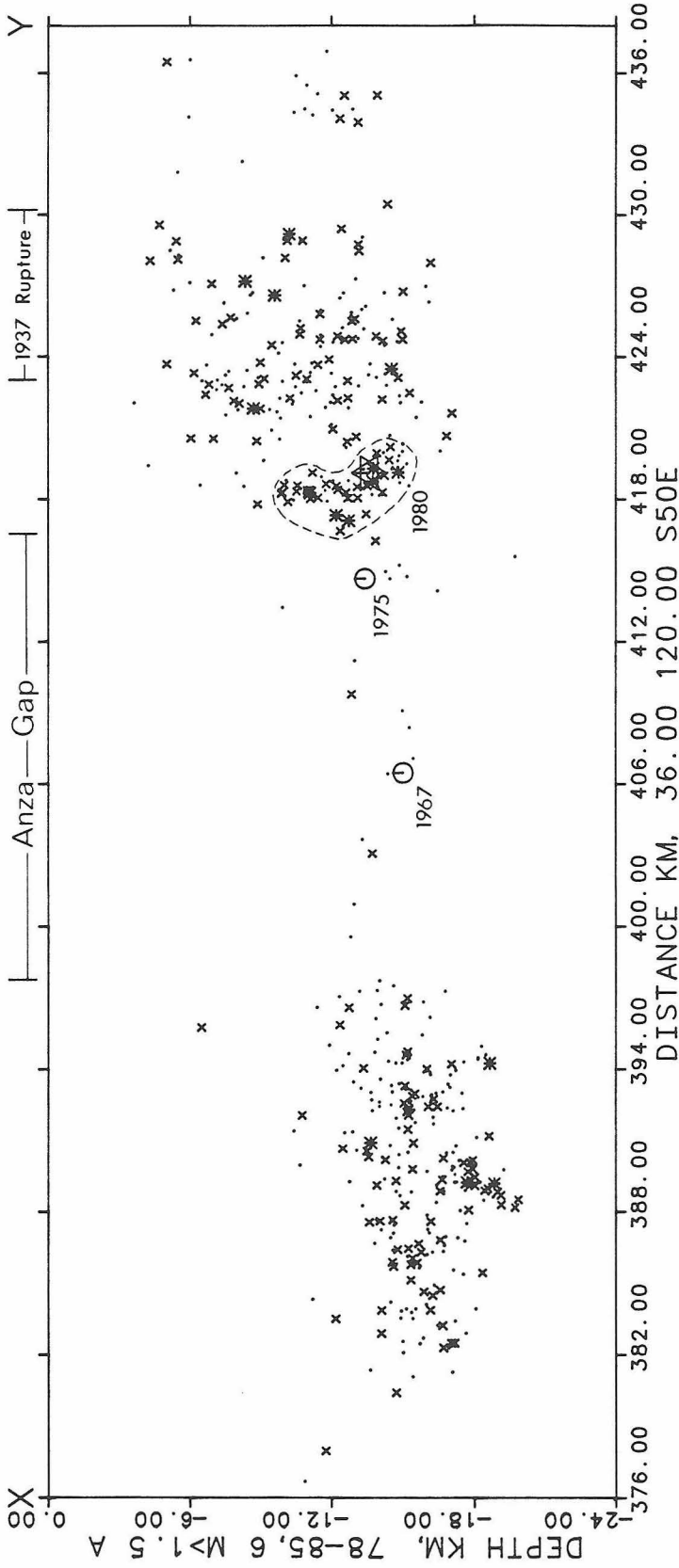


Figure 2.7. Vertical cross section along the San Jacinto fault near the Anza seismic gap (line X-Y, Figure 2.6). All events $M \geq 1.5$ with location quality A which occurred during the time period January 1978 through June 1985 are plotted. The earthquakes were taken from the box whose corners are marked by small black triangles in Figure 2.6. and thus include only events on the San Jacinto, Hot Springs, and Buck Ridge faults. The locations of the 1967 and 1975 earthquakes are indicated, and the after-shock zone of the 1980 earthquake is outlined. dot, $M 1.5+$; x, $M 2+$; *, $M 3+$; o, $M 4+$; star, $M_L 5.5$.

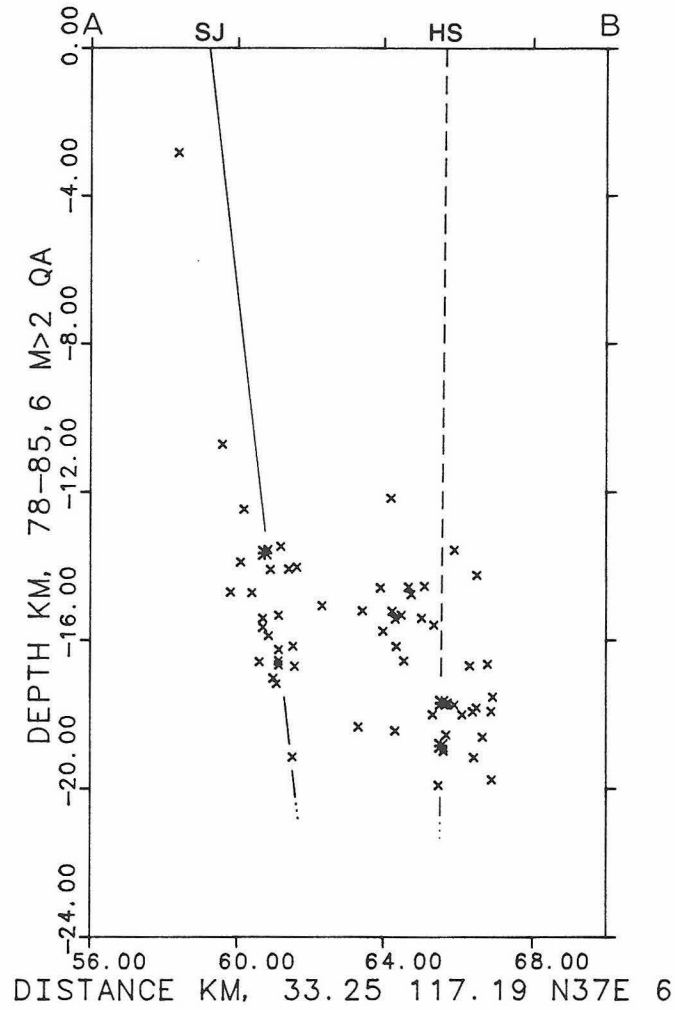


Figure 2.8. Vertical cross section along line A-B (Figure 2.6). Maximum projection distance 6 km. The probable dips of the San Jacinto (SJ) and Hot Springs (HS) faults are indicated by the deep seismicity on the two faults. x, M 2+; *, M 3+.

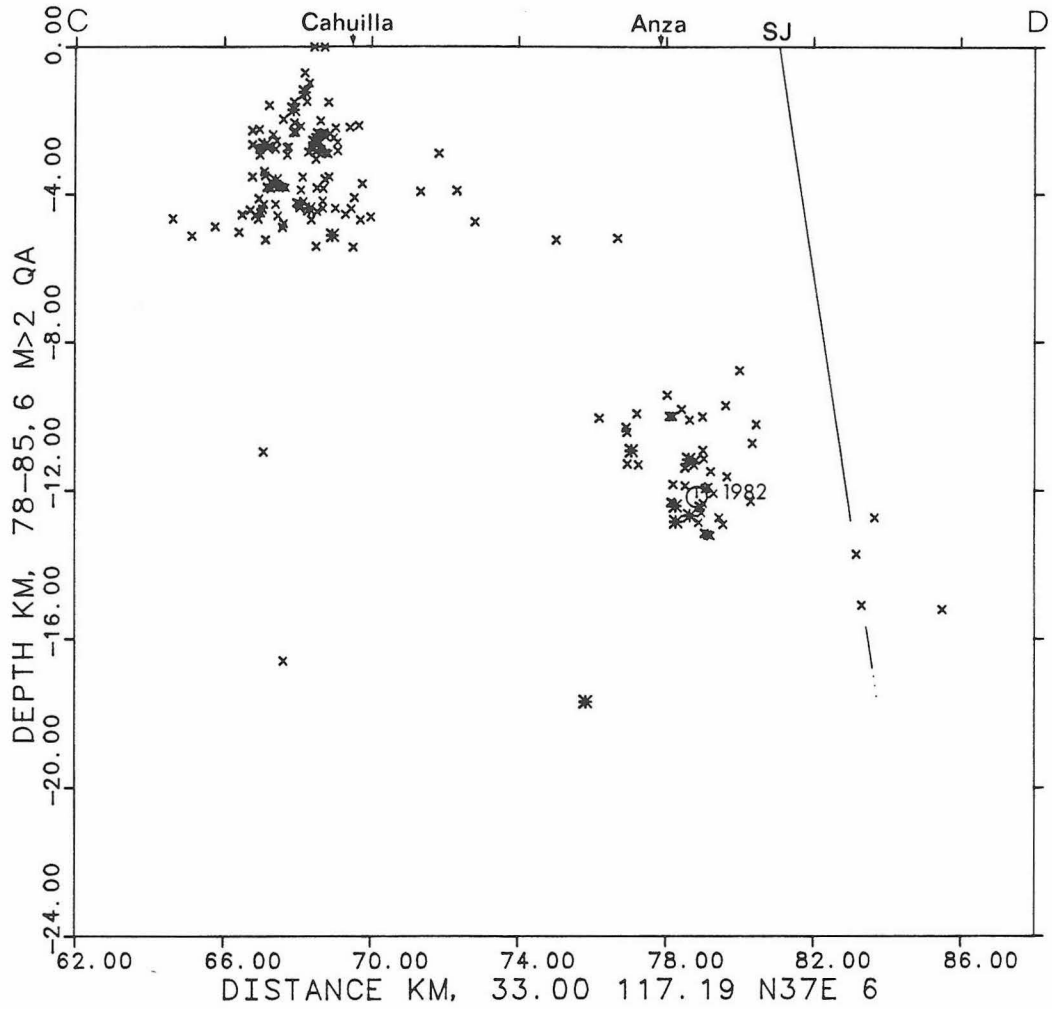


Figure 2.9. Vertical section along line C-D (Figure 2.6). Maximum projection distance 6 km. The dip of the San Jacinto fault (SJ) is inferred from alignments of hypocenters of earthquakes northwest (Figure 2.8) and southeast (Figure 2.10) of the Anza quiescent segment. The Cahuilla swarm events and the 1982 earthquakes and aftershocks are the prominent clusters in this figure. x, M 2+; *, M 3+; o, M 4+.

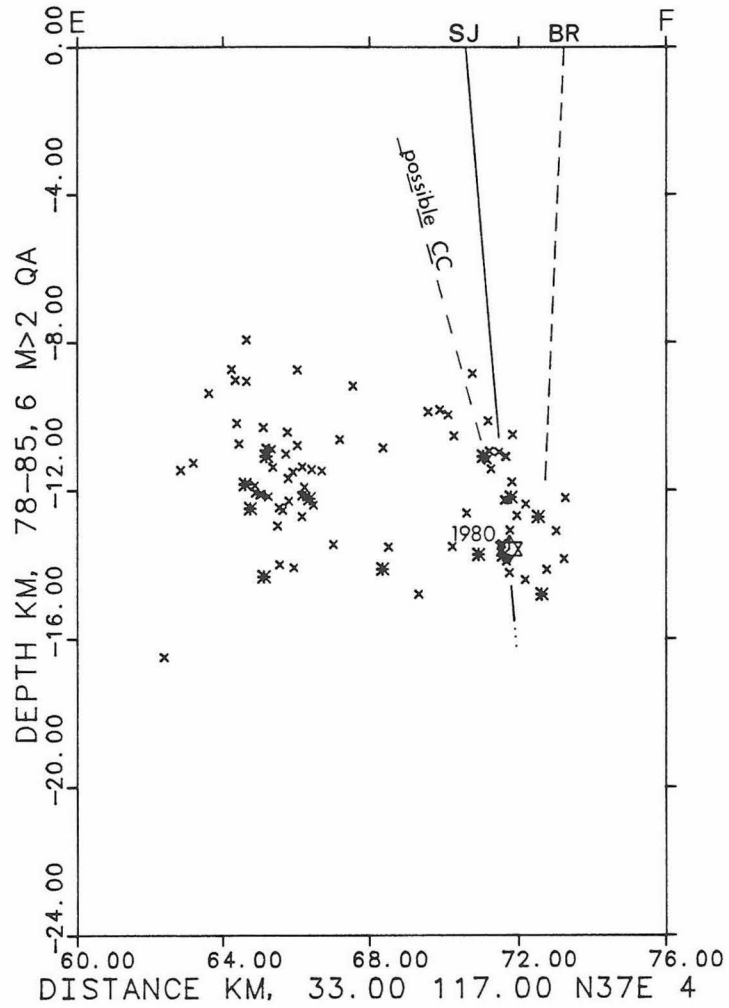


Figure 2.10. Vertical section along line E-F (Figure 2.6). Maximum projection distance 4 km. CC, inferred extension of the Coyote Creek fault; SJ, San Jacinto fault; BR, Buck Ridge fault. x, $M > 2$; *, $M > 3$; star, $M_L 5.5$.

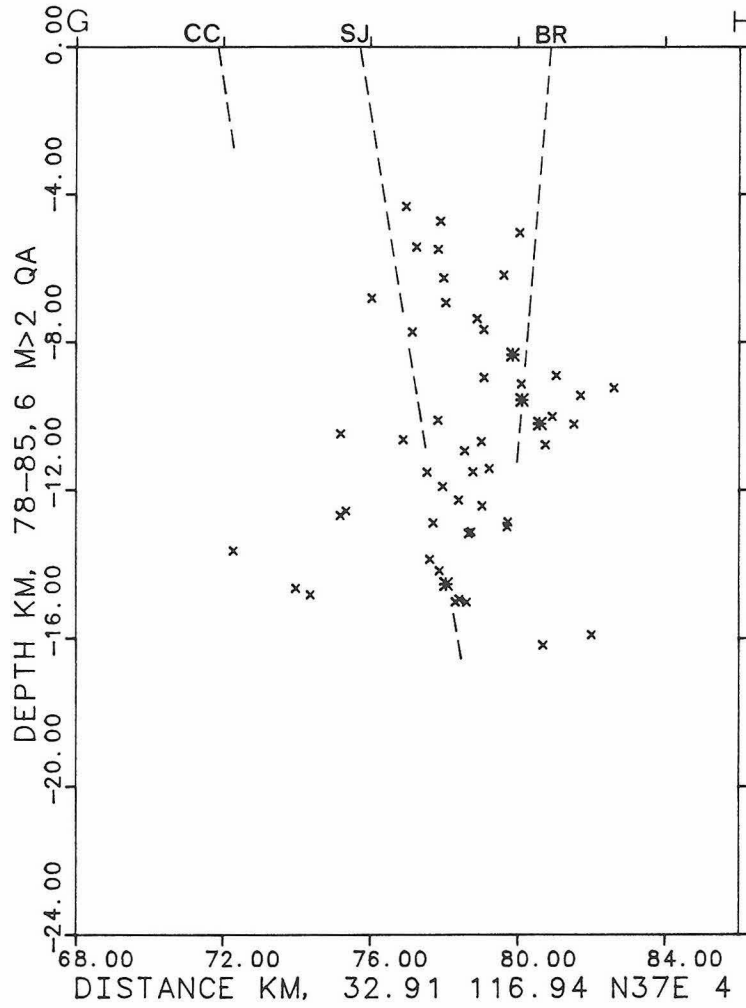


Figure 2.11. Vertical section along line G-H (Figure 2.6). Maximum projection distance 4 km. CC, Coyote Creek fault; SJ, San Jacinto fault; BR, Buck Ridge fault. x, M 2+; *, M 3+.

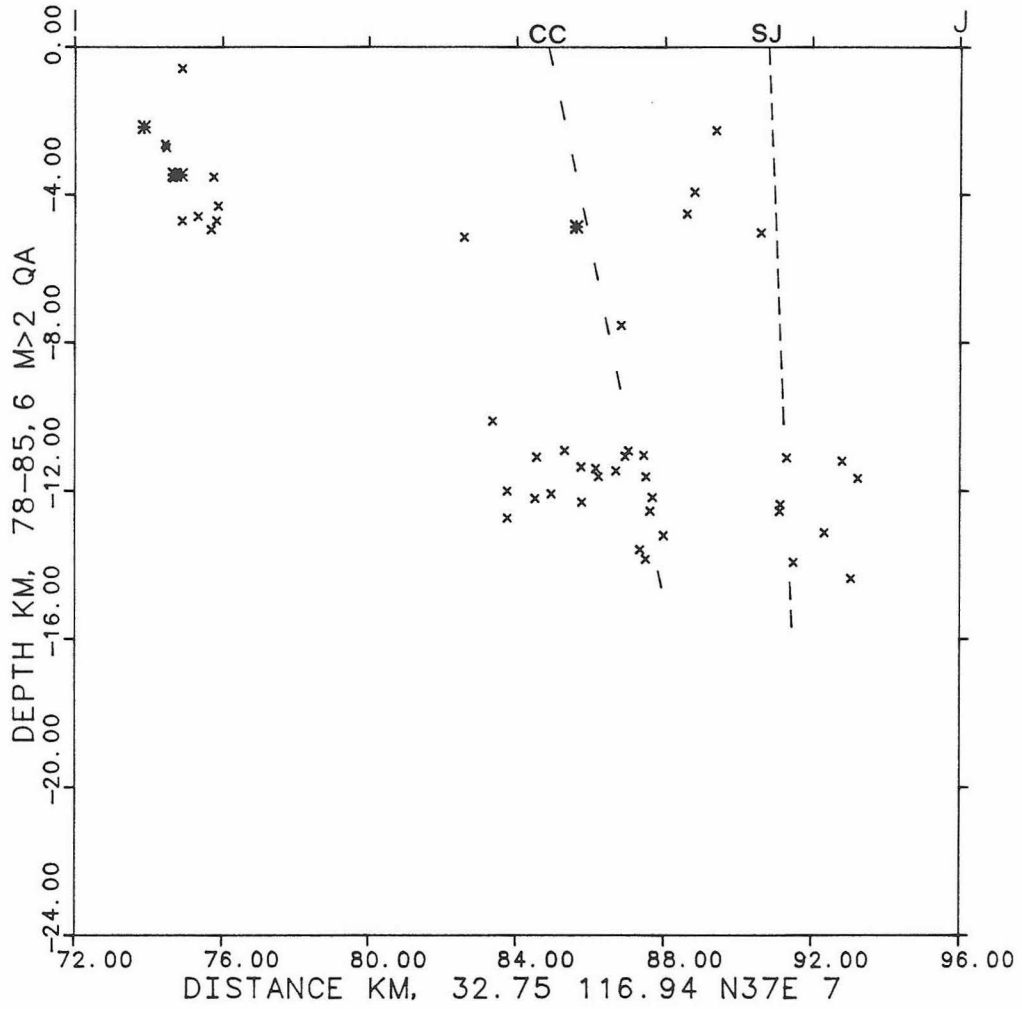


Figure 2.12. Vertical section along line I-J (Figure 2.6). Maximum projection distance 7 km. CC, Coyote Creek fault; SJ, San Jacinto fault. x, M 2+; *, M 3+.

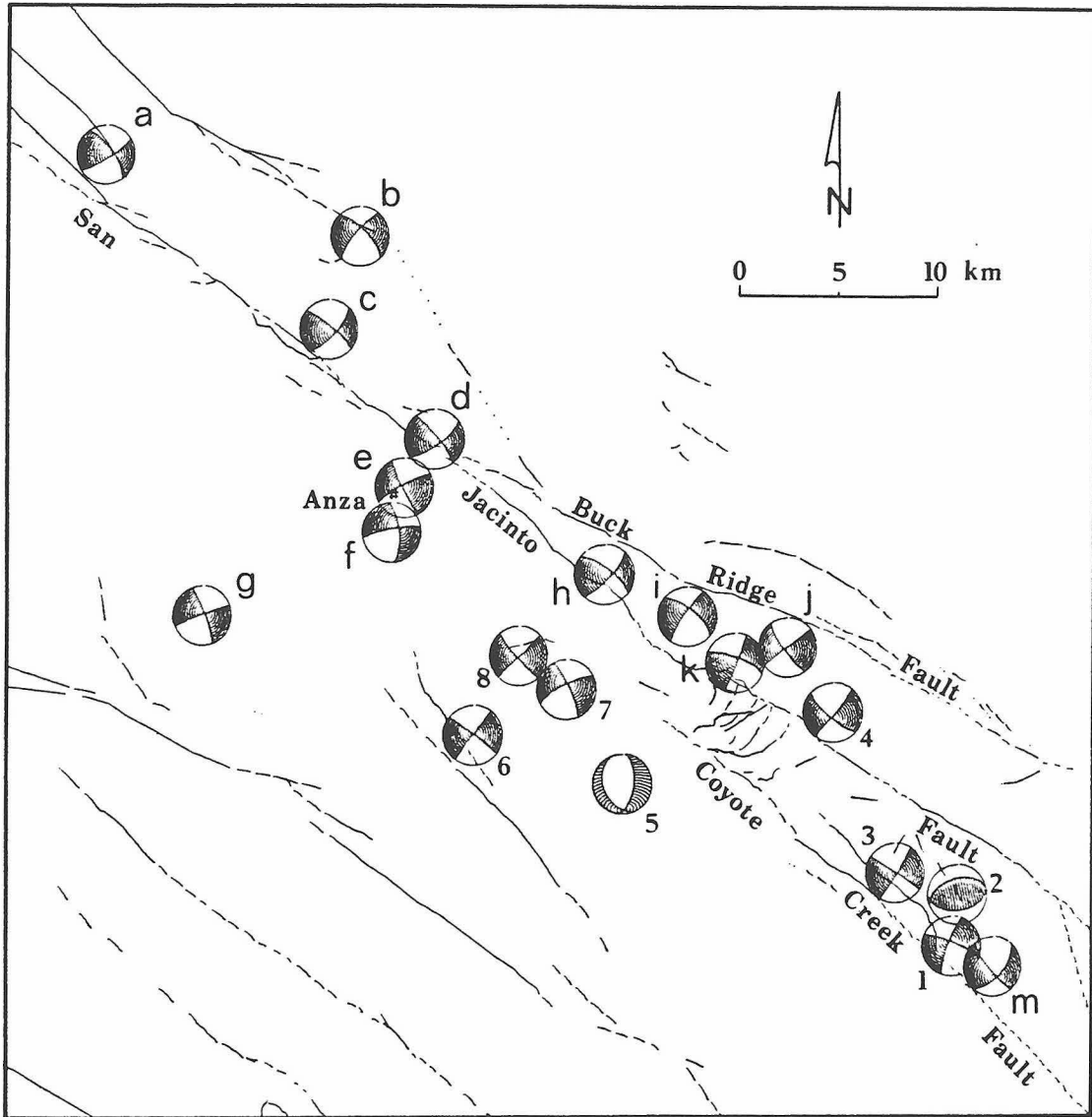


Figure 2.13. P-wave first motion source mechanisms for selected earthquakes near Anza. Lower hemisphere, equal-area projections. Shaded quadrants are compressional. Small letters and numbers refer to mechanisms discussed in the text. See Table 2.1 and the Appendix for more information about these source mechanisms.

TABLE 2.1. Earthquake Source Mechanisms Determined Near Anza

Event	Date	GMT	Latitude	Longitude	Depth, km	M_L	Nodal Planes			
a	Aug. 22, 1979	0201	33°42.50N'	116°49.89W'	16.5	4.1	N37°W	70°NE	N54°E	72°SE
b	Aug. 3, 1978	0430	33°40.32N'	116°41.54W'	16.1	3.5	N46°W	70°NE	N40°E	75°NW
c	July 2, 1977	0122	33°37.78N'	116°42.56W'	13.0	3.0	N52°W	80°NE	N43°E	70°SW
d	Nov. 9, 1974	1010	33°35.05N'	116°39.12W'	16	3.2	N40°W	80°NE	N54°E	72°SE
	Nov. 9, 1974	1012	33°34.82N'	116°39.06W'	16	3.3 ^a				
e	June 15, 1982	2349	33°28.05N'	116°34.70W'	12.2	4.8	N27°W	85°SW	N62°E	80°NW ^b
f	Aug. 30, 1980	2338	33°32.30N'	116°40.42W'	10.4	3.6	N06°W	72°E	N83°E	86°N
	Sept. 7, 1980	0326	33°32.71N'	116°40.50W'	11.3	2.7 ^a				
g	Feb. 1, 1981	1927	33°30.00N'	116°46.64W'	4.0	3.4	N22°W	82°E	N70°E	86°NW ^c
h	Aug. 1, 1975	0014	33°31.19N'	116°33.48W'	12.0	4.8	N53°W	72°NE	N42°E	75°SE ^d
i	Feb. 25, 1980	1047	33°30.06N'	116°30.79W'	13.5	5.5	N52°W	68°NE	N34°E	80°NW ^e
j	May 4, 1981	1841	33°29.23N'	116°27.51W'	14.3	3.1	N37°W	80°SW	N53°E	90 ^f
k	Sept. 16, 1979	0855	33°28.81N'	116°29.23W'	9.0	3.0	N70°W	75°N	N22°E	86°E
m	April 28, 1969	2320	33°20.60N'	116°20.80W'	13.0	5.8	N50°W	90°	N40°E	60°E ^g
1	Aug. 6, 1977	1222	33°21.14N'	116°22.17W'	13.2	2.9	N68°W	80°N	N20°E	78°N
2	May 16, 1979	0425	33°22.55N'	116°21.98W'	2.8	3.2	N72°E	46°N	N84°E	45°S
3	Sept. 7, 1979	1017	33°23.13N'	116°24.00W'	2.7	3.0	N58°W	88°SW	N32°E	84°SE
4	Feb. 12, 1979	0448	33°27.46N'	116°26.04W'	3.9	4.2	N50°W	76°SW	N39°E	84°SE
5	April 22, 1979	1652	33°25.52N'	116°32.88W'	12.5	3.3	N30°W	38°W	N02°E	56°E
6	Aug. 1, 1979	0831	33°26.80N'	116°37.76W'	10.5	2.8	N54°W	90°	N36°E	90 ^h
7	March 10, 1980	2332	33°28.05N'	116°34.70W'	11.1	3.0	N22°W	85°NE	N67°E	78°NW
	Aug. 2, 1979	1304	33°28.87N'	116°34.31W'	7.4	2.7 ^a				
8	Dec. 17, 1977	1427	33°28.96N'	116°36.27W'	8.3	3.0	N43°W	84°SW	N47°E	90 ⁱ

^aSame nodal planes as above and similar location.

^bAlso representative of two large aftershocks, M_L 3.0 (2356) and 3.3 (0014).

^cAlso representative of 17 other Cahuilla events, M_L 1.4-3.7, from June 1978 to May 1982.

^dFrom Kanamori (1976).

^eFrom D. Given (pers. comm., 1982).

^fAlso representative of 3 other M_L 1.8-2.7 events on the same day.

^gData from Thatcher and Hamilton (1973).

^hAlso representative of four other events here, M_L 2.3-3.0, in August 1979.

ⁱAlso representative of two other events in this area, M_L 2.6 (6 Oct 1978) and 2.9 (3 July 1978).

topographic expression of this fault (Sharp, 1967). Mechanism "j" (Figure 2.13, Table 2.1) is representative of several events which occurred in a small swarm on May 4, 1981. Their hypocentral locations suggest a dip of about 84° SW for the Buck Ridge fault. The dip of the Coyote Creek fault is less clear due to sparse and diffuse seismicity, but in the 18-km segment extending northwest from the Coyote Mountain region (Figure 2.6) the fault appears to be vertical to steeply northeast dipping (Figure 2.12). A near-vertical dip of the fault near the surface is also implied by the linear topographic expression of the fault and the nature of the gravity anomaly over the fault (Sharp, 1967). The southeastern half of the Coyote Creek fault which ruptured to produce the Borrego Mountain earthquake seems to dip steeply northeast as evidenced by the mainshock and aftershocks of that event (Figures 1.12 and 1.13). The northwest termination of the Coyote Creek fault is relatively aseismic, and thus subsurface geometry is not easily determined. The earthquakes which lie northwest of the end of the surface trace of the Coyote Creek fault (Figure 2.6) do not appear in cross section (Figure 2.10) to lie on the fault at depth, and instead may be due to stress concentrations off the end of the fault.

Evidence on the possible dip of the northwest end of the Coyote Creek fault was presented in a study by Given (1983). He used a master event earthquake relocation technique to study the relative hypocentral locations of the 1980 M_L 5.5 earthquake and aftershocks (Figures 2.1 and 2.10). Details in the earthquake sequence and the orientation of the focal mechanism of the main shock (Figure 2.13, mechanism i) suggest that some of the fault rupture was on a 70° NE dipping fault plane which would extend updip to the surface extension of the Coyote Creek fault. A dip of this angle for the northwesternmost Coyote Creek fault would suggest that it and the San Jacinto fault merge at about 12 km depth. This is consistent with the idea that fault motion in the San Jacinto fault zone is transferred from the San Jacinto fault to the Coyote Creek fault in this area (Sharp, 1975; Given, 1983). This particular fault geometry beneath the northwest end of Coyote Ridge would imply the existence of a

steep, northeast dipping ramp which could be associated with the uplift of the Coyote Ridge block (section 2.6).

Geologically the northwesternmost 10-km segment of the Coyote Creek fault is not similar in nature to the fault farther southeast. Rather than expressing itself as a linear, relatively simple fault trace, the northwestern segment "is marked by a broad and very complex zone of fracturing involving many branching faults and thrusts" (Sharp, 1967, p. 711). The crystalline rocks of Coyote Ridge are being, in part, thrust southwest over Quaternary sedimentary deposits (Sharp, 1967, plate 1). This change in character of the surficial expression of the northwest end of the Coyote Creek fault may be indicative of a similar change in the character of the fault at depth, that is, a shallower dipping fault plane and possible northward rotation of fault strike towards the San Jacinto fault.

Mechanism "k" (Figure 2.13) suggests that the kink in the fault mapped at the surface extends to at least about 9 km depth (see San Jacinto fault trace near letter "k").

2.4 Recent Moderate Earthquakes Near the Anza Gap

Since 1967 two earthquakes of M_L 4.7, one of M_L 4.8, and one of M_L 5.5 have occurred in and near the Anza seismic gap. The locations and aftershock distributions of these earthquakes are important for understanding the nature of this fault segment.

We relocated the May 21, 1967 M_L 4.7 using the technique described in Chapter 1. Delays at station HAY were determined from recent earthquakes in areas 1 and 4 (Figure 1.2) and recorded at existing stations CTW and BC2, each within 20 km of the HAY site and along the same azimuth from the Anza area. We used P-wave times from stations PLM, HAY, and BAR and S-wave times from stations RVR and BAR. The revised hypocenter is about 15 km deep on the San Jacinto fault near the center of the Anza gap (Figures 2.1 and 2.7). The largest recorded aftershock, M_L 2.5, occurred 10 hours later and is located about 10 km northwest of the main shock. Five first

motions from the main shock are consistent with right slip on the local trace of the San Jacinto fault. This is similar to the mechanism obtained for two recent small earthquakes in the same location (Figure 2.13, mechanism d).

The microearthquakes which occurred in this area both before and after the 1967 earthquake were located by Arabasz et al. (1970) using a portable microearthquake array of seven stations. Their array was operated before the earthquake for 3 weeks during the summer of 1966 and then after the earthquake from May 24 to 31 and June 13 to 20, 1967. Unfortunately, the epicenters of the M_L 4.7 earthquake and closest aftershocks were not contained within this array, so small aftershocks in the immediate epicentral area are not included in their presentation (Arabasz et al., 1970). Their data, though, show the aseismic nature of the southeast portion of the gap to the microearthquake level. A vertical section in their paper indicates that of the six small earthquakes which occurred within the gap, five are shocks which occurred after the larger nearby event. Such a small number of microearthquakes in the gap from 3 days to a month after this event is suggestive of the locked nature of the fault.

Two recent earthquakes similarly indicate the seismogenic but locked nature of the Anza gap. These occurred on August 2, 1975 (M_L 4.7), and February 25, 1980 (M_L 5.5), and both were located on the San Jacinto fault near the southeast end of the gap (Figures 2.1 and 2.7). The 1980 earthquake shows expansion of rupture upward and to the northwest into the gap, and the mechanisms of the 1975 and 1980 events indicate right slip on a steeply northeast dipping fault (Figure 2.13, mechanisms h and i). Both earthquakes had relatively few aftershocks for their size (1975, 5 $M_L > 2.5$; 1980, 13 $M_L > 2.5$; in 1 week). Figure 2.14 and Table 2.2 show the small number of M_L 2-3 aftershocks of the 1980 earthquake relative to several other southern California earthquakes of similar size. The 1980 aftershock zone is 3 km long and 6 km thick (where "thick" indicates the downdip width of the aftershock zone). By comparison, the 1966 Parkfield earthquake (M_L 5.5), which was located on a portion of the San Andreas fault that is creeping (implying relatively low fault strength), had 58 $M_L > 2.5$ aftershocks in

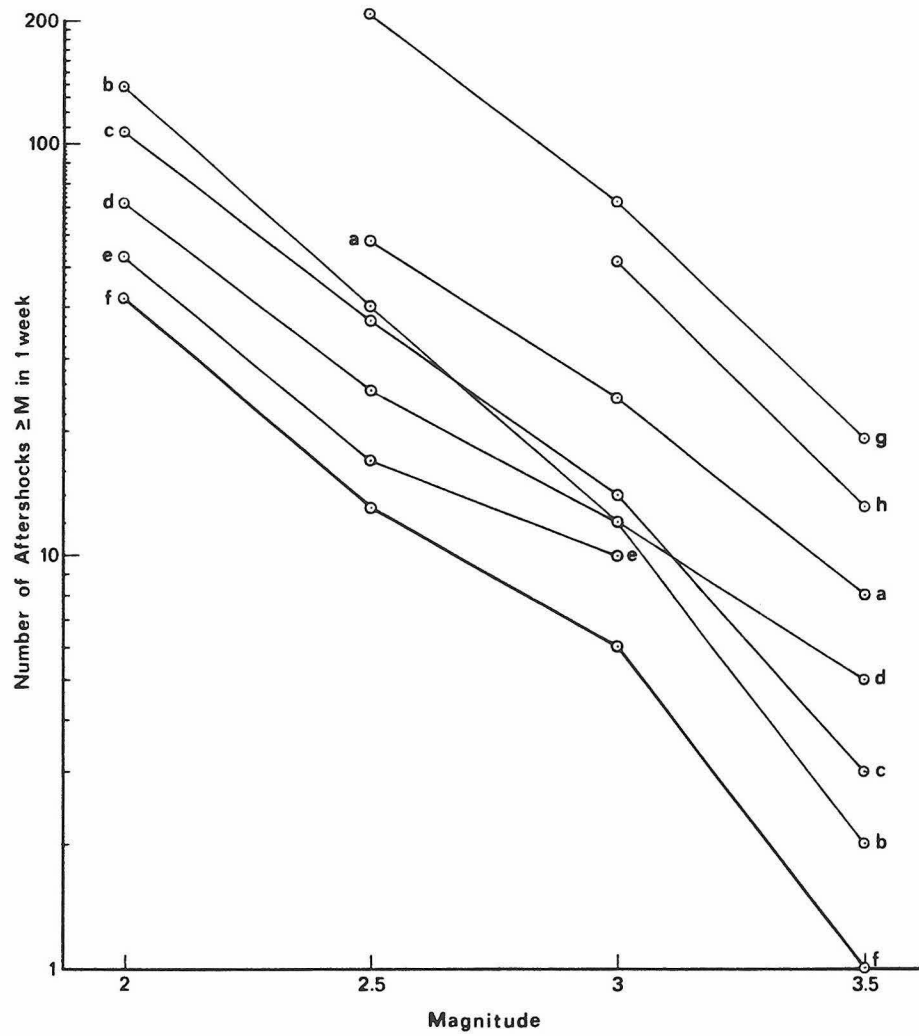


Figure 2.14. Plot of the number of $M_L \geq 2-3$ aftershocks which occurred in 1 week after the southern California earthquakes listed in Table 2.2. The letter reference to Table 2.2 is indicated. The heavier curve indicates the Anza earthquake aftershocks. The Anza event had fewer aftershocks even though its local magnitude is greater than or equal to the other main shock magnitudes. The number of aftershocks following moderate earthquakes may indicate the local strength of the fault.

TABLE 2.2. Number of Aftershocks Following Some M_L 5.0-5.9 Southern California Earthquakes

Name	Date	Latitude	Longitude	Depth	M_L	Number of Aftershocks				Source Mechanism
						$M_L \geq 2$	≥ 2.5	≥ 3	≥ 3.5	
a Parkfield	June 28, 1966	35°57.30'N	120°29.88'W	9	5.5		58	24	8	strike-slip
b Santa Barbara	Aug. 13, 1978	34°20.82'N	119°41.76'W	12.8	5.1	139	40	12	2	thrust
c Malibu	Jan. 1, 1979	33°56.70'N	118°40.92'W	11.3	5.0	108	37	14	3	thrust
d Catalina	Sept. 4, 1981	33°40.26'N	119°06.66'W	5	5.3	71	25	12	5	strike-slip
e Galway	June 1, 1975	34°30.96'N	116°29.76'W	4.5	5.2	53	17	10	0	strike-slip
f Anza	Feb. 2, 1980	33°30.30'N	116°30.84'W	13.6	5.5	42	13	6	1	strike-slip
g N. Palm Springs	July 8, 1986	33°59.91'N	116°36.38'W	11.7	5.9		207	72	19	strike slip
h Oceanside	July 13, 1986	32°58.24'N	117°52.19'W	6	5.3			51	13	strike slip

These events were chosen for comparison because they and their aftershocks are well located, and most of the aftershocks larger than M_L 2 are cataloged. The aftershocks are defined as those earthquakes occurring after the main shock (1-week time period) whose epicenters locate on a continuous trend which includes the main shock. Most of the events have strike-slip source mechanisms, and their aftershocks have trends consistent with the local fault strikes. Earthquakes not associated with the rupture zone are readily identified. The Santa Barbara and Malibu earthquakes have thrust source mechanisms, and their aftershock zones are relatively broad; however, there is little difficulty in distinguishing small earthquakes not associated with the continuous rupture zone. Depth is in km.

the following week, a large number of bigger aftershocks, and an extensive aftershock area (27 km long and 13 km deep) (McEvelly et al., 1967).

The source of the 1975 earthquake was studied by Hartzell and Brune (1979). By comparing local body wave and teleseismic surface wave moments, and by studying the distribution and signals of the main shock and aftershocks, they concluded that this earthquake had two-stage stress release with an initial rupture of 225 bars stress drop over 0.5-km source radius and a total rupture of 90 bars over 1-km radius. These observations indicate localized stress concentrations in the Anza gap.

The June 15, 1982, M_L 4.8 earthquake is the most recent moderate earthquake to occur near the Anza seismic gap. This earthquake was produced by rupture at a depth of 12 km directly beneath the town of Anza and is not associated with a mapped fault trace (Figures 2.1 and 2.6). The earthquake and aftershocks did not occur on the throughgoing San Jacinto fault (since it dips northeast here) but in the block just southwest (Figures 2.9 and 2.15). The hypocenters of the main shock and largest aftershocks define a vertical plane striking $N26^\circ W$. This is in agreement with the well-constrained focal mechanism of the main shock (Figure 2.13, mechanism e) and mechanisms of several larger aftershocks. Within the first 3 days the aftershocks with $M_L \geq 2$ define a tight rupture zone 2.5 km long, 1.5 km wide, and 3 km thick. During this same time period, microearthquakes extend 3 km northeast toward the San Jacinto fault (Figure 2.15). This event had seven aftershocks of $M_L \geq 2.5$ in the following week. No aftershocks occurred on the San Jacinto fault even though the main shock was only 4 km distant.

These four earthquakes in and near the Anza seismic gap reveal information about the stress conditions in the gap. The 1982 earthquake and aftershocks represent local fracturing and stress release as strain increases around the locked fault. The three other moderate earthquakes on the San Jacinto fault in the gap testify to the seismogenic and highly stressed but locked nature of the fault here. These three earthquakes can be pictured as resulting from the rupture of small asperities on the fault as stress

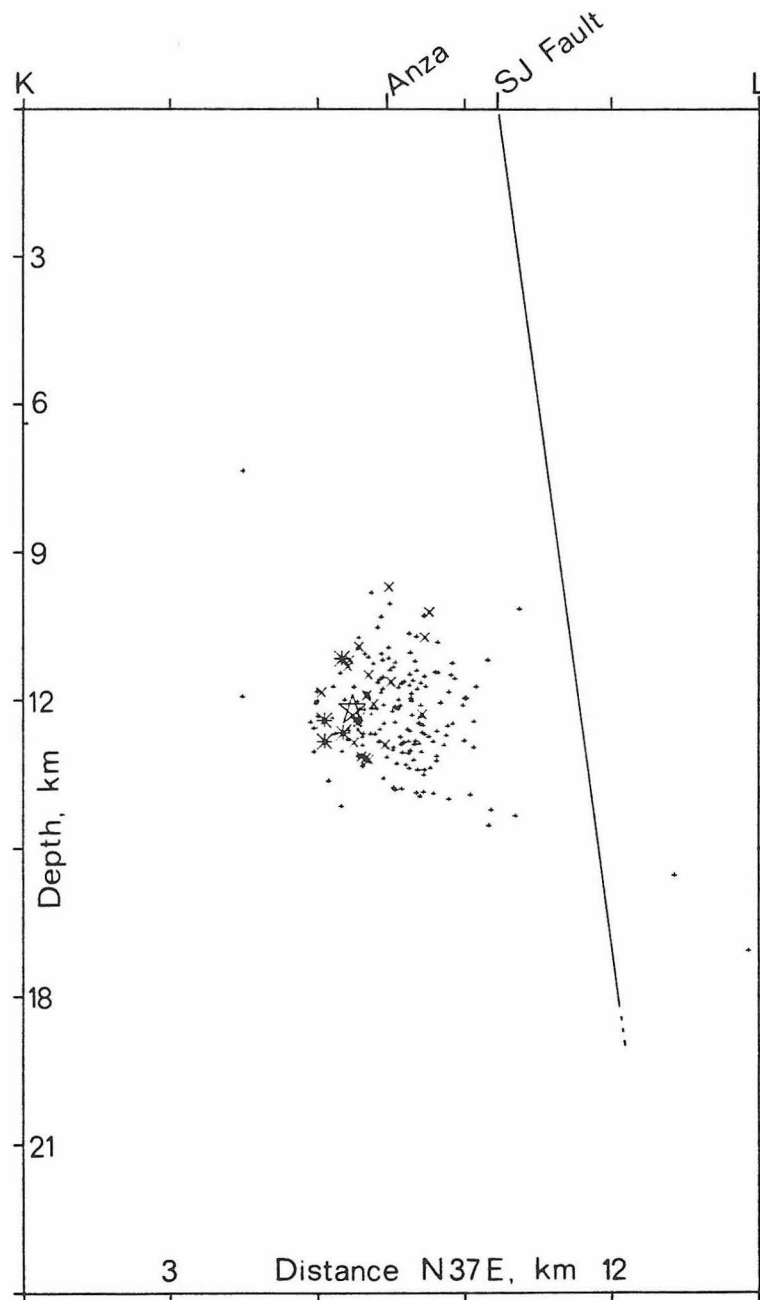


Figure 2.15. Vertical section along line K-L (Figure 2.6) showing the location of the June 15, 1982, M_L 4.8 earthquake (star) and the first three days of aftershocks relative to the inferred extension of the San Jacinto fault at depth. +, M 0+; x, M 2+; *, M 3+; star, M_L 4.8.

increases in the gap. Most asperities on the fault in the gap are stronger than the present level of tectonic stress. Aftershocks of these events are limited in size and extent by the adjacent stronger asperities (see Tajima and Kanamori, 1985, for a discussion of this phenomenon in relation to subduction zone earthquakes). The size and number of these stronger asperities and the time sequence of their rupture will determine the magnitudes of the earthquakes which relieve the built-up strain in the gap. If the entire 18-km-long quiescent segment ruptures, a magnitude 6.5 earthquake can be expected based on comparison with other historic strike-slip earthquakes and their rupture lengths (Slemmons, 1977). The seismic moment would be about 10^{26} dyne-cm if fault displacement was 1 m (1 cm/yr for 100 yr) over an 18 by 18 km fault plane. Historically, the size of the large earthquakes generated by the faults in the San Jacinto fault zone has been limited to M 6-7 (probably due to the segmented nature of the fault zone). Thus, if rupture were to propagate out of the Anza area, we would not expect an earthquake larger than about M 7.

2.5 Cahuilla Swarm

Four months following the February 25, 1980 M_L 5.5 earthquake a swarm of small earthquakes commenced beneath Cahuilla Valley, 10 km southwest of Anza (Figure 2.2). This swarm is interesting for several reasons including the time-space occurrence of the swarm relative to other moderate earthquakes in the area, the orientations of source mechanisms of small earthquakes in the swarm, and the prior history of increased earthquake activity in this same location before the 1918 (M 6.8) and 1937 (M_L 5.9) events. The swarm earthquakes occupy two volumes that extend about 7 km north-south, 5 km east-west, and from 1 to $5\frac{1}{2}$ km in depth (Figures 2.6 and 2.9). Small earthquake activity in the swarm was relatively constant from July 1980 through October 1981 with a peak of activity from October 1980 to March 1981. Between November 1981 and December 1983 earthquakes were less frequent and the magnitudes small. Earthquake activity increased again in January 1984 and continues, though at a

lesser rate than the 1980-81 swarm. The latest Cahuilla activity is located a few km northwest of the previous activity (Figure 2.6). The maximum magnitudes during both active periods were near M_L 3.7.

Figure 2.16 shows the time-space relationships between the Cahuilla swarm, the 1980 M_L 5.5 earthquake, and the June 15, 1982, M_L 4.8 earthquake. Since 1975, when microearthquake location accuracy improved in the southern California seismic array, but before July 1980, the Cahuilla area had been relatively quiet. The timing of the swarm, which began 4 months after the 1980 earthquake and ended 7 months before the June 1982 event, may suggest some sort of mechanical interaction of blocks near the Anza gap. Rupture of the 1980 earthquake loaded the crustal block to the northwest. The Cahuilla swarm began in response to this added strain and continued to release strain, spreading north and slightly east. After the swarm ceased in November 1981, strain continued and was not relieved in this block until 7 months later with the M_L 4.8 earthquake and aftershocks beneath Anza. A few months later small earthquakes again began to occur near Cahuilla though in a location a few km northwest of the original swarm location. Activity increased again in early 1984 indicating continued strain in the region.

The focal mechanisms of earthquakes beneath Cahuilla Valley have been remarkably consistent at least since June 1978. The mechanism is right slip on a N22°W striking, 82°NE dipping fault plane (Figure 2.13, mechanism g) (Sanders et al., 1981). No surface fault has been mapped near Cahuilla Valley (Sharp, 1967), though a hot spring is reported (Lee, 1983).

Many tremors were felt at Cahuilla in the years preceding the April 1918, M 6.8, San Jacinto-Hemet earthquake (Figure 2.1). Because these shocks were not reported at other small towns in the area which had been reporting earthquakes, such as Hemet, San Jacinto, and Idyllwild, the earthquakes were probably local and small. The intensities reported by Palmer (1917, 1918, 1919) and Townley and Allen (1939) imply local earthquake magnitudes between $2\frac{1}{2}$ and $4\frac{1}{2}$. Beginning $3\frac{1}{2}$ years before the 1918

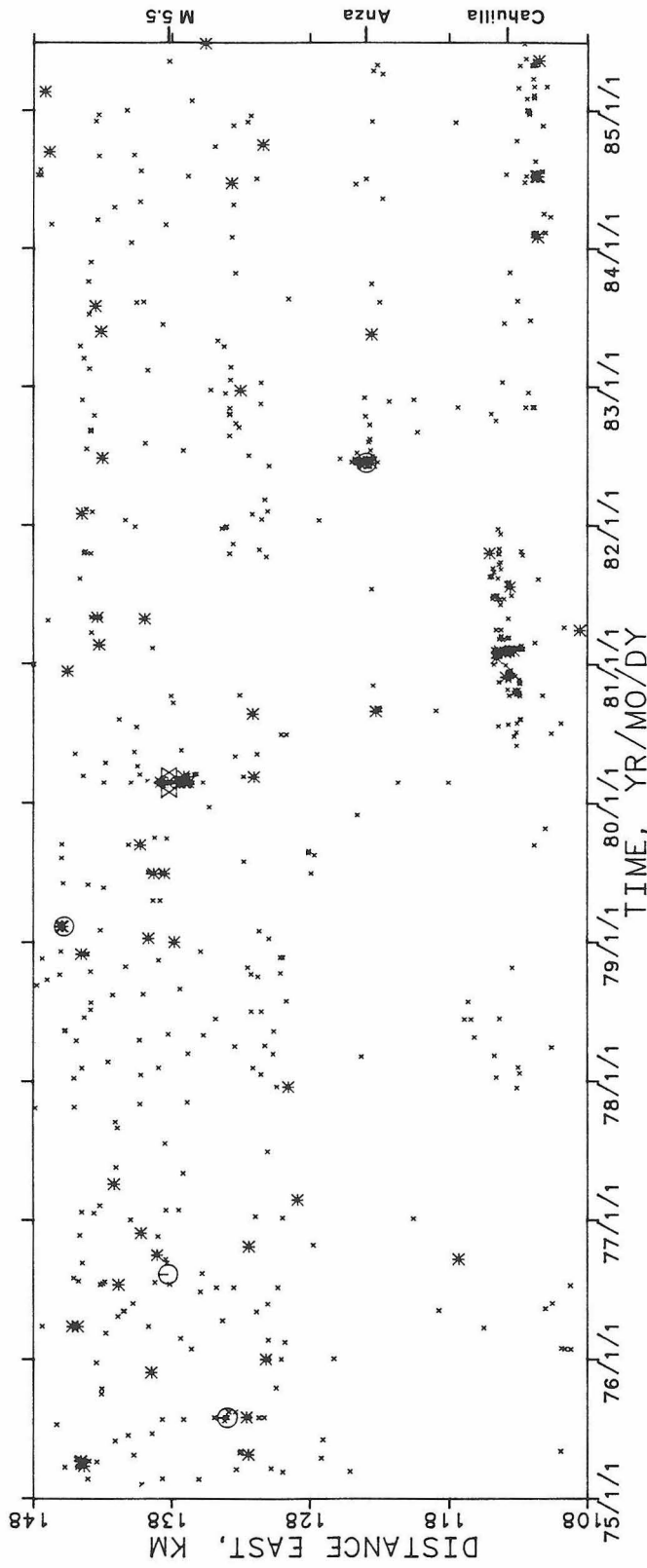


Figure 2.16. Earthquake locations with time projected onto an east-west line extending from the Cahuilla swarm area to the area of the 1980 M_L 5.5 earthquake. The area in which the events are located is shown in Figure 2.6. x, M 2+; *, M 3+; O, M 4+; star, M 5+.

earthquake, 16 local tremors were felt, and in the week following the earthquake, three more were reported (Figure 2.17). No further tremors were mentioned between then and December 1927, the end of the Townley-Allen catalog.

This indication of increased seismicity in the $3\frac{1}{2}$ years before the 1918 earthquake must be carefully evaluated in light of the method of recording felt earthquakes at Cahuilla during the years 1911-1919. The following important facts were related to us by D. Agnew (personal communication, 1983). The tremor reports from Cahuilla in the Townley-Allen catalog (Townley and Allen, 1939) were collected from the Weather Bureau, which operated a climatological station at Cahuilla from June 1911 to October 1919. This agency, however, did not begin collecting earthquake reports until after the fall of 1914 (a task that was assigned to them by Congress in June of that year). Thus the pre-1918 increase in seismicity may be interpreted as due to observational bias. Also, the regular observer at Cahuilla changed at the end of 1917, and although several $M\ 3\frac{1}{2}$ tremors were reported directly preceding the April 1918 earthquake, reports after the earthquake decline sharply. This may be due to decreased diligence on the part of the new observers or to lessening attention caused by becoming accustomed to felt earthquakes (because of all the aftershocks of the nearby 1918 event).

The data revealed by D. Agnew in the previous paragraph seem to throw some ambiguity into the interpretation of the pre- and post-1918 seismicity at Cahuilla. We feel, though, that if the magnitude estimates we give the pre-1918 felt earthquakes at Cahuilla are correct, then by comparison with the instrumental record of $M\geq 3$ shocks since 1932, the apparent increase in seismicity is indeed real (but may have begun earlier than fall 1914). The reason for the decline of felt earthquakes at Cahuilla after April 1918 is not clear. Information revealed in the following paragraphs seems to indicate that such a low level is normal for this area.

Another significant increase in the earthquake activity near Cahuilla began $1\frac{1}{2}$ years before the 1937 ($M_L\ 5.9$) earthquake (Figures 2.1 and 2.18). This swarm of earthquakes, according to the Caltech-USGS earthquake catalog and based on one epicenter

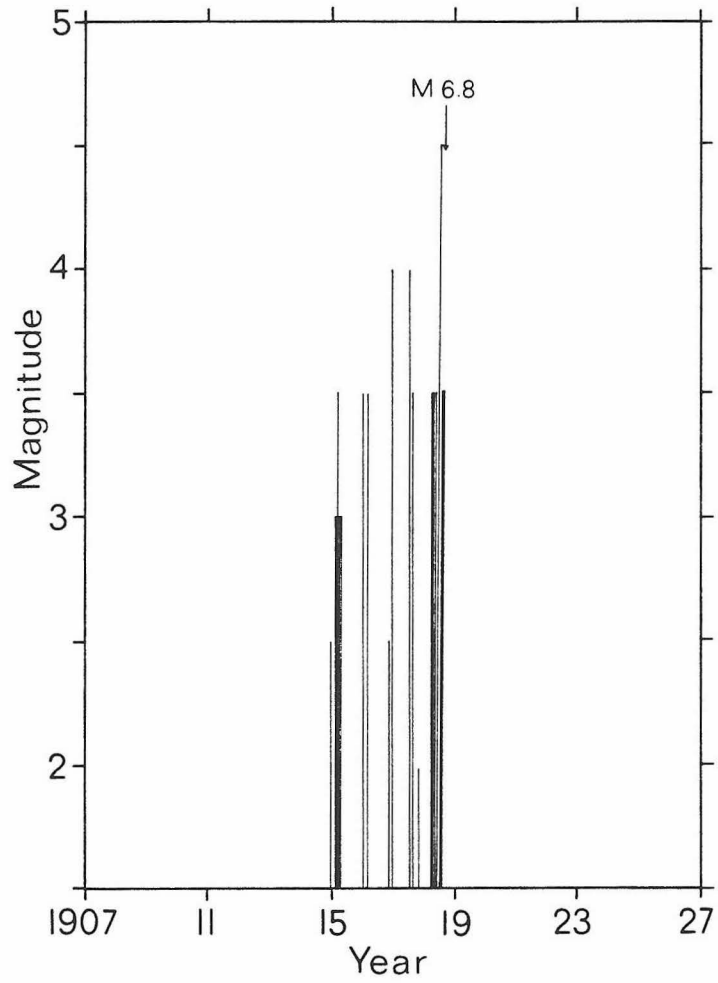


Figure 2.17. Plot of approximate earthquake magnitudes (determined from intensity versus magnitude relations) with time for the tremors reported felt only at Cahuilla in the years preceding the 1918 San Jacinto earthquake.

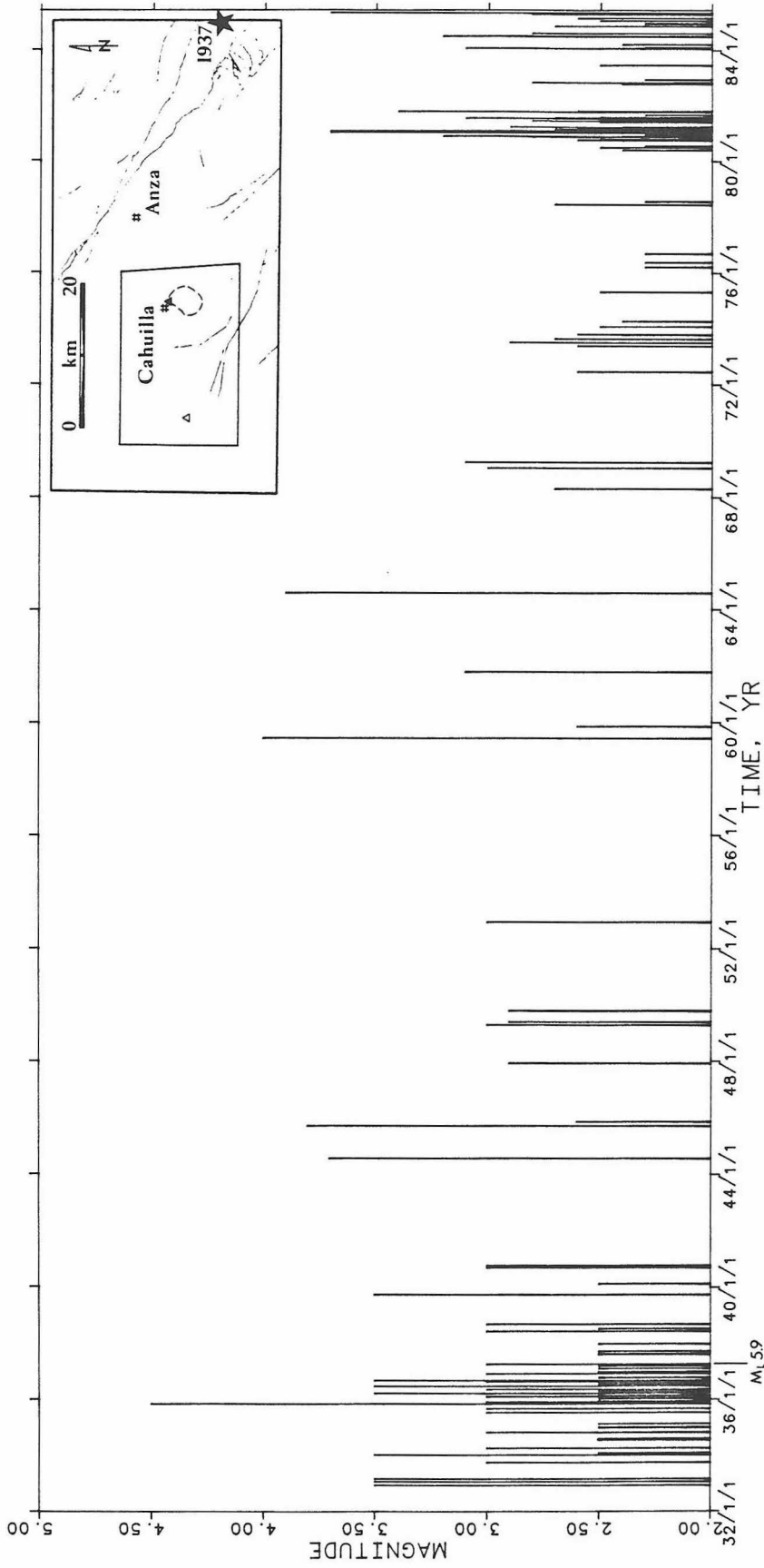


Figure 2.18. Plot of earthquake occurrence with time for all earthquakes $M \geq 2.3$ located from 1932 to 1985,6 in the Cahuilla swarm area. The index map shows the location of the box within which the Cahuilla swarm area. The open triangle marks the catalog location of the largest event (M_L 4.6) in the 1935-36 swarm. The solid triangle marks the relocated epicenter. Dashes outline the area of the 1982-1983 swarm. The location of the 1937 (M_L 5.9) earthquake is shown in space and time on the index map and the stick plot, respectively.

determination for the largest (M_L 4.6) earthquake in the swarm, had a location about 12 km west of Cahuilla. As explained in Chapter 1 our relocations of these events indicate that they were actually located very near Cahuilla in the same area as the 1980-1981 swarm (Figure 1.6). This is important information since it implies that the Cahuilla area experienced increased seismicity in the years preceding both of the largest historic earthquakes within a 35-km radius of Cahuilla.

The time-space relationship between the increased local earthquake activity at Cahuilla and the 1918 and 1937 earthquakes suggests that the Cahuilla tremors were related to the stress build-up process before the larger events. The ground beneath Cahuilla may be acting as a stress meter signaling the high stresses present before large nearby earthquakes. A similar concept was presented by Kanamori (1972) after studying the relationship between some great Japanese earthquakes and a swarm area on the island of Honshu. Clustering before large and moderate earthquakes in California and elsewhere has also been discussed by Evison (1977) and K.C. McNally (unpublished manuscript, 1977).

During the recent Cahuilla swarm, as many as 56 $M_L \geq 2.3$ earthquakes broke at shallow depths beneath Cahuilla. This is similar to the 56 $M_L \geq 2$ earthquakes recorded during the swarm prior to the 1937 event. Activity of this intensity was not reported in the Townley and Allen (1939) catalog for the years following the 1918 earthquake through 1927 (though with possible reporting ambiguity) and is not evident in the Caltech-USGS earthquake catalog from 1937 to 1980 (Figure 2.18). Thus the present swarm activity is probably the first recurrence of activity beneath Cahuilla since before the 1937 earthquake and may be indicating a recent increase of stress in the region.

The location of the Cahuilla swarm relative to the Anza quiescent segment is similar to the locations of some of the Borrego Mountain earthquake preshocks relative to the eventual 1968 rupture zone (Figures 2.2 and 1.12); both are located off the respective faults roughly normal to the sections of highest strain accumulation. In addition,

the Borrego Mountain preshocks are located in nearly the same positions as the off-fault clusters of aftershocks triggered by that earthquake (Figure 1.12). These aftershock clusters are shallow (Figure 1.13b) and coincide with areas of increased shear stress as predicted by analytic dislocation models (Chinnery, 1963; Niewiadomski and Ritsema, 1980; Kostrov and Das, 1982). Other examples of off-fault aftershocks are consistent with local shear stress increases and normal stress decreases caused by a dislocation in a half space (Das and Scholz, 1981; Kadinsky-Cade and Willemann, 1982; Stein and Lisowski, 1983) suggesting that these dislocation models can be applied to the earth. However, the off-fault stress changes due to the dislocation are so small, only a couple of bars, that they are probably manifested as earthquakes only when they coincide with a relatively weak area of ground or an area of ground already stressed to near its breaking point. Such a weak piece of crust would be sensitive to stress changes occurring both before and after a large earthquake. The nearly coincident positions of the Borrego Mountain off-fault preshocks and aftershocks indicate that this part of the crust is relatively weak and is acting as a stress meter sensing the stress changes during the preseismic and postseismic periods. A similar role is suggested for the Cahuilla earthquake swarm area.

Of course, one of the most likely weak crustal zones is a preexisting fault, and preshocks might be expected to occur on one if stress becomes high. However, the detailed locations of the Cahuilla swarm earthquakes and the less well-constrained locations of the Borrego Mountain preshocks suggest that stress release is taking place throughout a volume of rock on many discrete small rupture planes rather than on one throughgoing structure. This evidence for stress release on small fracture planes spread throughout a volume is consistent with Kanamori's (1981) asperity model for precursory swarm seismicity followed by precursory seismic quiescence. The numerous small fractures beneath Cahuilla may have a lower average breaking strength than the surrounding rock or the stress may be concentrated (Kanamori, 1972) and subsequently rupture when the regional strain reaches some limiting value. A swarm occurs when a

large number of these small fractures rupture over a relatively short period of time. The number of these fractures is limited, however, and the swarm eventually dies off after most of the fractures have broken or if the local stress level lowers. If the remaining fractures in the region have even higher breaking strengths, then relative seismic quiescence ensues until strain accumulates to the point where more ruptures occur.

2.6 Local Geologic Structure

Several geologic studies provide constraints on the ages and amounts of movement along the San Jacinto fault system. Significant late Cenozoic right-lateral displacements imply that this fault zone plays an important role in current southern California tectonics. The total offset along the entire zone southeast of San Jacinto and Hemet (Figures 0.1 and 2.1) is 29 km of right slip since early Tertiary. Right slip of 19 km is measured on the San Jacinto fault, 5 km on the Coyote Creek, and 5 km on the Hot Springs and related faults (Sharp, 1967; Hill, 1981). The Bautista sedimentary deposits, parts of which contain the 715,000-year-old Bishop Ash (Sharp, 1981), help constrain the timing of recent offsets along the fault. The San Jacinto fault near Anza offsets these deposits at least 5.7 km right laterally, and the Coyote Ridge block between the San Jacinto and Coyote Creek faults has been pushed up some amount less than 2.4 km since Bautista deposition (Figure 2.19) (Sharp, 1967, 1975). Offset stream courses show up to 0.72 km of recent right-slip along the San Jacinto fault near Anza (Sharp, 1967). Young scarps indicate Holocene to late Pleistocene movement on all faults mentioned above except for the Hot Springs fault (Sharp, 1967, 1972; Hill, 1981). Shallow thrust faults are present parallel to segments of the San Jacinto and Coyote Creek faults, and small blocks have been thrust at least 0.8 km outward from the strike-slip faults during Quaternary time (Sharp, 1967).

Geological, seismological, and geodetic data imply a slip rate of about 10-15 mm/yr for the San Jacinto fault zone since the mid-Pleistocene and also historically (Sharp, 1967, 1981; Brune, 1968; Thatcher et al., 1975; Savage and Prescott, 1976; King

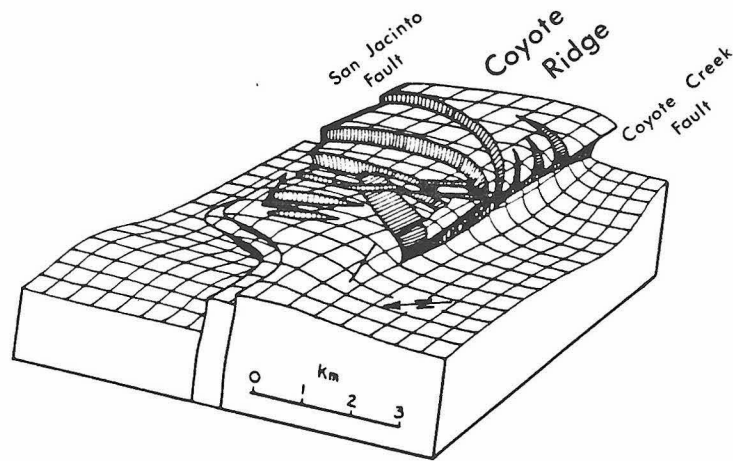


Figure 2.19. Diagrammatic sketch of extensional faults superimposed on the Coyote Ridge uplift block between the Coyote Creek and San Jacinto faults (after Sharp, 1975).

and Savage, 1983). This slip rate is less than those observed along several segments of the nearby San Andreas fault, including the 32 mm/yr historic creep rate between Cholame and Hollister (Burford and Harsh, 1980), 32 mm/yr historic slip rate between San Juan Bautista and Slack Canyon (Lisowski and Prescott, 1981), and Holocene slip rates of 34 mm/yr in the Carrizo Plain (Sieh and Jahns, 1984) and 25 mm/yr at Cajon Pass (Weldon and Sieh, 1985).

The significant geological features in the Anza area include the discontinuous and convergent fault geometries, the shallow thrust faults parallel to short segments of the fault zone, and the upthrown Coyote Ridge block. The fault geometries indicate a narrowing of the fault zone from about 11 km wide across the Buck Ridge, San Jacinto, and Coyote Creek faults southeast of Anza and from about 7 km wide across the San Jacinto and Hot Springs faults northwest of Anza to 1.5 km wide near Anza (Figure 2.1). Since these faults show considerable right-lateral offset and also recent movement and seismicity, this constriction of the fault zone must result in additional compression in the Anza area as material is displaced into the constricted area. The uplift of the Coyote Ridge block between the San Jacinto and Coyote Creek faults is an example of the transverse shortening in this area due to the convergent faults southeast of Anza (Figure 2.19). This uplift is even more interesting since it is situated where a depression or graben would be expected due to the right step from the northwest end of the Coyote Creek fault to the San Jacinto fault. Several steplike, listric, normal faults oriented perpendicular to the lateral slip faults at the northwest end of Coyote Ridge testify to the extensional strain regime near the right step (Sharp, 1967, 1975), but these are superimposed upon the Coyote Ridge horst.

The shallow thrust faults along the San Jacinto fault just northwest and southeast of Anza (Sharp, 1967, plate 1 and figure 3) appear to be manifestations of the lateral shortening in this area as material is squeezed out of the fault zone. The thrust faults along the San Jacinto fault show Mesozoic crystalline rocks thrust over Pleistocene sedimentary deposits. Where exposed, the shallow dipping thrust planes progressively

steepen with depth, suggesting that the faults become vertical at a relatively shallow depth (Sharp, 1967, figure 3). These are probably comparable to the thrust-slide blocks which have squeezed out along the San Andreas fault just northwest of the intersection with the Garlock fault (Davis and Duebendorfer, 1982). Shallow thrust faults are also mapped along the northwest end of the Coyote Creek fault where crystalline rocks of Coyote Ridge are thrust southwest over Quaternary deposits.

Seismological data from the Borrego Mountain and Coyote Mountain earthquakes presented in Chapter 1 demonstrate that the character of the Coyote Creek fault changes where the fault leaves Borrego Valley and becomes a bounding fault for the Coyote Mountain-Coyote Ridge block. In the vicinity of the Borrego Mountain earthquake and aftershocks the fault is in a region of apparently less strong local compression. The extended aftershock zone of the Borrego Mountain earthquake and the prolonged afterslip and continuing fault creep on the southern two thirds of the fault rupture are consistent with a relatively weaker fault here. Along the Coyote Ridge uplift, however, local compressive stresses normal to the Coyote Creek fault seem to be greater, possibly reflected in the abrupt northwest termination of the 1968 Borrego Mountain aftershocks at the southeast end of Coyote Ridge, the high stress drop and limited, deep aftershocks of the 1969 Coyote Mountain event, and the sudden deepening of the seismogenic zone at the southeast end of Coyote Ridge (Figures 1.13 and 2.5). The geological and seismological evidence indicates that this local more compressive stress regime continues northwest on the Coyote Creek and San Jacinto faults past Buck Ridge and through the Anza gap, becoming less compressional again near Hemet. Mechanisms of small earthquakes on the San Jacinto fault near Anza and Hemet are consistent with this later observation and show strike-slip and thrust movement near Anza (Figure 2.13) (Pechmann, 1983, figure 3-11) and some normal movement near Hemet (Pechmann, 1983, figure 3-10).

2.7 Regional and Local Strain

The strain in several areas of southern California has been determined repeatedly by several researchers (Savage and Prescott, 1976; Prescott et al., 1979; Savage et al., 1979, 1981, 1986). Strain rate measurements are important for evaluation of the overall spatial pattern of stress release in the Anza region. The principal strain in the Anza and nearby trilateration networks is north-south compression.

The strain accumulation for the years 1973-1981 in the trilateration networks extending from the Elsinore fault through the Anza area and eastward across the southern San Andreas fault has been presented by King and Savage (1983). Figure 2.20 shows the outline of the trilateration networks, the seismicity in the area, and the fault-parallel shear strain component across the three major faults. The data indicate minimal shear strain accumulation across the Elsinore fault with shear strain increasing progressively eastward in the block between the Elsinore and San Jacinto faults. The strain reaches a maximum of about $0.35 \mu\text{rad/yr}$ on the San Jacinto fault (about 16 mm/yr right slip beneath a 15-km-deep locked fault; Savage and Prescott, 1976), drops to zero between the San Jacinto and San Andreas faults, and then reaches a maximum of $0.4 \mu\text{rad/yr}$ across the San Andreas fault. The locations of $M_L \geq 2$ earthquakes for the same time period mimic the strain data. Few earthquakes are seen on the Elsinore fault with earthquakes increasing in the block between the Elsinore and San Jacinto faults to a maximum on the San Jacinto fault. No earthquakes occur between the San Jacinto and San Andreas faults, and activity increases again near the San Andreas fault.

An important coincidence in the strain and earthquake data is the lack of both shear strain and earthquakes in the block between the San Jacinto and San Andreas faults. The asymmetric pattern of earthquake swarms and clusters about the San Jacinto fault near Anza (Figure 2.2) may be related to this strain asymmetry.

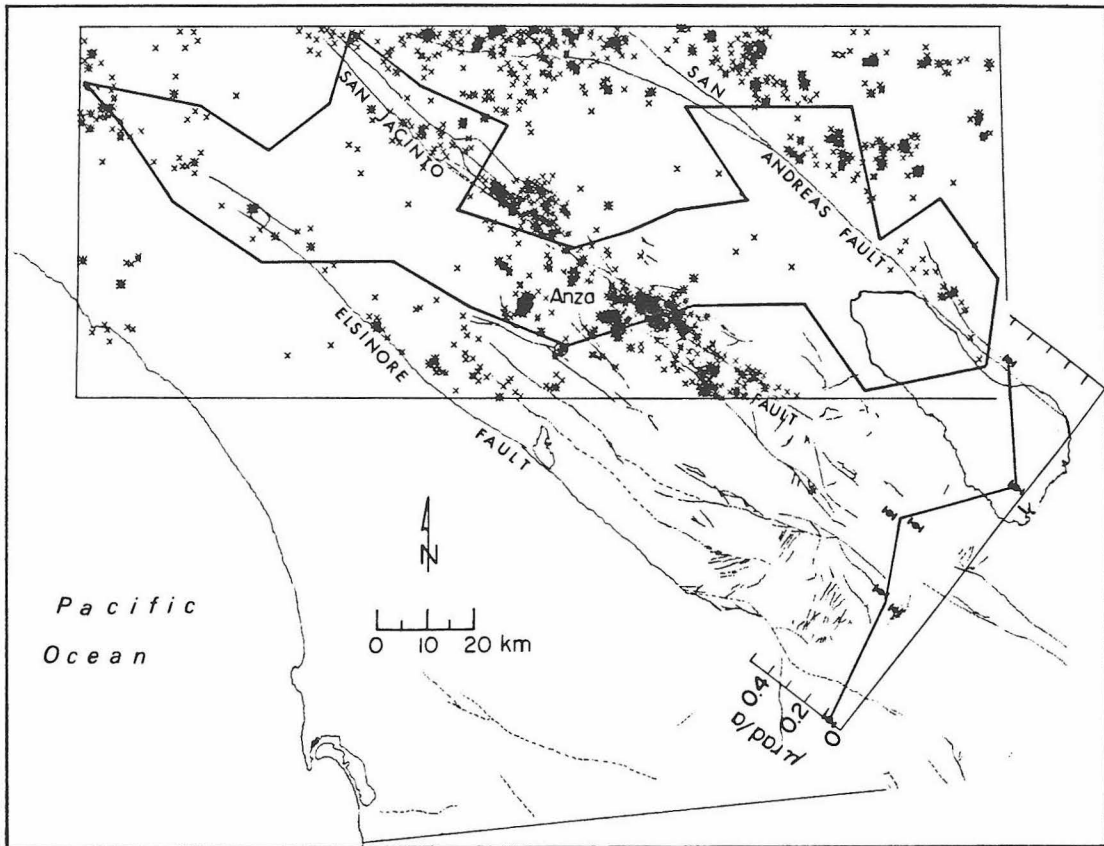


Figure 2.20. Map showing the $M \geq 2$ earthquakes during the years 1973-1981 in the region of the trilateration networks (heavy outline) centered on Anza. The corresponding fault parallel shear strain is plotted in the lower right corner (King and Savage, 1983).

2.8 Implications of Focal Mechanisms

The focal mechanisms for selected earthquakes and groups of earthquakes near Anza are plotted on Figure 2.13 (see Table 2.1 and the Appendix to this chapter for more information on these events). The earthquakes are mostly greater than M_L 3, so the mechanisms are representative of the larger stress release in the area. The nodal planes are all constrained by first motions to within several degrees. Besides mechanisms for certain earthquakes mentioned in the text, many mechanisms are shown which are characteristic of the local pattern of stress release.

The focal mechanisms of earthquakes located on the San Jacinto fault (Figure 2.13, mechanisms a,c,d,h,i,k) indicate right slip on an approximately $N53^\circ W$ trending, steeply northeast dipping fault. This is consistent with the trend of the San Jacinto fault, the geologic offset on the fault, and the hypocentral location of small earthquakes.

Of special interest are mechanisms e, f, and g. Mechanism e is representative of the June 15, 1982 M_L 4.8 earthquake and large aftershocks, mechanism f is for one M_L 3.6 earthquake which occurred 12 km beneath Anza in 1980, and mechanism g is representative of most of the earthquakes which occurred in the 1980-1981 Cahuilla swarm. The important feature of these well-constrained focal mechanisms is the orientation of the nodal plane along which right slip occurs. These planes have orientations (\pm few degrees) of $N26^\circ W$ (e), $N06^\circ W$ (f), and $N22^\circ W$ (g), which are rotated 27° - 47° clockwise relative to the local strike of the San Jacinto fault. Two explanations for this seem possible: (1) the stress field in the block southwest of the fault is warped locally and is different from that acting on the fault, or (2) the earthquakes in the block southwest of the fault are breaking on fractures favorably oriented for shear failure under the regional stress field (in which case, the San Jacinto fault is not favorably oriented but still controls the direction of shear failure for the earthquakes rupturing on it).

The former explanation was tested using a two-dimensional finite element computer model developed by G. Lyzenga (personal communication, 1981). We

hypothesized that if local rotations of the stress field near Anza and Cahuilla are the cause of the rotated mechanisms, then the local stress field is probably warped by stress perturbations caused by the discontinuous Coyote Creek fault and/or the locked fault segment near Anza (Sanders et al., 1981). The finite element model was formulated in the following manner. The San Jacinto fault northwest and southeast of the Anza gap and the Coyote Creek fault were introduced into the two-dimensional finite element grid as cracks with geometries mimicking the actual mapped surface geometries of these faults. These cracks were assumed to have no shear strength and to slip due to stresses applied at the boundaries of the finite element grid. The 18-km-long Anza seismic gap was the solid area between the ends of the cracks representing the slipping northwest and southeast San Jacinto fault segments. Far-field stresses (either uniaxial north-south compression or north-south compression and east-west extension) were applied at the grid boundaries, and the resultant principal stresses were computed for each grid element. The results indicate that the local stress axes in the grid elements representing the area near Cahuilla and Anza are not rotated more than a few degrees (G. Lyzenga, personal communication, 1982). This does not support our original hypothesis and suggests that this explanation for the rotated focal mechanisms is probably not correct.

The second explanation appears most valid. The regional principal stress is about N-S compression (Savage et al., 1986). Fractures oriented about N25°W are favorably oriented for right-lateral shear failure in this stress system. The small earthquakes beneath Anza and Cahuilla can be considered as occurring on fractures in homogeneous material relative to the main fault, these fractures rupturing more in accordance with the regional stress system and with orientations of N22-27°W. The San Jacinto fault is not preferentially oriented for shear failure under the present regional stress system, since it is oriented at a 53° angle to the axis of maximum compression. Such an orientation will tend to increase the component of stress normal to the fault plane, thereby increasing the shear strength of the fault (Chapter 3). Numerous earthquakes occur on

the fault, however, suggesting that parts of the fault are weaker than the surrounding rock and/or are subjected to larger shear stresses. The largest earthquakes in the area occur on the San Jacinto fault, indicating that there are local strong areas on the fault which are able to store strain over large slip surfaces. These strong spots on the fault near Anza must be relatively strengthened by the compression induced by the high angle between the regional stress axis and the fault surface. Some of the strongest may be responsible for the present quiescent nature of the gap.

2.9 Fault Creep Near Anza

An alignment array spanning the San Jacinto fault east of the town of Anza has been surveyed 13 times since its installation in August 1970. Between the time of the first survey of this array at its installation and the second survey in January 1973 Keller et al. (1978) reported that an apparent 110-mm slip event occurred over a 300-m wide zone on this part of the fault. Three subsequent surveys to April 1977 showed no significant further change (Keller et al., 1978) nor did eight surveys between April 1978 and December 1982 (Louie et al., 1985). Discussions with J. Louie (pers. comm., 1983, 1986) revealed that the early Anza alignment array may have been relatively unstable, since some of the survey targets are located on telephone poles, a tree, and a fence post. He has also noticed that large movements are often measured between the first survey of any alignment array (when it is installed) and the second survey some time later. Apparently, the various survey points need to go through a rainy season before becoming relatively stable. Keller et al. (1978) acknowledge that the large slip event measured between 1970 and 1973 may not be a valid observation, since many of the survey targets which were originally placed in visibly tilted structures may have tilted further.

Surface fault creep data for the Anza section of the San Jacinto fault, then, is ambiguous. The large slip event between 1970 and 1973 reported by Keller et al. (1978) may not be real. Eleven surveys of the Anza array over the years 1973-1982,

the last eight of which utilized the most stable buried stake targets, reveal no significant slip ($\pm 1-2$ mm) on the main surface trace of the fault here. In fact, all of the survey data when averaged between August 1970 and December 1982 actually indicate no net slip during the life of the array (Louie et al., 1985).

In addition to the short baseline alignment array near Anza measured by the Seismological Laboratory at the California Institute of Technology, Art Sylvester of the University of California at Santa Barbara frequently surveys a 400 m long leveling array across the San Jacinto fault in the center of the Anza gap using first-order, class I procedures. In twenty surveys of this array between 1980 and 1985 he has found no elevation changes greater than 1 mm (A. Sylvester, unpublished report, March 1985).

Based on this evidence, we conclude that the San Jacinto fault near Anza for at least the years 1973-1982 has not been relieving significant stress aseismically, at least as measured by surface fault creep.

2.10 Conclusions

The results of this study support the following conclusions:

1. The segment of the San Jacinto fault near Anza, California, has not ruptured in a large earthquake at least since 1892 and can be considered a historic seismic slip gap (Chapter 1).
2. Current seismicity defines a 18-km-long quiescent fault stretch, the Anza seismic gap, in the northern half of the historic seismic slip gap.
3. Moderate earthquakes on and near the San Jacinto fault in the seismic gap and their aftershocks indicate that the fault here is seismogenic and highly stressed but locked.
4. The locked and quiescent nature of the fault may be partly due to high compressive stress normal to the fault resulting from the local active fault geometries and the orientation of the regional stress field.
5. The Coyote Mountain-Coyote Ridge uplift block appears to be a manifestation

of transverse crustal shortening southeast of Anza between the Coyote Creek and San Jacinto faults. The implied large stress drop and limited aftershocks of the 1969 event, the abrupt northwest termination of the 1968 aftershocks, and the sudden change in the depth of the seismogenic zone are seismological evidence of the possible high compression normal to the fault planes due to this shortening.

6. No surface fault creep on the San Jacinto fault near Anza has been measured since at least 1973, suggesting that no aseismic release of stress is occurring.

7. The 1980-1981 Cahuilla earthquake swarm relieved stress in an area which was also active before the 1918 San Jacinto-Hemet earthquake and the 1937 Coyote Ridge earthquake. This suggests that the ground beneath Cahuilla may be acting as a stress level monitor signaling the presence of high stresses in the area before large local earthquakes.

8. The length of the quiescent fault segment suggests about M 6.5 potential if the entire segment ruptures during one earthquake.

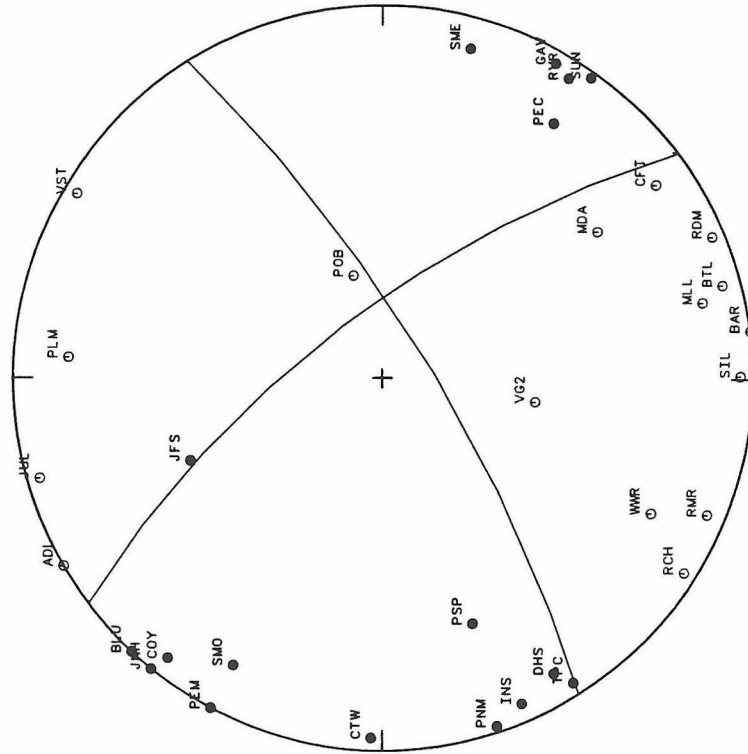
2.11 Appendix

This appendix contains the first motion data used to constrain the source mechanisms presented in Figure 2.13 and Table 2.1. These are lower-hemisphere, equal-area projections. Closed circles, compression; open circles, dilatation; n, nodal.

MECHANISM A

22 AUG 79 0201

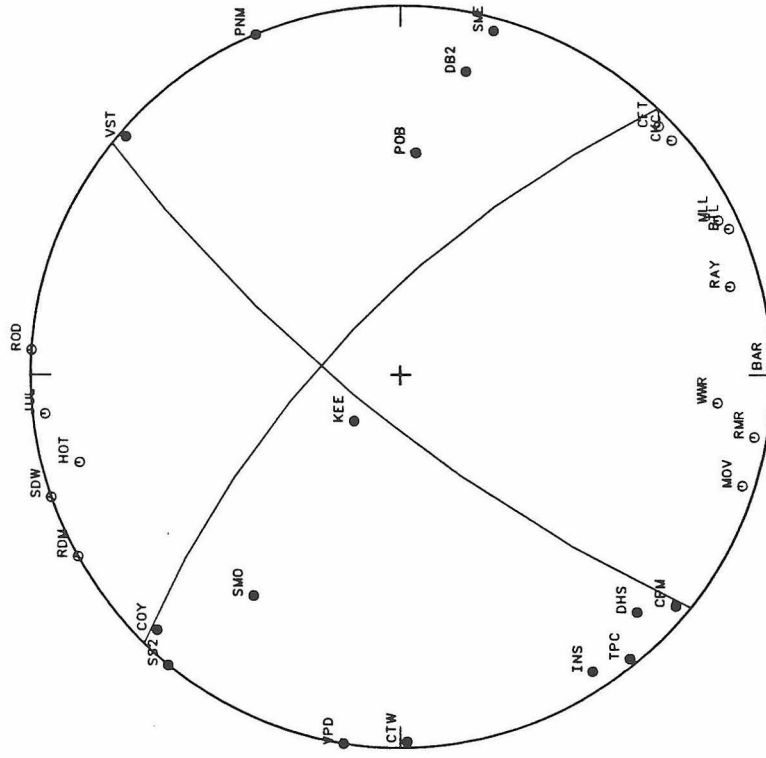
STRIKE = 323.
DIP = 70.
RAKE = 195.



MECHANISM B

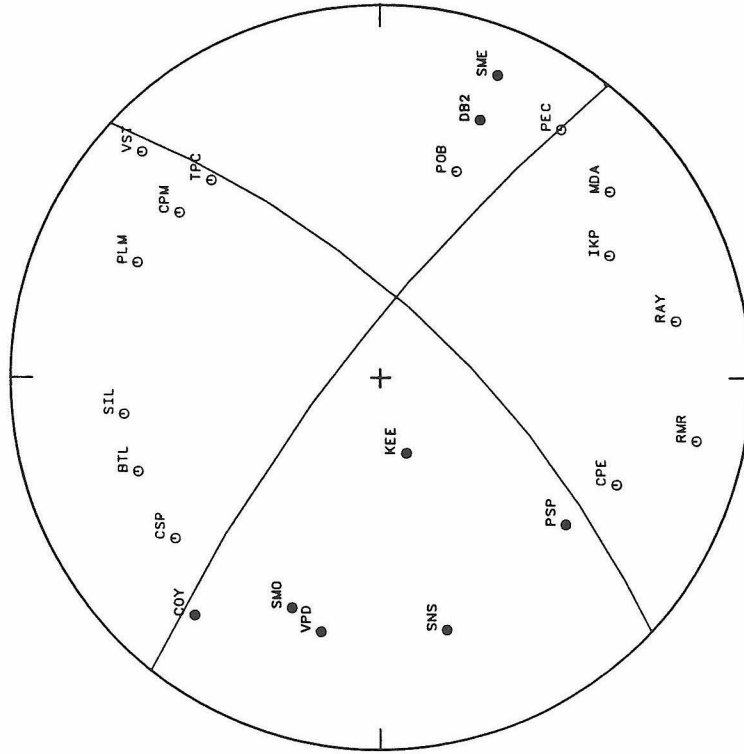
3 AUG 78 0430

STRIKE = 314.
DIP = 70.
RAKE = 15.



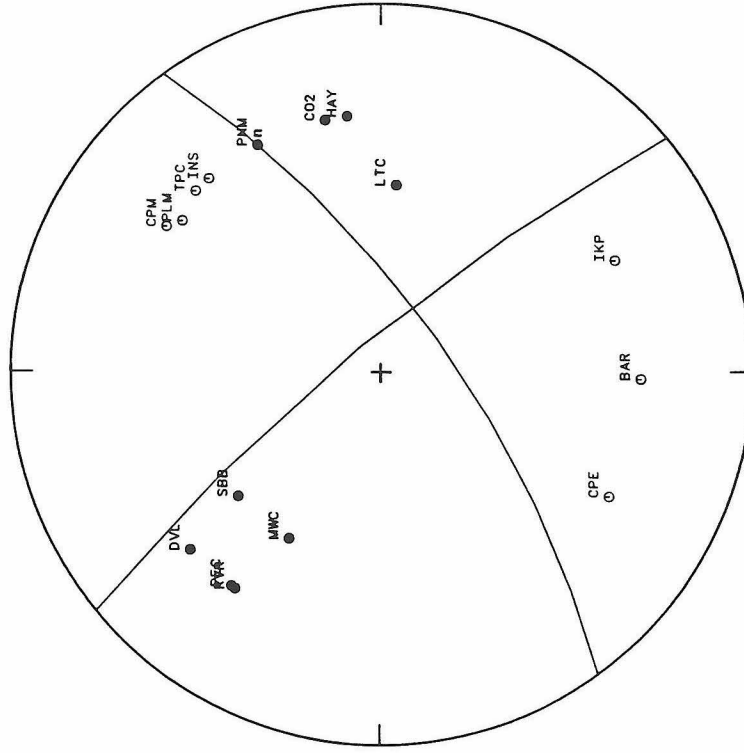
MECHANISM C
2 JULY 77 0122

STRIKE = 308.
DIP = 78.
RAKE = 202.

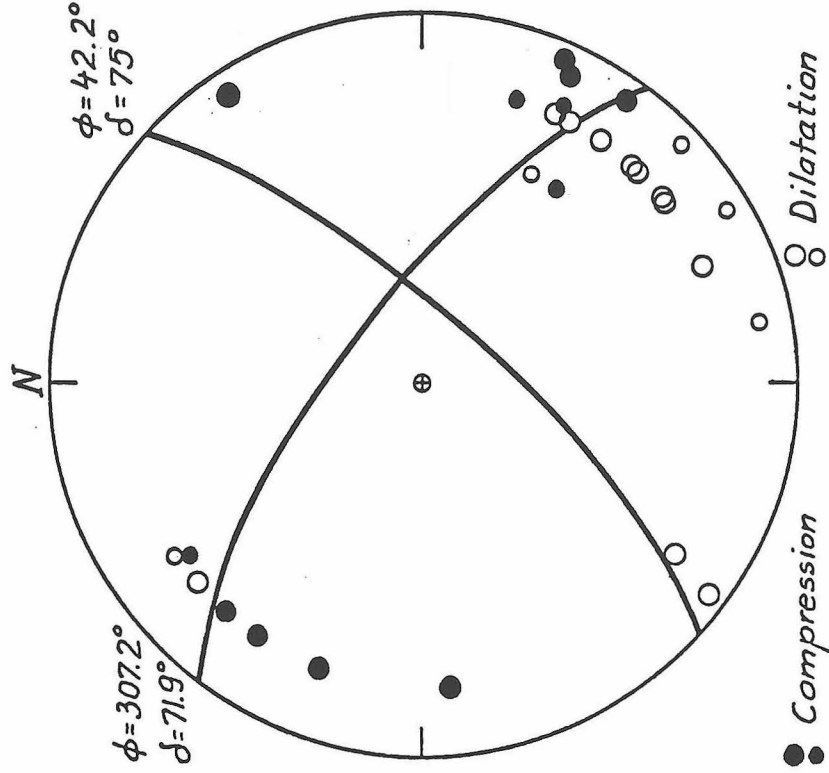


MECHANISM D
9 NOV 74 1010 1012

STRIKE = 320.
DIP = 80.
RAKE = 200.

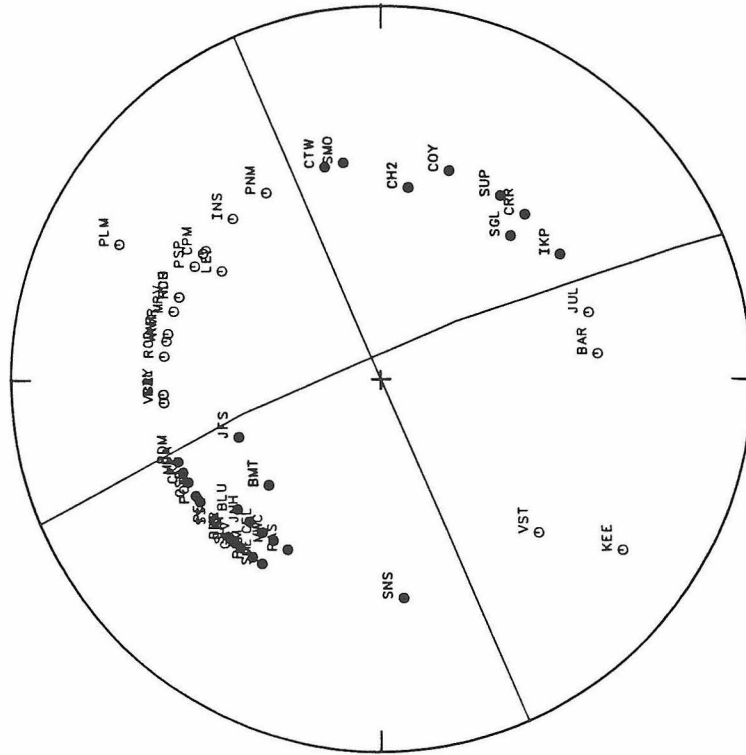


MECHANISM H
1 AUG 75 0014



STRIKE = 338.
DIP = 82.
RAKE = 4.

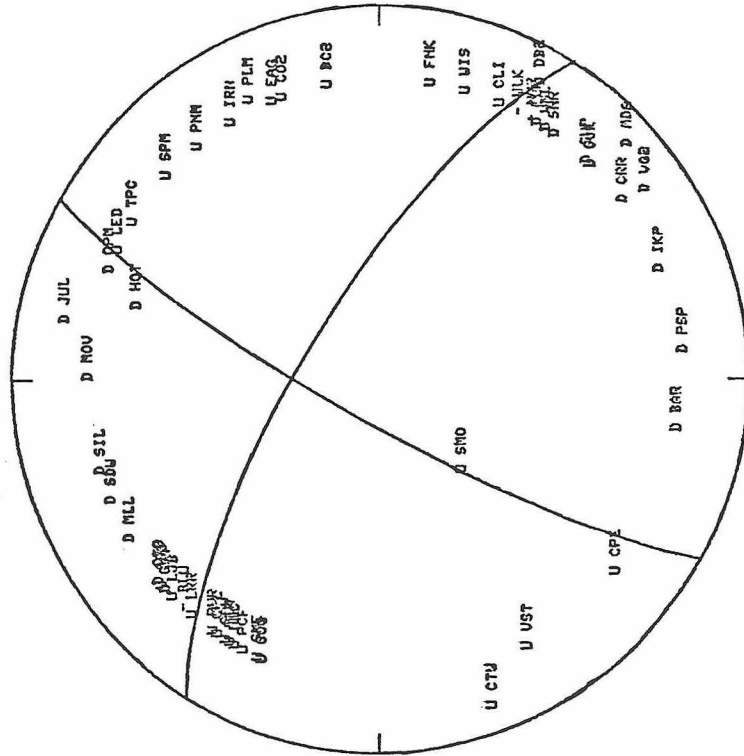
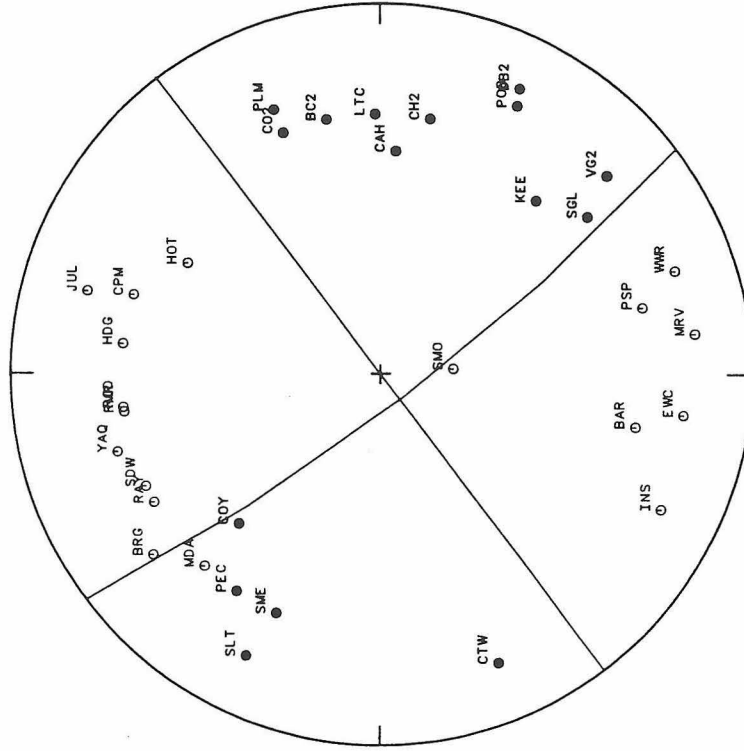
MECHANISM G
1 FEB 81 1927



MECHANISM J
4 MAY 81 1841

MECHANISM I
25 FEB 80 1047

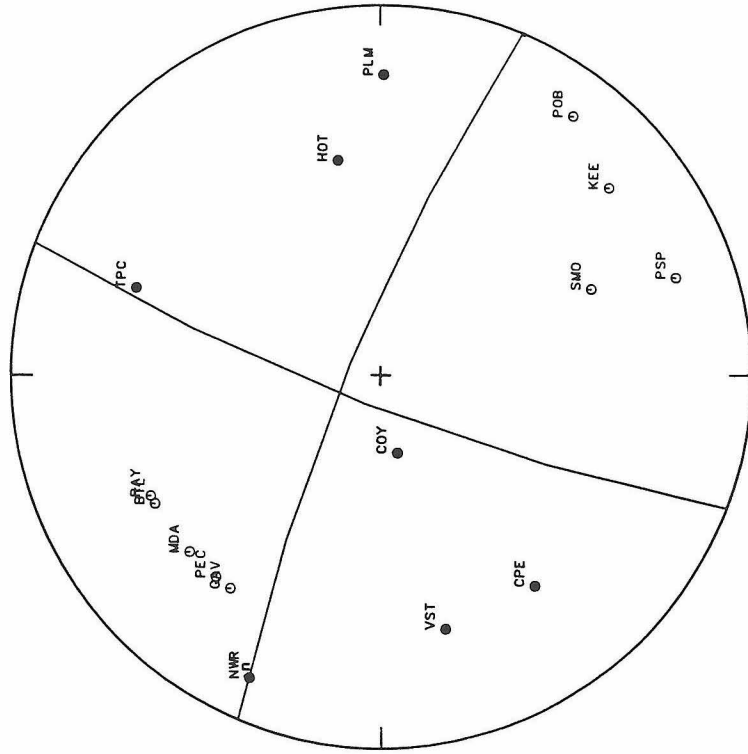
STRIKE = 143.
DIP = 80.
RAKE = 0.



MECHANISM 1

6 AUG 77 1222

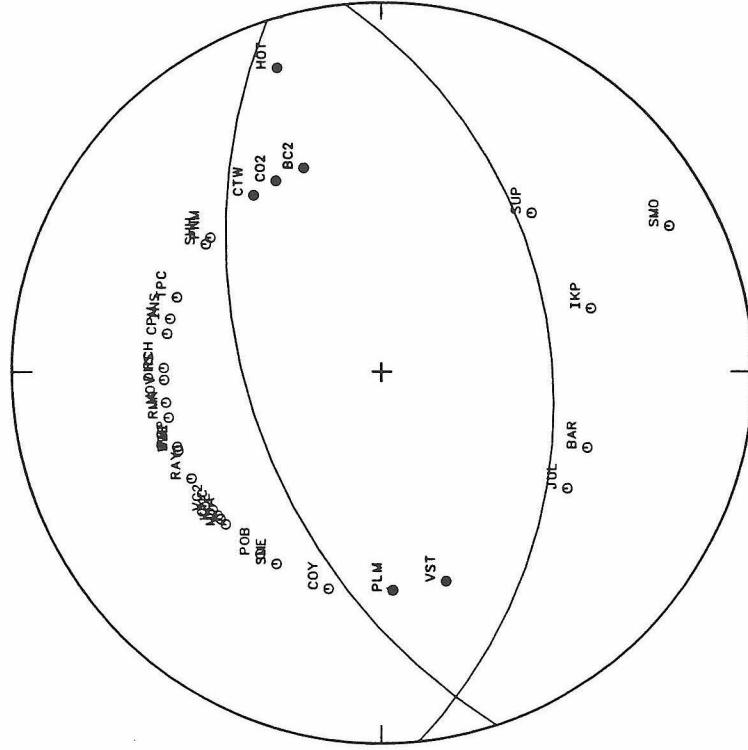
STRIKE = 292.
DIP = 80.
RAKE = 10.



MECHANISM 2

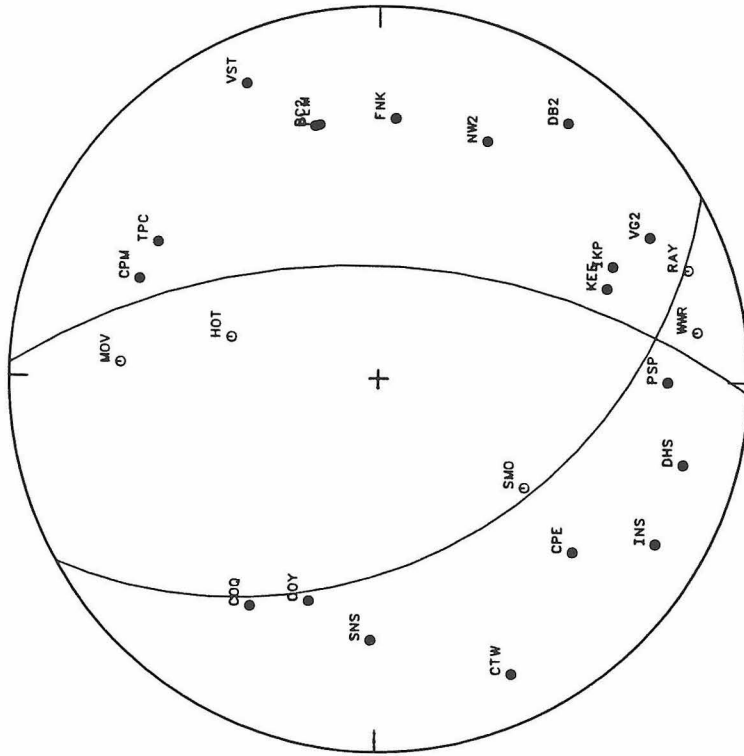
16 MAY 79 0425

STRIKE = 252.
DIP = 50.
RAKE = 278.



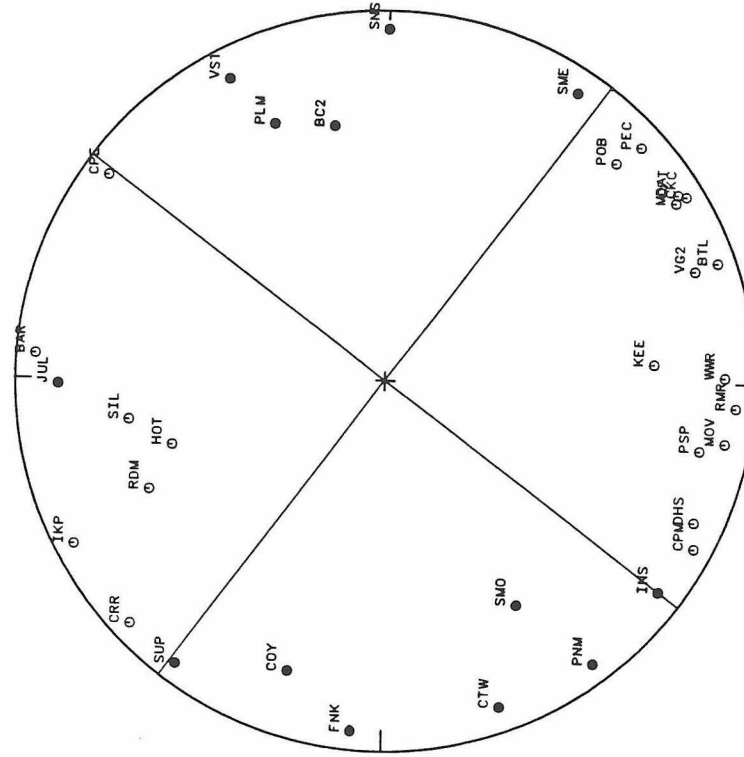
MECHANISM 5
22 APR 79 1652

STRIKE = 190.
DIP = 38.
RAKE = 84.



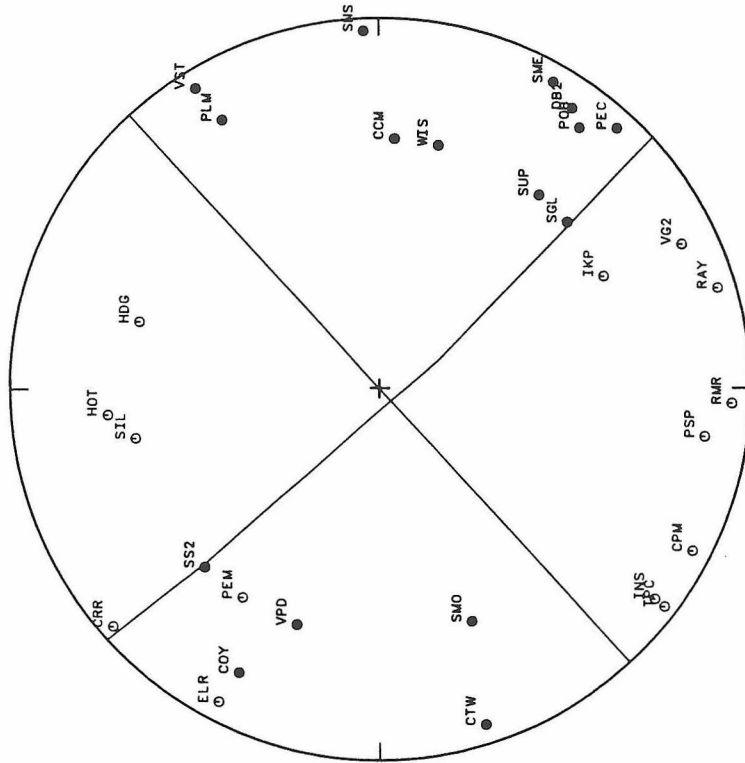
MECHANISM 6
1 AUG 79 0831

STRIKE = 308.
DIP = 90.
RAKE = 0.



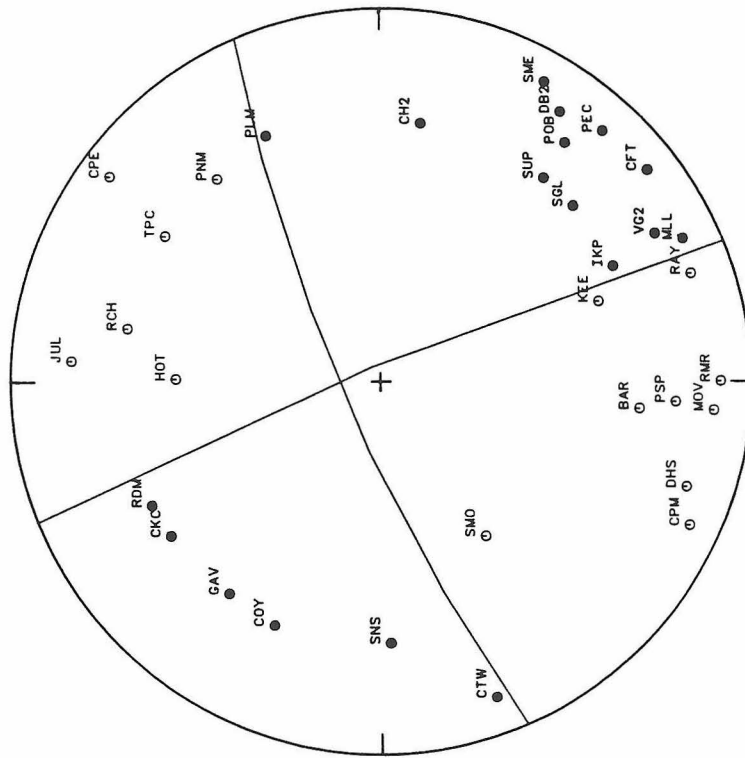
MECHANISM 8
17 DEC 77 1427

STRIKE = 137.
DIP = 84.
RAKE = 0.



MECHANISM 7
10 MAR 80 2332

STRIKE = 338.
DIP = 85.
RAKE = 12.



Chapter 3

Depths of Earthquakes in the San Jacinto-Southern San Andreas Region

3.1 Introduction

Quality-A earthquake locations for the years 1980 through 1985 are used to study the spatial variations in the depth distribution of seismicity in the southern California region that includes the San Jacinto, southern San Andreas, Banning, and Elsinore faults. This study initiated from two observations: (1) cross sections of earthquake hypocenters in the San Jacinto fault zone reveal that most earthquakes occur deep in the fault zone and that the maximum depth of seismicity changes by a factor of two along strike; (2) in general shallow and deep seismicity in the study area do not share epicentral regions; the deep seismicity occurs almost exclusively in association with major faults, while the shallow seismicity occurs in the crustal blocks adjacent to the faults. We would like to investigate what these observations imply about the state of stress in the crust and along the strike slip faults in the region.

3.2 Data

The data for this study are the earthquakes with quality-A locations (precision 1 km laterally and 2 km vertically) which occurred in the study area (Figure 3.1) during the years 1980 through June 1985. These are all routine locations obtained by use of the CalTech-USGS southern California seismic array and are archived in the CIT catalog. Several studies in the area indicate that the quality-A hypocenters are indeed located to the precision thought and can be used for local and regional structural studies. Corbett (1984) concluded from numerical experiments that most events in the central portion of our study area with quality-A locations do have a lateral precision of 1 km and a depth precision of 2 km. The percentage of events with quality-A locations, however, may decrease near sparsely instrumented parts of the southern

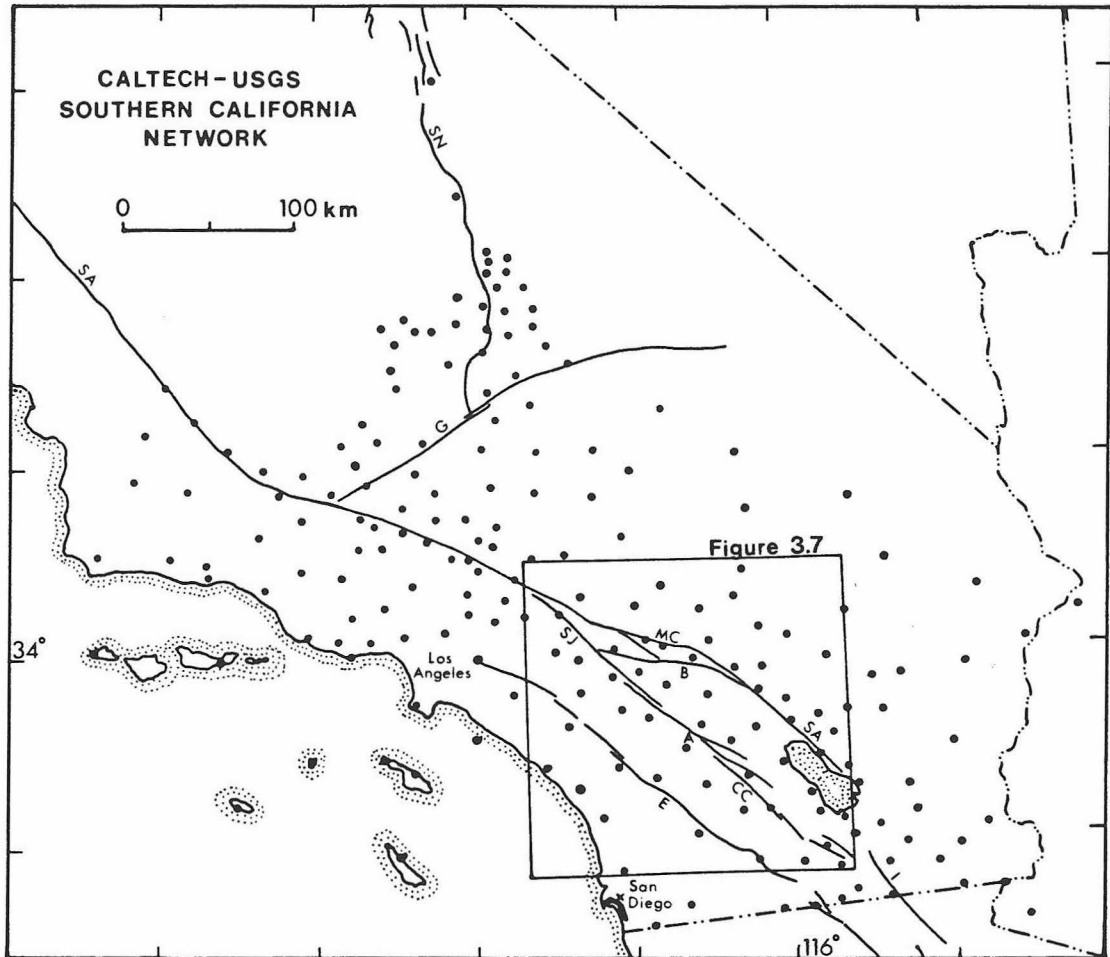


Figure 3.1. Map of the southern California region showing locations of seismograph stations of the CalTech-USGS array, major faults, and the outline of the study area (Figure 3.7).

California array. We find that 60 per cent of the $M \geq 1.5$ earthquakes in the study area during the years listed above have quality-A locations. These account for 92 per cent of the seismic moment in that area during that time. Earthquakes relocated using the master-event technique in the Anza gap area of the San Jacinto fault zone (Given, 1983) and in the region of the Banning and Mission Creek faults (Green, 1983) show changes in maximum hypocentral depths generally less than a kilometer from the quality-A catalog locations. This indicates that quality-A CIT catalog locations should be satisfactory for our study. We also limit this study to the general region in which the velocity model used for the routine catalog locations was developed (Hadley, 1978); this gives us more confidence in the absolute hypocentral depths.

3.3 Shear Strength of the Crust and the Depths of Earthquakes

Studies of the factors which effect the shear strength of the crust as a function of depth have been made possible by experimental data on the deformation behavior of various rock types at high pressures and temperatures. The factors which control the shear strength of a fault with depth include the normal stress and pore fluid pressure, temperature, mineralogy, strain rate, and water content. Sibson (1982) and Meissner and Strehlau (1982) analyzed the shear strength of a quartz-rich crustal fault zone and found that whereas the strength of the fault increases with depth in the upper, brittle crust it soon reaches a depth of maximum strength below which the shear strength falls off rapidly and ductile deformation occurs (Figure 3.2). These authors used experimentally determined flow laws for quartz-rich rock to model the loss of shear strength in the lower crust. They found that, all factors other than heat flow being equal, the depth to the boundary where frictional deformation in the fault zone becomes quasi-plastic deformation correlates with the maximum depth of earthquakes. Deformation in the quasi-plastic fault zone occurs by aseismic creep.

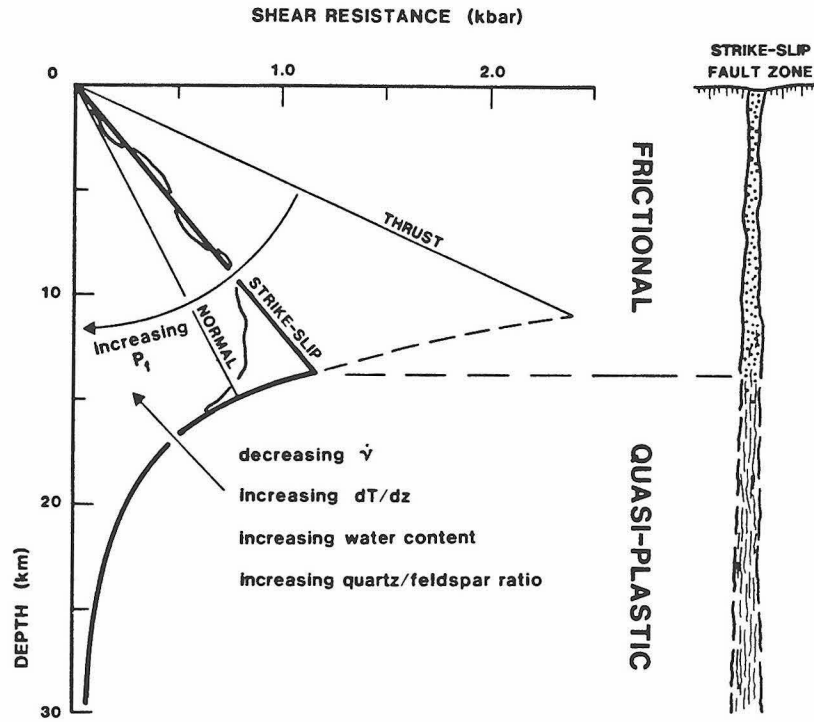


Figure 3.2. Diagram showing shear resistance with depth (constructed assuming $f = 0.75$, hydrostatic fluid pressures, a linear geotherm $dT/dz = 25^\circ \text{C}/\text{km}$, and a Westerly granite flow law at a strain rate of 10^{-11}s^{-1}) and a simple fault model. Effects of potential perturbing factors on the general profiles are indicated. This figure is from Sibson, 1986.

Fault Zone Model

The fault zone model for a strike-slip plate boundary shown in Figure 3.3 is commonly assumed today. The model has an elastic lithosphere overlying a visco-elastic asthenosphere, with the lithosphere divided into upper frictional and lower quasi-plastic layers (e.g. Savage and Burford, 1973; Turcotte and Spence, 1974; Sibson, 1982). The lithosphere is deformed by flow in the asthenosphere, this deformation concentrating predominantly along major fault zones in the lithosphere. The fault zone in the lower lithosphere (uppermost mantle and lower crust) responds to this deformation by aseismic creep. The deformation is thus propagated through the lower lithosphere to the locked fault zone in the upper lithosphere (upper and middle crust) which responds in a brittle manner with displacement occurring seismically. The frictional forces in the fault zone control displacement in the upper lithosphere. At the boundary between the frictional and quasi-plastic lithosphere there is a transition zone of unknown thickness.

Analysis of Stresses

In a strike-slip stress regime the maximum (σ_1) and minimum (σ_3) principal stresses are horizontal, and the intermediate (σ_2) principal stress is vertical (Anderson, 1951). σ_2 is essentially the stress due to the lithostatic load, $\sigma_2 = \rho_c g z$ where ρ_c is the average density of the crust above depth z , g is the acceleration due to gravity, and z is the depth in the crust in km. Measurements of vertical stress to depths of $2\frac{1}{2}$ km in the continental crust are generally consistent with this assumption (McGarr and Gay, 1978).

The frictional shear strength of the fault zone is

$$\tau_f = \tau_o + f\sigma_n' = \tau_o + f(\sigma_n - P) = \tau_o + f\sigma_n(1-\lambda),$$

where τ_o is the cohesive strength of the fault rock, f is the coefficient of static friction, σ_n' is the effective normal stress on the fault plane, σ_n is the applied normal stress on the fault, P is the pore fluid pressure, and λ is the pore fluid factor (Hubbert and Rubey, 1959). This frictional shear strength must be overcome by the tectonic

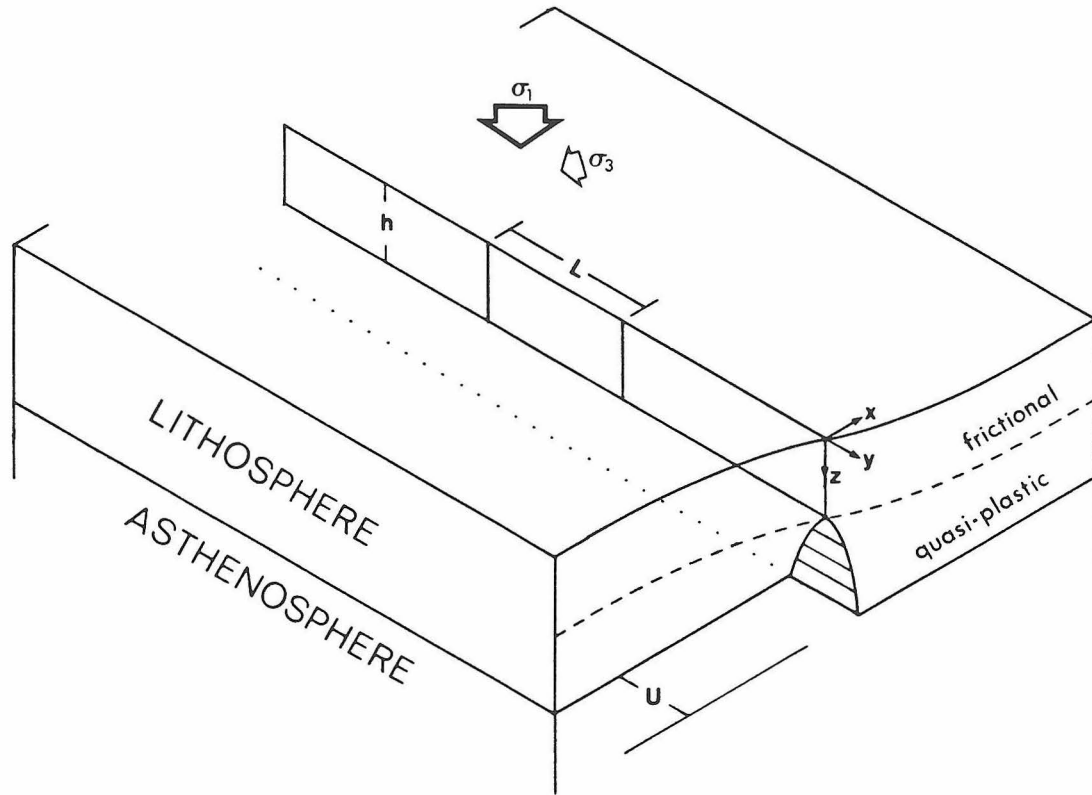


Figure 3.3. Fault zone model of a strike-slip plate boundary fault. σ_1 and σ_3 are the maximum and minimum principal tectonic stresses, h is the thickness of the brittle crust, and U is the displacement in the creeping lower lithosphere.

(deviatoric) stress before fault rupture can occur. In order to evaluate the magnitude of τ_f at various levels in the crust we need more information on the variables σ_n and λ . We first look at σ_n .

The applied normal stress on the fault plane is composed of lithostatic and tectonic components,

$$\sigma_n = \sigma_{nL} + \sigma_{nT}.$$

The magnitude of the lithostatic component lies within the range

$$\left(\frac{\nu}{1-\nu}\right)\rho_c g z \leq \sigma_{nL} \leq \rho_c g z,$$

where the left hand limit assumes a vertical fault in an elastic crust with ν the Poisson's ratio and horizontal displacements due to rock creep constrained to zero. The right hand limit assumes a horizontal fault or that crustal rocks can creep over long time periods. The latter possibility would result eventually in the stress state $\sigma_1 = \sigma_2 = \sigma_3 = \rho_c g z$ which is rarely if ever observed in nature (McGarr and Gay, 1978). With the constraint of no flow in the crust, σ_{nL} can be approximated by

$$\sigma_{nL} \approx \left[1 + \left(\frac{\nu}{1-\nu} - 1\right) \sin^2 \phi \right] \rho_c g z,$$

where ϕ is the dip angle of the fault in degrees. In this form σ_{nL} at a given depth increases almost linearly as the dip of the fault decreases. For a nearly vertical strike-slip fault $\phi \approx 90^\circ$ and

$$\sigma_{nL} = \left[\frac{\nu}{1-\nu} \right] \rho_c g z.$$

The tectonic component of the applied normal stress on a vertical strike-slip fault is related to the tectonic principal stresses by

$$\sigma_{nT} = \sigma_1 \cos^2 \theta + \sigma_3 \sin^2 \theta = \frac{1}{2}(\sigma_1 + \sigma_3) + \frac{1}{2}(\sigma_1 - \sigma_3) \cos 2\theta,$$

where θ is the angle between the maximum principal stress, σ_1 , and the normal to the fault plane (e.g. Jaeger and Cooke, 1979). If we assume that $\frac{1}{2}(\sigma_1 + \sigma_3) = \sigma_2$, which fits the limited data of McGarr et al. (1982) for the Palmdale, California area, then

$$\sigma_{nT} = \sigma_2 + \frac{1}{2}(\sigma_1 - \sigma_3) \cos 2\theta = \rho_c g z + \frac{1}{2}(\sigma_1 - \sigma_3) \cos 2\theta.$$

Thus,

$$\sigma_n = \left(\frac{\nu}{1-\nu} + 1 \right) \rho_c g z + \frac{1}{2}(\sigma_1 - \sigma_3) \cos 2\theta. \quad (3.1)$$

We next look at the pore fluid factor,

$$\lambda = \frac{P}{\sigma_n} = \frac{\text{fluid pressure}}{\text{gravitational} + \text{tectonic pressure}}.$$

λ has a value between 0 and 1. A value of $\lambda = 0$ means that no fluid pressure exists in the fault zone. A value of $\lambda = \frac{\rho_f}{\rho_c} = 0.37$ (for $\rho_f = 1.0 \text{ g/cm}^3$, $\rho_c = 2.7 \text{ g/cm}^3$) means that the crust is saturated with fluid (density ρ_f) that can move freely, and the fluid pressure at a particular point is due solely to the weight of the column of fluid above which extends to the surface, i.e., the hydrostatic pressure. This is a situation that is commonly assumed. A value of $\lambda = 1$ means that the fluid pressure in the fault zone equals the applied normal stress, and subsequently the fault has no shear strength. Values of $\lambda > \rho_f/\rho_c$ are obtained if movement of fluid is hindered; such may be the case in clay-rich fault gouge or during earthquake rupture, with rupture propagation possibly enhanced as a result (e.g. Morrow, et al., 1981; Sibson, 1977).

Combining the above we obtain

$$\tau_f = \tau_o + f(1-\lambda) \left[\left(\frac{\nu}{1-\nu} + 1 \right) \rho_c g z + \frac{1}{2}(\sigma_1 - \sigma_3) \cos 2\theta \right].$$

The tectonic (deviatoric) shear stress on the fault plane is given by (e.g. Jaeger and Cooke, 1979)

$$\tau_d = \frac{1}{2}(\sigma_1 - \sigma_3) \sin 2\theta.$$

The maximum tectonic shear stress in a region occurs at $\theta = 45^\circ$, $\tau_{\max} = \frac{1}{2}(\sigma_1 - \sigma_3)$.

Fault rupture occurs at $\tau_d > \tau_f$ or

$$\frac{1}{2}(\sigma_1 - \sigma_3) > \frac{\tau_o + f(1-\lambda) \left(\frac{\nu}{1-\nu} + 1 \right) \rho_c g z}{\sin 2\theta - f(1-\lambda) \cos 2\theta}. \quad (3.2)$$

This relation will be used to estimate the expected shear stresses at various depths in the crust where earthquakes are occurring.

State of Stress in the Lithosphere

Arguments about the state of stress in the continental lithosphere and along fault zones are summarized in a review article by Kanamori (1980b). The principal controversy concerns *low-stress* and *high-stress* models of the stress state in the lithosphere. The low-stress model assumes that much of the lithosphere can support large stress differences (which must exist due to surface relief) but that fault zones and plate boundaries are much weaker and can maintain only low stress levels. This model is supported by the remarkably low and constant stress drops of large earthquakes and by the lack of a heat flow anomaly along major faults such as the San Andreas fault. The high-stress model assumes that stresses are high throughout the lithosphere and that earthquake stress drops represent only a small fraction of the ambient stress. This model is supported principally by laboratory data on the fracturing of rock which suggest great strength for crustal rocks. Kanamori argues for the low-stress model noting that it is difficult to explain the low and constant stress drops with the high stress drop model and that fault zones can easily be made much weaker than the surrounding lithosphere by the presence of fault gouge and high pore fluid pressures. The low stress model implies average shear stresses of less than about 100 bar on the crustal fault zones.

Calculation of Stresses

The magnitude of shear stresses in the upper and middle crust has been estimated by several techniques. Data from laboratory experiments on rock fracture suggest kilobar level stresses if this data is extrapolated to the earth. A summary of the data (all from dry experiments, i.e., $\lambda = 0$) by Byerlee (1978) gives $\tau = 0.85\sigma_n$ for $\sigma_n \leq 2$ kbar (i.e. $\tau = 300$ bar/km above 5.7 km) and $\tau = 0.5 + 0.6\sigma_n$ for $\sigma_n > 2$ kbar (i.e. $\tau = 500$

bar + 212 bar/km below 5.7km). These values are plotted in Figure 3.4 (g) with σ_n calculated from equation 3.1 with $\nu = 0.25$, $\rho_c = 2.7 \text{ g/cm}^3$, and $\theta = 45^\circ$. Measurements of stresses in boreholes in the upper few km of the crust indicate τ_{\max} increases by an average of about 80-90 bar/km in that depth range (Figure 3.4, c) (McGarr and Gay, 1978; McGarr et al., 1982). The former value is from measurements near the San Andreas fault. Analysis of wellhole breakouts in the deep Kola Peninsula borehole by Zoback and Mastin (1986) suggests maximum shear stresses increase with depth and reach about 1500 bar at 11.6 km depth (130 bar/km) (Figure 3.4, d). Vetter and Ryall (1983) used data from focal mechanisms which indicate the change in orientation of σ_1 to estimate τ_{\max} with depth in the crust of the western Basin and Range province. Assuming hydrostatic pore pressures, $f = 0.85\text{--}0.65$ depending on depth, and $\rho_c = 2.7 \text{ g/cm}^3$ they determine $\tau_{\max} \approx 68 \text{ bar/km}$ in the upper and middle crust (Figure 3.4, b). This estimate of stress at earthquake rupture is well below that predicted by laboratory data and would be even lower if smaller values of f were assumed.

In the above studies only that by Vetter and Ryall gives data on the shear stress levels in the crust that initiate fault rupture. The Byerlee study presents data from fracturing of rock in the laboratory which only indirectly suggest stress levels during rupture of pre-existing faults in the crust. The two borehole studies indicate the prevailing stress levels in the crust at those locations but not the stress levels at fault rupture.

We can use relation 3.2 to estimate the maximum shear stresses, τ_{\max} , in the crust at various depths where strike-slip earthquakes are occurring. The San Jacinto fault zone and Cahuilla swarm area near Anza are used as examples. We assume general values of $\tau_o \approx 0$, $\nu = 0.25$, $\rho_c = 2.7 \text{ g/cm}^3$, and $\lambda = 0.37$ (hydrostatic pore pressure). Values of f vary from $f = 0.85, 0.6$ (rock; Byerlee, 1978) to $f = 0.1$ (clay fault gouge; Chu et al., 1981). The maximum principal stress in the Anza area as determined from strain data is nearly N-S (Savage et al., 1986). Focal mechanisms on the San Jacinto fault and beneath Cahuilla imply that rupture occurs on fault planes oriented about

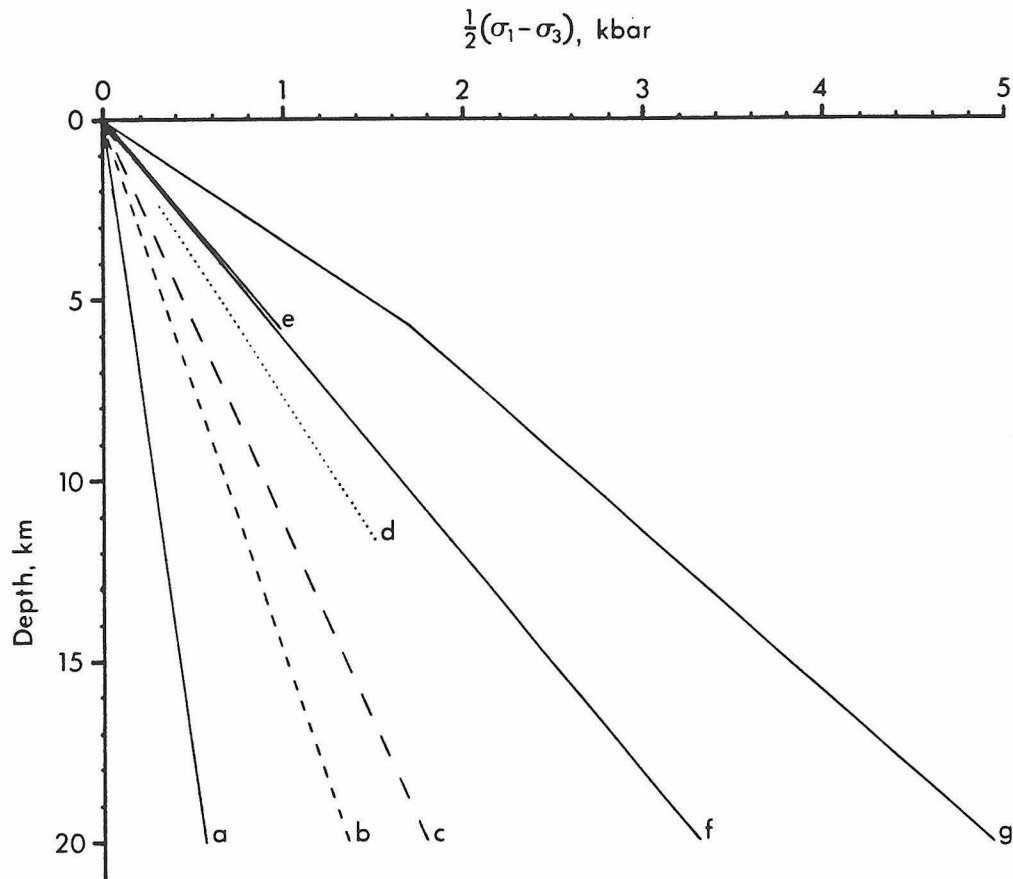


Figure 3.4. Plots of maximum shear stress at failure versus depth. *a*, Eqn. 3.2 with $f = 0.1$ (SJ fault, Cahuilla); *b*, Basin and Range earthquakes; *c*, borehole stress measurements (extrapolated beyond 3 km); *d*, Kola penninsula deep borehole breakouts; *e*, Eqn. 3.2 with $f = 0.85$, $\theta = 65^\circ$ (Cahuilla); *f*, Eqn. 3.2 with $f = 0.60$, $\theta = 35^\circ$ (SJ fault); *g*, rock fracture experiments. See text for references and general values in equation 3.2.

N 55° W and N 25° W, respectively (Chapter 2); thus, $\theta_{SJ} = 35^\circ$ and $\theta_{CAH} = 65^\circ$. Figure 3.4 (*a, e, f*) shows the expected values of τ_{max} at rupture for various depths in the crust in these areas. The depths where earthquakes occur along the San Jacinto fault north of Anza and beneath Cahuilla are indicated. With $f = 0.85, 0.6$ we see that the earthquakes deep on the San Jacinto fault and shallow beneath Cahuilla should occur at very different initial stress levels and at levels much higher than that found for earthquakes in the Basin and Range province or measured in the upper crust near the San Andreas fault. The stress levels are, however, close to those calculated for the crust in the Kola Peninsula. Values of shear stress required for earthquake rupture on the deep San Jacinto fault are near 3 kbar while that in the shallow crust beneath Cahuilla is about 1 kbar or less (high-stress model). With $f = 0.1$ we get average shear stresses of about 250 bar on the fault zone (\approx low-stress model). In this case the variation in the shear stress with depth is much less and earthquakes on the deep San Jacinto fault break at about 400-500 bar and earthquakes below Cahuilla break at less than about 150 bar. Note that low stress levels on faults in the crust can be obtained merely by assuming the low values of f which are found in laboratory studies of clay-rich fault gouge (Chu et al., 1981) and hydrostatic fluid pressures. Super-hydrostatic fluid pressures will also lower the shear strength of the fault, however these may not develop until after fault rupture has initiated.

3.4 Depths of Earthquakes in the San Jacinto Fault Zone

The variation in the depths of earthquakes and seismic slip in the San Jacinto fault zone is shown graphically in fault-parallel cross sections (Figures 3.5 and 3.6). The earthquakes plotted were carefully selected to be only those associated with the major strike-slip faults in the fault zone (Figure 2.3). Two first-order features are apparent in the cross sections. First, the bottom of the seismogenic zone changes in depth along strike and becomes shallower nearer to the Imperial Valley region of high heat flow. Second, earthquakes are generally concentrated in a band along the bottom

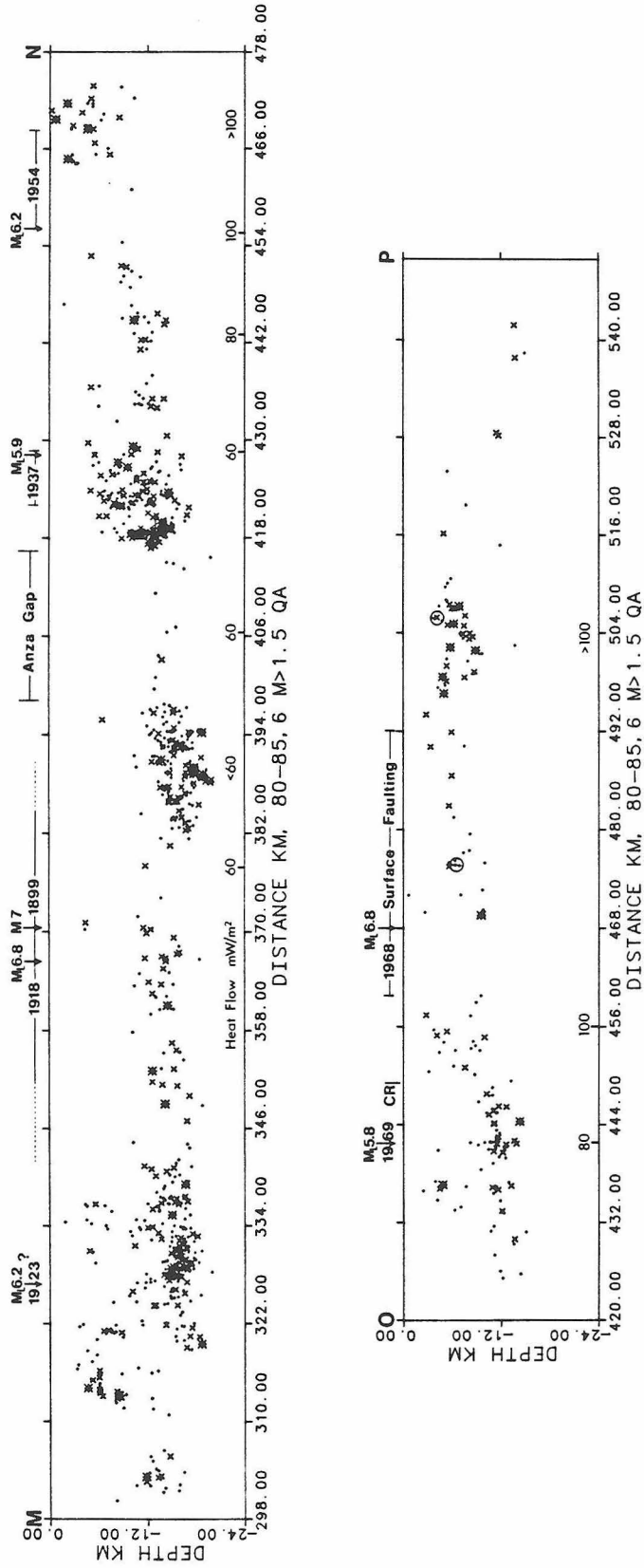


Figure 3.5. Vertical cross sections M-N and O-P along the San Jacinto and Coyote Creek-Superstition Mountain faults. The earthquakes plotted are all $M \geq 1.5$ with quality A locations located in the boxes shown in Figure 2.3 during the time period January 1980 to June 1985. The local heat flow is plotted along the bottom of each cross section (from Lachenbruch et al., 1985) The rupture zones of historic large earthquakes are shown. CR, southeast end of Coyote Ridge. dot, M 1.5-2; x, M 2-3; *, M 3-4; o, M 4-5; star, M 5+.

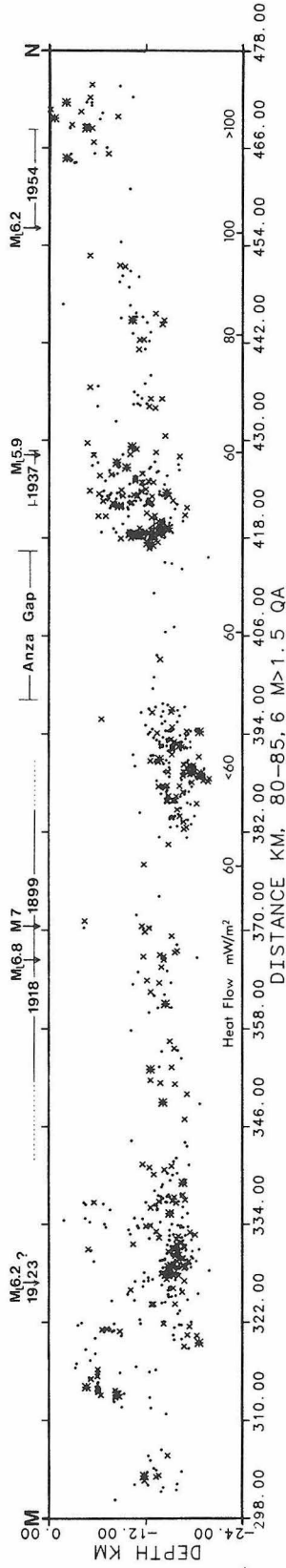
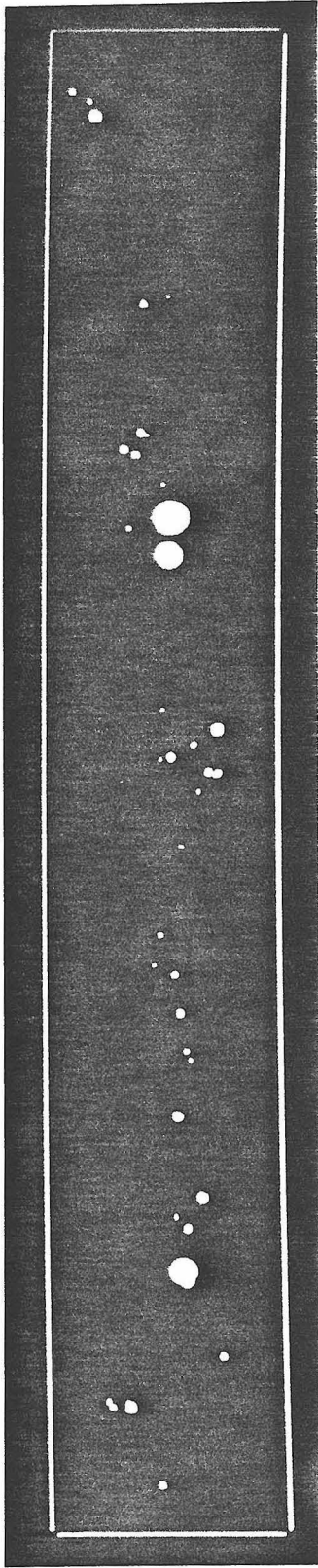


Figure 3.6. Vertical cross section M-N along the San Jacinto fault showing the distribution of cumulative seismic slip with depth for the years 1980-1985,6 (upper plot). For reference the lower plot shows the seismicity along the same fault section (see Figure 3.5). The light areas in the upper plot indicate cumulative seismic slip of greater than 1 cm. The large and larger circular areas near the Anza gap have cumulative slip of greater than 10 and 20 cm, respectively. The radius of the rupture area and the slip during each earthquake ($M \geq 2$) were determined using an empirical relation between M_L and M_o (Archuleta et al., 1982), assuming circular rupture, and assuming average stress drops of 30 bars.

fault. The latter is true whether the base of the seismogenic zone lies at 20 or 10 km depth.

The first observation indicates that the maximum depth of the seismogenic zone along different sections of the San Jacinto fault zone varies by as much as a factor of two from about 20 km near Anza to about 10 km at the southern end of the San Jacinto fault and the southern half of the Coyote Creek fault. This gradual shallowing of the seismicity in the fault zone as it extends southeast from Anza is probably mostly related to the increased heat flow nearer to the Imperial Valley region. This idea was suggested by Given (1983) for earthquakes in the area of the Anza gap and by Doser and Kanamori (1986*a*) for earthquakes along the southern San Jacinto fault zone and in the Imperial Valley. Doser and Kanamori correlated their relocated earthquake depths with the regional heat flow map (Lachenbruch et al., 1985). Sibson (1982) and Meissner and Strehlau (1982) are cited for an explanation of the connection between heat flow and the maximum depth of crustal earthquakes.

Since the seismogenic zone narrows along the San Jacinto fault zone from about 20 km north of Anza to about 10 km at the fault's southeastern end, and since the strength of the fault presumably decreases as it approaches the surface (Figures 3.2 and 3.4), we would expect that the size and stress drop of large earthquakes might also decrease to the southeast as well. Though no information is available on stress drops, we do know that two large earthquakes nucleated where the base of the seismogenic zone is at about 10 km; these are the 1954 M_L 6.2 Arroyo Salada earthquake and the 1968 M_L 6.8 Borrego Mountain earthquake (Chapter 1). Large earthquakes also occurred where the base of the seismogenic zone lies at about 20 km; these are the 1899 M 7 and 1918 M_L 6.8 San Jacinto-Hemet earthquakes. Thus, the varying thickness of the seismogenic zone in the San Jacinto fault zone does not seem to affect the potential for, nor size of, large earthquake rupture along different sections of the fault zone. The stress levels needed to initiate the rupture may be somewhat different, however, and the surface strains observed prior to and after an earthquake may also be different.

The second observation that most earthquakes occur near the base of the seismogenic zone and not above suggests that the deeper parts of the faults are under higher shear stresses than the shallower parts. We discussed earlier that depending on the local heat flow and other factors there is a maximum thickness of the brittle crust within which earthquakes can occur. The shear strength of the brittle crust increases with depth until a maximum is reached below which shear strength falls off rapidly and deformation becomes quasi-plastic (Figure 3.2). With this fault model in mind if the entire fault plane were loaded simultaneously to a given stress level we would expect the weaker, shallow parts of the fault to fail first, and that failure would deepen as stress increased. This is not seen in the data. Earthquakes occur deep on the fault, and aftershocks of larger events tend to rupture upward along the fault plane. Since the deeper parts of the fault zone are strongest and since most of the earthquakes have deep focuses, the shear stress must be greater on the deeper part of the fault to overcome the frictional strength and cause fault rupture. These observations imply that loading of the brittle crust must occur primarily by movement below the crust and that strain is transferred upward (this is also discussed by Meissner and Strehlau, 1982). This is in accord with the fault model discussed earlier which has ductile flow in the upper mantle and lower crust (lower lithosphere) transferred to the brittle upper crust along the deeper parts of faults such as the San Andreas and San Jacinto (Figure 3.3). Displacement is hindered as the strong, shallow part of the fault is encountered, and considerable stress builds up at this boundary between the frictional fault and the quasi-plastic fault. Essentially a screw dislocation exists at this boundary. Since the brittle fault is theoretically at its maximum strength at this boundary it becomes a barrier which effectively inhibits strains and therefore stresses from occurring on the portions of the fault above the boundary. Displacement propagates into the shallower, weaker fault only when a large earthquake occurs at the boundary. This may explain why seismicity is generally absent from the shallow parts of the fault plane.

Consequences of the model just discussed are that we should find that large

earthquakes nucleate near the base of the seismogenic zone and also that precursors to these earthquakes which occur in the fault zone should be deep where stress is the highest (Sibson, 1982; Meissner and Strehlau, 1982). Recent studies indicate that both of these are observed. Sibson (1982) compiled depth information on many large earthquakes in California and found that the main shock usually lies near the bottom of the aftershock zone and near the base of the seismogenic zone. The 1980 M_L 5.5 earthquake which occurred on the San Jacinto fault zone southeast of Anza had a focus near the base of the seismogenic zone there and aftershocks extended about 6 km towards the surface (Figure 2.7). Doser and Kanamori (1986a) found that events on the Imperial fault precursory to the 1979 Imperial Valley earthquake occurred just below the zone of greatest displacement during the event.

3.5 Deep and Shallow Seismicity in the San Jacinto-Southern San Andreas Region

In Figure 3.7 (a) through (e) the $M \geq 1.5$ quality-A hypocenters for the years 1980-1985,6 are plotted on maps of the study area in 4 km-thick depth slices from 0 to 22 km. The principal observation we make from this data is that the shallower seismicity from 0 to about 8 km deep does not occur on the major regional faults while the deeper seismicity from 12 to 22 km is almost entirely along the major San Jacinto fault zone or in the Banning-Mission Creek fault area. The deep stress release occurs almost exclusively along the major fault zones, while shallow stress release occurs predominantly in the adjacent crustal blocks. This data does not include any major earthquakes whose aftershocks would be expected to occur from near the hypocenter of the main shock up along the fault plane to near the surface. The San Andreas fault southeast of the Banning-Mission Creek faults is virtually aseismic at the $M \geq 1.5$ level. Near the San Jacinto and southern San Andreas faults the shallow seismicity occurs principally in clusters located about 10-20 km away from the surface trace of the faults. This distance is similar to the depth of the locked portions of these faults.

of the seismogenic zone with few earthquakes occurring on the shallower parts of the fault. The latter is true whether the base of the seismogenic zone lies at 20 or 10 km depth.

The first observation indicates that the maximum depth of the seismogenic zone along different sections of the San Jacinto fault zone varies by as much as a factor of two from about 20 km near Anza to about 10 km at the southern end of the San Jacinto fault and the southern half of the Coyote Creek fault. This gradual shallowing of the seismicity in the fault zone as it extends southeast from Anza is probably mostly related to the increased heat flow nearer to the Imperial Valley region. This idea was suggested by Given (1983) for earthquakes in the area of the Anza gap and by Doser and Kanamori (1986*a*) for earthquakes along the southern San Jacinto fault zone and in the Imperial Valley. Doser and Kanamori correlated their relocated earthquake depths with the regional heat flow map (Lachenbruch et al., 1985). Sibson (1982) and Meissner and Strehlau (1982) are cited for an explanation of the connection between heat flow and the maximum depth of crustal earthquakes.

Since the seismogenic zone narrows along the San Jacinto fault zone from about 20 km north of Anza to about 10 km at the fault's southeastern end, and since the strength of the fault presumably decreases as it approaches the surface (Figures 3.2 and 3.4), we would expect that the size and stress drop of large earthquakes might also decrease to the southeast as well. Though no information is available on stress drops, we do know that two large earthquakes nucleated where the base of the seismogenic zone is at about 10 km; these are the 1954 M_L 6.2 Arroyo Salada earthquake and the 1968 M_L 6.8 Borrego Mountain earthquake (Chapter 1). Large earthquakes also occurred where the base of the seismogenic zone lies at about 20 km; these are the 1899 M 7 and 1918 M_L 6.8 San Jacinto-Hemet earthquakes. Thus, the varying thickness of the seismogenic zone in the San Jacinto fault zone does not seem to affect the potential for, nor size of, large earthquake rupture along different sections of the fault zone. The stress levels needed to initiate the rupture may be somewhat different, however, and

the surface strains observed prior to and after an earthquake may also be different.

The second observation that most earthquakes occur near the base of the seismogenic zone and not above suggests that the deeper parts of the faults are under higher shear stresses than the shallower parts. We discussed earlier that depending on the local heat flow and other factors there is a maximum thickness of the brittle crust within which earthquakes can occur. The shear strength of the brittle crust increases with depth until a maximum is reached below which shear strength falls off rapidly and deformation becomes quasi-plastic (Figure 3.2). With this fault model in mind if the entire fault plane were loaded simultaneously to a given stress level we would expect the weaker, shallow parts of the fault to fail first, and that failure would deepen as stress increased. This is not seen in the data. Earthquakes occur deep on the fault, and aftershocks of larger events tend to rupture upward along the fault plane. Since the deeper parts of the fault zone are strongest and since most of the earthquakes have deep focuses, the shear stress must be greater on the deeper part of the fault to overcome the frictional strength and cause fault rupture. These observations imply that loading of the brittle crust must occur primarily by movement below the crust and that strain is transferred upward (this is also discussed by Meissner and Strehlau, 1982). This is in accord with the fault model discussed earlier which has ductile flow in the upper mantle and lower crust (lower lithosphere) transferred to the brittle upper crust along the deeper parts of faults such as the San Andreas and San Jacinto (Figure 3.3). Displacement is hindered as the strong, shallow part of the fault is encountered, and considerable stress builds up at this boundary between the frictional fault and the quasi-plastic fault. Essentially a screw dislocation exists at this boundary. Since the brittle fault is theoretically at its maximum strength at this boundary it becomes a barrier which effectively inhibits strains and therefore stresses from occurring on the portions of the fault above the boundary. Displacement propagates into the shallower, weaker fault only when a large earthquake occurs at the boundary. This may explain why seismicity is generally absent from the shallow parts of the fault plane.

Consequences of the model just discussed are that we should find that large earthquakes nucleate near the base of the seismogenic zone and also that precursors to these earthquakes which occur in the fault zone should be deep where stress is the highest (Sibson, 1982; Meissner and Strehlau, 1982). Recent studies indicate that both of these are observed. Sibson (1982) compiled depth information on many large earthquakes in California and found that the main shock usually lies near the bottom of the aftershock zone and near the base of the seismogenic zone. The 1980 M_L 5.5 earthquake which occurred on the San Jacinto fault zone southeast of Anza had a focus near the base of the seismogenic zone there and aftershocks extended about 6 km towards the surface (Figure 2.7). Doser and Kanamori (1986a) found that events on the Imperial fault precursory to the 1979 Imperial Valley earthquake occurred just below the zone of greatest displacement during the event.

3.5 Deep and Shallow Seismicity in the San Jacinto-Southern San Andreas Region

In Figure 3.7 (a) through (e) the $M \geq 1.5$ quality-A hypocenters for the years 1980-1985,6 are plotted on maps of the study area in 4 km-thick depth slices from 0 to 22 km. The principal observation we make from this data is that the shallower seismicity from 0 to about 8 km deep does not occur on the major regional faults while the deeper seismicity from 12 to 22 km is almost entirely along the major San Jacinto fault zone or in the Banning-Mission Creek fault area. The deep stress release occurs almost exclusively along the major fault zones, while shallow stress release occurs predominantly in the adjacent crustal blocks. This data does not include any major earthquakes whose aftershocks would be expected to occur from near the hypocenter of the main shock up along the fault plane to near the surface. The San Andreas fault southeast of the Banning-Mission Creek faults is virtually aseismic at the $M \geq 1.5$ level. Near the San Jacinto and southern San Andreas faults the shallow seismicity occurs principally in clusters located about 10-20 km away from the surface trace of

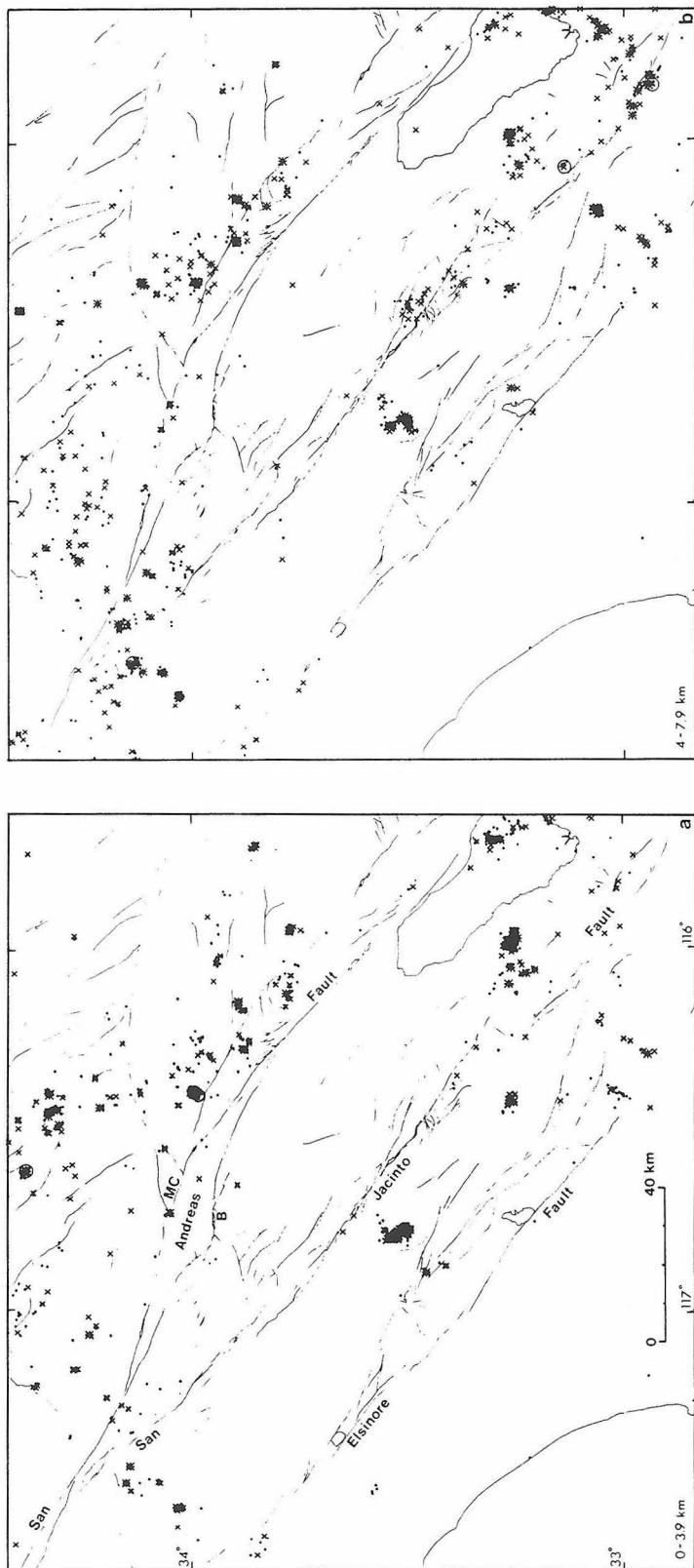
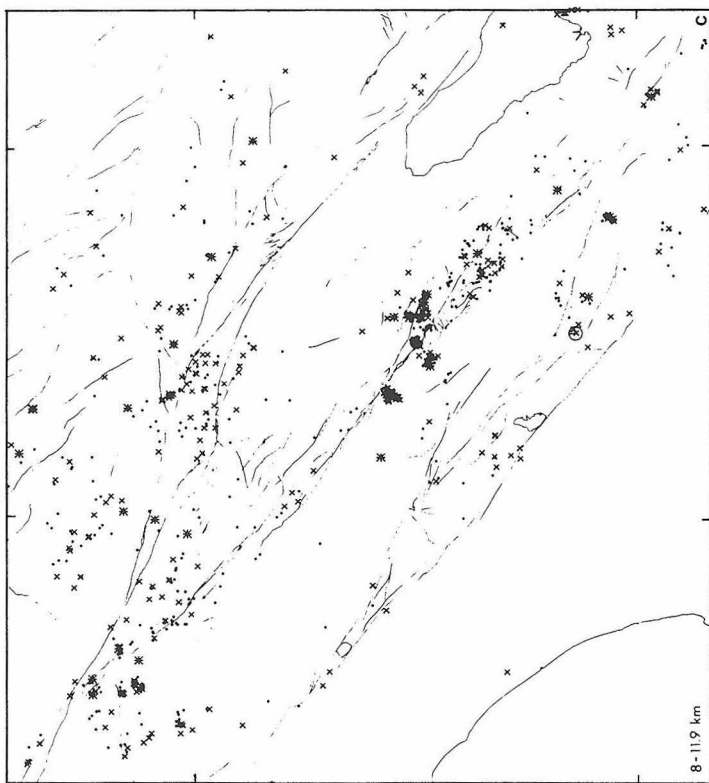
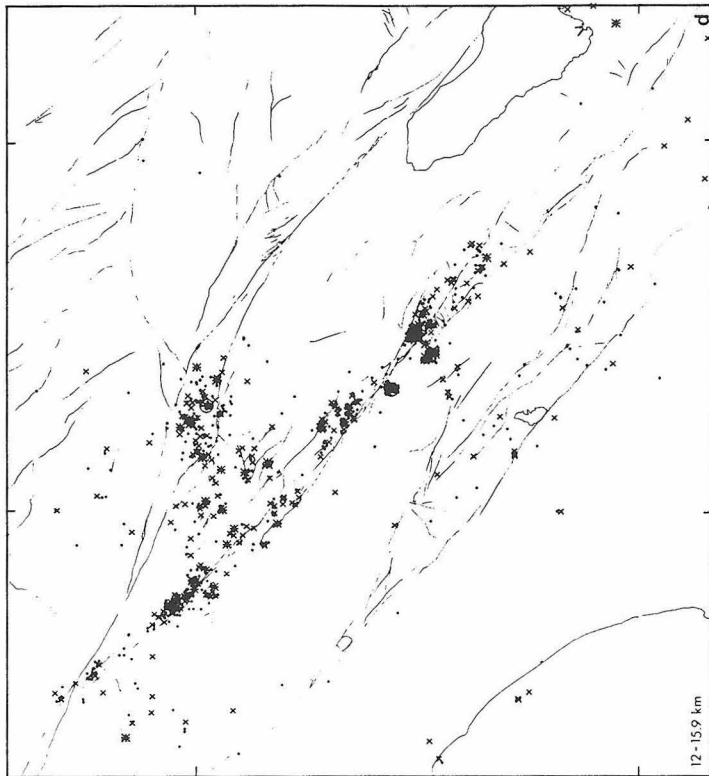
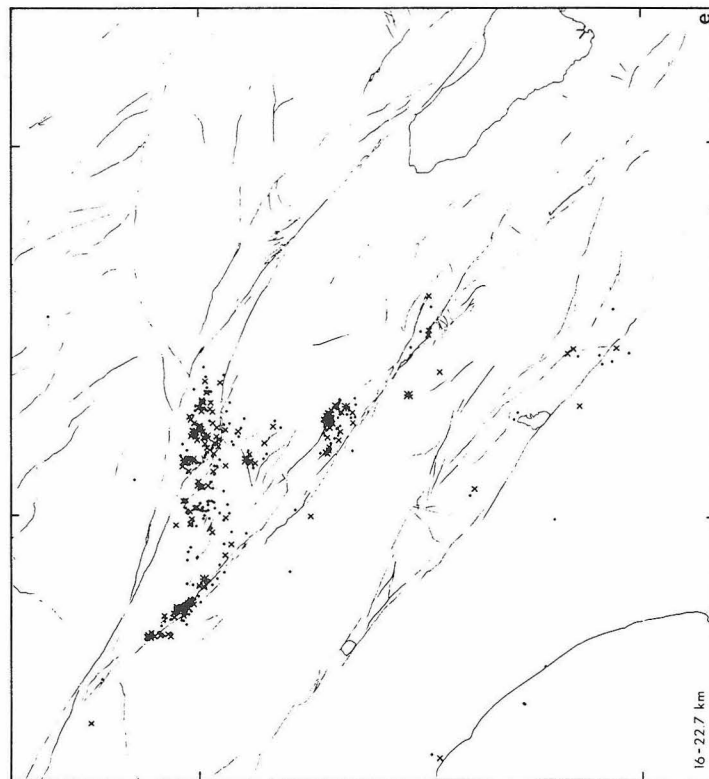
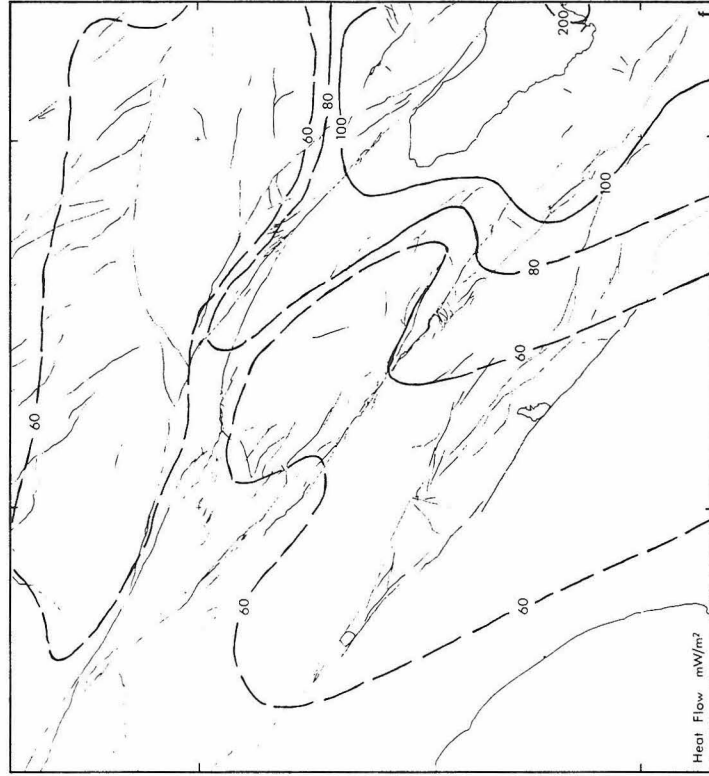


Figure 3.7. Maps of the region containing the San Jacinto and southern San Andreas faults with epicenters of quality-A $M_L \geq 1.5$ earthquakes which occurred during the years 1980-1985,6. The events are grouped into 4 km depth intervals; (a) 0-3.9 km, (b) 4-7.9 km, (c) 8-11.9 km, (d) 12-15.9 km, (e) 16-22.7 km, (f) heat flow (Lachenbruch et al., 1985). small +, M 1.5-2; x, M 2-3; *, M 3-4; o, M 4-5; star, M 5+.





the faults. This distance is similar to the depth of the locked portions of these faults.

As discussed earlier, the maximum depth of earthquakes in an area is thought to be related to a change from brittle to ductile deformation in the middle to lower crust, this change in the style of strain accommodation controlled principally by the local heat flow if other factors are constant (Sibson, 1982; Meissner and Strehlau, 1982). The maps in Figure 3.7 indicate that the predominant depth of seismicity is different by a factor of about 2 to 4 in the crustal blocks adjacent to the major faults compared to the major faults themselves. The broad variations in heat flow in this region (Figure 3.7f) (Lachenbruch et al., 1985) seem to rule out a heat flow origin for these ubiquitous major changes in depth over horizontal distances of less than about 20 km. We will try to understand something about these phenomenon by analyzing the earthquake depth variations near Anza on the San Jacinto fault in more detail.

Depth Variations of Seismicity Near Anza

Figures 3.8 and 3.9 show the variation in depths of earthquakes in the Anza area, from a maximum depth of about 20 km on the San Jacinto fault to a maximum depth of about 6 km beneath Cahuilla in the crustal block 12 km southwest of the fault. The percentage of events (and moment) versus depth plots (Figure 3.9) clearly show the preferential location of seismic displacement at certain depths in the crust. Northwest of Anza earthquakes on the San Jacinto and Hot Springs faults occur almost exclusively between depths of 12 and 20 km with most displacement in the 18-20 km depth range. Southeast of Anza earthquakes of the San Jacinto and Buck Ridge faults are more spread through depth with most events between 6 and 16 km depth and most displacement at 12-14 km depth. In the crust beneath Cahuilla earthquakes occur from 0 to 6 km depth with displacement distributed about evenly with depth. The number of events in each area decreases rapidly beneath the depths of maximum occurrence. Maximum displacement in the fault zone occurs at the base of the seismogenic zone.

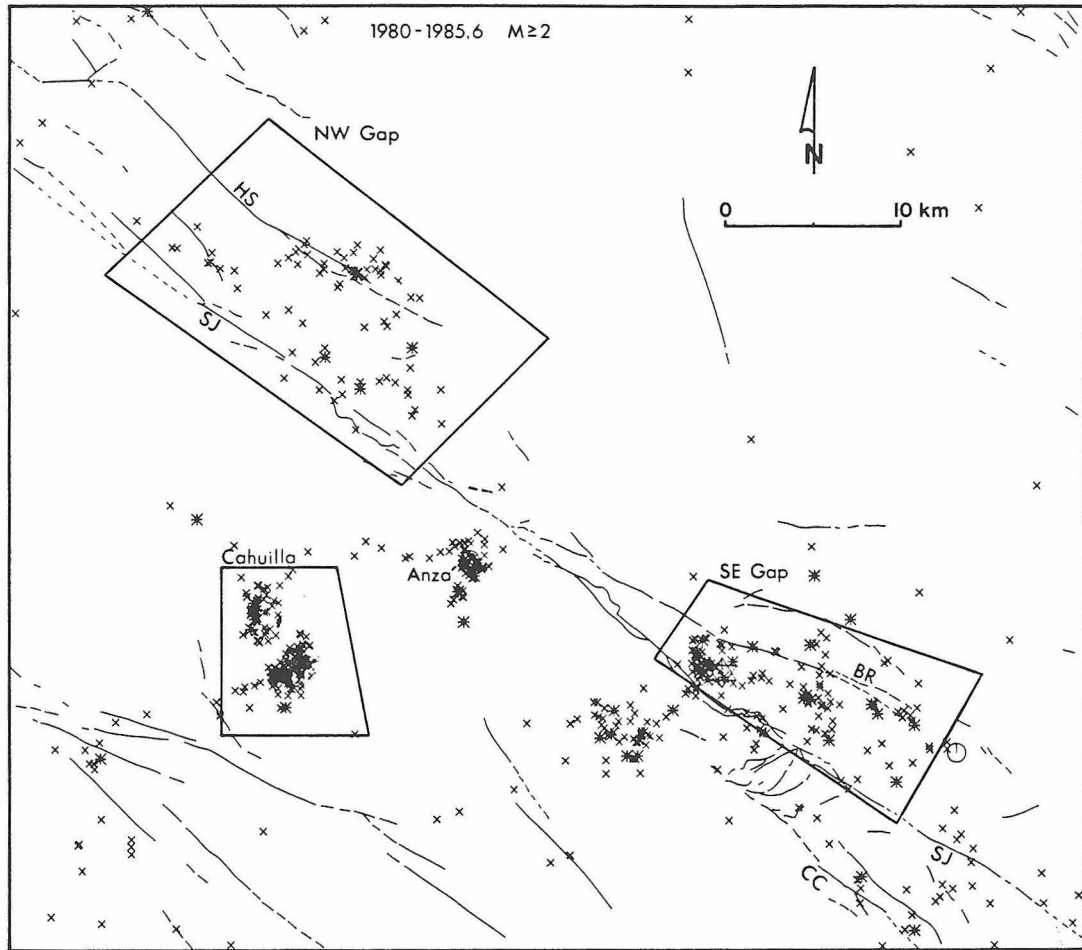


Figure 3.8. Map showing the locations of the areas from which quality-A earthquakes were taken for calculation of depth-frequency plots (Figure 3.9). The earthquakes are all $M \geq 2$ during the years 1980-1985,6. x, $M 2-3$; *, $M 3-4$; o, $M 4-5$; star, $M 5+$.

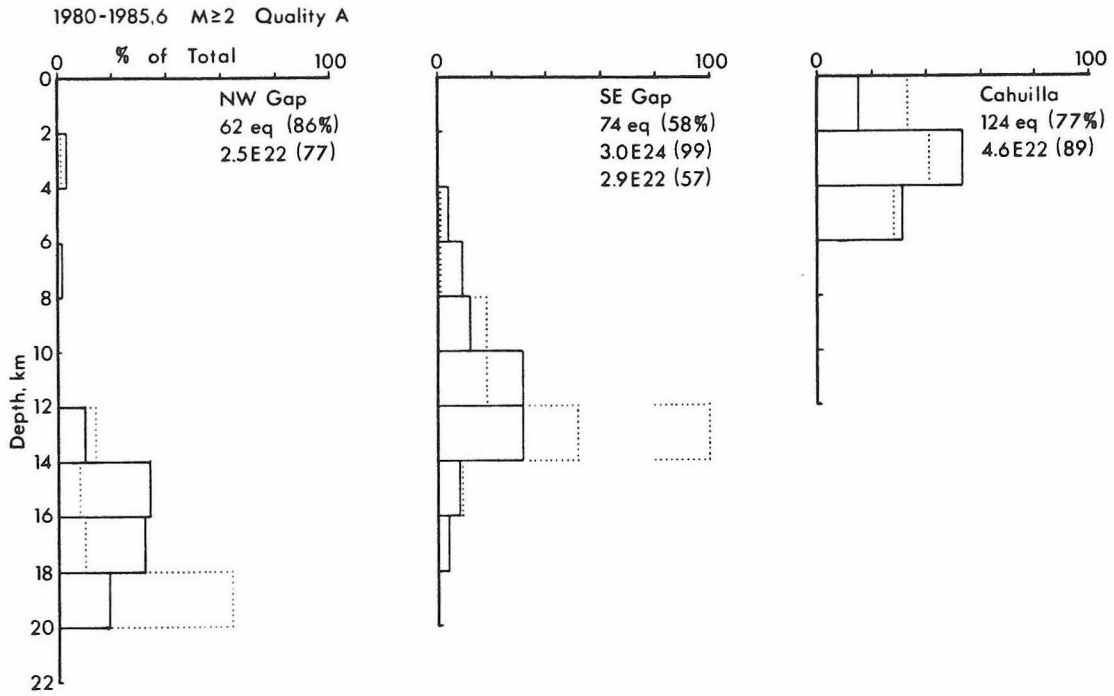


Figure 3.9. Frequency of earthquake occurrence with depth for three areas in the region of Anza on the San Jacinto fault zone (Figure 3.8). The text in the upper right corner of each plot indicate the geographic location, the number of quality-A earthquakes (per cent of all quality earthquakes), and the moment sum of the quality-A events (per cent of total moment from all quality events). In the SE Gap plot two total moment values are given, one including the 1980 M_L 5.5 earthquake and one excluding it.

The maximum depth of earthquakes on the San Jacinto fault zone northwest of Anza (about 20 km) is seemingly well modeled by relations given by Sibson (1982) with heat flow about 60 mW/m^2 , strain rate about 10^{-11} s^{-1} (1 cm/yr slip in a 100 m wide fault zone), $f = 0.75$, and hydrostatic fluid pressures. The maximum depth of earthquakes beneath Cahuilla (6 km), which apparently has similar heat flow (Lee, 1983), is poorly modeled however. Even at strain rates of 10^{-17} s^{-1} the expected thickness of the brittle crust is 10 km (Meissner and Strehlau, 1982).

As discussed earlier, studies of large earthquake stress drops indicate consistently low values for the stress drop (Kanamori and Anderson, 1974; Kanamori, 1980*b*). This also seems to be true for small earthquakes in the Anza area where maximum $\Delta\tau$ is generally less than a couple hundred bars, average $\Delta\tau$ is 10 bar or less, and little difference is seen in average or maximum $\Delta\tau$ with depth or location (Frankel and Kanamori, 1983; Frankel, 1984; Fletcher et al., 1985). Frankel and Kanamori (1983) and Frankel et al. (1985) found up to a factor of 10 variation in stress drops for adjacent events of similar size, indicating that the physical properties of the fault zone or of the shallow crust can locally depart significantly from the average.

We need to explain four observations; first, that deep earthquakes occur only in the fault zone; second, that shallow earthquakes occur in the block adjacent to the fault zone but not in the fault zone; third, that the stress drops of events deep in the fault zone and shallow in the block adjacent to the fault zone are consistently low and similar; and fourth, that earthquakes beneath Cahuilla occur almost exclusively above a depth of 6 km, even though heat flow models indicate that the crust there is brittle to a depth of at least 10 km. What do these observations indicate? We can propose some explanations below.

The first observation indicates that the deep brittle fault zone is weaker than the deep brittle crust in general and/or that stresses are higher in the deep fault zone. Both possibilities seem likely in view of the large displacement on the fault zone (24 km; Sharp, 1967), which would not have occurred had the fault zone not been weaker

than the surrounding crust, and in view of the model of deep strain transfer presented earlier.

The second observation seems to indicate either that the stress is similar throughout the shallow crust but that the fractured area beneath Cahuilla is weaker than the shallow fault zone, or that the shallow crust beneath Cahuilla is experiencing higher stresses than the shallow fault zone. The first possibility seems unlikely, since the shallow San Jacinto fault (which has experienced about 24 km of displacement) should have well-developed gouge and be as weak as, if not weaker than, small fractures beneath Cahuilla. The second possibility is more likely. As was discussed in the previous section (3.4), it appears that stress levels on the shallow, brittle fault zone are much lower than on the deep, brittle fault zone; somehow higher stress levels can exist in the shallow crust away from the fault zone, possibly enhanced by local stress concentrations (Kanamori, 1972).

Referring to Figure 3.4 we can describe two ways to explain the third observation that the stress drops of events in the two areas are consistently low and similar. One possibility is that the San Jacinto fault zone has strength similar to relation a , and is much weaker than the fractures beneath Cahuilla, which have strength similar to relation b . Another possibility is that the strength of both earthquake areas is described by a relation similar to a . In either case the rupture stress would be similar on the deep fault zone and in the shallow crust. It seems unlikely that the strength of the fault zone is similar to relation f given the many mechanisms possible which would encourage complete stress release during large earthquake rupture (Sibson, 1977: Kanamori, 1980*b*).

A possible explanation for the fourth observation is that given a strength versus depth relation similar to b in Figure 3.4 the stress level in the crust near Cahuilla is such that only the weaker fractures above 6 km are loaded to failure. This situation is likely since the fractures beneath Cahuilla probably do not root in the lower crust as the major fault zones do and, thus, loading of the fractures would occur from the sides

as well as from beneath. The shallower, weaker fractures would tend to rupture first as the ambient stress in the crust increased.

These explanations presented for the four observations suggest a scenario such as the following: The brittle fault zone has strength similar to relation *a* in Figure 3.4, and the surrounding crust has strength similar to relation *b*, that is the strength of the deep fault is similar to the strength of the shallow crust. The strength maximum (barrier) in the deep, brittle fault controls the tectonic strain propagating from the lower lithosphere. This barrier inhibits the propagation of strain to the shallow fault zone, though significant strains do develop in the crust adjacent to the fault. As the stress level increases in the deep fault zone it also increases in the surrounding crust. The strength of the fault zone and the crust are such that only deep in the brittle fault zone and shallow in the adjacent crust do the stresses exceed the strength of the fractures.

This scenario of strain accumulation on and near the San Jacinto fault is simple and major features in the observed seismicity are consistent with it. The observation of deep earthquakes on the fault zone and shallow earthquakes in the nearby crust is not unique to the San Jacinto fault as is seen in Figure 3.7. This suggests that similar scenarios might exist throughout the study area. These ideas are preliminary and further studies may add considerably to the data.

3.6 Conclusions

The primary purpose of this study is to present new observations about the depths of earthquakes associated with the major strike-slip faults in southern California. Some explanations are also suggested. The seismicity in the San Jacinto fault zone shallows from a maximum of about 20 km deep near Anza to a maximum of about 10 km deep near the Imperial Valley. This is most likely due to the increased heat flow nearer to the Imperial Valley region (Doser and Kanamori, 1986). The concentration of earthquakes in a band along the bottom of the seismogenic San Jacinto fault zone and

the absence of earthquakes in the shallow fault zone indicate that high stresses are present at the bottom of the brittle fault zone and that stresses are much less on the shallower fault zone. This is evidence that loading of the brittle crust occurs primarily from below along deeper extensions of the fault zones.

If the observation window is broadened to include the crust adjacent to the fault zones several other features of the depths of earthquakes become apparent. In general deep earthquakes occur only in the major fault zones, while shallow earthquakes occur only in the adjacent crustal blocks. Explanations for these observations, and for other observations about earthquakes in the Anza area of the San Jacinto fault in particular, are less conclusive, though simple scenarios can be imagined. The principal unanswered question is how stresses can be smaller than the rupture stress in the shallow fault zone and greater than the rupture stress in the adjacent shallow crust.

3.7 References for Part I

- Agnew, D. C. and K. E. Sieh, A documentary study of the felt effects of the great California earthquake of 1857, *Bull. Seis. Soc. Am.*, 68(6), 1717-1729, 1978.
- Allen, C. R., and J. M. Nordquist, Foreshock, main shock, and larger aftershocks of the Borrego Mountain earthquake, *U.S. Geol. Surv. Prof. Pap.*, 787, 16-23, 1972.
- Anderson, E. M., The dynamics of faulting, Oliver and Boyd, London, 1951.
- Arabasz, W. J., J. N. Brune, and G. R. Engen, Locations of small earthquakes near the trifurcation of the San Jacinto fault southeast of Anza, California, *Bull. Seis. Soc. Am.*, 60(2), 617-627, 1970.
- Archuleta, R. J., E. Cranswick, C. Mueller, and P. Spudich, Source parameters of the 1980 Mammoth Lakes, California, earthquake sequence, *J. Geophys. Res.*, 87, 4595-4608, 1982.
- Bartholomew, M. J., San Jacinto fault zone in the northern Imperial Valley, California, *Geol. Soc. Am. Bull.*, 81, 3161-3166, 1970.
- Brune, J. N., Seismic moment, seismicity, and rate of slip along major fault zones, *J. Geophys. Res.*, 73, 777-784, 1968.
- Burdick, L. J. and G. R. Mellman, Inversion of the body waves from the Borrego Mountain earthquake to the source mechanism, *Bull. Seis. Soc. Am.*, 66(5), 1485-1499, 1976.
- Burford, R. O., Continued slip on the Coyote Creek fault after the Borrego Mountain earthquake, *U.S. Geol. Surv. Prof. Pap.*, 787, 105-111, 1972.
- Burford, R. O., and P. W. Harsh, Slip on the San Andreas fault in central California from alignment array surveys, *Bull. Seis. Soc. Am.*, 70(4), 1233-1261, 1980.
- Byerlee, J., Friction of rocks, *Pageoph*, 116, 615-626, 1978.
- Chinnery, M. A., The stress changes that accompany strike-slip faulting, *Bull. Seis. Soc. Am.*, 53(5), 921-932, 1963.
- Chu, C. L., C. Y. Wang, and W. Lin, Permeability and frictional properties of San Andreas fault gouges, *Geophys. Res. Lett.*, 8(6), 565-568, 1981.
- Claypole, E. W., The earthquake at San Jacinto, December 25, 1899, *Am. Geol.*, 25, 106-108, 1900.
- Corbett, E. J., Seismicity and crustal structure studies of southern California: tectonic implications from improved earthquake locations, *Ph.D. Thesis, California Institute of Technology, Pasadena*, 1984.
- Corbett, E. J., and K. C. McNally, Changes in stress indicated by "preshocks" to the 1968 Borrego Mountain earthquake (abs.), *Eos*, 59(12), 1127, 1978.
- Danes, J. V., Das Erdbeben von San Jacinto am 25. Dezember 1899, *Mitt. Geogr. Ges. Wein*, 6-7, 339-347, 1907.
- Das, S., and C. H. Scholz, Off-fault aftershock clusters caused by shear stress increase, *Bull. Seis. Soc. Am.*, 71(5), 1669-1675, 1981.
- Das, S., and C. H. Scholz, Why large earthquakes do not nucleate at shallow depths, *Nature*, 305, 621-623, 1983.
- Davis, T., and E. Duebendorfer, Surficial structure and geomorphology of the San Andreas fault, western portion of the Big Bend, in, *Neotectonics in Southern California*, 79-106, Geological Society of America, Boulder, Colo., 1982.
- Doser, D. I. and H. Kanamori, Depth of seismicity in the Imperial Valley region (1977-1983) and its relationship to heat flow, crustal structure, and the October 15, 1979, earthquake, *J.*

- Geophys. Res.*, 91(B1), 675-688, 1986a.
- Doser, D. I. and H. Kanamori, Spatial and temporal variations in seismicity in the Imperial Valley (1902-1984), *Bull. Seis. Soc. Am.*, 76(2), 421-438, 1986b.
- Ebel, J. E., and D. V. Helmberger, P-wave complexity and fault asperities, The Borrego Mountain California earthquake of 1968, *Bull. Seis. Soc. Am.*, 72(2), 413-437, 1982.
- Evison, F. F., The precursory earthquake swarm, *Phys. Earth Planet. Inter.*, 15, 19-23, 1977.
- Fletcher, J., L. Harr, T. Hanks, F. Vernon, J. Berger, and J. Brune, The digital array at Anza, CA: processing and initial interpretation of source parameters, 5th Ewing Symposium on Earthquake Source Mechanics, Harriman, N.Y., 1985.
- Frankel, A., Source parameters of two $M_L \approx 5$ earthquakes near Anza, California, and a comparison with an Imperial Valley aftershock, *Bull. Seis. Soc. Am.*, 74(5), 1509-1527, 1984.
- Frankel, A. and H. Kanamori, Determination of rupture duration and stress drop for earthquakes in southern California, *Bull. Seis. Soc. Am.*, 73(6), 1527-1551, 1983.
- Frankel, A., J. Fletcher, F. Vernon, L. Haar, T. Hanks, J. Berger, and J. Brune, Observations of stress drop variation and rupture complexity for $M_L \approx 3$ earthquakes near Anza, California (abs.), *Eos*, 66(46), 954, 1985.
- Given, D. D., Seismicity and structure of the trifurcation in the San Jacinto fault zone, southern California, *Masters Thesis, California State University, Los Angeles*, 1983.
- Green, S. M., Seismotectonic study of the San Andreas, Mission Creek, and Banning fault system, *Masters Thesis, University of California, Los Angeles*, 1983.
- Gutenberg, B., Earthquakes and structure in southern California, *Geol. Soc. Am. Bull.*, 54, 499-526, 1943.
- Hadley, D. M., Geophysical investigation of the structure and tectonics of southern California, *Ph.D. Thesis, California Institute of Technology, Pasadena*, 1978.
- Hadley, D. and H. Kanamori, Seismic structure of the Transverse Ranges, California, *Geol. Soc. Am. Bull.*, 88, 1469-1478, 1977.
- Hamilton, R. M., Aftershocks of the Borrego Mountain earthquake from April 12 to June 12, 1968, *U.S. Geol. Surv. Prof. Pap.*, 787, 31-54, 1972.
- Hanks, T. C., J. A. Hileman, and W. Thatcher, Seismic moments of the larger earthquakes of the southern California region, *Geol. Soc. Am. Bull.*, 86, 1131-1139, 1975.
- Hanks, T. C. and M. Wyss, The use of body-wave spectra in the determination of seismic source parameters, *Bull. Seis. Soc. Am.*, 62(2), 561-589, 1972.
- Hartzell, S., and J. N. Brune, The Horse Canyon earthquake of August 2, 1975 - Two-stage stress-release process in a strike-slip earthquake, *Bull. Seis. Soc. Am.*, 69(4), 1161-1173, 1979.
- Heaton, T. H. and D. V. Helmberger, A study of the strong ground motion of the Borrego Mountain, California earthquake, *Bull. Seis. Soc. Am.*, 67(2), 315-330, 1977.
- Hileman, J. A., C. R. Allen, and J. M. Nordquist, Seismicity of the southern California region 1 January 1932 to 31 December 1972, *Seismological Laboratory, California Institute of Technology*, 1973.
- Hill, R. I., Geology of Garner Valley and vicinity, in *Geology of the San Jacinto Mountains, Field Trip Guideb. 9*, edited by A. R. Brown and R. W. Ruff, South Coast Geological Society, Irvine, Calif., pp. 90-99, 1981.
- Hill, R. I., Petrology and petrogenesis of batholithic rocks, San Jacinto Mountains, southern California, *Ph.D. Thesis, California Institute of Technology, Pasadena*, 1984.
- Hubbert, M. K. and W. W. Rubey, Role of fluid pressure in mechanics of overthrust faulting,

- Bull. Geol. Soc. Am.*, 70, 115-166, 1959.
- Jaeger, J. C. and N. G. Cook, Fundamentals of rock mechanics, Chapman and Hall, London, 1979.
- Johnson, C. E., CEDAR — an approach to the computer automation of short-period local seismic networks, *Ph.D. Thesis, Calif. Inst. Tech.*, Pasadena, 332 p., 1979.
- Kadinsky-Cade, K., and R. J. Willemann, Towards understanding aftershock patterns, the basic pattern for strike-slip earthquakes (abs.), *Eos*, 63(18), 384, 1982.
- Kanamori, H., Relation between tectonic stress, great earthquakes, and earthquake swarms, *Tectonophysics*, 14, 1-12, 1972.
- Kanamori, H., California Institute of Technology Final Technical Report, October 1, 1975 to September 30, 1976, U. S. Geol. Surv. Contract 14-08-001-15254, 1976.
- Kanamori, H., Seismicity and earthquake prediction examples in southern California, in *Proceedings of the Earthquake Prediction Research Symposium*, Seismological Society of Japan, Tokyo, 1980a.
- Kanamori, H., The state of stress in the Earth's lithosphere, *Physics of the Earth's Interior*, Soc. Italiana di Fisica, Bologna, 1980b.
- Kanamori, H., The nature of seismicity patterns before large earthquakes, in *Earthquake Prediction, An International Review, Maurice Ewing Ser., v. 4*, edited by D. W. Simpson and P. G. Richards, pp. 1-19, AGU, Washington, D. C., 1981.
- Kanamori, H. and D. L. Anderson, Theoretical basis of some empirical relations in seismology, *Bull. Seis. Soc. Am.*, 65, 1073-1095, 1975.
- Kanamori, H. and D. Hadley, Crustal structure and temporal velocity change in southern California, *Pageoph*, 113, 257-280, 1975.
- Kanamori, H., and P. C. Jennings, Determination of local magnitude, M_L , from strong-motion accelerograms, *Bull. Seis. Soc. Am.*, 68(2), 471-485, 1978.
- Keller, R. P., C. R. Allen, R. Gilman, N. R. Goulety, and J. A. Hileman, Monitoring slip along major faults in southern California, *Bull. Seis. Soc. Am.*, 68(4), 1187-1190, 1978.
- King, N. E., and J. C. Savage, Strain rate profile across the Elsinore, San Jacinto, and San Andreas faults near Palm Springs, California, 1973-1981, *Geophys. Res. Lett.*, 10(1), 55-57, 1983.
- Kostrov, B. V., and S. Das, Idealized models of fault behavior prior to dynamic rupture, *Bull. Seis. Soc. Am.*, 72(3), 679-703, 1982.
- Lachenbruch, A. H., J. H. Sass, and S. P. Galanis, Jr., Heat flow in southernmost California and the origin of the Salton Trough, *J. Geophys. Res.*, 90(B8), 6709-6736, 1985.
- Laughlin, H., R. Arnold, and W. S. W. Kew, Southern California earthquake of July 22, 1923, *Bull. Seis. Soc. Am.*, 13(3), 105-106, 1923.
- Lee, T.-C., Heat flow through the San Jacinto fault zone, southern California, *Geophys. J. R. astr. Soc.*, 72, 721-731, 1983.
- Lisowski, M., and W. H. Prescott, Short-range distance measurements along the San Andreas fault system in central California, 1975 to 1979, *Bull. Seis. Soc. Am.*, 71(5), 1607-1624, 1981.
- Louie, J. N., C. R. Allen, D. C. Johnson, P. C. Haase, and S. N. Cohn, Fault slip in southern California, *Bull. Seis. Soc. Am.*, 75(3), 811-833, 1985.
- McEvelly, T. V., W. H. Bakun, and K. B. Casady, The Parkfield, California, earthquakes of 1966, *Bull. Seis. Soc. Am.*, 57(6), 1221-1244, 1967.
- McGarr, A. and N. C. Gay, State of stress in the Earth's crust, *Ann. Res. Earth Planet. Sci.*, 6,

- 405-436, 1978.
- McGarr, A., M. D. Zoback, and T. C. Hanks, Implications of an elastic analysis of in situ stress measurements near the San Andreas fault, *J. Geophys. Res.*, 87(B9), 7797-7806, 1982.
- Meissner, R., and J. Strehlau, Limits of stresses in continental crusts and their relation to the depth-frequency distribution of shallow earthquakes, *Tectonics*, 1(1), 73-89, 1982.
- Minster, J. B. and T. H. Jordan, Present-day plate motions, *J. Geophys. Res.*, 83, 5331-5354, 1978.
- Morrow, C., L. Q. Shi, and J. Byerlee, Permeability and strength of San Andreas fault gouge under high pressure, *Geophys. Res. Lett.*, 8(4), 325-328, 1981.
- Niewiadomski, J., and A. R. Ritsema, The stress field induced by cracks and the occurrence of earthquakes, *Proc. K. Ned. Akad. Wet. Ser. B*, 83(4), 361-377, 1980.
- Palmer, A. H., California earthquakes during 1916, *Bull. Seis. Soc. Am.*, 7(1), 1-17, 1917.
- Palmer, A. H., California earthquakes during 1917, *Bull. Seis. Soc. Am.*, 8(1), 1-12, 1918.
- Palmer, A. H., California earthquakes during 1918, *Bull. Seis. Soc. Am.*, 9(1), 1-7, 1919.
- Pechmann, J. C., The relationship of small earthquakes to strain accumulation along major faults in southern California, *Ph.D. Thesis, California Institute of Technology*, Pasadena, 1983.
- Prescott, W. H., J. C. Savage, and W. T. Kinoshita, Strain accumulation rates in the western United States between 1970 and 1978, *J. Geophys. Res.*, 84(B10), 5423-5435, 1979.
- Rasmussen, G. S., Nature of surface rupture and recurrence interval, Casa Loma fault, in *Geology of the San Jacinto Mountains, Field Trip Guideb. 9*, edited by A. R. Brown and R. W. Ruff, pp. 48-54, South Coast Geological Society, Irvine, Calif., 1981.
- Richter, C. F., *Elementary Seismology*, 768 pp., W. H. Freeman, San Francisco, Calif., 1958.
- Richter, C. F., C. R. Allen, and J. M. Nordquist, The Desert Hot Springs earthquakes and their tectonic environment, *Bull. Seis. Soc. Am.*, 48, 315-337, 1958.
- Rogers, T. H., Geologic map of California, San Bernardino 1:250,000 sheet, Calif. Div. of Mines and Geol., Sacramento, 1967.
- Rolfe, F., and A. M. Strong, The earthquake of April 21, 1918 in the San Jacinto mountains, *Bull. Seis. Soc. Am.*, 8(2-3), 63-67, 1918.
- Sanders, C. O., and H. Kanamori, Seismicity patterns near the Anza seismic gap (abs.), AGU Chapman Conference on Fault Behavior and the Earthquake Generation Process, Snowbird, Utah, 1982.
- Sanders, C. O. and H. Kanamori, A seismotectonic analysis of the Anza seismic gap, San Jacinto fault zone, southern California, *J. Geophys. Res.*, 89(B7), 5873-5890, 1984.
- Sanders, C., K. McNally, and H. Kanamori, The state of stress near the Anza Seismic Gap, San Jacinto fault zone, southern California, in *Geology of the San Jacinto Mountains, Field Trip Guideb. 9*, edited by A. R. Brown and R. W. Ruff, pp. 61-67, South Coast Geological Society, Irvine, Calif., 1981.
- Sanders, C., H. Magistrale, and H. Kanamori, Rupture patterns and pre-shocks of large earthquakes in the southern San Jacinto fault zone, *Bull. Seis. Soc. Am.*, 76(5), 1187-1206, 1986.
- Savage, J. C. and R. O. Burford, Geodetic determination of relative plate motion in central California, *J. Geophys. Res.*, 78(5), 832-845, 1973.
- Savage, J. C., and W. H. Prescott, Strain accumulation on the San Jacinto fault near Riverside, California, *Bull. Seis. Soc. Am.*, 66(5), 1749-1754, 1976.

- Savage, J. C., W. H. Prescott, M. Lisowski, and N. King, Deformation across the Salton Trough, California, 1973-1977, *J. Geophys. Res.*, 84(B6), 3069-3079, 1979.
- Savage, J. C., W. H. Prescott, M. Lisowski, and N. King, Strain accumulation in southern California, 1973-1980, *J. Geophys. Res.*, 86(B8), 6991-7001, 1981.
- Savage, J. C., W. H. Prescott, and G. Gu, Strain accumulation in southern California, 1973-1984, *J. Geophys. Res.*, 91(B7), 7455-7473, 1986.
- Sharp, R. V., San Jacinto fault zone in the Peninsular Ranges of southern California, *Geol. Soc. Am. Bull.*, 78, 705-730, 1967.
- Sharp, R. V., Map of recently active breaks along the San Jacinto fault zone between the San Bernardino area and Borrego Valley, California, *U.S. Geol. Surv. Misc. Geol. Invest. Map, I-675*, 1972.
- Sharp, R. V., En echelon fault patterns of the San Jacinto fault zone, in *San Andreas Fault in Southern California*, edited by J. C. Crowell, *Spec. Rep. Calif. Div. Mines Geol.*, 118, 147-154, 1975.
- Sharp, R. V., Variable rates of Late Quaternary strike-slip on the San Jacinto fault zone, southern California, *J. Geophys. Res.*, 86(B3), 1754-1762, 1981.
- Sibson, R. H., Kinetic shear resistance, fluid pressures and radiation efficiency during seismic faulting, *Pageoph*, 115, 388-400, 1977.
- Sibson, R. H., Fault zone models, heat flow, and the depth distribution of earthquakes in the continental crust of the United States, *Bull. Seis. Soc. Am.*, 72(1), 151-163, 1982.
- Sibson, R. H., Roughness at the base of the seismogenic zone: contributing factors, *J. Geophys. Res.*, 89(B7), 5791-5799, 1984.
- Sibson, R. H., Earthquakes and rock deformation in crustal fault zones, *Ann. Rev. Earth Planet. Sci.*, 14, 149-175, 1986.
- Sieh, K. E., Slip along the San Andreas fault associated with the great 1857 earthquake, *Bull. Seis. Soc. Am.*, 68(5), 1421-1448, 1978.
- Sieh, K. E., and R. H. Jahns, Holocene activity of the San Andreas fault at Wallace Creek, California, *Geol. Soc. Am. Bull.*, 95, 883-896, 1984.
- Slemmons, D. B., Faults and earthquake magnitude, *Misc. Pap. S-73-I*, 166 pp., Chief of Eng., U.S. Army, Washington, D. C., 1977.
- Stein, R. S., and M. Lisowski, The 1979 Homestead Valley earthquake sequence, California: control of aftershocks and postseismic deformation, *J. Geophys. Res.*, 88(B8), 6477-6490, 1983.
- Tajima, F. and H. Kanamori, Aftershock area expansion and mechanical heterogeneity of fault zone within subduction zones, *Geophys. Res. Lett.*, 12, 345-348, 1985.
- Thatcher, W., and R. M. Hamilton, Aftershocks and source characteristics of the 1969 Coyote Mountain earthquake, San Jacinto fault zone, California, *Bull. Seis. Soc. Am.*, 63(3), 647-661, 1973.
- Thatcher, W. and T. C. Hanks, Source parameters of southern California earthquakes, *J. Geophys. Res.*, 78(35), 8547-8576, 1973.
- Thatcher, W., J. A. Hileman, and T. C. Hanks, Seismic slip distribution along the San Jacinto fault zone, southern California and its implications, *Geol. Soc. Am. Bull.*, 86, 1140-1146, 1975.
- Topozada, T. R., C. B. Real, and D. L. Parke, Preparation of isoseismal maps and summaries of reported effects for pre-1900 California earthquakes, *Open File Rep. 81-11 SAC*, Calif. Div. Mines and Geol., Sacramento, 1981.
- Topozada, T. R., and C. R. Parke, Areas damaged by California earthquakes 1900-1949, *Open*

- File Rep. 82-17 SAC*, Calif. Div. Mines and Geol., Sacramento, 1982.
- Townley, S. D., The San Jacinto earthquake of April 21, 1918, *Bull. Seis. Soc. Am.*, 8(2-3), 44-62, 1918.
- Townley, S. D., and M. W. Allen, Earthquakes in California, 1769 to 1928, *Bull. Seis. Soc. Am.*, 29, 1-258, 1939.
- Turcotte, D. L. and D. A. Spence, An analysis of strain accumulation on a strike slip fault, *J. Geophys. Res.*, 79(29), 4407-4412, 1974.
- Vetter, U. R. and A. S. Ryall, Systematic change of focal mechanism with depth in the western Great Basin, *J. Geophys. Res.*, 88(B10), 8237-8250, 1983.
- Weldon, R. J., and K. E. Sieh, Holocene rate of slip and tentative recurrence interval for large earthquakes on the San Andreas fault in Cajon Pass, southern California, *Geol. Soc. Am. Bull.*, 96, 793-812, 1985.
- Wood, H. O., The Terwilliger Valley earthquake of March 25, 1937, *Bull. Seis. Soc. Am.*, 27, 305-312, 1937.
- Zoback, M. D. and L. Mastin, Implications of wellbore breakouts for the state of stress at mid-crustal depths in the Kola Peninsula ultradeep borehole (abs.), *Eos*, 67(16), 382, 1986.

**Part II: Imaging the Shallow Crust in Volcanic Areas with
Earthquake Shear Waves**

Chapter 4

Anomalous S-Wave Attenuation in the Coso Region, California

4.1 Introduction

The utility of S-wave seismograms for imaging the crust and upper mantle in volcanic/geothermal areas has been shown in studies of S-wave attenuation in several regions of the world including Kamchatka, USSR (Gorshkov, 1956; Fedotov and Faberov, 1966), Mount Katmai, Alaska (Kubota and Berg, 1967; Matumoto, 1971), Iceland (Einarsson, 1978), New Zealand (Latter, 1981), Long Valley, California, (Ryall and Ryall, 1981; Sanders, 1984), and Imperial Valley, California (P. Ho-Liu, pers. comm., 1985). These studies used S-wave attenuation data from seismograms of local and/or distant earthquakes recorded on local seismic arrays and employed back projection in order to map the S-wave attenuation anomalies in the regions.

In this study we use a technique similar to Sanders (1984) to explore the shallow crust in the region of the Coso geothermal field in eastern California (Figure 4.1). The Coso-southern Sierra Nevada area has hundreds of small earthquakes each year, and the CIT-USGS southern California seismic array is unusually dense in that area. Thus, we have a data set consisting of earthquake rays which have traveled through the local crust from many different azimuths and with varying take-off angles. We first visually examine the S-wave seismograms to map the areas of strong S-wave attenuation. Although the crustal structure in the region varies laterally, we think we are able to place constraints on the location of large anomalies to within a few kilometers. We also invert the attenuation data using a tomographic inversion scheme and compare the results with the forward model. Comparison is also made with a tomographic inversion for P-wave velocity variations (Walck and Clayton, 1986).

Our preliminary results were reported by Sanders, Rinn, and Kanamori (1984). D. Rinn assisted in data acquisition and interpretation during the summer of 1984. The

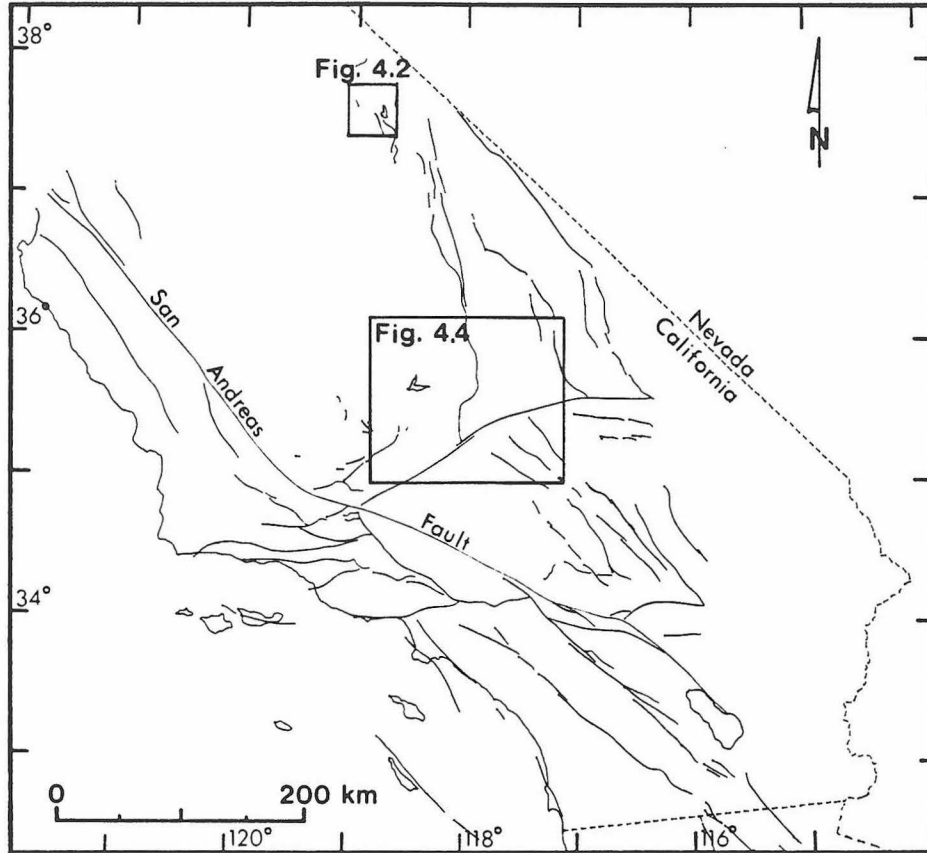


Figure 4.1. Map of southern California showing major faults and the location of the Coso and Long Valley study areas.

results presented herein will be published in Sanders, Rinn, Ho-Liu, and Kanamori (1986 or 1987). P. Ho-Liu is primarily responsible for the tomographic inversion of the S-wave attenuation data.

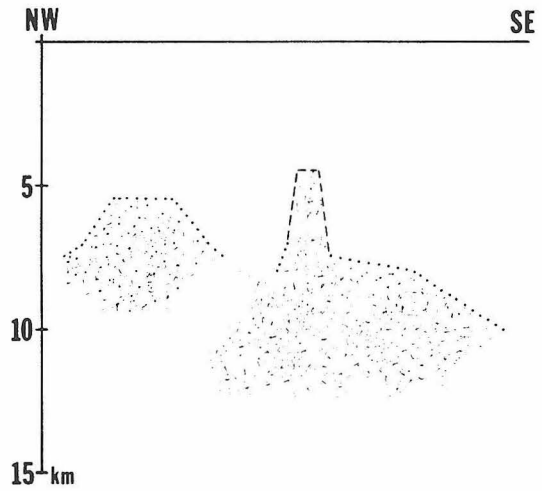
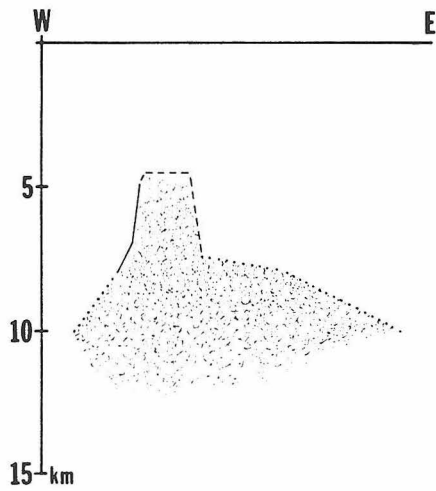
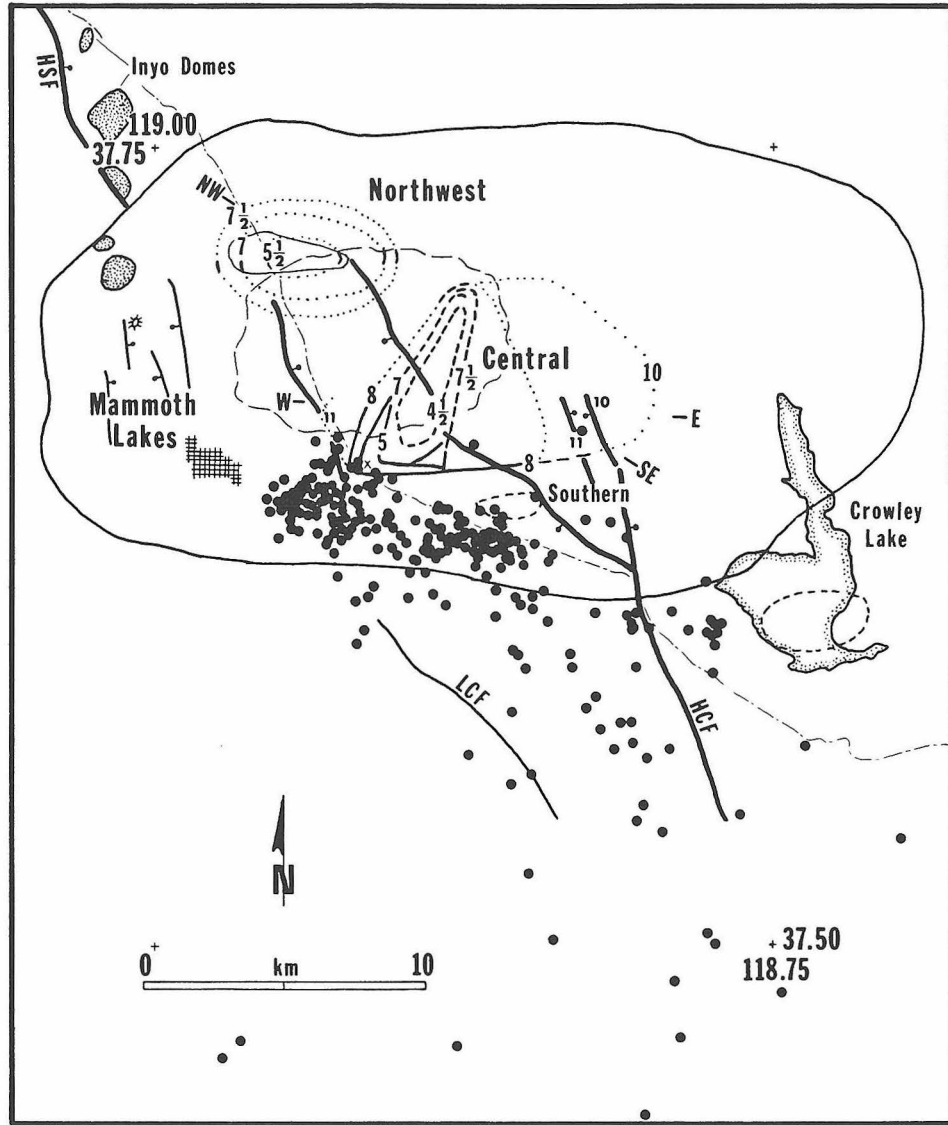
Because of the motivation provided by the S-wave attenuation studies of Long Valley caldera, we will summarize them below.

4.2 Long Valley Caldera, California

Intensive study of earthquakes in Long Valley caldera began following the series of four M 6+ earthquakes which occurred near the southern rim of the caldera in May 1980 (Cramer and Toppozada, 1980). Aftershocks of these large events were numerous, and additional local seismographs were soon installed to record the ground motions. During routine analysis of the aftershock seismograms for arrival times and first motions Ryall and Ryall (1981) noticed that many of the seismograms had diminished S-wave amplitudes and were deficient in high frequency P- and S-wave arrivals. They compiled the event locations and ray paths for some of the anomalous signals and determined that a region in the south central caldera deeper than about 7-8 km was responsible for the filtering effects. The selective filtering of S waves suggested that the rays were traveling through a body of molten rock.

The Long Valley caldera is an ideal place to study seismic wave transmission through an area of active volcanism. The numerous aftershocks of the 1980 earthquake, which continue today at a reduced rate, are spread over about 15-20 km of the southern caldera rim and extend from near the surface to about 14 km in depth (Figure 4.2). These small earthquakes provide P- and S-wave energy which traverses most parts of the caldera. The local seismograph coverage is relatively dense providing good hypocentral locations, and the regional seismograph coverage is good at the northerly and easterly azimuths (Figure 4.3). Sanders and Ryall (1983) and Sanders (1984) used vertical component analog data principally from the regional seismograph stations ($\Delta = 10-100$ km) to map variations in S-wave attenuation in the Long Valley caldera.

Figure 4.2. (a) Map of Long Valley caldera showing epicenters of the earthquakes used in the study by Sanders (1984), the locations of the central and northwest magma bodies and the southern and Crowley Lake anomalous areas, and related geological features. The earthquake epicenters are indicated by solid dots. The northwest and central caldera magma bodies are outlined at various depth intervals indicated by the large numbers. The smaller numbers near the central body show the shallowest depth at which attenuation is actually "seen" in those areas. The solid lines indicate well-located boundaries. The dashed contours are more interpretive; the dotted contours are the most interpretive. The cross in the SW corner of the central body marks the location of Casa Diablo Hot Springs. The surface projections of the areas of anomalous crust in the southern caldera and beneath Crowley Lake are represented by dashed outlines. Major faults in and near the caldera are drawn with heavy lines, and the area of the resurgent dome is outlined by long, thin dashes. HCF, Hilton Creek Fault; LCF, Laurel-Convict Fault; HSF, Hartley Springs Fault. The late-Holocene Inyo Domes and craters (last active about 700 years ago) are shown in the northwest caldera. The thin, solid line in the northwest caldera encloses the approximate area of the deep "magma roof" reflection seen by Hill (1976). The location of U.S. Highway 395 is indicated by the line of long and short dashes running diagonally across the map. (b) West-east cross section through the central magma body. (c) Northwest-southeast cross section through the northwest and central magma bodies.



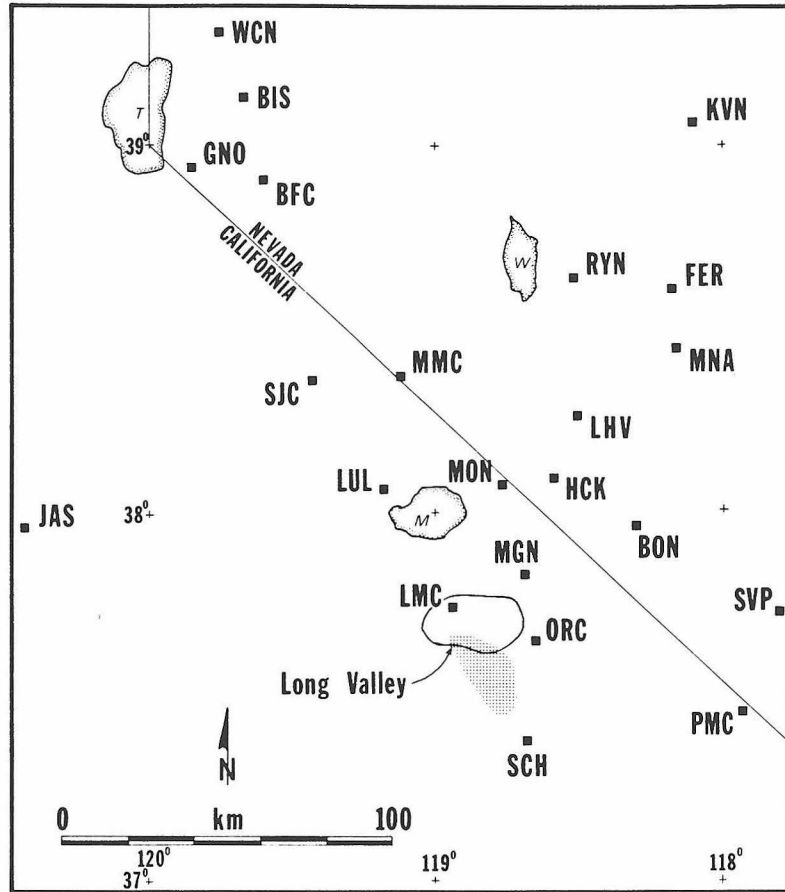


Figure 4.3. Map of western Nevada and eastern California showing the locations of seismicograph stations which recorded the Long Valley earthquake signals. Long Valley caldera is outlined and labeled, and the epicentral area of the earthquakes used is shaded. The three lakes shown are from north to south Tahoe, Walker, and Mono.

Using back projection and noting the geometry of anomalous ray intersections and normal ray paths they were able to map bodies in the caldera which severely attenuate S-waves. These anomalies cover an area of about 10 by 20 km and extend from about 5 km to greater than 13 km depth (Figure 4.2). The density of ray coverage allowed some boundaries to be sharply defined. The S-wave seismograms used to define these anomalies were graded from 0 to 3 depending on the qualitative degree of attenuation of the S-wave signal, with 0 assigned to seismograms with normal S-wave amplitudes and 3 assigned to seismograms with very attenuated S-wave amplitudes. Classifications 2 and 1 corresponded to intermediate attenuations. It was determined from focal mechanism analysis that source radiation effects were not responsible for the large relative differences in S-wave amplitude.

The anomalies in Long Valley caldera are coincident with many geological and geophysical anomalies in the caldera (Sanders, 1984). Geologically the S-wave attenuation anomalies lie beneath the resurgent dome of the caldera which formed due to reinjection of magma into the shallow crust following the massive caldera-forming eruption 720,000 years ago (Bailey et al., 1976). This part of the caldera is also the site of intermittent volcanism which has occurred since the initial caldera forming eruption and as recently as about 600 years ago (Bailey et al., 1976; Wood, 1977; Miller, 1985). Numerous hot springs and fumeroles are located near the southern resurgent dome (Lachenbruch et al., 1976). Geophysical anomalies associated spatially with the S-wave attenuation bodies include teleseismic P-wave travel-time delays (Steeple and Iyer, 1976), local earthquake P-wave travel-time delays (Kissling and Ellsworth, 1984), and uplift of the surface of the central caldera indicating inflation of shallow magma chambers (Savage and Clark, 1982; Rundle and Whitcomb, 1984).

The Long Valley studies show the usefulness of local earthquakes and local and regional seismic arrays for detailed investigation of the shallow crust in volcanic/geothermal regions. Also the correlation between the various geological and geophysical anomalies indicates that they probably are related to the same

phenomenon.

4.3 Coso Seismogram Analysis

The technique we employ is simple. Seismic waves from small earthquakes in the Coso-southern Sierra Nevada region are recorded by the vertical component seismograph network operating in the area. The resulting seismograms are stored on magnetic tape and paper records archived at the Seismological Laboratory of the California Institute of Technology. We examined the records of many of these earthquakes and chose sixteen for detailed analysis. These sixteen were selected based on magnitude (the earthquakes are recorded at most of the local stations and the signals are not clipped), epicentral location (azimuthal coverage of 360° is obtained), depth (earthquake depths range from 3 to 14 km), and location quality (all are quality A or B locations, Hutton et al., 1985). Each earthquake was recorded at dozens of stations of the CIT-USGS southern California seismic array, but we limited our detailed analysis to those records corresponding to travel paths through the area of interest and to stations whose first arrival was P_g (Figure 4.4). This amounted to 10 to 30 seismograms (average 20) per event which gave a total of 330 rays through the area. For each event the seismograms were visually examined for P- and S-wave amplitudes and each was given an index number (AN) corresponding to the degree of S-wave attenuation. Most of the seismograms had *normal* (AN-0) appearing S waves, while some appeared *somewhat attenuated* (AN-1, AN-2) and a few were *very attenuated* (AN-3). Examples of these qualitative ratings are shown in seismograms from two earthquakes on Figure 4.5. In Figure 4.5*b* the *attenuated* ray paths from one earthquake occur within a small azimuthal range and are bounded by *normal* rays at other azimuths. In Figure 4.5*c* the *attenuated* ray path is bounded by normal rays at different take off angles but along a similar azimuth. They indicate that S waves are attenuated when the rays travel through a localized region in the crust. P-wave first motion focal mechanisms for all of the earthquakes studied indicate that the low S-wave amplitudes cannot be explained

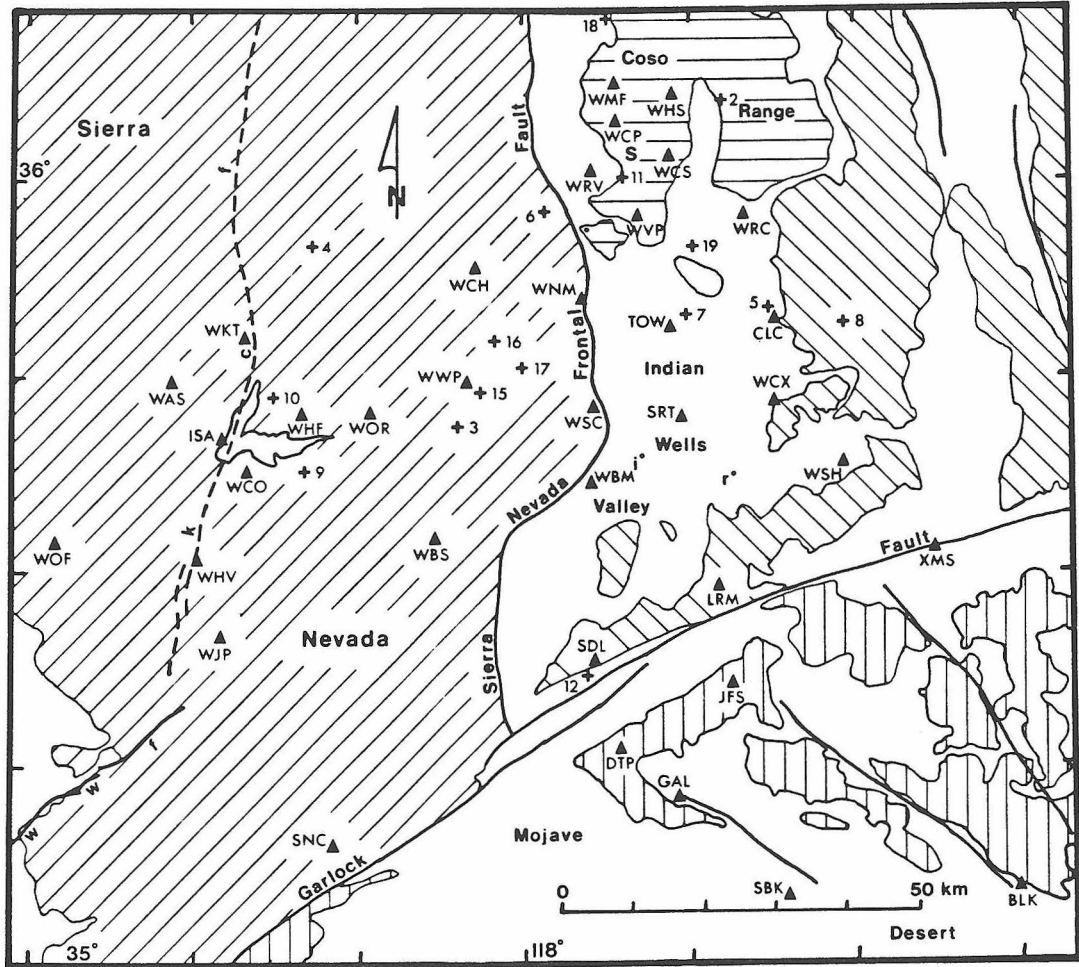


Figure 4.4. Tectonic map of the Coso-southern Sierra Nevada region. Major faults are labeled and bedrock outcrops in the crustal blocks are indicated by shading. Station locations and earthquake epicenters used in this study are plotted. S, Sugarloaf Mountain; i, Inyokern; r, Ridgecrest; wwf, White Wolf fault; kcf, Kern Canyon fault.

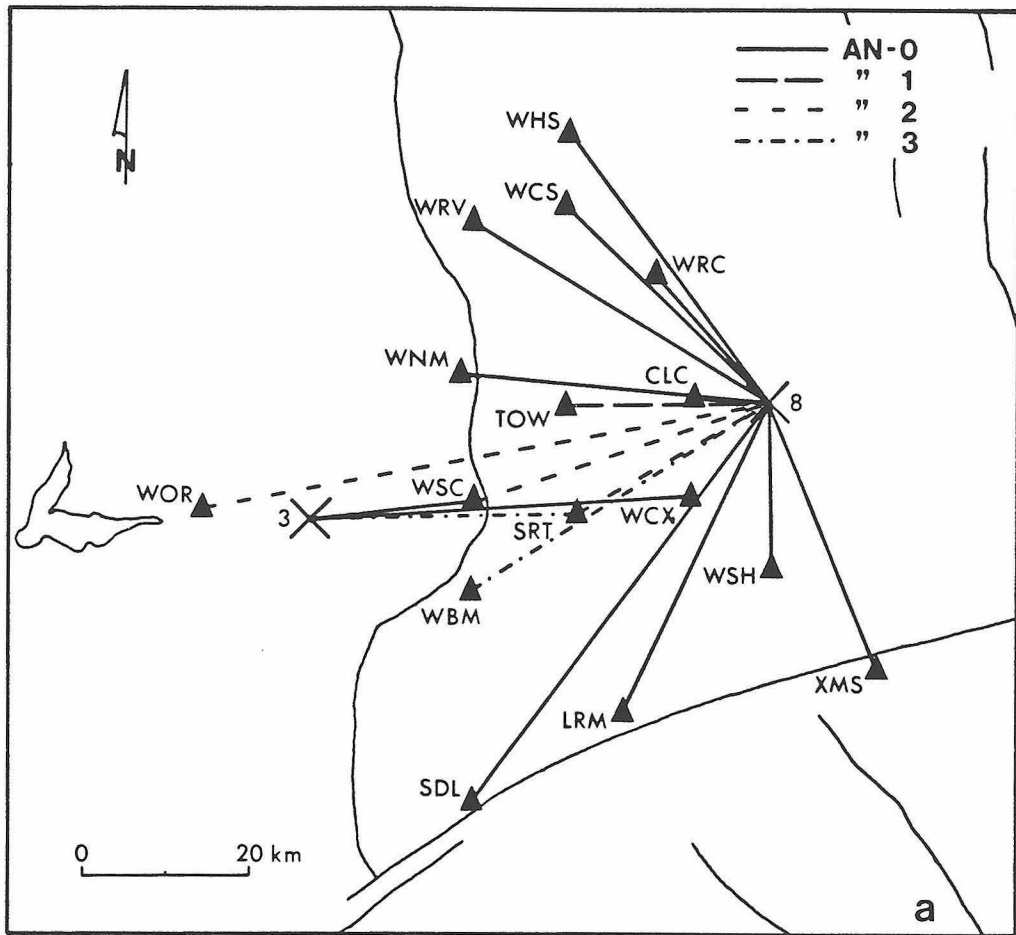
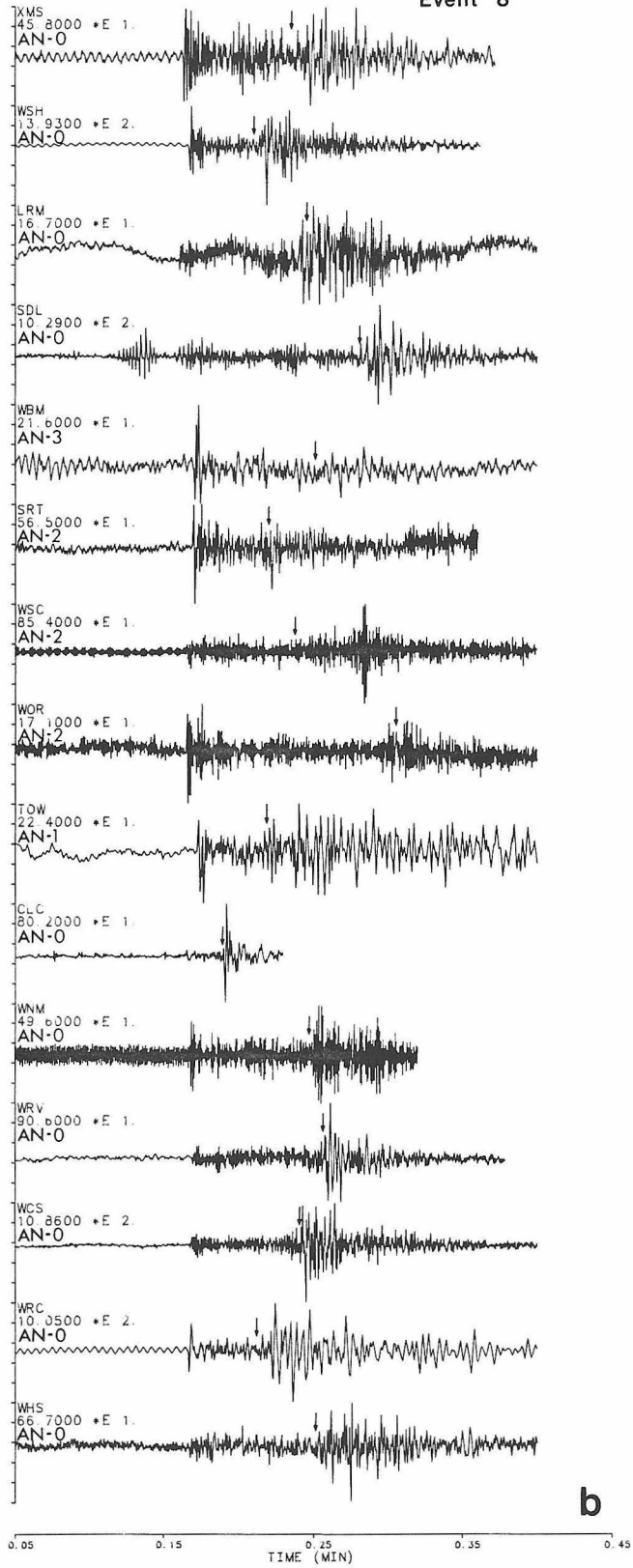
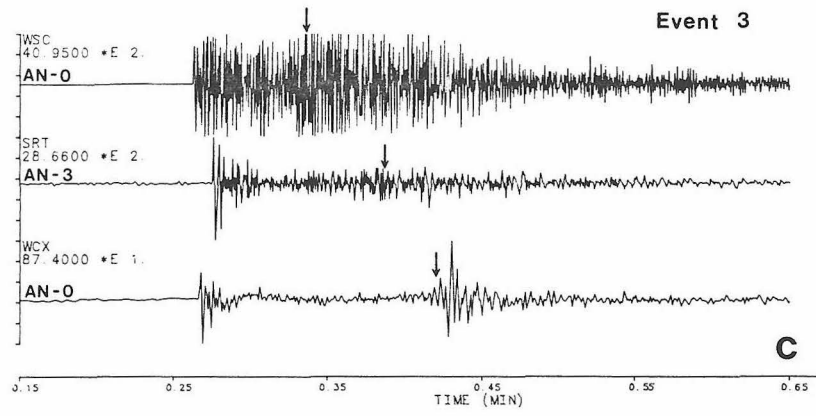


Figure 4.5. (a) Map of ray paths from events 3 and 8. These events illustrate the localized nature of the S-wave attenuation anomalies. (b) Seismograms from event 8. On each seismogram the expected S-wave arrival is marked by an arrow, and the qualitative attenuation number (AN) is indicated. Note the low S-wave amplitudes at stations WBM, SRT, WSC, and WOR, which are in a particular azimuthal range from the event. (c) Seismograms from event 3. Note the low S-wave amplitude at station SRT compared to stations WSC and WCX. These stations lie on nearly the same azimuth from the event but at different takeoff angles. These ray paths can be seen in cross section on Figure 4.7e.

Event 8



b



by source radiation effects.

The qualitative assessment of attenuation was quantified by measuring on each record the maximum peak-to-peak P- and S-wave amplitudes (within about one half second of their expected arrival times) (Table 4.1). Table 4.2 shows the relation between the qualitative attenuation numbers and the S-wave/P-wave amplitude ratios (A_S/A_P). The *very attenuated* S waves (AN-3) have average A_S/A_P of 0.33, whereas the *somewhat attenuated* S waves (AN-2, AN-1) have average A_S/A_P of 0.52 and 0.72. The *normal* seismograms (AN-0) have average A_S/A_P of 2.11. There is some overlap in the range of A_S/A_P values of the seismograms assigned different attenuation numbers, but this is partly due to individual subjective judgement based on other factors of the S-wave seismogram such as presence of later S-wave arrivals, ragged appearance, or quality of the recording. This indicates that our qualitative determination of the relative degree of attenuation is also supported by amplitude measurements.

By combining the ray paths from all sixteen earthquakes and noting the geometry of anomalous and normal rays we are able to determine the approximate areas of the crust which are causing the anomalous S-wave attenuation.

4.4 Earthquake Locations

Before proceeding with detailed back-projection of the data we relocated all of the earthquakes studied in order to obtain precise hypocentral parameters, especially depth. The crustal velocity structure in this region is heterogeneous with the Sierra Nevada, Coso, and Mojave geologic provinces juxtaposed. A single crustal velocity model is not adequate for locating earthquakes which span the three provinces with stations which also span the three provinces. To partially avoid the problem of crustal heterogeneity we relocated each event using the velocity model of the province within which the event lies and stations closer than 60 km and also within or very near the edge of the province. Hopefully the P waves used to locate the earthquakes have ray-paths predominantly in a single crustal province. The velocity models used are shown

TABLE 4.1. Ray Attenuation Numbers and A_s/A_p Ratios

Station	Event																		
	2	3	4	5	6	7	8	9	10	11	12	15	16	17	18	19			
BLK	0-1.26	0-2.22	0-0.62	0-5.14	0-1.47	0-16.50	0-4.0				0-2.18	0-6.14	0-1.21		0-6.00	0-1.95			
CLC	0-0.63	0-2.16		0-1.73	0-3.44	0-1.88		0-1.71				0-1.22	0-1.18		0-1.88	0-0.95			
DTP	0-1.67		0-13.33	0-1.97				0-1.27	0-4.52	0-1.45				0-1.18					
ISA	0-3.26			0-1.76	0-2.63	0-6.60		0-1.33	0-3.52	0-0.98									
JFS		0-1.20	0-0.93	0-0.66	0-1.40	0-2.45	0-3.52	0-1.33	0-3.52	0-0.98	0-1.15		2-0.46	0-1.71	0-1.45	0-1.72			
LRM	3-0.34			0-1.14	0-3.23	1-0.57	0-2.0									0-0.89			
SBK	3-0.23			0-1.14	0-3.23	2-0.36	0-2.0	2-0.62											
SDL	0-1.33			0-1.14	0-3.23	3-0.32													
SNC			0-1.07											0-0.83					
SRT	3-0.47	3-0.33	3-0.30	0-1.88	0-0.95		2-0.61	3-0.44	3-0.29	3-0.45	3-0.33		3-0.43	1-0.87	3-0.37	0-0.94			
TOW	2-0.68	1-0.75	3-0.34	0-1.48	0-0.82		1-0.93	2-0.36	1-0.84	2-0.39	3-0.17		0-1.22	0-1.12	0-1.62				
WAS			0-1.20	0-1.37	0-2.13			0-1.22					0-1.53	0-4.13	0-2.65	1-0.67			
WBM	0-1.30	1-0.60	3-0.40	0-1.15	0-1.00	1-0.52	3-0.19	0-1.10	2-0.47	1-0.72	0-2.08		0-0.72	0-1.47	1-0.54	1-1.02			
WBS	0-6.40	0-1.02	0-0.80	0-2.43	0-1.72	0-0.82		0-1.96			0-1.38	0-3.33	0-1.06	0-2.55	0-0.95	0-5.42			
WCH	0-2.05	0-0.93	0-1.74	0-6.39	0-1.72			0-6.50	0-2.50						0-1.27	0-0.96			
WCO	0-2.09	0-0.93	0-1.23	0-1.63															
WCP		0-3.12	0-1.0	0-1.17				0-1.14	0-1.12			0-1.86	0-1.0	0-1.0	0-1.0				
WCS		0-3.51	0-0.70	0-4.40			0-4.12	0-2.53	0-0.80			0-5.86	0-1.05	0-1.19	0-1.13				
WCX	2-0.47	0-1.34	3-0.33	0-1.85	3-0.24	0-1.18		1-0.82	3-0.36	0-1.69	0-4.71	3-0.38	1-0.64	2-0.44	0-2.73	0-1.22			
WHF	0-1.42	0-0.97	0-1.38	0-0.88		0-1.14							0-1.97	0-1.0	0-1.08	1-0.67			
WHS		0-6.25	0-0.84	0-0.88	0-1.34	0-1.15	0-3.79	0-3.47			3-0.26		0-3.43	0-0.98	0-1.45	0-1.19			
WHV	0-3.89	0-2.50	0-6.50	0-4.38	0-3.84			0-2.03					0-0.97	0-1.29	0-1.59	0-1.38			
WJP	0-2.77		0-1.96	0-2.00	0-4.69	0-1.17		0-1.07				0-3.00	0-0.97	0-1.29	0-1.25	0-6.00			
WKT	0-2.54	0-1.61	0-1.80	1-0.55		0-5.45			0-1.10	0-1.10		1-0.63	0-1.17	1-0.72	0-4.25	1-0.68			
WMT		0-6.25	0-0.68	0-4.11	0-1.24	0-1.09		0-1.98	0-1.00	0-1.29			0-0.97	1-0.63	0-4.25	1-0.68			
WNM	0-1.94		1-0.54	1-0.65			0-1.44	0-1.70	1-0.54	0-1.80	0-0.89	0-1.97	0-1.57	0-1.88	0-3.78	0-1.89			
WOF								0-0.98											
WOR	0-3.27		0-0.87	0-1.69	0-1.39	0-1.16	2-0.59				0-2.36		0-1.34	0-2.49	0-3.04	0-2.25			
WRC		0-1.71	1-0.48	1-0.64	0-1.08	0-1.28	0-1.67	0-1.96	2-0.39			0-1.69	0-1.34	0-1.0	0-0.85	0-1.96			
WRV			1-0.73	0-1.30			0-4.82	0-3.89				0-1.26	0-0.96	0-1.0	0-4.50	0-1.16			
WSC	0-2.92	0-1.22	0-0.87	0-2.19		0-0.97	2-0.69	0-1.00	0-0.99		1-0.67		0-1.0	2-0.71	0-1.00	0-1.00			
WSH	0-0.83	0-1.02	3-0.37	0-1.28	3-0.50	2-0.62	0-1.16	0-1.23	0-2.63	1-0.68	0-2.07		0-1.0	2-0.39	0-2.32	0-2.66			
WVP			1-1.0	0-1.0				0-1.56	0-1.09		3-0.25	0-1.52		0-1.0	0-1.18	0-1.38			
WWP			0-0.87	0-0.84	0-1.79			0-1.10			0-4.03			0-1.0	0-2.74	0-3.54			
XMS	0-1.31	0-1.09	3-0.26	1-0.92	1-0.76	1-0.78	0-0.99			0-2.08			3-0.32	3-0.25	0-1.95	0-2.08			

A_s/A_p = ratio peak-to-peak S-wave amplitude to P-wave amplitude

TABLE 4.2. Attenuation Number - A_s/A_p Statistics

Attenuation Number	0	1	2	3
Number of Seismograms	254	32	17	27
Average A_s/A_p	2.11	0.72	0.52	0.33
σ	1.78	0.16	0.12	0.08
max. A_s/A_p	16.50	1.23	0.71	0.50
min. A_s/A_p	0.62	0.48	0.36	0.17

in Table 4.3 and the earthquake locations in Table 4.4.

4.5 Results

The data used in this study are sufficient to resolve some of the details of the attenuation structure beneath the Indian Wells Valley-Coso region. The 330 rays from the selected earthquakes indicate large variations in S-wave attenuation in the area and that certain small areas of the shallow crust are responsible for the high attenuation. The size and number of anomalies we image are approximate due to the sparse data set.

The interpretation of the ray data is made more difficult by the laterally varying crustal structure in the Indian Wells Valley-Coso-Sierra region. Two major faults, the Sierra Nevada frontal fault and the Garlock fault, separate crustal blocks in this area. The two principal crustal blocks are the Sierra and Coso-Indian Wells Valley blocks, and most of the rays in this study traverse parts of both. The idealized P-wave velocity models for each block are shown in Table 4.3. This laterally varying crustal structure in the area makes the position of the ray path uncertain, and we rely on some approximations when analyzing the data.

As a first approximation we use straight ray paths through a homogeneous half-space and attempt to find the anomalies which can explain the attenuation data in the simplest manner. A map of the surface projection of the *very attenuated* ray paths is shown on Figure 4.6, and the area through which most of the rays pass is outlined. It is obvious that an anomaly of this size and extending over many kilometers in depth is the simplest explanation of the data, however many smaller anomalies could also explain the data.

Homogeneous Half-space

In a homogeneous half-space ray paths follow straight lines. Using these ray paths we examined the data on several vertical cross sections (Figure 4.7). The resulting

TABLE 4.3. Crustal Velocity Models

Coso		Sierra		Mojave	
V_p , km/s	Depth to Top of Layer, km	V_p , km/s	Depth to Top of Layer, km	V_p , km/s	Depth to Top of Layer, km
3.5	0.0	5.4	0.0	5.5	0.0
4.8	0.2	5.8	1.0	6.2	5.5
5.6	1.0	6.2	8.0	6.7	27.0
6.0	3.0	6.9	22.0	7.8	31.0
6.3	12.5	7.9	40.0		
7.8	24.5				

Coso - Walter and Weaver, 1980

Sierra - Jones and Dollar, 1986

Mojave - Hadley and Kanamori, 1977

TABLE 4.4. Locations of Events

Event #	YRMODA	HRMN	LAT	LON	D (km)	M _L	VM
2	831030	1352	36° 06.89'	117° 40.35'	3.2	2.2	Coso
3	840224	1343	35° 41.11'	118° 06.02'	10.5	1.6	Sierra
4	840224	1156	35° 55.10'	118° 19.27'	5.5	2.2	Sierra
5	840109	1518	35° 49.87'	117° 36.29'	7.5	1.7	Coso
6	840127	0119	35° 57.44'	117° 57.93'	9.8	2.3	Coso
7	840120	0118	35° 49.34'	117° 44.64'	6.8	2.2	Coso
8	831006	0720	35° 48.72'	117° 29.72'	6.5	1.2	Coso
9	840202	0824	35° 37.75'	118° 20.48'	13.6	1.9	Sierra
10	830724	2046	35° 43.48'	118° 24.46'	12.0	1.7	Sierra
11	830731	1608	35° 59.04'	117° 50.91'	7.4	2.0	Coso
12	840406	0906	35° 21.62'	117° 54.30'	10.2	1.3	Mojave
15	830907	2225	35° 43.07'	118° 03.63'	7.0	1.6	Sierra
16	840411	0554	35° 47.37'	118° 02.21'	9.4	1.9	Sierra
17	840412	2245	35° 45.51'	117° 59.71'	7.7	1.9	Sierra
18	850816	0753	36° 11.31'	117° 53.11'	9.6	4.3	Coso
19	850822	0052	35° 54.18'	117° 43.56'	9.5	4.5	Coso

Earthquakes 2, 5, 6, 7, 8, 11, 18, and 19 were located with Coso stations within 60 km and the Coso velocity model (VM). The Coso stations are CLC, LRM, SRT, TOW, WBM, WCH, WCP, WCS, WCX, WHS, WMF, WNM, WRV, WSC, WSH, and WVP. Earthquakes 3, 9, 10, 15, 16, and 17 were located with Sierra stations within 60 km and the Sierra velocity model. The Sierra stations are ISA, WAS, WBM, WBS, WCH, WCO, WHF, WJP, WKT, WNM, WOF, WOR, WSC, and WWP. Earthquake 4 was located with Sierra stations within 60 km, the Sierra velocity model, and additional stations WCP, WMF, and WRV. Earthquake 12 was located with all stations within 60 km and a Mojave velocity model.

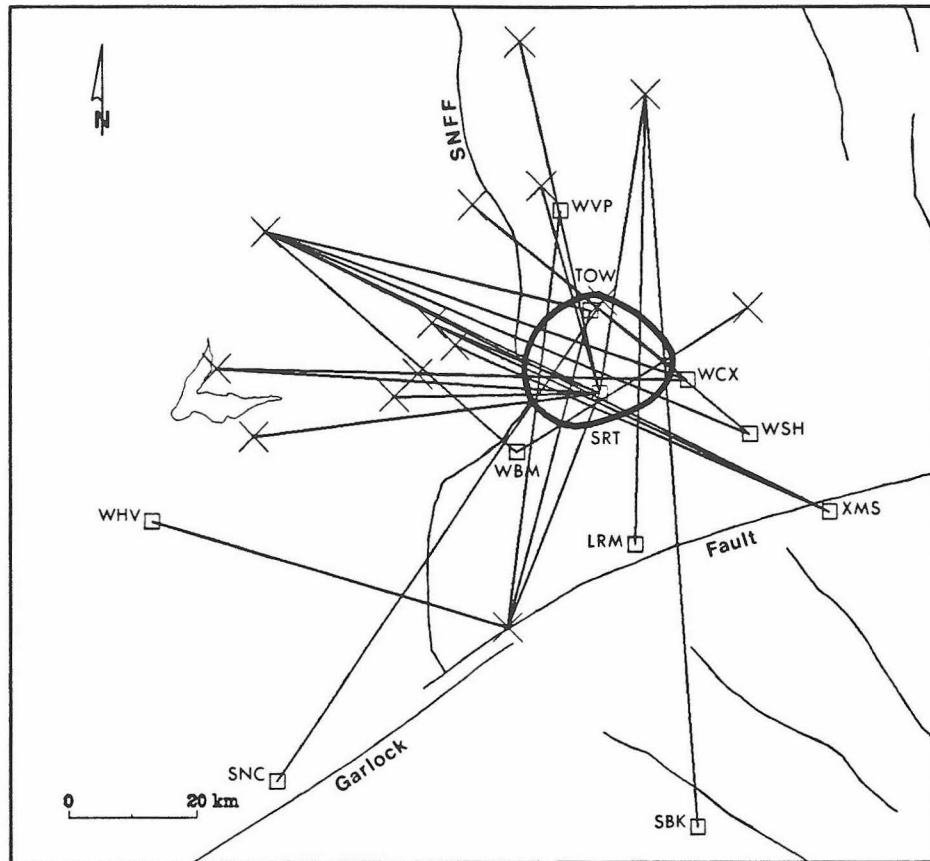


Figure 4.6. Map of very attenuated ray paths (AN-3). The outline of the single, simple anomaly which can explain most of the observations is shown.

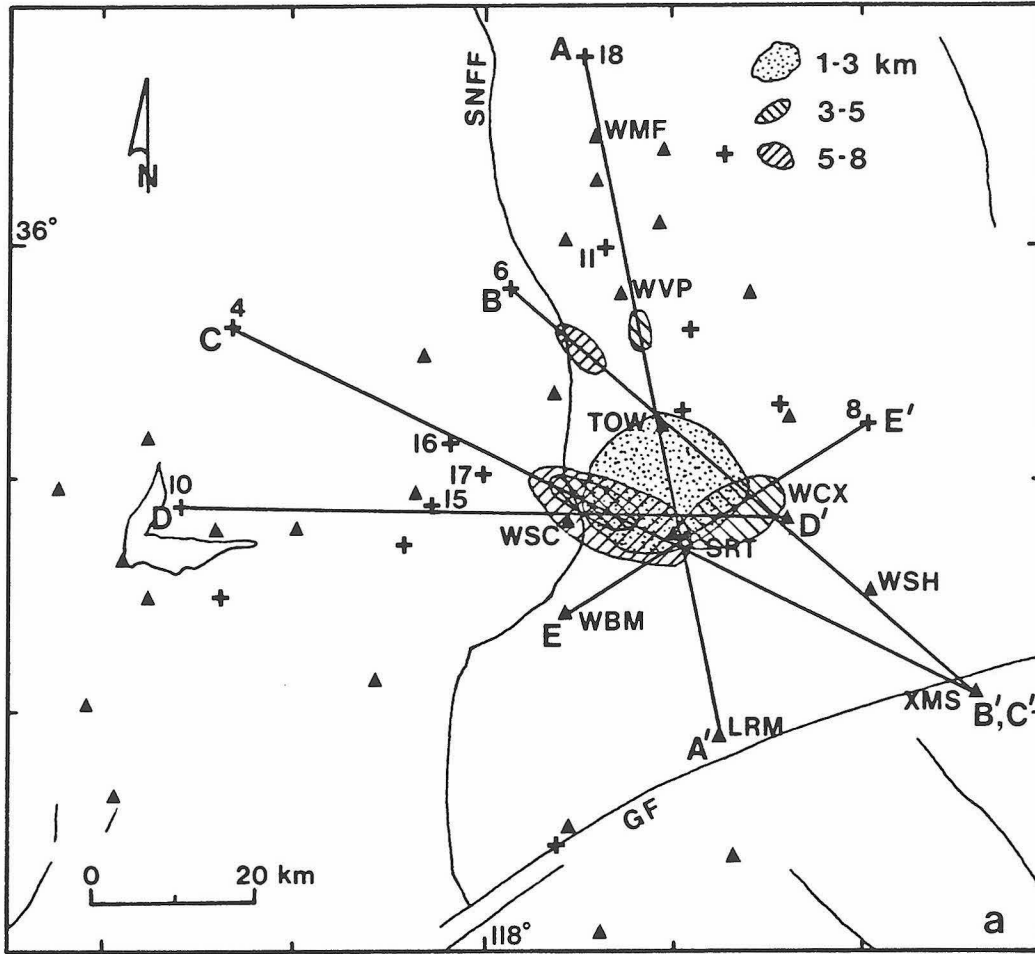
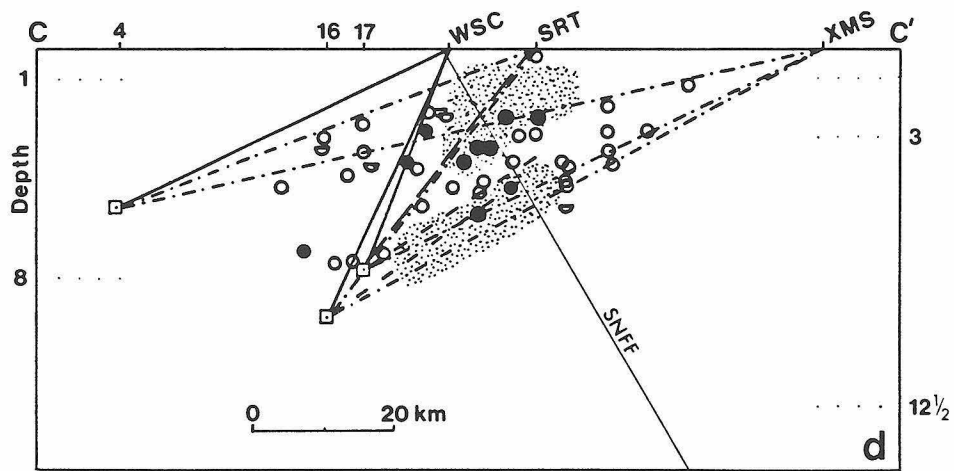
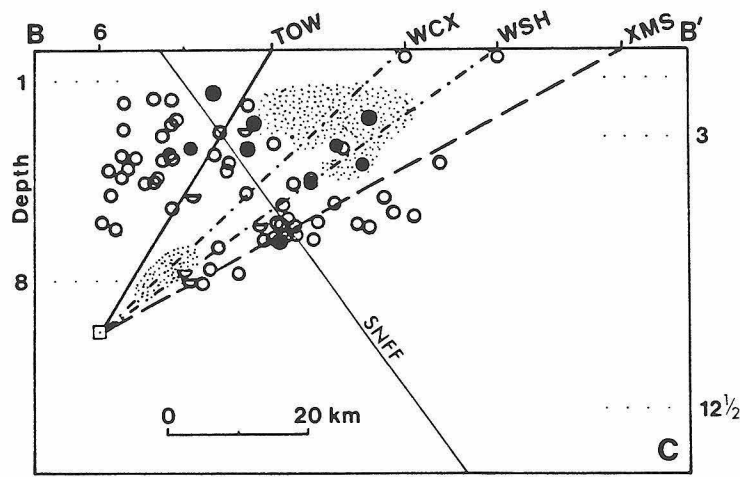
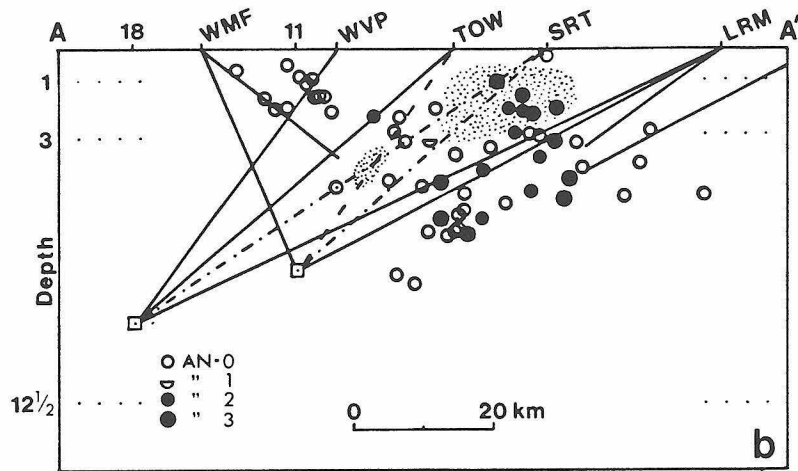
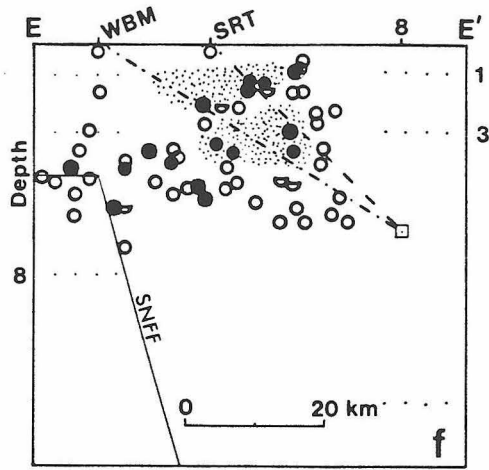
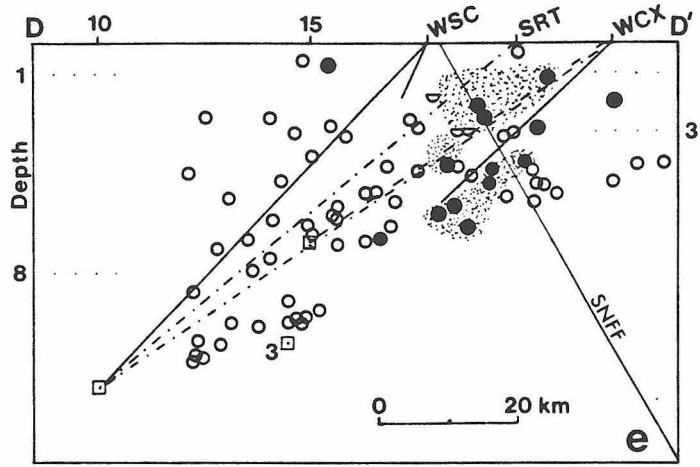


Figure 4.7. (a) Map showing locations of cross sections and locations of S-wave anomalies. The different depths of the anomalies are indicated by shading. (b) - (f) Cross sections A-A', B-B', C-C', D-D', and E-E'. The attenuation numbers (AN) corresponding to the different ray path line types are defined on Figure 4.5a. The circular symbols show where out-of-plane rays intersect the cross section and are defined in the lower left corner of the figure. The interpreted attenuation anomalies are indicated by shading. We have assumed a homogeneous, halfspace velocity model to construct the ray paths in these cross sections, however we indicate the positions of velocity boundaries for the appropriate models (Table 4.3) at the edges of each section. SNFF, Sierra Nevada frontal fault; GF, Garlock fault.





plots help place approximate constraints on the three-dimensional locations of attenuation anomalies. Figure 4.7a is a map showing the locations of the cross sections and also the interpreted location of some attenuation anomalies. Figures 4.7 b - f are the cross sections. The Sierra Nevada frontal fault is drawn in each section where appropriate, and the velocity boundaries in the Sierra and Coso crustal blocks are indicated by four horizontal dots near the edges of each figure. The sections have a vertical exaggeration of four. Each of the cross sections was constructed to be along an alignment of earthquakes and stations. In this way several ray paths are plotted on a given section in their entirety. Out-of-plane ray data is plotted where the rays intersect the vertical plane of the section. AN-0 ray paths are plotted as solid lines or hollow circles, AN-1 rays as long-dashed lines or half circles, AN-2 rays as short-dashed lines or solid dots, and AN-3 rays as dash-dot lines or solid dots. The AN-0 data constrain where the attenuation anomalies cannot be located in each section.

The locations of the attenuation anomalies we determined for various depth ranges are shown in Figure 4.7a. The best resolved anomaly occurs between depths of about 1 and 3 km and is located beneath the 20 by 20 km area centered between stations TOW and SRT. Another well-resolved anomaly lies beneath stations WSC and SRT in the depth interval 5-8 km. Less well-resolved anomalies lie in the 3-5 km depth range beneath station WSC and between stations SRT and WCX, and two small anomalies may lie at depth near stations WNM and WVP.

From this simple analysis we can identify with some certainty two S-wave attenuation anomalies beneath the western Indian Wells Valley. One large anomaly lies in the very shallow crust, definitely above 5 km depth, and seems to be bounded on the west by the Sierra Nevada frontal fault. Another anomaly between about 5 and 8 km depth lies beneath the western part of the shallower anomaly, possibly in the Sierra block just west of the downdip extension of the Sierra Nevada frontal fault. These anomalies may be connected. In addition, there appears to be no anomalous S-wave attenuation in the upper 5 km or so beneath the Coso geothermal area. This is

consistent with the results of earlier studies that indicate relatively normal crust beneath Coso to a depth of about 10 km (e.g. special issue on the Coso geothermal area, *J. Geophys. Res.*, 85(B5), 1980).

The ray paths through the half-space are simplified from the more complex ray paths through the layered and laterally heterogeneous crust. In general the half-space ray paths tend to be shallower. Next we compare the results obtained from visual inspection of the data with the results of a tomographic inversion of the data. The tomographic inversion uses the layered Coso P-wave velocity model (Walter and Weaver, 1980) and thus may give a better estimate of the depths of the anomalies.

4.6 Tomographic Inversion

The S-wave attenuation data were tomographically inverted for the relative S-wave attenuation structure in the Coso-Indian Wells Valley region. The version of the tomographic inversion scheme used here is the one used by Walck and Clayton (1986) for inversion of P-wave residuals. Here the method is applied to attenuation data instead of travel-time data. A similar application has been made previously to attenuation data for the Imperial Valley, California (P. Ho-Liu, pers. comm., 1985).

In the tomographic inversion for velocity structure the crust under study is divided into blocks within which a constant slowness is assumed. Then the problem is formulated as

$$t_i = \sum_j l_{ij} s_j \quad (4.1)$$

where t_i is the travel time of the i -th ray, l_{ij} is the path length of the i -th ray in the j -th block, and s_j is the slowness of the j -th block. A straightforward modification of (4.1) for attenuation data is

$$\ln(a_i) = \sum_j l_{ij} k_j \quad (4.2)$$

where a_i is the amplitude of the i -th ray and k_j is the attenuation constant of the j -th

block. Since (4.1) and (4.2) are identical in form the standard tomographic method can be applied to attenuation data.

One difficulty is that the absolute amplitude data, a_i , are seldom available. In our case, the qualitative measures of attenuation are used, and therefore we use (4.2) to determine only the location and shape of the anomalous bodies. By assigning values which are proportional to the degree of attenuation to the left hand side of (4.2) we can formally solve (4.2) for k_j . Of course, the result depends on the values assigned. However, inasmuch as the shape of the attenuating body mainly determines the spatial distribution of the attenuated paths, we hope that the geometry of the anomalous body can be approximately determined by this inversion. The absolute value of k_j itself has no physical significance.

We present here the results of the tomographic inversion using a crust parameterized into blocks 2 km square and 1 km deep. The values of a_i used are the same within each attenuation group and corresponded to the approximate characteristic A_S/A_P in each group. The a_i values are 0.1, 0.4, 0.7, and 1.0, corresponding to attenuation groups AN-3, AN-2, AN-1, and AN-0, respectively. Inversions with different sets of values of a_i are essentially the same. Though the data set is relatively sparse it samples the study area from many different azimuths and take-off angles. The resolution of the tomographic inversion of this data set is not discussed, since we only wish to compare the forward and inverse results in a general way.

The data were first inverted with a homogeneous half-space velocity model so that comparison could be made with the forward model described earlier. This comparison helps us understand how the inversion resolves structure from the data set. The inversion results are shown in Figure 4.8. Only blocks with at least two rays traversing them are plotted. As can be seen the anomalies mapped from visual inspection (Figure 4.7) are also resolved from the tomographic inversion. This gives us confidence that the inversion is for the most part correctly resolving structure. The significance of all of the tomographically resolved anomalies is not known, however, and the sizes of the

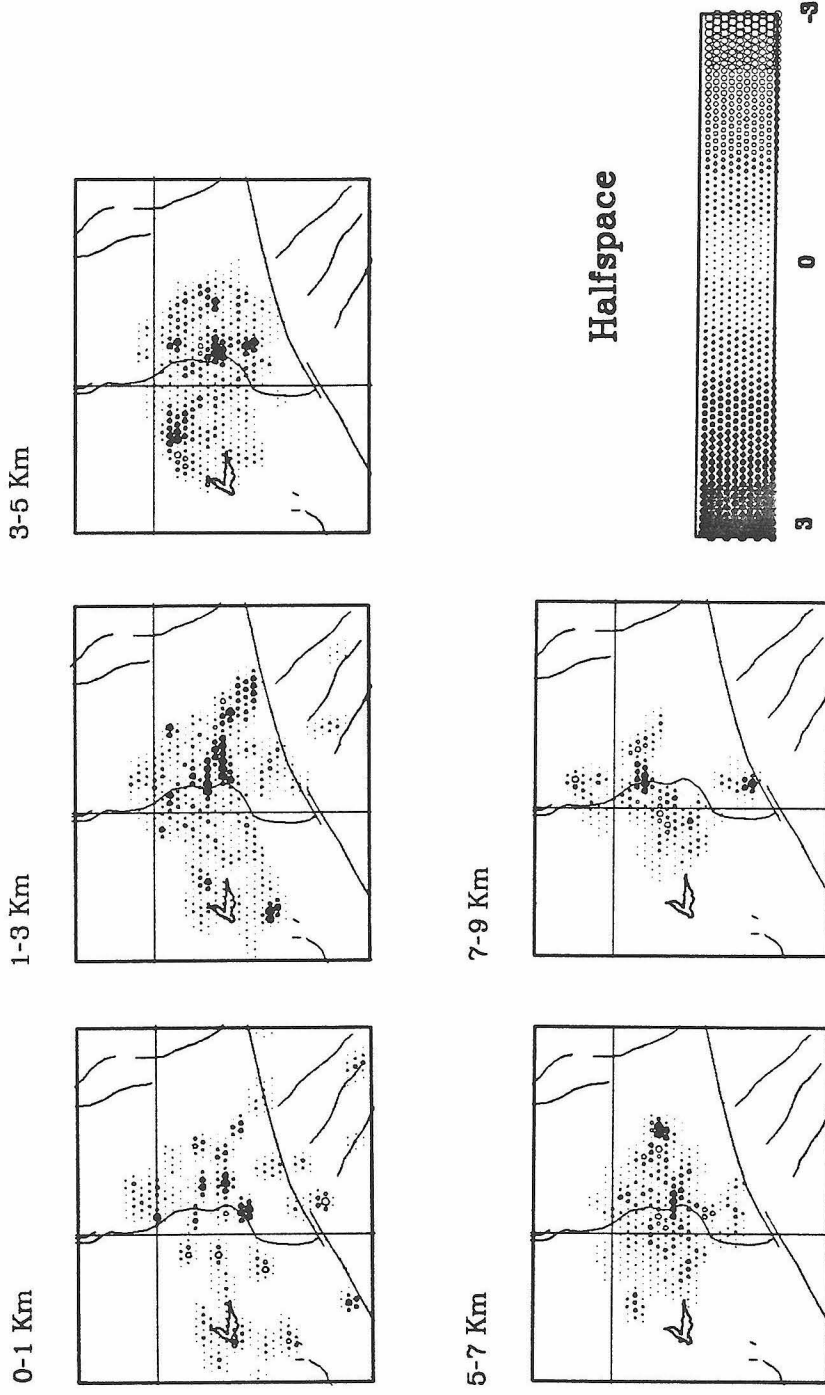


Figure 4.8. Maps showing the results of a tomographic inversion of the attenuation data for various depth ranges. The velocity model used for ray tracing is a halfspace. Shading scale: the degree of attenuation ranges from 3 (*very attenuating*) to 0 (*normal*); values from 0 to -3 are all normal. The well resolved anomalies are the dark shaded areas in the center of the maps for depth ranges 1-3, 3-5, and 5-7 km. For geographic reference see Figures 4.4 and 4.7a.

principal anomalies are approximate.

The crustal velocity structure in the area is not well represented by a homogeneous half-space, so we next inverted the data using the layered crustal velocity model determined for the Coso area (Walter and Weaver, 1980). The results of this inversion give us a better estimate of the depths of the anomalies. Figure 4.9 shows the results for five different depth ranges. The principal shallow attenuation anomaly lies in the 3-5 km depth range beneath the Indian Wells Valley and is bounded on the west by the Sierra Nevada frontal fault. This anomaly extends into the 5-7 km depth range where it lies more westerly beneath the surface trace of the fault. As was determined in the forward modeling these are the best constrained of the anomalies. A single anomaly is seen in the 7-9 km depth range north of station WNM. The principal results of this inversion can be seen clearly in the color plates in Figure 4.10.

It is instructive to compare the S-wave attenuation results with those of the tomographic inversion of over 4000 P-wave travel time delays in the same area (Walck and Clayton, 1986). We compare the results in three depth ranges, 3-5, 5-7, and 7-9 km (Figure 4.11). In short, the results of the inversions of the two data sets agree remarkably well, and the well-resolved individual anomalies correlate closely. In the 3-5 km depth range the large, well-resolved anomaly beneath stations SRT, WSC, and TOW is seen in both the P- and S-wave data as is an anomaly in the 5-7 km depth range beneath stations WSC and SRT and also the single anomaly in the 7-9 km depth range north of station WNM.

The good correlation between the S-wave attenuation and P-wave travel time anomalies is encouraging since it indicates that the two different wave transmission phenomena are sensitive to the same conditions in the anomalous crust in this area. It also gives some indication of the resolution possible using seismic tomography when a relatively homogeneous ray data set is available.

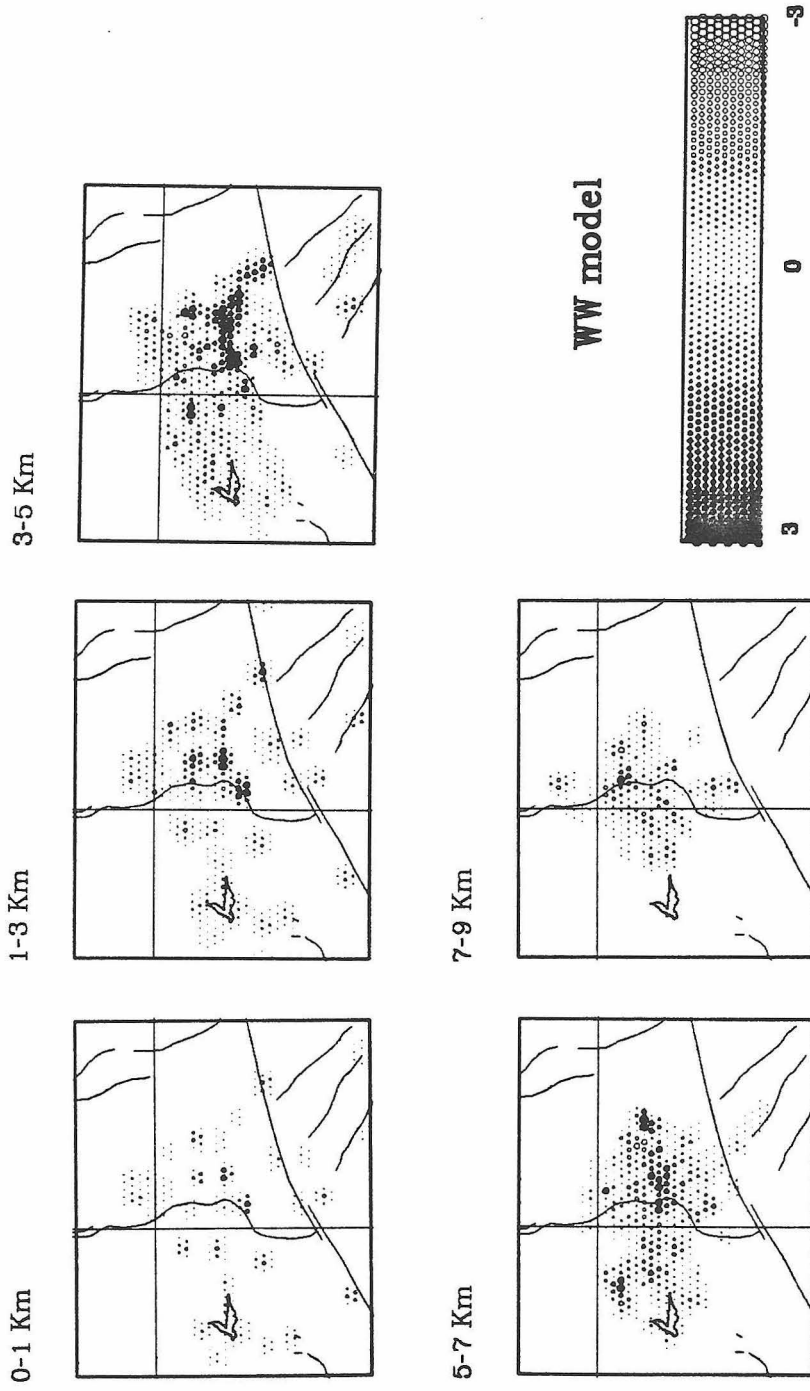


Figure 4.9. Maps similar to Figure 4.8 except that the Coso velocity model is used (Table 4.3). The principal attenuation anomalies lie in the 3-5 and 5-7 km depth ranges.

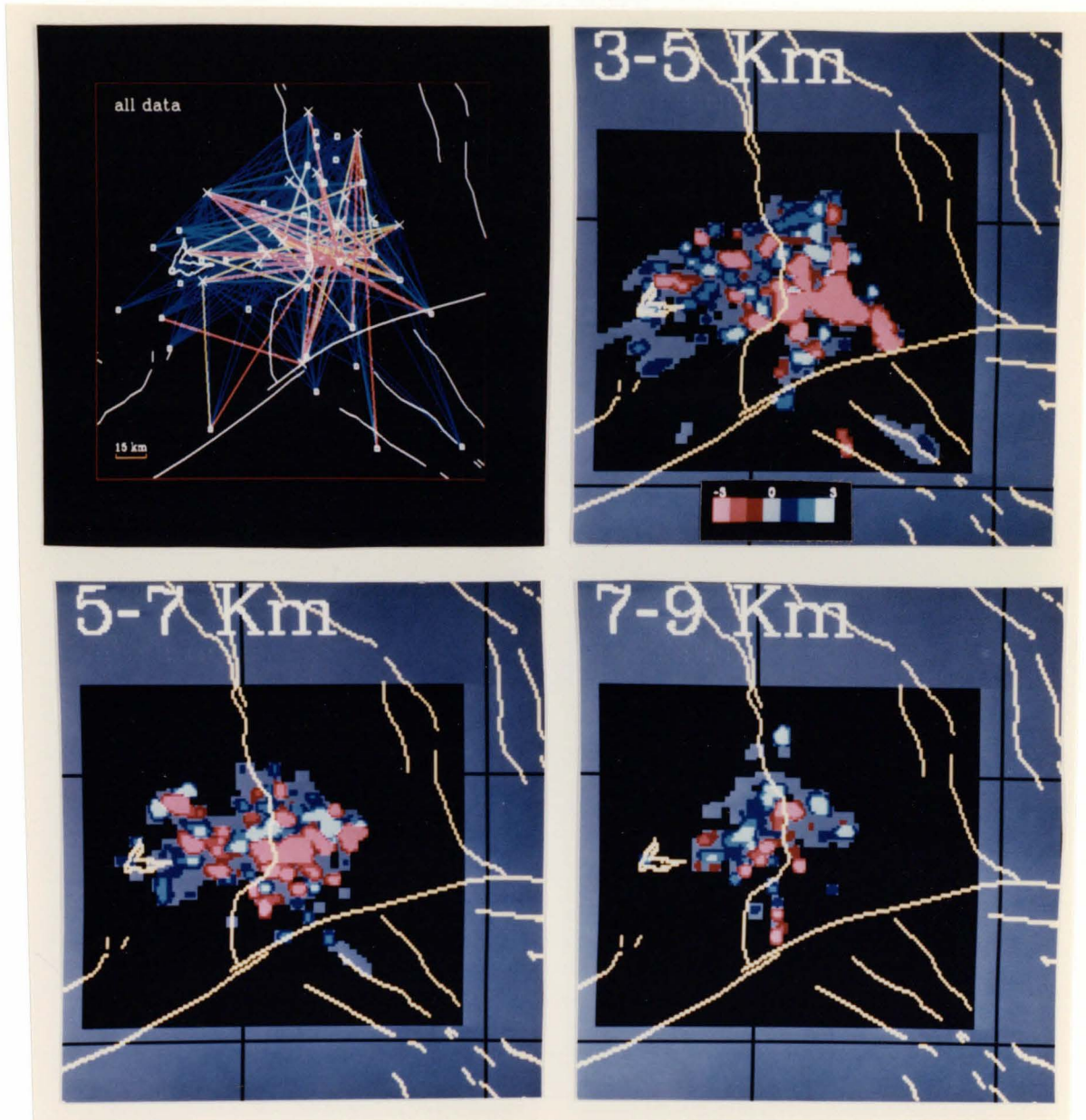


Figure 4.10. Color pictures of some S-wave attenuation results. The upper left frame shows all of the ray paths used in this study. The Xs are event epicenters, and the small squares are station locations. The major faults in the area are added for reference (see Figure 4.4). The ray colors decode as follows: dark blue, no anomalous attenuation, AN-0; light blue, minor attenuation, AN-1; yellow, moderate attenuation, AN-2; red, severe attenuation, AN-3. The other frames are color versions of three depth slices in Figure 4.9. The color-value scale is shown in the upper right frame and compares with the scale in Figure 4.8.

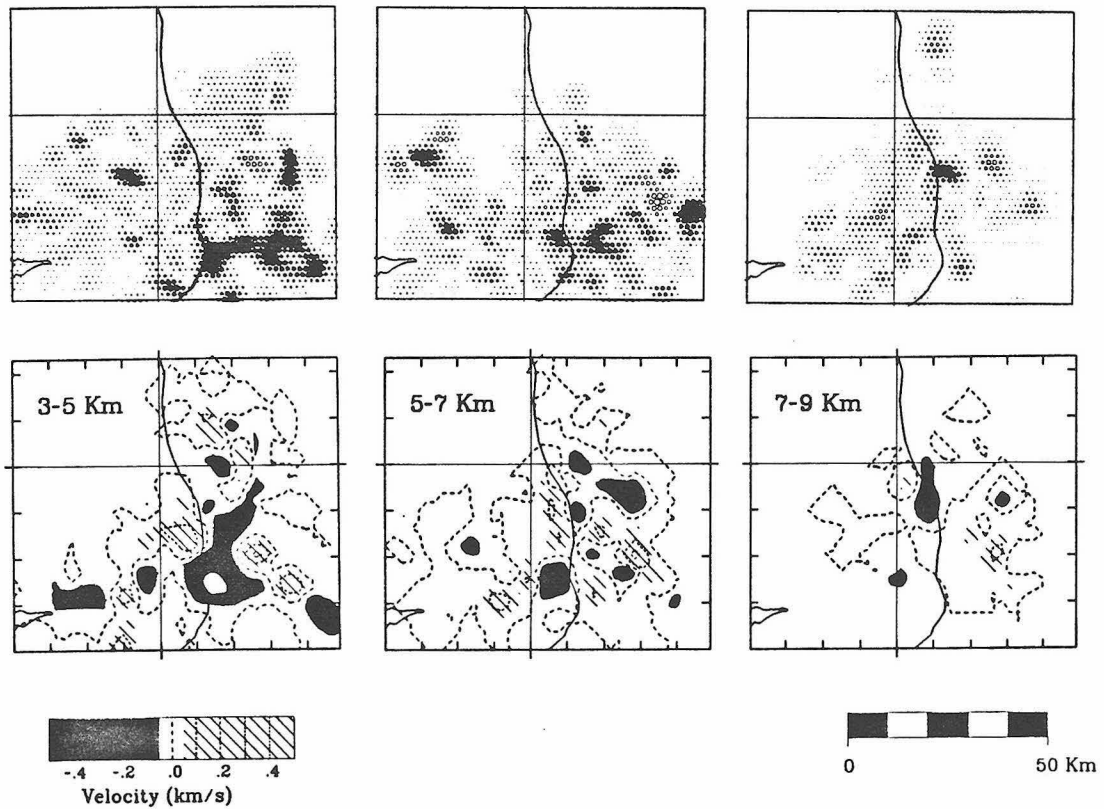


Figure 4.11. Comparison of S-wave attenuation (upper) and P-wave velocity (lower) anomalies in three depth zones beneath the Coso-Indian Wells Valley area. Both data sets were inverted tomographically using the Coso velocity model (Table 4.3) for ray tracing. Note the correlation of anomalies in the lower right quadrant of each frame. The dark shaded anomalies correspond to high S-wave attenuation (upper frames) or low P-wave velocities (lower frames). The P-wave velocity perturbation scale is shown in the lower right corner, and the S-wave attenuation scale is explained in Figure 4.8. The P-wave results are from Walck and Clayton (1986).

4.7 Earthquake Swarms

The area of Indian Wells Valley coincident with the observed S-wave attenuation and P-wave velocity anomalies was also the site of swarms of small earthquakes from February 1982 to March 1983. Figure 4.12 shows the locations of the main S-wave attenuation anomaly and the earthquake swarms. Four principal periods of swarm activity are illustrated. From the epicenter plots we see that principal earthquake activity began in a single cluster and later expanded north and south into two separate clusters. The time-distance plot (Figure 4.13) also illustrates this earthquake migration. This migratory behavior may be related to a migrating fluid phase (magma filled dikes or pore fluids) as has been suggested by Hill (1977) and Johnson (1979) for migrating Imperial Valley swarm seismicity.

Master-event relocation of the earthquakes in this swarm sequence indicates that most of the events occur deeper than 5 km and principally between 5 and 10 km depth (A. Bent, pers. comm., 1986). This is below the principal attenuation anomaly. If the Sierra Nevada frontal fault dips about 60° in this area, as may be expected for a major normal fault, then these earthquakes are probably occurring beneath the Indian Wells Valley sediments and within the Sierra Nevada block near and below the frontal fault. This fault is a boundary fault of the Basin and Range extensional province. This extension is also manifested further west in the Sierra block, in focal mechanisms of the Durwood earthquake sequence (Jones and Dollar, 1986). Passive intrusion of magma into the shallow crust in areas of local or regional extension is suggested in models described by Hill (1977) and Lachenbruch and Sass (1978). Thus the Indian Wells Valley S-wave attenuation and P-wave velocity anomalies and earthquake swarms may be related to local magmatic activity associated with the extensional processes in the area.

4.8 Conclusions

In this study we have used S_V -wave seismograms of local earthquakes recorded on the dense, local Caltech-USGS seismic array to image S-wave attenuation anomalies in

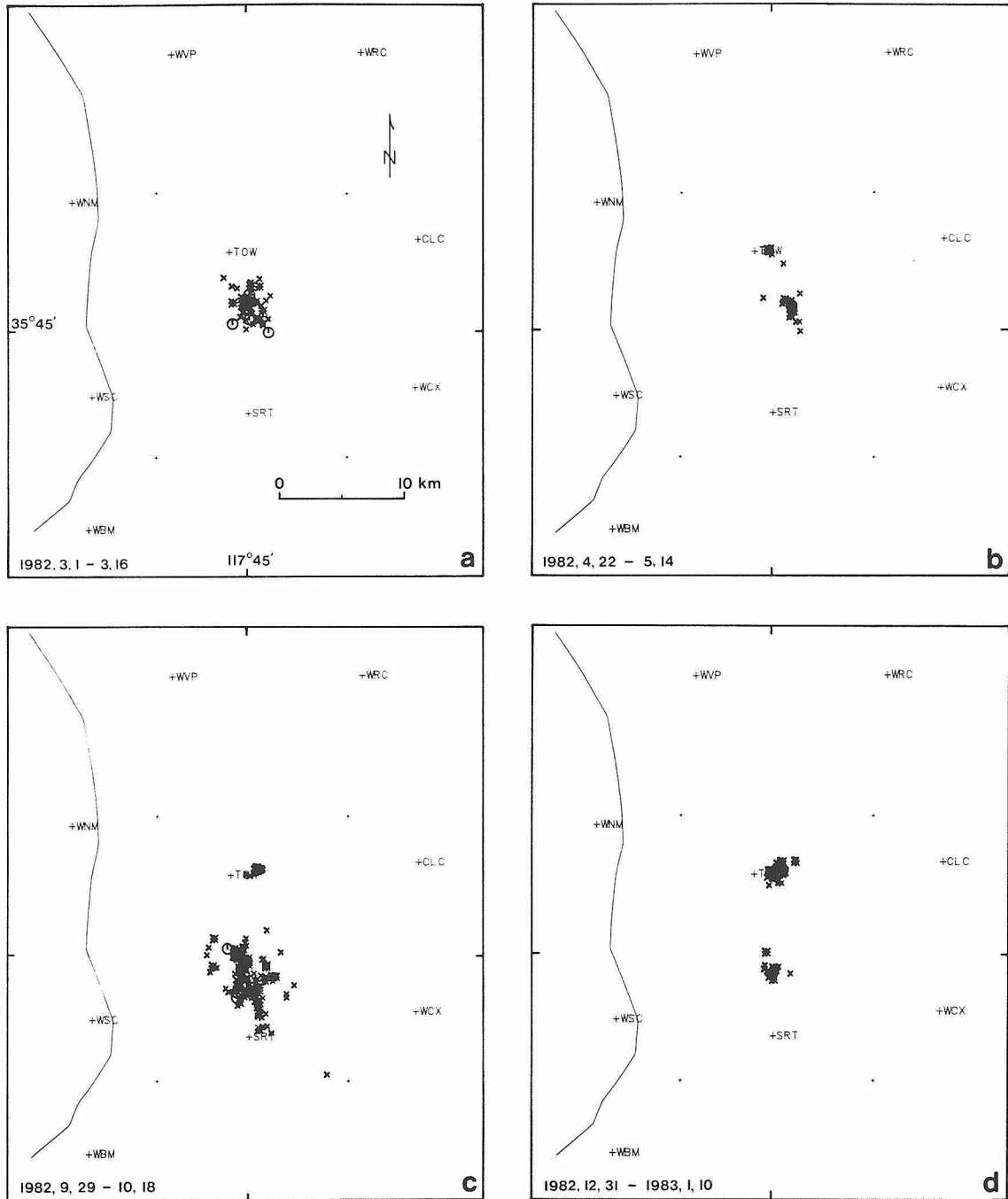


Figure 4.12. (a) - (d) Maps of epicenters of earthquakes which occurred in the area of the S-wave attenuation anomalies (Figure 4.7a) for the time periods indicated. The magnitude symbol scale is: x = M 2-3, * = M 3-4, o = M 4-5.

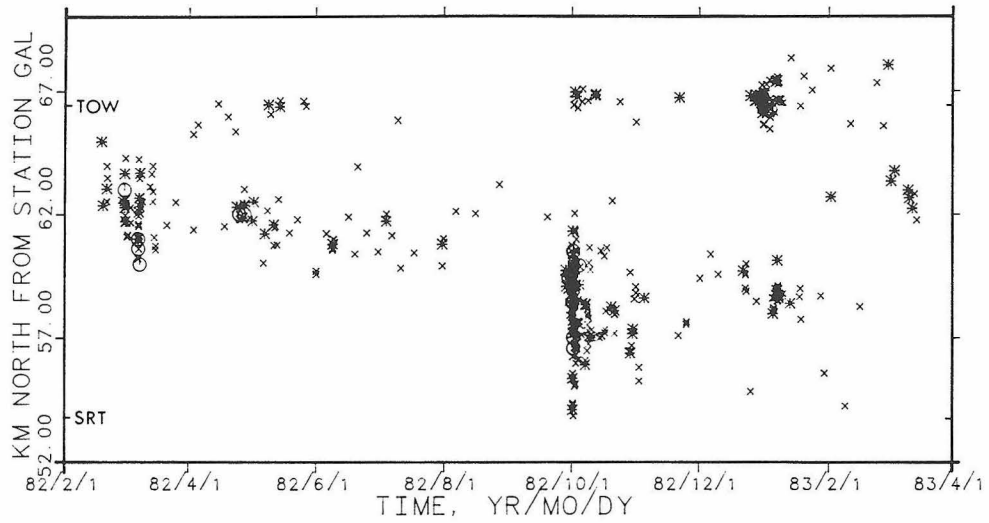


Figure 4.13. Time-distance plot of swarm earthquakes projected onto a N-S line through stations TOW and SRT. Note the migration with time of the locus of earthquake activity. Magnitude symbols are the same as in Figure 4.12.

the shallow crust beneath the Coso-Indian Wells Valley region, California. This is done principally by visual inspection of the data, though a tomographic inversion of the data resolves the same structure. These anomalies spatially coincide with P-wave velocity anomalies (slow) imaged by Walck and Clayton (1986). The close association of the anomalies with the Sierra Nevada frontal fault suggests a relation between the local extensional stresses and the anomalies. Propagating earthquake swarms, thermal wells, and anomalous ground deformation suggest magmatic/hydrothermal associations as well (Roquemore and Zellmer, 1983; Zellmer et al., 1985). An electrical conductivity study by Lienert (1979) found that conductivity in the deep crust along a profile line from the Sierra Nevada Mountains into Indian Wells Valley increases sharply east of the Sierra Nevada frontal fault. The shallow crust above about 5 km beneath the Coso geothermal area appears normal on length scales of about a kilometer.

This and previous studies have shown the usefulness of S-wave seismograms recorded on dense local arrays for imaging the relative S-wave attenuation structure in the shallow crust in volcanic/geothermal regions. When coupled with P-wave velocity studies these can be useful for constraining the character of crustal heterogeneities in these regions.

4.9 References

- Bailey, R. A., G. B. Dalrymple, and M. A. Lanphere, Volcanism, structure, and geochronology of Long Valley caldera, Mono County, California, *J. Geophys. Res.*, *81*, 725-744, 1976.
- Cramer, C. H. and T. R. Toppozada, A seismological study of the May 1980 and earlier earthquake activity near Mammoth Lakes, California, *Calif. Div. Mines Geol. Spec. Rept. 150*, 91-130, 1980.
- Einarsson, P., S-wave shadows in the Krafla caldera in NE-Iceland, evidence for a magma chamber in the crust, *Bull. Volcanol.*, *41-43*, 1-9, 1978.
- Fedetov, S. A. and A. E. Faberov, On screening of transverse seismic waves and magmatic chamber in the upper mantle of the Avacha group volcanoes region, in *Volcanism and deep structure of the Earth*, *3*, Moscow, 1966 (in Russian).
- Gorshkov, G. S., On the depth of the magmatic chamber of the Kliuchevskiy volcano, *DAN USSR*, *106(4)*, 703-705, 1956 (in Russian).
- Hadley, D. and H. Kanamori, Seismic structure of the Transverse Ranges, California, *Geol. Soc. Am. Bull.*, *88*, 1469-1478, 1977.
- Hill, D. P., Structure of Long Valley caldera from a seismic refraction experiment, *J. Geophys. Res.*, *81*, 745-753, 1976.
- Hill, D. P., A model for earthquake swarms, *J. Geophys. Res.*, *82(8)*, 1347-1352, 1977.
- Hutton, L. K., C. R. Allen, and C. E. Johnson, Seismicity of southern California - earthquakes of M_L 3.0 and greater, 1975 through 1983, *Seism. Lab., Calif. Inst. Tech.*, Pasadena, CA, 1985.
- Johnson, C. E., CEDAR — an approach to the computer automation of short-period local seismic networks, *Ph.D. Thesis, California Institute of Technology*, Pasadena, 332 p., 1979.
- Jones, L. M. and R. S. Dollar, Evidence of Basin-and-Range extensional tectonics in the Sierra Nevada: the Durrwood Meadows swarm, Tulare County, California (1983-1984), *Bull. Seism. Soc. Am.*, *76(2)*, 439-461, 1986.
- Kissling, E., W. L. Ellsworth, and R. S. Cockerham, Three-dimensional structure of Long Valley caldera, California, region by geotomography, in *U.S.G.S. Open-File Report 84-939*, 188-220, 1984.
- Kubota, S. and E. Berg, Evidence for magma in the Katmai volcanic range, *Bull. Volcanol.*, *31*, 175-214, 1967.
- Lachenbruch, A. H., M. L. Sorey, R. E. Lewis, and J. H. Sass, The near-surface hydrothermal regime of Long Valley caldera, *J. Geophys. Res.*, *81*, 763-768, 1976.
- Lachenbruch, A. H. and J. H. Sass, Models of an extending lithosphere and heat flow in the Basin and Range province, *Geol. Soc. Am. Mem.*, *152*, 209-250, 1978.
- Latter, J. H., Location of zones of anomalously high S-wave attenuation in the upper crust near Ruapehu and Ngauruhoe volcanoes, New Zealand, *J. Volc. Geotherm. Res.*, *10*, 125-156, 1981.
- Lienert, B. D., Crustal electrical conductivities along the eastern flank of the Sierra Nevadas, *Geophysics*, *44(11)*, 1830-1845, 1979.

- Matumoto, T., Seismic body waves observed in the vicinity of Mount Katmai, Alaska, and evidence for the existence of molten chambers, *Geol. Soc. Am. Bull.*, *82*, 2905-2920, 1971.
- Miller, D., Holocene eruptions at the Inyo volcanic chain, California: implications for possible eruptions in Long Valley caldera, *Geology*, *13*, 14-17, 1985.
- Roquemore, G. R. and J. T. Zellmer, Tectonics, seismicity, and volcanism at the Naval Weapons Center, *Naval Res. Rev.*, *35*, 3-9, 1983.
- Rundle, J. B. and J. A. Whitcomb, A model for deformation in Long Valley, California, 1980-1983, in *U.S.G.S. Open-File Report 84-939*, 584-616, 1984.
- Ryall, A., and F. Ryall, Attenuation of P- and S-waves in a magma chamber in Long Valley caldera, California, *Geophys. Res. Lett.*, *8*, 557-560, 1981.
- Sanders, C. O., Location and configuration of magma bodies beneath Long Valley, California determined from anomalous earthquake signals, *J. Geophys. Res.*, *89*(B10), 8287-8392, 1984.
- Sanders, C. O., and F. Ryall, Geometry of magma bodies beneath Long Valley, California, determined from anomalous earthquake signals, *Geophys. Res. Lett.*, *10*(8), 690-692, 1983.
- Sanders, C., D. Rinn, and H. Kanamori, Anomalous shear-wave attenuation in the shallow crust beneath the Indian Wells Valley-Coso region, California, *EOS*, *65*(45), 1009, 1984.
- Sanders, C., D. Rinn, P. Ho-Liu, and H. Kanamori, Anomalous shear-wave attenuation in the shallow crust beneath the Coso region, California, *J. Geophys. Res.*, 1986 or 1987.
- Savage, J. C., and M. M. Clark, Magmatic resurgence in Long Valley caldera, California: Possible cause of the 1980 Mammoth Lakes earthquakes, *Science*, *217*, 531-533, 1982.
- Steeple, D. W., and H. M. Iyer, Low-velocity zone under Long Valley as determined from teleseismic events, *J. Geophys. Res.*, *81*, 849-860, 1976.
- Walck, M. C. and R. W. Clayton, P-wave velocity variations in the Coso region, California, derived from local earthquake travel times, *accepted JGR*, 1986.
- Walter, A. W. and C. S. Weaver, Seismicity of the Coso Range, California, *J. Geophys. Res.*, *85*(B5), 2441-2458, 1980.
- Wood, S. H., Distribution, correlation, and radiocarbon dating of late Holocene tephra, Mono and Inyo craters, eastern California, *Geol. Soc. Am. Bull.*, *88*, 89-95, 1977.
- Zellmer, J. T., C. O. Sanders, and G. R. Roquemore, Tectonic and possible volcanic interactions within Indian Wells Valley, southeastern California (abs.), *Geol. Soc. Am. Abs. Progs.*, *17*(6), 1985.